

Aus dem Institut für Immunologie der Ludwig-Maximilians-Universität München

Leitung: Prof. Dr. Thomas Brocker

# **Screening for cofactors in Roquin-mediated post-transcriptional gene regulation**

Dissertation

zum Erwerb des Doktorgrades

der Naturwissenschaften (Dr. rer. nat.)



an der Medizinischen Fakultät der  
Ludwig-Maximilians-Universität zu München

vorgelegt von

**Nina Beate Rehage**

aus Bayreuth

München, 2016

Für meine Eltern

**Gedruckt mit Genehmigung der Medizinischen Fakultät der  
Ludwig-Maximilians-Universität München**

Betreuer:	Prof. Dr. Vigo Heissmeyer
Zweitgutachter:	Prof. Dr. Peter Becker
Dekan:	Prof. Dr. med. dent. Reinhard Hickel
Tag der mündlichen Prüfung:	08.11.2016



# Eidesstattliche Versicherung

Rehage, Nina

---

Name, Vorname

Ich erkläre hiermit an Eides statt, dass ich die vorliegende Dissertation mit dem Thema

***“Screening for cofactors in Roquin-mediated post-transcriptional gene regulation”***

selbständig verfasst, mich außer der angegebenen keiner weiteren Hilfsmittel bedient und alle Erkenntnisse, die aus dem Schrifttum ganz oder annähernd übernommen sind, als solche kenntlich gemacht und nach ihrer Herkunft unter Bezeichnung der Fundstelle einzeln nachgewiesen habe.

Ich erkläre des Weiteren, dass die hier vorgelegte Dissertation nicht in gleicher oder in ähnlicher Form bei einer anderen Stelle zur Erlangung eines akademischen Grades eingereicht wurde.

---

Ort, Datum

---

Unterschrift Doktorandin



## Summary

Roquin paralogs are RNA-binding proteins and crucial regulators of T cell differentiation. Roquin-1 binds to the 3' UTR of its target mRNAs, which are cytokines, costimulatory receptors and transcription factors or modulators, leading to post-transcriptional repression of mRNA expression. Mutation of Roquin-1 or T cell-specific ablation of Roquin-1 and its paralog Roquin-2 in mice causes spontaneous activation of T cells and the accumulation of T follicular helper cells and Th17 cells. The resulting autoimmune phenotypes and pathology in mice are similar to systemic lupus erythematosus (SLE) for the Roquin-1 point mutant or show lung pathology for mice that lack Roquin proteins in T cells. Still, the mechanism of Roquin-mediated post-transcriptional gene regulation and especially the identities of regulators and cofactors of Roquin have not been resolved.

In order to identify cofactors of Roquin-1 in its gene regulatory pathway, we performed two high-throughput screens with reporter cell lines. First, new cofactors of Roquin-1 in post-transcriptional gene regulation of the T cell costimulatory receptor ICOS were identified in a targeted RNAi screen. In a second approach, a genome-wide CRISPR/Cas9 screen led to the identification of protein networks involved in a new pathway of Roquin-induced cell death. Focusing on RNA-binding proteins, I developed a hit validation strategy and could confirm the uncharacterized protein Nufip2 as a novel player in this pathway. The burning question how Roquin-mediated ICOS repression involves Nufip2 was subsequently addressed in in-depth analyses. These uncovered that Nufip2 interacts with Roquin-1 in cells. This interaction was direct and showed high affinity. The *cis*-elements in human *ICOS* that are targeted by Roquin-1 and which are potentially coregulated by Nufip2 were mapped and the kinetics of *Icos* regulation during effector T cell differentiation was determined. In this time course of T cell activation Nufip2 and other potential cofactors of Roquin-1 showed strikingly different expression patterns, suggesting that different cofactors contribute to Roquin's function and *Icos* regulation in a dynamic manner. Overall, the identification and validation of new cofactors of Roquin-1 in this research project strongly expands current knowledge on the assembly of mRNA-protein complexes that coordinate Roquin-mediated mRNA degradation, and thus contributes to our understanding of its role in mediating immunological tolerance.



## Zusammenfassung

Die Paraloge Roquin-1 und Roquin-2 sind RNS-bindende Proteine, welche einen wichtigen Beitrag zur Kontrolle der T-Helferzell-Differenzierung leisten. Roquin-1 bindet an Sekundärstrukturen im untranslatierten Bereichen seiner Ziel-mRNS, die für Zytokine, kostimulatorische Rezeptoren, Transkriptionsfaktoren und Transkriptionsmodulatoren kodieren, und induziert eine post-transkriptionelle Repression der mRNA-Expression. Eine Punktmutation in Roquin-1 oder die Deletion beider Roquin-Paraloge in T-Zellen führt in Mausmodellen zu einem spontanen T-Zellaktivierungs-Phänotyp und einer Anreicherung von follikulären T-Helferzellen beziehungsweise von Th17 Zellen. Im Falle der Roquin-Punktmutation kommt es hierdurch zu Lupus-ähnlicher Autoimmunität, während das Fehlen von Roquin in T-Zellen krankhafte Veränderungen des Lungengewebes hervorruft. Der Mechanismus der Roquin-vermittelten post-transkriptionellen Genregulation ist jedoch noch nicht vollständig aufgeklärt, und insbesondere essentielle Kofaktoren und Regulatoren der Roquin-Funktion sind weitestgehend unbekannt.

Um neue Kofaktoren von Roquin-1 in seinem genregulatorischen Signalweg zu identifizieren, wurden im Zuge dieser Arbeit zwei verschiedene Hochdurchsatz-Screenings mit Reporter-Zelllinien durchgeführt. In einem RNS-Interferenz-Screening wurden sieben verschiedene Kategorien von Genen nach Kofaktoren der Roquin-1-vermittelten Inhibition des T-Zell-Kostimulators ICOS systematisch durchsucht, während die CRISPR/Cas Screening-Technologie angewandt wurde, um Protein-Netzwerke zu identifizieren, welche an Roquin-vermitteltem Zelltod beteiligt sind. Im Zuge der Entwicklung einer Hit-Validierungs-Strategie wurde ein RNS-bindender Kandidat, das noch unerforschte Protein Nufip2, als neuer Kofaktor von Roquin-1 bestätigt. Um die noch unbekannte Rolle von Nufip2 in der durch Roquin-1 vermittelten Genregulation weiter aufzuschlüsseln, wurden detaillierte Funktionsstudien durchgeführt. In diesen wurde gezeigt, dass Nufip2 eine direkte und hochaffine Protein-Protein-Wechselwirkung mit Roquin-1 eingeht. Außerdem wurden die wichtigsten Roquin-1-regulierten *Cis*-Elemente im 3' untranslatierten Bereich der ICOS mRNA als Orte potenzieller Nufip2-Koregulation bestimmt. Abschließend wurde in einer detaillierten Kinetik dargestellt, wie Icos in der Effektor-T-Zelldifferenzierung reguliert wird. Nufip2 und weitere potentielle Kofaktoren von Roquin-1 wiesen in diesem Zeitraum unterschiedliche Expressionsmuster auf. Hieraus ergibt sich ein

neues Modell zur Regulation der Roquin-1-Funktion und der Expression von Icos durch den dynamischen Beitrag verschiedener Kofaktoren von Roquin-1.

Insgesamt wurden im Zuge dieser Arbeit neue Kofaktoren von Roquin-1 erfolgreich identifiziert und validiert. Die so gewonnenen Erkenntnisse sind bedeutsam für die Aufklärung der dynamischen Ausbildung von Proteinkomplexen mit mRNA als Koordinatoren der Roquin-Funktion und tragen somit zum Verständnis der Rolle von Roquin-1 im Kontext der Entstehung immunologischer Toleranz bei.

# Directory

<b>Eidesstattliche Versicherung</b> .....	<b>5</b>
<b>Summary</b> .....	<b>7</b>
<b>Zusammenfassung</b> .....	<b>9</b>
<b>List of figures</b> .....	<b>15</b>
<b>List of tables</b> .....	<b>17</b>
<b>Abbreviations</b> .....	<b>18</b>
<b>1 Introduction</b> .....	<b>25</b>
1.1 Post-transcriptional gene regulation .....	25
1.1.1 Deadenylation- and decapping-dependent mRNA decay .....	26
1.1.2 Storage of translationally silenced mRNAs in granule-like structures .....	28
1.1.3 Mechanisms of RNA-interference .....	30
1.1.4 RNA-binding proteins .....	32
1.1.4.1 The FMR protein family .....	33
1.1.4.2 Roquin family proteins .....	33
1.1.4.3 Regnase family proteins .....	35
1.2 The immune system .....	36
1.2.1 The adaptive immune response in mammals .....	36
1.2.1.1 T cell priming and activation of antigen-presenting B cells .....	37
1.2.1.2 Initiation of a T cell-dependent antibody response .....	39
1.2.1.3 Lineage determination of T cell differentiation .....	40
1.2.1.4 The costimulatory receptors CD28 and Icos regulate T <sub>FH</sub> cell differentiation ...	43
1.2.2 The CRISPR/Cas system: adaptive immunity in prokaryotes .....	45
1.3 Post-transcriptional gene regulation in the mammalian immune system .....	48
1.3.1 ARE-mediated decay of cytokine mRNAs .....	48
1.3.2 The stem-loop binding proteins Roquin-1, Roquin-2 and Regnase-1 control immunomodulatory mRNAs .....	48
1.3.3 Roquin proteins mediate peripheral immune tolerance .....	50
<b>2 Aim of the project</b> .....	<b>51</b>
<b>3 Material and methods</b> .....	<b>53</b>
3.1 Material .....	53
3.1.1 Mice and MEF cells .....	53
3.1.2 Cell lines and cell culture .....	53
3.1.3 Plasmids .....	54
3.1.3.1 Entry vectors .....	55
3.1.3.2 Transient transfection destination vectors .....	56

---

3.1.3.3	Retro- and lentiviral destination vectors .....	56
3.1.3.4	Non-Gateway® expression vectors.....	58
3.1.4	Oligonucleotides.....	59
3.1.4.1	DNA oligonucleotides .....	59
3.1.4.2	siRNA duplexes.....	63
3.1.5	Artificially synthesized DNA sequences.....	65
3.1.6	cDNA clones.....	65
3.1.7	Antibodies and fluorescent dyes .....	65
3.1.8	Cytokines .....	66
3.1.9	Chemicals, enzymes and kits .....	67
3.1.10	Buffers.....	69
3.1.11	Instruments .....	70
3.1.12	Software .....	72
3.2	Methods .....	72
3.2.1	Cloning of cDNA and amplification of DNA plasmids.....	72
3.2.1.1	Polymerase chain reaction and TOPO cloning.....	72
3.2.1.2	Bacterial culture and plasmid preparation .....	73
3.2.1.3	Restriction enzyme digestion and ligation of DNA fragments .....	73
3.2.1.4	Site-directed mutagenesis .....	74
3.2.2	Extraction of RNA and qPCR.....	74
3.2.2.1	Isolation of RNA .....	74
3.2.2.2	Reverse transcription .....	74
3.2.2.3	Quantitative PCR.....	74
3.2.3	Cell culture.....	75
3.2.3.1	Cultivation of cell lines .....	75
3.2.3.2	Isolation of genomic DNA .....	75
3.2.3.3	Preparation and stimulation of primary mouse CD4 <sup>+</sup> T cells .....	75
3.2.3.4	Retro- and lentivirus production.....	75
3.2.3.5	Virus transduction .....	76
3.2.3.6	Lentiviral doxycycline-inducible overexpression system .....	77
3.2.3.7	siRNA transfection of HeLa cells .....	77
3.2.4	Confocal microscopy .....	78
3.2.5	Expression and purification of recombinant proteins.....	78
3.2.6	Surface plasmon resonance.....	79
3.2.7	Flow cytometry.....	80
3.2.7.1	Surface staining.....	80
3.2.7.2	Intracellular staining.....	80
3.2.8	Coimmunoprecipitation and immunoblotting.....	80
3.2.9	High-throughput siRNA screen.....	81
3.2.9.1	siRNA Transfection .....	81

3.2.9.2	Fluorescent cell surface barcoding and ICOS staining.....	82
3.2.10	Pooled CRISPR/Cas9 screen.....	83
3.2.10.1	Library amplification.....	83
3.2.10.2	Lentivirus production and virus transduction.....	83
3.2.10.3	Amplification of sgRNA sequences from genomic DNA.....	83
<b>4</b>	<b>Results .....</b>	<b>85</b>
4.1	Targeted siRNA screen for cofactors of Roquin-1 in post-transcriptional gene regulation.....	85
4.1.1	Generating a reporter cell line .....	86
4.1.2	Characterization of Roquin-1-induced post-transcriptional regulation of <i>ICOS</i> .....	88
4.1.3	Pilot experiments to prepare the screen .....	89
4.1.3.1	Calculation of the Z' factor .....	90
4.1.3.2	Establishing fluorescent cell surface barcoding.....	93
4.1.4	Arrayed RNAi screening.....	95
4.1.4.1	Screening of arrayed subset libraries.....	95
4.1.4.2	Overexpression of individual candidates of the ubiquitin conjugation system in MEF reporter cell lines.....	98
4.1.4.3	Screening of RBPs, P body-, stress granule- and mRNA decay-factors .....	100
4.1.5	Regnase-1 is dispensable for Roquin-1-mediated regulation of <i>ICOS</i> .....	101
4.1.6	Establishment of a target list of candidate genes .....	102
4.1.7	Deconvolution of siRNA pools identifies false positive hits .....	104
4.1.8	Functional validation of NUFIP2 as a cofactor of Roquin.....	110
4.1.8.1	Rescue through expression of siRNA-resistant NUFIP2.....	110
4.1.8.2	Rescue of Roquin-1-mediated ICOS repression in <i>Nufip2</i> <sup>-/-</sup> MEF cells.....	112
4.1.9	Characterization of the Roquin-1/Nufip2 interaction.....	116
4.1.9.1	Investigating protein/protein interactions of Roquin-1 and Nufip2.....	117
4.1.9.2	Subcellular localization of Nufip2 .....	121
4.1.10	Expression of Nufip2 in immune cells.....	122
4.1.10.1	Analysis of Nufip2 protein expression in different mouse tissues.....	123
4.1.10.2	Correlating expression levels of ICOS, Roquin-1 and potential Roquin-1 cofactors in a time course of T cell activation.....	124
4.1.11	Analysis of cis-elements in the human <i>ICOS</i> 3' UTR.....	127
4.1.11.1	Identification of the main regulatory regions of human <i>ICOS</i> mRNA.....	127
4.1.11.2	A new stem-loop structure in the miR-101 target site is a putative <i>cis</i> -element targeted by Roquin-1.....	131
4.2	Genome-wide CRISPR/Cas9 screen for cofactors of Roquin-1-induced cell death	135
4.2.1	Overexpression of Roquin-1 induces cell death .....	135
4.2.2	Genome-wide CRISPR/Cas9 screen.....	136
4.2.2.1	Producing a stable Cas9-GFP-expressing reporter cell line.....	137

4.2.2.2	Primary CRISPR/Cas9 screen and data analysis.....	138
4.2.2.3	Identification of candidates using MAGeCK.....	142
4.2.2.4	Secondary CRISPR/Cas9 screen.....	145
4.2.2.5	Identification of promising candidates .....	147
<b>5</b>	<b>Discussion .....</b>	<b>151</b>
5.1	Accomplishment and data analysis of two high-throughput screens .....	151
5.1.1	Targeted siRNA screen for cofactors of Roquin-1-mediated ICOS regulation .....	151
5.1.2	CRISPR/Cas9 screen for cofactors of Roquin-1-induced cell death.....	155
5.1.3	Comparison of both screening approaches .....	156
5.2	Candidates arising from the CRISPR screen: Towards a pathway of Roquin-1- induced cell death?.....	158
5.2.1	Possible cell death pathways and their validation.....	158
5.2.2	Ubiquitin conjugation as a potential pathway linked to Roquin-1 effector functions 162	
5.3	Nufip2 as a new cofactor of Roquin-1-mediated <i>ICOS</i> repression.....	164
5.3.1	Molecular analysis of Roquin-1 <i>cis</i> -elements in human <i>ICOS</i> mRNA .....	165
5.3.1.1	Experimentally determined <i>ICOS cis</i> -elements compared to the CDE .....	166
5.3.1.2	Future aspects concerning the coregulation of Roquin-1 <i>cis</i> -elements by Nufip2 169	
5.3.2	Interactions between Roquin-1, Nufip2 and other potential cofactors .....	170
5.3.3	Roquin-1 cofactors regulate <i>ICOS</i> in different phases after T cell activation .....	174
5.4	Conclusion .....	175
	<b>References .....</b>	<b>177</b>
	<b>Appendices .....</b>	<b>191</b>
	<b>Publications .....</b>	<b>196</b>
	<b>Curriculum vitae.....</b>	Fehler! Textmarke nicht definiert.
	<b>Acknowledgements .....</b>	<b>198</b>

## List of figures

<i>Figure 1: Mechanisms of deadenylation-dependent mRNA decay.....</i>	<i>27</i>
<i>Figure 2: miRNA biogenesis and RNA-interference.....</i>	<i>30</i>
<i>Figure 3: Roquin proteins possess multiple RBDs and protein-interaction domains.....</i>	<i>34</i>
<i>Figure 4: T cell priming and B cell activation.....</i>	<i>38</i>
<i>Figure 5: Cytokine profiles determine T helper cell differentiation.....</i>	<i>41</i>
<i>Figure 6: CRISPR/Cas9 genome editing.....</i>	<i>46</i>
<i>Figure 7: Tet-ON inducible gene expression system.....</i>	<i>77</i>
<i>Figure 8: Evaluation of dox-inducible overexpression of Roquin-1-P2A-mCherry.....</i>	<i>87</i>
<i>Figure 9: Validation of the reporter system for Roquin-1-mediated post-transcriptional gene regulation.....</i>	<i>88</i>
<i>Figure 10: Time course of Roquin-1-dependent ICOS regulation.....</i>	<i>89</i>
<i>Figure 11: Schematic representation of data variation and dynamic range of a high-throughput screen (adapted from (Zhang et al., 1999)).....</i>	<i>90</i>
<i>Figure 12: Calculation of the Z' factor in induced versus non-induced Rc3h1/2<sup>-/-</sup> MEF and HeLa reporter cell lines.....</i>	<i>92</i>
<i>Figure 13: Calculation of the Z' factor after siRNA knockdown of Roquin-1 in HeLa reporter cells.....</i>	<i>93</i>
<i>Figure 14: Fluorescent cell surface barcoding allows multiplexing of different samples for antibody staining and data acquisition.....</i>	<i>94</i>
<i>Figure 15: Screening of six siGENOME arrayed subset libraries.....</i>	<i>97</i>
<i>Figure 16: Validation of four candidates from the ubiquitin conjugation system by overexpression.....</i>	<i>99</i>
<i>Figure 17: Screening of a customized siRNA library targeting RBPs and factors of mRNA decay.....</i>	<i>100</i>
<i>Figure 18: Analysis of post-transcriptional regulation of the TNF CDE260 or full-length ICOS by Roquin-1 and Regnase-1.....</i>	<i>102</i>
<i>Figure 19: Deconvolution of the CNOT1 siRNA pool confirms its role as an internal positive control of the siRNA screen.....</i>	<i>105</i>
<i>Figure 20: Deconvolution of siRNA pools identifies TNRC6A as a false positive hit.....</i>	<i>107</i>
<i>Figure 21: Deconvolution of the NUFIP2 siRNA pool shows a strong correlation between ICOS derepression and knockdown of NUFIP2 mRNA.....</i>	<i>108</i>
<i>Figure 22: Knockdown of NUFIP2 leads to a strong derepression of ICOS.....</i>	<i>109</i>
<i>Figure 23: Generation of NUFIP2-targeting siRNA#2 resistant NUFIP2 cDNA.....</i>	<i>110</i>
<i>Figure 24: Overexpression of siRNA-resistant NUFIP2 rescues ICOS repression.....</i>	<i>111</i>
<i>Figure 25: Generating Nufip2 knockout MEF cells using the CRISPR/Cas9 system.....</i>	<i>113</i>

<i>Figure 26: Rescue of Roquin-1-mediated ICOS repression in Nufip2 knockout cells.....</i>	<i>114</i>
<i>Figure 27: Domain organization of NUFIP2.....</i>	<i>116</i>
<i>Figure 28: NUFIP2 and Roquin-1 interact in an RNase-independent manner.....</i>	<i>118</i>
<i>Figure 29: Co-immunoprecipitation of endogenous Roquin-1 or Roquin-1<sup>san</sup> with Nufip2.....</i>	<i>119</i>
<i>Figure 30: Binary interaction of NUFIP2 and Roquin-1 fragments.....</i>	<i>120</i>
<i>Figure 31: NUFIP2 and Roquin-1 colocalize in stress granules upon arsenite treatment.....</i>	<i>121</i>
<i>Figure 32: Nufip2 is strongly expressed in the brain and in lymphoid tissues.....</i>	<i>123</i>
<i>Figure 33: Correlating Icos levels with the expression of different trans-acting factors.....</i>	<i>125</i>
<i>Figure 34: Identification of Roquin-1 cis-elements present in the 3' UTR of human ICOS mRNA.</i>	<i>129</i>
<i>.....</i>	<i>.....</i>
<i>Figure 35: Multiple sequence and structure alignments for the CDE-like stem-loop and the miR-101 target site stem-loop.....</i>	<i>132</i>
<i>Figure 36: Two stem-loop structures contribute to Roquin-1-dependent regulation of ICOS mRNA.</i>	<i>133</i>
<i>.....</i>	<i>.....</i>
<i>Figure 37: Long-term overexpression of full-length Roquin-1 in MEF cells interferes with cell survival.....</i>	<i>136</i>
<i>Figure 38: Producing a stable Cas9-GFP-expressing reporter cell line.....</i>	<i>138</i>
<i>Figure 39: Positive selection CRISPR/Cas9 screen.....</i>	<i>139</i>
<i>Figure 40: Genome-wide CRISPR/Cas9 screen for mediators of Roquin-1-induced cell death.....</i>	<i>140</i>
<i>Figure 41: Raw counts of individual sgRNA sequences.....</i>	<i>142</i>
<i>Figure 42: Clustering of screen candidates according to known and predicted protein interactions.....</i>	<i>144</i>
<i>Figure 43: Sorting of mCherry<sup>+</sup> cells from the Roquin-1-overexpression-surviving cell pool.....</i>	<i>146</i>
<i>Figure 44: sgRNA sequence representation in mCherry<sup>+</sup> and mCherry<sup>-</sup> cells for candidates of the heparan sulfate biosynthesis pathway.....</i>	<i>148</i>
<i>Figure 45: sgRNA sequence representation in mCherry<sup>+</sup> and mCherry<sup>-</sup> cells for candidates of the ubiquitin conjugation and deubiquitination pathway.....</i>	<i>149</i>
<i>Figure 46: Morphological changes of MEF cells undergoing Roquin-1-induced cell death.....</i>	<i>159</i>
<i>Figure 47: Roquin-1-bound stem-loop structures.....</i>	<i>167</i>
<i>Figure 48: Different cofactors are involved in Roquin-1-mediated post-transcriptional gene regulation.....</i>	<i>172</i>

## List of tables

<i>Table 1: Abbreviations</i> .....	18
<i>Table 2: Cell culture components</i> .....	54
<i>Table 3: List of Gateway® entry vectors</i> .....	55
<i>Table 4: Gateway® destination vectors for transient transfection</i> .....	56
<i>Table 5: Retro- and lentiviral Gateway® destination vectors</i> .....	57
<i>Table 6: lentiCRISPR vectors</i> .....	59
<i>Table 7: Primers for cDNA cloning</i> .....	59
<i>Table 8: Primers for site-directed mutagenesis</i> .....	60
<i>Table 9: Primers for qPCR</i> .....	61
<i>Table 10: Primers for the second CRISPR PCR</i> .....	62
<i>Table 11: Oligonucleotides for cloning of sgRNAs into lentiCRISPR vectors</i> .....	63
<i>Table 12: siRNA duplexes</i> .....	63
<i>Table 13: IMAGE cDNA clones</i> .....	65
<i>Table 14: Antibodies and fluorescent dyes</i> .....	66
<i>Table 15: Cytokines</i> .....	67
<i>Table 16: Chemicals</i> .....	67
<i>Table 17: Enzymes</i> .....	68
<i>Table 18: Kits</i> .....	68
<i>Table 19: Buffers</i> .....	69
<i>Table 20: Consumables</i> .....	70
<i>Table 21: Instruments</i> .....	70
<i>Table 22: Software</i> .....	72
<i>Table 23: PCR composition and cycling conditions</i> .....	72
<i>Table 24: Composition of the DNA mix for calcium-phosphate transfection</i> .....	76
<i>Table 25: Composition of SDS PAGE gels</i> .....	81
<i>Table 26: Master mix for the first CRISPR/Cas9 PCR</i> .....	84
<i>Table 27: Ranked candidate list of the customized siRNA screen</i> .....	103
<i>Table 28: Ranked list of candidates resulting from MAGeCK analysis comparing the sample d23-dox with sample d23+dox</i> .....	143
<i>Table 29: MAGeCK analysis of candidate enrichment in mCherry<sup>+</sup> and mCherry<sup>-</sup> cells</i> .....	147
<i>Table 30: Comparison of high-throughput screening methods</i> .....	157
<i>Table 31: Comparison of morphological features of different types of regulated cell death (adapted from (Xie et al., 2016))</i> .....	161

# Abbreviations

**Table 1: Abbreviations**

<b>Abbreviation</b>	<b>Full name</b>
<b>aa</b>	Amino acid
<b>AF488</b>	Alexa Fluor 488
<b>Ago/AGO</b>	Mouse/human argonaute protein
<b>APC</b>	Antigen-presenting cell
<b>APS</b>	Ammonium persulfate
<b>ARE</b>	AU-rich element
<b>Ascl2</b>	Mouse achaete-scute complex homolog 2
<b>Ask-1/ASK-1</b>	Mouse/human apoptosis-signal regulating kinase 1
<b>ATP2A</b>	Ca <sup>++</sup> transporting ATPase in the cardiac muscle
<b>b-isox</b>	Isoxazole
<b>B3galt</b>	Mouse beta-1,3-galactosyltransferase
<b>Bcl-6/BCL-6</b>	Mouse/human B cell lymphoma 6
<b>BCR</b>	B cell receptor
<b>Blast</b>	Blasticidin
<b>BSA</b>	Bovine serum albumin
<b>C-terminus</b>	Carboxy-terminus
<b>Cacybp</b>	Mouse calyculin binding protein
<b>CAR</b>	Coxsackie virus and adenovirus receptor
<b>Cas</b>	CRISPR-associated nuclease
<b>CCR</b>	C-C chemokine receptor type
<b>CD</b>	Cluster of differentiation
<b>CDE</b>	Constitutive decay element
<b>CDE260</b>	The last 260 nts of <i>TNF</i> 3' UTR including the CDE
<b>cDNA</b>	Complementary DNA
<b>CDS</b>	Coding sequence
<b>Cerk/CERK</b>	Mouse/human ceramide kinase
<b>CLIP</b>	Crosslinking and immunoprecipitation
<b>CMV</b>	Cytomegalovirus
<b>Cnot/CNOT</b>	Mouse/human CCR4-NOT complex subunit
<b>conc</b>	Concentration
<b>CRISPR</b>	Clustered regularly interspaced short palindromic repeats
<b>crRNA</b>	CRISPR-derived RNA
<b>CSTF</b>	Cleavage stimulation factor
<b>CTLA-4</b>	Cytotoxic T lymphocyte-associated protein 4
<b>CVID</b>	Common variable antibody deficiency
<b>CXCR</b>	Chemokine (C-X-C Motif) receptor
<b>Cy5</b>	Cyanine 5
<b>DNA</b>	Deoxyribonucleic acid

<b>Dcp/DCP</b>	Mouse/Human decapping protein
<b>DEPC</b>	Diethylpyrocarbonate
<b>DEST</b>	Destination vector
<b>DMEM</b>	Dulbecco's Modified Eagle's Medium
<b>dNTP</b>	Deoxynucleotide
<b>dox</b>	Doxycyclin
<b>dsDNA</b>	Double-stranded DNA
<b>DSRM</b>	Double-stranded RNA binding motif
<b>DTT</b>	Dithiothreitol
<b>DUB</b>	Deubiquitination enzyme
<b><i>E. coli</i></b>	Escherichia coli
<b>ECL</b>	Enhanced chemiluminescence
<b>Edc/EDC</b>	Mouse/Human enhancer of mRNA decapping
<b>EDTA</b>	Ethylenediaminetetraacetic acid
<b>eIF</b>	Eukaryotic translation initiation factor
<b>env</b>	Envelope gene
<b>ER</b>	Endoplasmatic reticulum
<b>EtBr</b>	Ethidium bromide
<b>Ext/EXT</b>	Mouse/human exostosin protein
<b>FACS</b>	Fluorescence-activated cell sorting
<b>FBS</b>	Fetal bovine serum
<b>Fbx1/FBXL</b>	Mouse/human F-Box and leucine-rich repeat protein
<b>Fchange</b>	Fold change
<b>FDR</b>	False discovery rate
<b>FL</b>	Full-length
<b>Fmr/FMR</b>	Mouse/human fragile X mental retardation gene family
<b>Fmrp/FMRP</b>	Mouse/human fragile X mental retardation protein
<b>4-OH-TAM</b>	4-OH-tamoxifen
<b>Foxo1</b>	Mouse forkhead box protein O1
<b>Foxp3/FOXP3</b>	Mouse/human forkhead-box-protein P3
<b>FSC</b>	Forward scatter
<b>Fxr/FXR</b>	Mouse/human fragile X mental retardation autosomal homolog
<b>G3bp/G3BP</b>	Mouse/human GTPase activating protein
<b>gag</b>	Group-specific antigen
<b>GAPDH</b>	Glyceraldehyde-3-phosphate dehydrogenase
<b>Gata</b>	Mouse GATA binding protein
<b>GC</b>	Germinal center
<b>gDNA</b>	Genomic DNA
<b>GeCKO</b>	Genome-scale CRISPR/Cas9 knockout
<b>GESS</b>	Genome-wide enrichment for seed sequence match
<b>GFP</b>	Green fluorescent protein
<b>GPCR</b>	G-protein coupled receptor
<b>H<sub>2</sub>O</b>	Water

---

<b>HA</b>	Human influenza hemagglutinin
<b>HBS</b>	Hepes buffered saline
<b>HCl</b>	Hydrochloric acid
<b>HEK293T</b>	Human embryonic kidney cells
<b>HELA</b>	Human cervical cancer cells
<b>HEPES</b>	N-2-hydroxyethylpiperazine-N-2-ethane sulfonic acid
<b>HEPN</b>	Higher eukaryotes and prokaryotes nucleotide-binding domain
<b>His<sub>6</sub></b>	Hexa histidine-tag
<b>HMO</b>	Hereditary multiple osteochondromas
<b>Hprt/HPRT</b>	Mouse/human hypoxanthine phosphoribosyltransferase
<b>HR</b>	Homology-directed repair
<b>HRP</b>	Horseradish peroxidase
<b>HTS</b>	High-throughput screening
<b>Hygro</b>	Hygromycin
<b>Icos/ICOS</b>	Mouse/human inducible T cell costimulator
<b>Icosl/ICOSL</b>	Mouse/human inducible T cell costimulatory ligand
<b>IFN<math>\gamma</math></b>	Interferon $\gamma$
<b>Ig</b>	Immunoglobulin
<b>IL</b>	Interleukin
<b>Indel</b>	Insertions or deletion
<b>Iono</b>	Ionomycin
<b>IP</b>	Immunoprecipitation
<b>IPTG</b>	Isopropyl- $\beta$ -D-thiogalactopyranosid
<b>IRES</b>	Internal ribosomal entry site
<b>Irf/IRF</b>	Mouse/Human interferon regulatory factor
<b>iTreg</b>	Induced regulatory T cells
<b>kb</b>	kilobase
<b>KD</b>	knockdown
<b>Kda</b>	Kilodalton
<b>KH</b>	K-homology domain
<b>Klf2</b>	Mouse Krüppel-like Factor 2
<b>KO</b>	knockout
<b>LB medium</b>	lysogeny broth
<b>LC</b>	low complexity
<b>LC3-I</b>	Microtubule-associated protein 1 light chain 3
<b>LC3-II</b>	PE-conjugated microtubule-associated protein 1 light chain 3
<b>Lsm/LSM</b>	Mouse/human Like sm protein
<b>LTR</b>	Long terminal repeats
<b>M199R</b>	Methionine to arginine mutation at amino acid position 199
<b>m7G cap</b>	7-methylguanosine cap
<b>MAGeCK</b>	Model-based analysis of genome-wide CRISPR/Cas9 knockout
<b>March/MARCH</b>	Mouse/human membrane-associated RING finger (C3HC4)
<b>MCPIP</b>	Monocyte chemotactic protein-induced protein

---

<b>Mdm2</b>	Mouse double minute 2 homolog
<b>Med</b>	Mediator complex subunit
<b>MEF</b>	Mouse embryonic fibroblast
<b>MFI</b>	Mean fluorescence intensity
<b>MgCl<sub>2</sub></b>	Magnesium chloride
<b>MHC</b>	Major histocompatibility complex
<b>μl</b>	Microliter
<b>μ<sub>c</sub></b>	Mean of control data
<b>μ<sub>s</sub></b>	Mean of sample data
<b>min</b>	Minute
<b>miRNA or miR</b>	MicroRNA
<b>miRISC</b>	MicroRNA-induced silencing complex
<b>ml</b>	Milliliter
<b>MMR</b>	DNA mismatch repair
<b>MOI</b>	Multiplicity of infection
<b>mRNA</b>	Messenger RNA
<b>mRNP</b>	Messenger ribonucleoprotein
<b>mTOR</b>	Mechanistic target of rapamycin (serine/threonine kinase)
<b>N-terminus</b>	Amino-terminus
<b>NaCl</b>	Sodium chloride
<b>Neo</b>	Neomycin
<b>NFκB</b>	Nuclear factor 'kappa-light-chain-enhancer' of activated B cells
<b>Nfκbid/NFκBID</b>	Nuclear factor 'kappa-light-chain-enhancer' of activated B cells inhibitor, delta
<b>Nfκbiz/NFκBID</b>	Nuclear factor 'kappa-light-chain-enhancer' of activated B cells inhibitor, zeta
<b>ng</b>	Nanogram
<b>NGS</b>	Next-generation sequencing
<b>NHEJ</b>	Non-homologous end-joining
<b>NLS</b>	Nuclear localization signal
<b>nM</b>	Nanomolar
<b>NMD</b>	Nonsense-mediated mRNA decay
<b>NMR</b>	Nuclear magnetic resonance
<b>nTreg</b>	Natural regulatory T cell
<b>nts</b>	Nucleotides
<b>Nufip2/NUFIP2</b>	Mouse/human nuclear FMRP interaction partner
<b>#</b>	Number
<b>OD<sub>600</sub></b>	Optical density of a sample measured at a wavelength of 600 nm
<b>Ox40</b>	Mouse tumor necrosis factor receptor superfamily, member 4
<b>Ox40l</b>	Mouse tumor necrosis factor receptor superfamily, member 4 ligand
<b>P body</b>	Processing body
<b>P2A</b>	Porcine teschovirus-1 self-cleaving peptide 2A
<b>PABP</b>	Poly(A)-binding protein
<b>PAM</b>	Protospacer adjacent motif
<b>PAMP</b>	Pathogen associated molecular pattern

---

<b>Pan/PAN</b>	Mouse/human poly(A) specific ribonuclease
<b>PB</b>	Pacific blue
<b>P body</b>	Processing body
<b>PBS</b>	Phosphate buffered saline
<b>PCR</b>	Polymerase chain reaction
<b>PD-1</b>	Programmed cell death 1
<b>%</b>	Percent
<b>PI3K</b>	Phosphatidylinositol 3-kinase
<b>PI4KA</b>	Phosphatidylinositol 4-kinase $\alpha$
<b>pg</b>	Picogram
<b>PMA</b>	Phorbol-12-myristate-13-acetate
<b>pMol</b>	Picomolar
<b>pol</b>	Polymerase
<b>polyA</b>	Multiple adenosine monophosphates
<b>pri-miRNA</b>	Primary microRNA
<b>PRR</b>	Pattern recognition receptor
<b>PSGL</b>	P-selectin glycoprotein ligand
<b>PTBP</b>	Polypyrimidine tract binding protein
<b>puro</b>	Puromycin
<b>PVDF</b>	Polyvinylidene fluoride
<b>Q/N rich</b>	Rich in glutamine and asparagine residues
<b>qPCR</b>	Real-time quantitative PCR
<b>Rab</b>	Member of the RAS oncogene family
<b>RBD</b>	RNA-binding domain
<b>RBP</b>	RNA-binding protein
<b>Rck/Ddx6</b>	DEAD (Asp-Glu-Ala-Asp) box helicase 6
<b>rev</b>	Regulator of expression of virion proteins
<b>RG-rich</b>	Arginine-glycine rich
<b>RING</b>	Really interesting new gene
<b>RIP kinase</b>	Receptor-interacting serine-threonine kinase
<b>RLR</b>	RIG-I-like receptor
<b>RNA</b>	Ribonucleic acid
<b>RNAi</b>	RNA-mediated interference
<b>Rnf/RNF</b>	Mouse/human RING finger protein
<b>RNP</b>	Ribonucleoprotein
<b>RNS</b>	Ribonukleinsäure
<b>RORyt</b>	Retinoic acid receptor-related orphan receptor gamma
<b>RPMI</b>	Roswell Park Memorial Institute medium
<b>RRM</b>	RNA recognition motif
<b>RT</b>	Room temperature
<b>RU</b>	Response units
<b>rtTA3</b>	TET-ON transactivator
<b>S1PR</b>	Sphingosine-1-phosphate receptor

---

<b>san</b>	<i>Sanroque</i> mutation (Roquin M199R)
<b>SAP</b>	SLAM-associated protein
<b>SD</b>	Standard deviation
<b>SDS PAGE</b>	Sodium dodecyl sulfate polyacrylamide gel electrophoresis
<b>sec</b>	Seconds
<b>SG</b>	Stress granule
<b>sgRNA</b>	Single guide RNA
<b>SHM</b>	Somatic hypermutation
<b>shRNA</b>	Short hairpin RNA
<b>siCtrl</b>	Non-targeting siRNA
$\sigma_c$	Standard deviation of control data
$\sigma_s$	Standard deviation of sample data
<b>siNUFIP2</b>	NUFIP2-targeting siRNA
<b>siRNA</b>	Small interfering RNA
<b>siRoquin-1</b>	Roquin-1-targeting siRNA
<b>Slc35</b>	Solute carrier family 35 (adenosine 3'-phospho 5'-phosphosulfate transporter)
<b>SLE</b>	Systemic lupus erythematosis
<b>SM</b>	Stem-loop mutant
<b>SOC</b>	Super optimal broth
<b>SRP</b>	Surface plasmon resonance
<b>SSC</b>	Side scatter
<b>Stat/STAT</b>	Mouse/human signal transducer and activator of transcription
<b>Stau/STAU</b>	Mouse/human Staufen double-stranded RNA binding protein
<b>Stk/STK</b>	Mouse/human serine/threonine kinase
<b>SUMO</b>	Small ubiquitin-related modifier
<b>TAC</b>	Tetradecyldimethylbenzylammonium chloride
<b>Taq</b>	<i>Thermus aquaticus</i> polymerase
<b>TBE</b>	Tris-borate-EDTA
<b>TBS</b>	Tris buffered saline
<b>TCR</b>	T cell receptor
<b>TE</b>	Tris-EDTA
<b>TEMED</b>	Tetramethylethylenediamine
<b>Temp</b>	Temperature
<b>TES</b>	Testin LIM domain protein
<b>T<sub>FH</sub> cell</b>	T follicular helper cell
<b>TGF-<math>\beta</math></b>	Transforming growth factor beta
<b>Th</b>	T helper cell
<b>Thy1.1</b>	Thymus cell antigen-1
<b>TLR</b>	Toll-like receptor
<b>T<sub>m</sub></b>	Melting temperature
<b>TNF</b>	Tumor necrosis factor
<b>TNRC6</b>	Trinucleotide repeat containing protein 6
<b>tracrRNA</b>	Trans-acting antisense RNA

---

<b>TRE</b>	Tet-response element
<b>Treg</b>	Regulatory T cell
<b>TRIM</b>	Tripartite motif containing protein
<b>TRUB</b>	TruB pseudouridine (Psi) synthase family member
<b>TS</b>	Target site
<b>TTP</b>	Tristetraprolin
<b>TYW</b>	tRNA-YW synthesizing protein
<b>Upf/UPF</b>	Mouse/human regulator of nonsense transcripts homolog (Yeast)
<b>Usp/USP</b>	Mouse/human ubiquitin specific peptidase
<b>UTR</b>	Untranslated region
<b>wt</b>	Wildtype
<b>Xrn/XRN</b>	Mouse/human exoribonuclease
<b>YTHDC</b>	YTH domain containing protein
<b>Ywhaz/YWHAZ</b>	Tyrosine 3-monooxygenase/tryptophan 5-monooxygenase activation protein, zeta
<b>ZnCl<sub>2</sub></b>	Zinc dichloride
<b>ZnF</b>	Zinc finger
<b>Zyx/ZYX</b>	Mouse/human Zyxin

---

# 1 Introduction

The work presented in this thesis centers around the RNA-binding protein Roquin-1, which controls T cell differentiation to prevent autoimmunity. Two large-scale screens were performed to explore functional interactions of Roquin-1. An RNAi screen was set up to identify cofactors of Roquin-1 protein in the process of post-transcriptional repression of the important T cell costimulatory receptor ICOS. In a CRISPR/Cas9-mediated whole-genome knockout screen, we explored the newly discovered function of Roquin-1 to induce cell death. Before I start to describe the results of my work in detail, I will begin by introducing the principles of post-transcriptional gene regulation in general, and the function of the RNA-binding proteins Roquin-1, its paralog Roquin-2 and their putative cofactors Regnase-1 and Fmrp in more detail. After describing the aspects of adaptive immunity including the differentiation of distinct T helper subsets and the special role of the T cell costimulator Icos in linking T- and B cell immunity that are relevant to this study, I will end the introduction by providing examples from the current literature to show how post-transcriptional repression mediated by RNA-binding proteins influences functions and fate of immune cells.

## 1.1 Post-transcriptional gene regulation

Gene expression in mammalian cells is a tightly controlled process ensuring that each living cell expresses a specific RNA and protein repertoire at the correct level and in a spatial and time-dependent manner. The first level of gene regulation is the initiation of transcription. Since eukaryotic DNA is wrapped in chromatin, access to the genomic region of interest by epigenetic regulatory mechanisms is a first requirement for gene expression. Next, the DNA polymerase needs to be guided to the promoter region, a regulatory DNA sequence located upstream of the protein coding sequence. This is accomplished by sequence-specific transcription factors, which are supported or inhibited by transcriptional enhancers and silencers, respectively (Phillips, 2008). During the course of transcription, the polymerase generates a primary pre-mRNA transcript, which is co-transcriptionally spliced, removing the non-coding sequences (introns), and capped, by the addition of a 7-methyl-guanosine ( $m^7G$ ) cap to the 5' end. The final modification of the nascent mRNA is the addition of a poly-adenosine (poly(A)) tail at the 3' end (McKee & Silver, 2007). Mature messenger RNAs (mRNAs) thus consist of a 5' cap, followed by a 5' untranslated sequence (5' UTR), the protein-coding sequence (CDS), a 3' untranslated region (3' UTR) and the poly(A) tail. Mature

mRNAs are translocated from the nucleus to the cytoplasm for the pioneer round of translation. During this process mRNAs are subjected to quality control mechanisms, such as nonsense-mediated RNA decay (NMD), which acts to eliminate all mRNAs containing premature stop codons (Hug et al., 2016). After 5' cap-binding proteins and poly(A)-binding proteins (PABPs) interact to circularize the mRNA and enable the recruitment of translation initiation factors, ribosomes can bind to the mRNAs and start translation (Wells et al., 1998). Several ribosomes can translate the same mRNA at the same time and arrange in so-called polysomes, which cover the whole length of the coding sequence, and synthesize growing polypeptide chains in parallel (Warner et al., 1963). After termination of translation the newly synthesized full-length proteins are folded, mostly with the help of chaperones (Ellis, 1996), to become functional. Different mechanisms of post-transcriptional gene regulation can interfere with translation, resulting in silencing or degradation of the respective transcripts.

Overall, it is thought that transcriptional gene regulation is responsible for long-term changes in the mRNA profiles, while quick adaptations in the expression of specific genes is performed via regulation of translation efficiencies of existing mRNAs by post-transcriptional gene regulation (Rabani et al., 2011). Genes that are extensively regulated on the post-transcriptional level often possess long 3' UTRs (e.g. ICOS, 1948 nts), which accommodate multiple different *cis*-regulatory elements. This is in stark contrast to so-called housekeeping genes, which are constitutively expressed (e.g. GAPDH, 224 nts). *Cis*-elements can occur as linear or structured motives and are regulated by *trans*-acting factors, such as short regulatory RNAs or RNA-binding proteins. Different *trans*-acting factors might either inhibit each other's function, or coregulate the same mRNA independently or in a cooperative manner. These interactions impose a high level of complexity to expression-promoting or -repressing networks (Jeltsch & Heissmeyer, 2016).

### **1.1.1 Deadenylation- and decapping-dependent mRNA decay**

*Trans*-acting factors can adjust the translation efficiency of mature mRNAs by inhibition of translation or mRNA degradation, or a combination thereof. mRNA degradation in eukaryotic cells is achieved via two possible pathways of deadenylation-dependent mRNA decay (Figure 1).

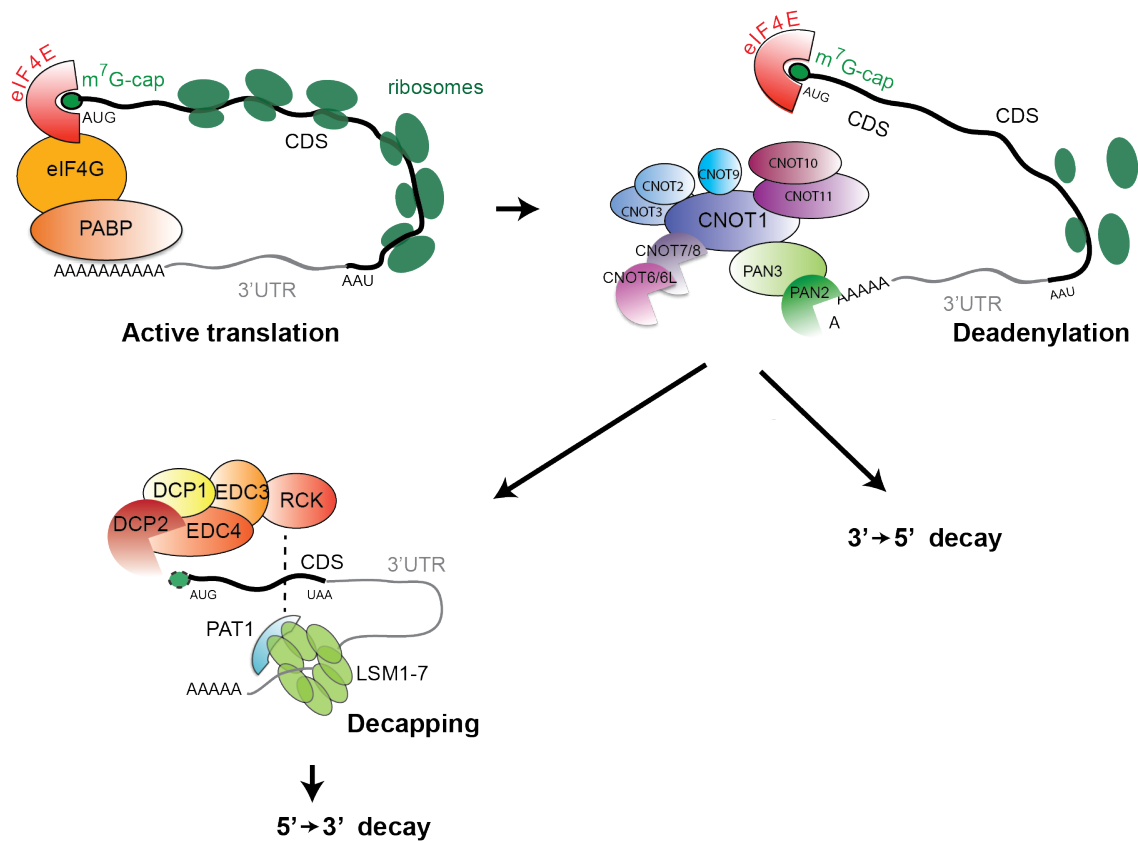


**Figure 1: Mechanisms of deadenylation-dependent mRNA decay.**

Schematic representation of eukaryotic deadenylation-dependent mRNA degradation pathways. Actively translated polysomal mRNAs form a circle, which is mediated by an interaction between poly(A) binding proteins (PABPs) bound to the poly(A) tail of the transcript and the cap-binding protein eIF4E via the scaffolding factor eIF4G. Upon initiation of deadenylation, PABPs are displaced and translation rates decrease. Shortening of the poly(A) tail by the deadenylases PAN2, CCR4 (CNOT6/CNOT6L) and CAF1 (CNOT7/CNOT8) is either followed by 3'-5' degradation by the exosome, or by 5'-3' directed decay via mRNA decapping. Hydrolysis of the 7-methyl-guanosine cap (m<sup>7</sup>G-cap) by the decapping enzyme DCP2 results in XRN1-mediated 5'-3' decay (Braun et al., 2012; Chen & Shyu, 2011; Huntzinger & Izaurralde, 2011; Jonas & Izaurralde, 2015; Sharif & Conti, 2013; Shirai et al., 2014; Zheng et al., 2008).

Both start with the degradation of the poly(A) tail of actively translated, polysomal mRNAs performed by the CCR4-CAF1-NOT multi-protein deadenylase complex, which assembles around the large scaffolding subunit CNOT1 (Shirai et al., 2014). The CCR4-CAF1-NOT complex contains two catalytic subunits CCR4 (CNOT6/CNOT6L) and CAF1 (CNOT7/CNOT8) and can additionally engage in a supercomplex with the deadenylase PAN2 and its binding partner PAN3 (Chen & Shyu, 2011; Zheng et al., 2008). PAN2 is responsible for an initial shortening of the poly(A) tail, while further degradation to < 25 oligo(A) is accomplished by CCR4 and CAF1. Loss of PAN2/PAN3 can be compensated by CCR4 and CAF1 (Chen & Shyu, 2011; Yamashita et al., 2005), whereas knockdown of CAF1 severely impairs deadenylation, indicating that the function of

this catalytic subunit of the CCR4-CAF1-NOT complex is non-redundant (Zheng et al., 2008). As a result of deadenylation, PABPs are displaced from the mRNA tail, thereby weakening the interaction with the cap-binding protein eIF4E. The resulting decircularization of the transcript leads to a lower translation efficiency, as well as a high accessibility to degradation enzymes (Huntzinger & Izaurralde, 2011). Deadenylated transcripts can now be degraded by the exosome in 3'-5' directed mRNA decay. However, the 5'-3' degradation pathway prevails, because in most cases the decapping activator complex LSM1-7 binds to oligo(A) tails and thereby inhibits exosomal access to the 3' end (Tharun, 2009). Together with PAT1 the heteroheptameric LSM1-7 complex recruits components of the decapping complex, such as RCK, EDC3, EDC4, DCP1 and DCP2 (Jonas & Izaurralde, 2015; Sharif & Conti, 2013). During the course of decapping, DCP2 as well as XRN1 directly bind to the scaffolding protein EDC4 (Braun et al., 2012). While the enzymatic activity of DCP2 causes the hydrolysis of the 5' m<sup>7</sup>G-cap, the exonuclease XRN1 degrades the mRNA in the 5'-3' direction. This molecular pathway holds the advantage that ribosomes, which have undergone translation initiation, will always be able to produce a functional full-length protein without running off a partially degraded transcript.

### **1.1.2 Storage of translationally silenced mRNAs in granule-like structures**

Translational repression of transcripts can be achieved by a variety of different mechanisms. The frequently observed inhibition of the translation initiation step can be monitored by a shift of the respective target mRNAs from the polysomal into monosomal fractions after separation of ribosomes in sucrose gradients, whereas blockage of the elongation step would lead to an accumulation of target mRNAs in higher-molecular weight fractions (Huntzinger & Izaurralde, 2011). Translationally silenced transcripts can accumulate in two different types of cytoplasmic granules, stress granules and P bodies. Following treatment with arsenite, a chemical substance that causes oxidative stress (Li et al., 2013), the translation initiation factor eIF2 $\alpha$  is phosphorylated and thereby converted into an inhibitor of the translation initiation complex. As a result, cellular protein synthesis is globally stalled at the initiation stage (Ivanov & Anderson, 2013). Ribosomes stop translation and polysomes disassemble, which is followed by an aggregation of the respective mRNAs and their bound translation initiation components in large cytoplasmic aggregates called stress granules (SG) (Anderson & Kedersha, 2009). Essential SG components are the

structurally highly similar RNA-binding proteins TIA1 and TIAR, and the RNA-binding protein G3BP1, which forms a complex with the deubiquitinase USP10 (Anderson & Kedersha, 2009). The glutamine- and asparagine- (Q/N)-rich prion-like protein domains of TIA1/TIAR and the glycine-rich RGG domain of G3BP1 promote self-aggregation and thereby strongly contribute to the formation of higher-order protein complexes, such that overexpression of any of the three proteins can induce SG formation even in the absence of cellular stress (Gilks et al., 2004). Other essential SG components are translation initiation factors like eIF3, ribosomal subunits, and PABPs (Anderson & Kedersha, 2009; Ohn et al., 2008). Furthermore, proteins implicated in translational repression, such as the RNA-binding protein FMRP, proved to be important for stress granule formation (Didiot et al., 2009).

Another kind of cytoplasmic granules are the so-called processing bodies (P bodies), which are even present in unstressed cells. P body formation is initiated by mRNA deadenylation (Zheng et al., 2008). Degradation of the poly(A) tail of an mRNA leads to the disruption of the interaction between PABPs and cap-binding proteins, resulting in linear mRNAs with lower translation efficiency. Subsequently, polysome disassembly is accompanied by the translocation of the mRNP complexes from the cytoplasm into P bodies. Some stress granule components are also found in P bodies, such as the RNA helicase RCK (Bish et al., 2015), the cap-binding protein eIF4E or the 5'-3' exonuclease XRN1 (Kedersha et al., 2005). However, as a general rule, components of the translation initiation complex are missing in P bodies, which are instead characterized by an accumulation of mRNA deadenylation/decapping/decay factors (Bish et al., 2015; Decker & Parker, 2012). Essential P body components are LSM proteins, as well as GW182, a well-characterized translational silencer after which P bodies were originally named (GW bodies) (Ohn et al., 2008). Similar to stress granules, P body assembly is also believed to be mediated by protein aggregation domains (Reijns et al., 2008).

Overall, sequestration into stress granules is thought to provide a storage possibility for mRNA molecules whose translation became disadvantageous, while the high density of mRNA decay proteins in P bodies indicates a strong bias towards mRNA turnover. Although mRNA decay can occur in P bodies, translational repression and mRNA decay are not dependent on P body formation (Eulalio et al., 2007). The functional difference between P bodies and stress granules is still not well understood and awaits further investigation (Decker & Parker, 2012).

### 1.1.3 Mechanisms of RNA-interference

Important players of post-transcriptional gene regulation are ~22 nts short double-stranded microRNAs (miRNAs), which bind in a sequence-specific manner to linear *cis*-elements in the 3' untranslated region (UTR) of mRNAs to induce translational inhibition and RNA degradation. This prominent pathway is called RNA-mediated interference (RNAi).

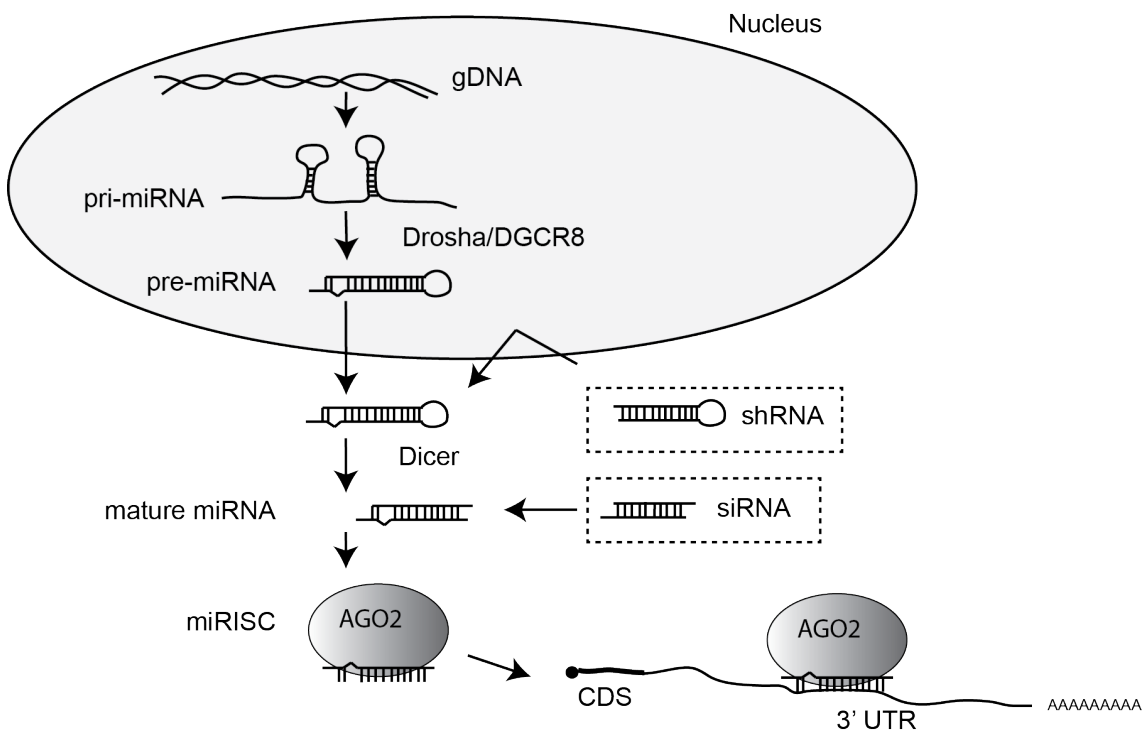


**Figure 2: miRNA biogenesis and RNA-interference.**

In the nucleus, long primary miRNAs (pri-miRNAs) arise from polymerase II or polymerase III transcription of genomic sequences (gDNA). Pri-miRNAs are cleaved by Drosha and DGCR8 into pre-miRNAs, which are exported into the cytoplasm as short hairpins. Here, Dicer processing results in the generation of mature miRNA duplexes. One strand is loaded onto Ago to form a miRNA-induced silencing complex (miRISC), which scans 3' UTRs of potential target mRNAs for complementary sequences. Perfect complementarity can induce endonucleolytic cleavage of the target, while the more frequently observed partial complementarity induces deadenylation-dependent mRNA decay (Hoefig & Heissmeyer, 2008; Huntzinger & Izaurralde, 2011). Synthetic RNAi reagents are delivered as short interfering RNA (siRNA) or short hairpin RNA (shRNA). Retrovirally delivered shRNA-encoding sequences integrate into the host genome and enable the transcription of shRNA hairpins, which are cleaved into mature duplexes by Dicer. siRNAs, on the other hand, are delivered as mature 21 nt-long duplexes by transient transfection. One strand of the mature siRNA or shRNA duplex is incorporated into the RISC complex and induces endonucleolytic cleavage of a perfectly complementary target sequence in the CDS or 3' UTR of its target mRNA (Sharma & Rao, 2009). This scheme was adapted from (Hoefig & Heissmeyer, 2008).

miRNAs are transcribed as long primary transcripts (pri-miRNAs) in the nucleus (Figure 2). Pri-miRNAs are processed by the RNase Drosha, assisted by the RNA-binding protein DGCR8 (Han et al., 2004), into pre-miRNAs, hairpin structures of ~70 nts, which are exported from the nucleus into the cytoplasm (Lee et al., 2003). Further processing is accomplished by the RNase Dicer, which cleaves off the loop of the hairpin structure to result in a 18-25 nt-long double-stranded RNA sequence (Bernstein et al., 2001). One strand of the duplex is loaded onto an Ago protein to form the miRNA-induced silencing complex (miRISC), which scans the transcriptome for target mRNAs (Schwarz et al., 2003). Target recognition is mediated by Watson-Crick base pairing between the miRNA and a fully or partially complementary sequence in the 3' UTR of target mRNAs. Although fully complementary base-pairing is possible and results in Ago-mediated endonucleolytic mRNA cleavage of some transcripts, miRNAs can additionally target hundreds of partially complementary sequences where target complementarity is limited to the miRNA seed region (nts 2-7) (Hoefig & Heissmeyer, 2008). Repression of target mRNAs with partially complementary sequences involves the recruitment of GW182 proteins and subsequent translational inhibition and mRNA decay (Chapter 1.1.1) (Huntzinger & Izaurralde, 2011).

The endogenous RNAi pathway can be harnessed to create targeted gene knockdowns. In mammals, synthetic RNAi reagents comprise short interfering RNAs (siRNAs) and short hairpin RNAs (shRNAs). shRNAs are usually delivered retro- or lentivirally as pre-miRNA-like longer hairpin structures that require Dicer processing (Figure 2, upper dashed box). Since retroviral sequences are stably integrated into the genome, shRNAs can be employed to create stable knockdown cell lines for the gene of interest (Sharma & Rao, 2009). Disadvantages lie, however, in the cumbersome efforts of virus production and target cell infection, as well as in biosafety considerations when working with lentiviruses. Moreover, since genome integration, hairpin transcription and dicer processing are necessary to produce functional shRNAs, manifestation of the knockdown can take several days. siRNAs, on the other hand, are delivered into cells as 21-bp long duplexes with characteristic 3' dinucleotide overhangs by transient transfection (Figure 2, lower dashed box). They mimic mature miRNAs, and therefore do not require Dicer cleavage. miRNA duplexes consist of a sense (passenger) and an antisense (guide) strand. Only the guide is transferred into the RISC, where it functions by identifying perfect complementary sequences in the CDS or the 3' UTR of the intended target mRNA to induce endonucleolytic cleavage by Ago2 (Dharmacon). Due to their ease of use, siRNAs can be employed for knocking down multiple genes of

interest in parallel, and are commonly used in loss-of-function screens where thousands of samples can be transfected with different siRNAs in parallel (Sharma & Rao, 2009).

#### **1.1.4 RNA-binding proteins**

RNA-binding proteins play a crucial role in RNA metabolism and function. Throughout their whole life, RNAs are decorated with RNA-binding proteins in complexes called ribonucleoproteins (RNP). Already during the transcription process, RBPs guide intron-containing pre-mRNAs through initial processing events, such as splicing, capping and polyadenylation. They are also involved in the nuclear export of mature transcripts, and play a major role in quality control- and regulatory mechanisms of mRNA translation, which are taking place in the cytoplasm (McKee & Silver, 2007). In this study, we focus on RNA-binding proteins with a role in post-transcriptional regulation of protein-coding mRNAs.

In the past, protein domains were characterized which could confer RNA-binding and subsequent homology searches across the genome led to the identification of several hundred human RBPs, which were classified according to their RNA-binding domains (RBD) (Calabretta & Richard, 2015). Recent approaches for a genome-wide identification of human RNA-binding proteins resulted in the discovery of many new RBPs (Baltz et al., 2012; Castello et al., 2012), leading to a current estimation of ~700 mRNA-binding proteins being present in human cells (Gerstberger et al., 2014). Almost 60 % of these possess one of the few very abundant RBDs, such as the RNA-recognition motif (RRM), the K-homology (KH) domain, the double-stranded RNA-binding motif (DSRM), DEAD boxes and RNA-binding zinc-finger (ZnF) domains (Gerstberger et al., 2014). However, about half of the RBPs discovered by Castello et al lack known RBDs, suggesting that many more modes of RNA-binding are still to be discovered (Castello et al., 2012). Comparison of known structural organizations of several dozen well-studied RBPs led to the striking observation that RBPs often possess multiple repeats of one or multiple RBDs, suggesting that one RBP might employ multiple domains in order to combine multiple low-affinity binding sites for binding the same or different target mRNAs (Gerstberger et al., 2014). Furthermore, a combination of different RBPs might cooperate in the recognition of one or multiple target mRNAs (Jeltsch & Heissmeyer, 2016).

#### 1.1.4.1 The FMR protein family

The well-studied fragile X mental retardation (FMR) protein family employs both modes of cooperativity. The three highly homologous family members FMRP, FXR1 and FXR2 each contain three classical RBDs: two type-I KH domains in the center of the protein and an arginine-glycine (RG)-rich region close to the C-terminus (Winograd & Ceman, 2011). Since loss of FMRP expression or a single point mutation in the second KH domain can cause severe mental retardation in humans (De Boulle et al., 1993; Jin & Warren, 2000), its mode of action in the brain has been studied intensively. FMRP was found to bind to a large number of mRNAs expressed in the brain and can either activate or suppress translation (Winograd & Ceman, 2011). All three RBDs are involved in target recognition, with the KH domains binding primarily to the linear binding motives ACUK (K= G/U) and WGGGA (W= U/A) (Ascano et al., 2012), while the RGG box specifically recognizes guanine (G)-quadruplexes (Vasilyev et al., 2015). The former are linear sequence motives, while the latter are higher-order structures of guanine-rich RNA sequences. In addition to the use of multiple RBDs for RNA binding, FMR family members were observed to form both homo- and heterodimers, with the protein/protein interaction being mediated by a coiled-coil region in the C-terminus of the protein (Winograd & Ceman, 2011).

#### 1.1.4.2 Roquin family proteins

Another example of RBPs is the Roquin protein family, consisting of Roquin-1 and Roquin-2. Roquin-1 and -2 share a common domain structure with an N-terminal RING finger, the RNA-binding ROQ domain, which is embedded in a second RNA-binding domain created by amino-terminal HEPN<sub>N</sub> and carboxy-terminal HEPN<sub>C</sub> sequences that come together to form the so-called HEPN domain. In addition Roquin proteins contain a classical CCCH-type zinc finger (ZnF) RBD and a proline-rich region involved in protein/protein interactions (Figure 3) (Athanasopoulos et al., 2010; Jeltsch & Heissmeyer, 2016; Pratama et al., 2013). The N-terminal domains of both proteins are highly homologous (80-99 % sequence similarity), while the C-terminal domains display a lower sequence similarity (45-50 %) (Pratama et al., 2013). This is due to a differential organization of the proline-rich region and the lack of the coiled-coil region in Roquin-2. Instead, Roquin-2 possesses a hydrophobic region, which was initially suspected to be a membrane anchor (Siess et al., 2000). Since coiled-coil domains are frequently involved in protein dimerization (Burkhard et al., 2001), the presence of a coiled-coil domain in Roquin-1 might mediate its specific protein

interactions. So far, however, no factor has been found to exclusively interact with Roquin-1, but not Roquin-2.

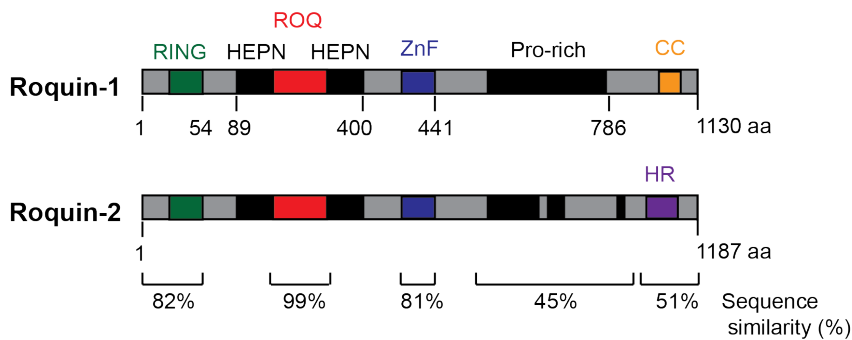


**Figure 3: Roquin proteins possess multiple RBDs and protein-interaction domains.**

Schematic representation of the domain organization of mouse Roquin-1 and Roquin-2. The ROQ domain, the HEPN domain and Zinc finger (ZnF) represent experimentally validated RBDs, while the RING domain that confers E3 ligase function and the C-terminal proline-rich (Pro-rich) and coiled-coil (CC) sequences are predicted to be important for protein/protein interactions. In Roquin-2, the CC domain was replaced by a hydrophobic region (HR). This scheme was adapted from (Jeltsch & Heissmeyer, 2016; Pratama et al., 2013).

The RNA-binding mode of the ROQ domain was recently solved in crystal structures. It binds with high affinity to tri-loop and hexa-loop RNA motifs by engaging in hydrogen bonding and electrostatic interactions with negatively charged phosphodiester groups of the RNA backbone, thereby recognizing its target sequences in a structure- and not sequence-dependent manner (Codutti et al., 2015; Janowski et al., 2016; Schlundt et al., 2014). Although the ROQ domain seems to be sufficient for binding of certain motifs, such as a conserved tri-loop structure occurring in the *tumor necrosis factor (TNF)* 3' UTR (Leppek et al., 2013), both HEPN and ZnF domains may contribute to RNA binding by recognizing alternative *cis*-elements or additional sequences or structures. The HEPN domain can bind double-stranded RNA independent from the ROQ domain (Srivastava et al., 2015; Tan et al., 2014), and both domains were shown to be able to simultaneously bind to different target mRNAs. Moreover, cooperative recognition of distinct *cis*-elements by the ROQ domain and the ZnF has been proposed to be required for high-affinity binding of *A20* mRNA (Murakawa et al., 2015). Like FMRP, Roquin-1 might thus employ all three RNA-binding modules in a cooperative way for binding the same or different target mRNAs. Upon Roquin binding, the respective target mRNAs are post-transcriptionally repressed. The mechanism of Roquin-induced post-transcriptional gene regulation is elusive for the most part. However, it has been shown that Roquin primarily induces mRNA deadenylation by

recruiting the CCR4-CAF1-NOT-deadenylation complex (Leppek et al., 2013), which is followed by mRNA decapping (Glasmacher, 2010) and subsequent decapping-dependent 5' - 3' decay (Chapter 1.1.1).

#### 1.1.4.3 Regnase family proteins

The Regnase (MCPIP) family of RNA-binding proteins consists of the four family members Regnase-1 to -4. They share two highly conserved domains: an NYN nuclease domain of ~170 nts that is followed by a CCCH-type Zinc finger (Lin et al., 2013). Of all family members, only the function of Regnase-1 has been investigated in greater detail. Regnase-1 has been shown to regulate target mRNA expression via endonucleolytic cleavage (Uehata & Akira, 2013). Interestingly, Regnase-1 target mRNAs showed a strong overlap with Roquin-1-regulated mRNAs (Jeltsch et al., 2014; Uehata et al., 2013; Vogel et al., 2013), and indeed, it was recently shown that Regnase-1 preferentially binds to stem-loop structures that resemble predicted Roquin-1 *cis*-elements (Mino et al., 2015). Since structural evidence for Regnase-1 binding to *cis*-elements is still missing, it remains elusive whether shared recognition of the same *cis*-elements by Roquin-1 and Regnase-1 is part of a mechanism that works in a cooperative or a mutual exclusive manner. Regnase-1 colocalized in cells with the rough ER, and was furthermore detected in the polysomal fractions of a sucrose gradient (Mino et al., 2015), while Roquin-1 localized to P bodies (Glasmacher, 2010) and was found in the non-polysomal fractions (Mino et al., 2015). It was consequently proposed that although recognizing the same set of mRNAs, Roquin-1 and Regnase-1 operated in distinct subcellular locations with Regnase-1 targeting actively translated mRNAs, while Roquin-1 was supposed to regulate translationally silenced mRNAs only (Mino et al., 2015). However, Roquin-1 and Regnase-1 have previously been shown to repress certain motifs in a cooperative way (Jeltsch et al., 2014), suggesting that their function is not completely redundant and both can repress the same target mRNA independent of its translation state. Moreover, Roquin was recently found to repress the actively translated *Ox40* mRNA in T cells (Janowski et al., 2016), indicating that the relationship of the two regulatory proteins is more complicated than previously thought and will require further investigation.

In contrast to Roquin-1, Regnase-1 does not seem to employ deadenylation-dependent mRNA decay for target regulation. Instead, Regnase-1 function depended on its endonuclease activity (Jeltsch et al., 2014; Liang et al., 2010; Mino et al., 2015) and on a specific protein/protein interaction with UPF1, an RNA helicase with a major role in

nonsense-mediated RNA decay (NMD) (Mino et al., 2015). Since only UPF-1, but no other proteins of the NMD pathway were required for Regnase-1-dependent degradation of target mRNAs and Regnase-1 function furthermore depended on the RNA helicase function of UPF-1, it was suggested that Regnase-1 induces post-transcriptional gene regulation of stem-loop-containing mRNAs via a new pathway of UPF-1-induced RNA-unwinding followed by Regnase-1-induced endonucleolytic cleavage (Mino et al., 2015).

## **1.2 The immune system**

Immune systems have evolved to protect organisms against harmful intruders. In mammals, a functional immune system depends on the interplay of innate and adaptive immunity. Innate immune cells, such as tissue-resident macrophages and neutrophils, recognize common pathogen associated molecular patterns (PAMPs) like bacterial lipopolysaccharides or virus-specific double-stranded RNA with their pattern recognition receptors (PRRs) (Alberts et al., 2002). This heterogeneous gene family includes transmembrane receptors like toll-like receptors (TLRs) but also cytoplasmic receptors such as RIG-I-like receptors (RLRs) (Kawai & Akira, 2009). Following PAMP recognition, pathogen clearance is mediated by engulfment and internal digestion or extracellularly via secretion of toxic effector molecules. Additionally, activated innate immune cells secrete small effector molecules called cytokines and chemokines. Cytokines mediate communication with other types of immune cells, also of the adaptive immune system, while chemokines are responsible for the recruitment of chemokine receptor-bearing neutrophils and monocytes. Recruitment of large numbers of neutrophils and macrophages to the site of infection is facilitated by dilation and increased permeability of the blood vessels and noticed as heat, redness and swelling of the respective tissue, a process that is called inflammation (Janeway et al., 2005).

### **1.2.1 The adaptive immune response in mammals**

Throughout evolution, pathogens have invented strategies to circumvent the innate immune response by hiding their PAMPs from cells equipped with PRRs. The development of the adaptive immune system is a late evolutionary response to this phenomenon, enabling a tailor-made immune response to a large diversity of pathogens (Alberts et al., 2002). Major players of the adaptive immune system are lymphocytes on the cellular level, complemented by antibodies and cytokines as

soluble factors. Lymphocytes arise from common lymphoid progenitor cells in the bone marrow, which give rise to many different lymphocyte populations of the B cell or T cell lineage (Janeway, 2001). The primary function of B cells is the production of antigen-specific antibodies, the key component of the humoral immune response. For generation of high-affinity antibodies and antibody memory B cells obtain help from so-called helper T cells. T cells develop from double positive CD4<sup>+</sup>CD8<sup>+</sup> precursor cells in the thymus into single positive CD4<sup>+</sup> and CD8<sup>+</sup> effector T cells. CD8<sup>+</sup> cytotoxic T cells recognize peptides presented on MHC class I complexes and mediate killing of cells that are transformed or have been infected with intracellular pathogens, while CD4<sup>+</sup> T cells differentiate into distinct subsets of helper T cells upon activation in the periphery.

Although CD8<sup>+</sup> T cells play a critical role in the fight against tumors and viral infections, I will concentrate on the CD4<sup>+</sup> T cell lineage in the following paragraphs as a cellular model of this study. First of all, I will describe initial mechanisms of T cell priming and B cell activation and how a specific subset of helper T cells called T follicular helper cells (T<sub>FH</sub> cells) contributes to the generation of high-affinity antibody-producing B cells. I will then elucidate the complex network of regulatory mechanisms that direct T helper cell differentiation and finally explain the special role of costimulatory receptors in T<sub>FH</sub> cell differentiation.

### **1.2.1.1 T cell priming and activation of antigen-presenting B cells**

Activation of the adaptive immune response starts with pathogen engulfment by professional antigen-presenting cells (APCs), such as dendritic cells, macrophages and B cells, followed by the presentation of pathogen-derived antigenic peptides on surface MHC class II proteins. Upon activation, dendritic cells migrate to the T cell zone of secondary lymphoid organs, where the peptide-MHC class II complexes are presented to naïve CD4<sup>+</sup> T lymphocytes (Janeway et al., 2005). Approximately 10<sup>12</sup> T cells are estimated to be present in the human organism, each carrying a cell surface receptor called T cell receptor (TCR) with a different peptide specificity (Goronzy et al., 2015). T cell receptors are randomly assembled by differential joining of a large number of variable receptor gene segments, leading to a combinatorial diversity of up to 10<sup>20</sup> possible TCRs (Goronzy et al., 2015; Janeway et al., 2005). TCR-mediated recognition of a specific peptide-MHC complex is the first signal to activate a naïve peripheral T cell and additional costimulatory signals are required for full activation. This process, after which T cells undergo excessive proliferation and subsequent

differentiation into designated subsets (Figure 4, left-hand side), is called T cell priming.

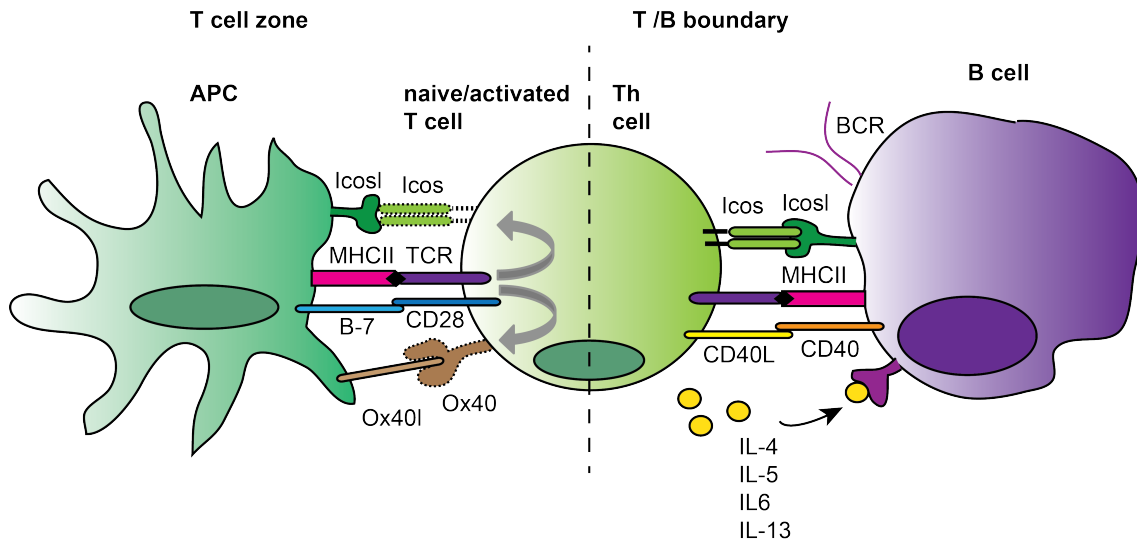


**Figure 4: T cell priming and B cell activation.**

*Schematic representation of T cell priming mediated by professional antigen-presenting cells (APCs) in the T cell zone of secondary lymphoid organs (left-hand side) and subsequent activation of antigen-presenting B cells at the border between the T cell and the B cell zone (T/B boundary) (right-hand side). Professional APCs engulf and digest pathogens and present antigenic peptides on MHC class II molecules. Naïve T cells recognize the peptide-MHC complex with their TCR, which provides the primary signal for T cell activation. Activation-induced expression of B7 on the APC leads to costimulatory signals via CD28, which is constitutively expressed on naïve T cells. The combination of TCR and CD28 signaling induces the expression of the inducible T cell costimulators Icos and Ox40 on the T cell surface. Icos and Ox40 binding to Icosl and Ox40l on the APC surface, respectively, completes the secondary costimulatory signaling. T cell activation induces proliferation and differentiation into helper T cells (Th). These travel to the T/B boundary and activate antigen-presenting B cells via costimulatory signals and secreted cytokines (Heissmeyer et al., 2005; Janeway et al., 2005).*

Naïve B cells reside in follicles of secondary lymphoid organs, which are surrounded by T cell zones (De Silva & Klein, 2015). Similar to T cells, B cells recognize antigens via variable cell surface receptors. Their B cell receptor (BCR) is a membrane-bound version of the secreted antibody. Like TCRs, BCR- and thus also antibody-encoding genes are assembled by genetic rearrangement, leading to a similarly high diversity of antibodies and BCRs. B cells can function as professional APCs by recognizing their respective antigen with the BCR followed by antigen engulfment and digestion into peptides, which are presented on MHC class II molecules on the B cell surface. Upon antigen uptake, B cells travel to the boundary of the T cell and the B cell zone (T/B boundary) in secondary lymphoid organs. Here, they encounter primed T helper cells,

which have also migrated to the T/B boundary in response to initial activation and T helper cell differentiation in the T cell zone (Figure 4, right-hand side). Peptide-MHC complexes displayed on the B cell surface are recognized by the TCR of the antigen-specific T helper cell. Subsequent expression of CD40L on the T<sub>H</sub> cell surface and its interaction with CD40 expressed on the B cell surface provides critical costimulatory signaling. T helper cells additionally secrete cytokines, such as IL-4, IL-5 and IL-13, which promote B cell proliferation and their differentiation into antibody-producing plasma cells (Janeway et al., 2005).

### **1.2.1.2 Initiation of a T cell-dependent antibody response**

Primed B cells proliferate and either migrate to the center of primary lymphoid follicles to form germinal centers (GC) or undergo extrafollicular plasma cell differentiation (Vinuesa et al., 2016). Germinal centers and the action of a special T helper cell subset called follicular helper T cells (T<sub>FH</sub> cells) are critical for mounting a high-affinity antibody response. T<sub>FH</sub> cells were discovered in 2001 as the most potent inducers of antibody production from B cells (Breitfeld et al., 2000; Kim et al., 2001). They express the master transcription factor Bcl-6, the follicular homing receptor CXCR5, high levels of the costimulatory receptor Icos and the coinhibitory receptor PD-1 and secrete IL-21 (Vinuesa et al., 2016).

In the dark zone of the germinal center, B cells proliferate and undergo somatic hypermutation (SHM), a process in which the specificity of the BCR is altered by random mutations. B cell clones carrying mutated BCRs migrate to the GC light zone for affinity selection. Clones carrying mutated BCRs are selected according to their ability to pick up antigen from a network of follicular dendritic cells (De Silva & Klein, 2015) and present it to T<sub>FH</sub> cells. B cell clones with a low affinity BCR are eliminated in this process, while high-affinity BCR clones receive help from T<sub>FH</sub> cells to migrate back to the dark zone to resume SHM (Oropallo & Cerutti, 2014). The whole process of multiple rounds of SHM followed by affinity selection is called affinity maturation. During affinity maturation IgM<sup>+</sup> B cells receive signals to switch the constant domain of their heavy chain from IgM towards IgG in a process called antibody class switching (McHeyzer-Williams et al., 2015). While B cells undergo affinity maturation, T<sub>FH</sub> cells develop in parallel from primed helper T cells via an intermediate step called pre-T<sub>FH</sub>. Pre-T<sub>FH</sub> cells have upregulated the transcription factor Bcl-6, and express low levels of PD-1 and Icos (Lee et al., 2011). They can reside outside the follicle and provide help to B cells to form short-lived extrafollicular plasma cells, which produce low-affinity

antibodies that are important for a fast response against intruding pathogens (Lee et al., 2011). Pre-T<sub>FH</sub> cells that enter the follicle mature into GC T<sub>FH</sub> cells via repeated interactions with B cells. Upon maturation, GC T<sub>FH</sub> cells provide cognate B cells that have undergone affinity maturation with costimulatory signals and IL-21, which initiates their differentiation into antibody-producing plasma cells and memory cells (Vinuesa et al., 2016). GC plasma cells produce high amounts of high-affinity IgG antibodies that are capable of fighting long-lasting infections due to a long serum half-life of 20 days (Brekke & Sandlie, 2003), while long-lived memory B cells reside in the secondary follicles with the option of differentiating into plasma cells upon secondary exposure with the same antigen. Memory cells also arise from activated T<sub>FH</sub> cells, which circulate in the blood stream as central memory T<sub>FH</sub> cells and enable a fast GC formation upon secondary antigen exposure (Vinuesa et al., 2016). In response to secondary antigen stimulation, reactivated class-switched memory B cells can again go through the process of mutation and selection in secondary GC reactions (McHeyzer-Williams et al., 2015). The GC reaction thus continuously improves the antibody specificity both during primary and secondary immune responses, and is therefore essential for mounting a high-affinity antibody response and antibody memory.

### **1.2.1.3 Lineage determination of T cell differentiation**

The fate of a naïve CD4<sup>+</sup> T cell is mainly determined during its initial interaction with the antigen-presenting dendritic cell in the T cell zone of secondary lymphoid organs (Schmitt & Ueno, 2015). Here, a combination of the TCR signal strength, costimulatory signals and the surrounding cytokine milieu are believed to skew T cell differentiation towards the specified lineages (Huang & August, 2015). T helper cells are subdivided into Th1, Th2, Th17, iTreg and T<sub>FH</sub> cells based on effector functions and secreted cytokines. Early on, cytokine signaling sets the course for differentiation into the one or the other subset by inducing the phosphorylation and activation of distinct signal transducer and activators of transcription (Stat) proteins. These determine the T cell fate by imposing specific gene expression programs leading to the expression of a master transcription factor, which is responsible for the expression of subset-specific effector proteins (Yamane & Paul, 2013).

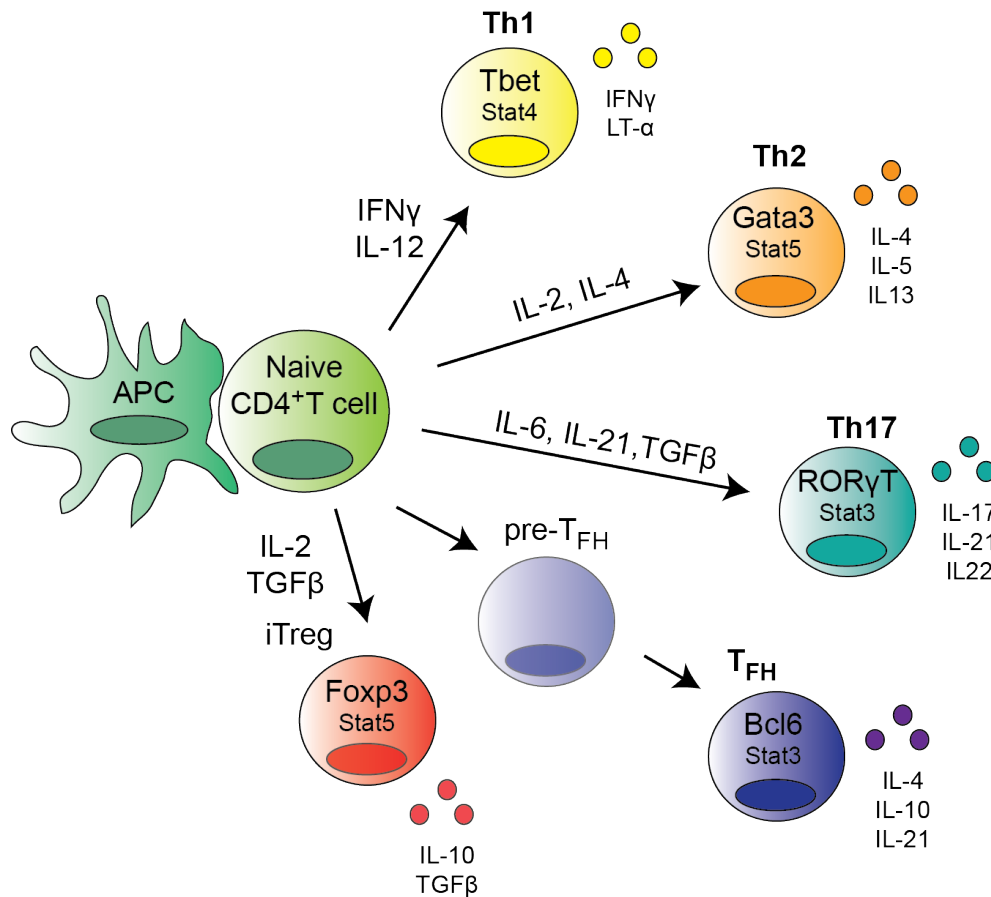


**Figure 5: Cytokine profiles determine T helper cell differentiation.**

Upon recognition of a specific peptide-MHC complex on a professional antigen-presenting cell (APC), naive CD4<sup>+</sup> T cells proliferate and differentiate into distinct populations of T helper cells. Each Th subset (Th1, Th2, Th17, T<sub>FH</sub> and iTreg) is characterized by the expression of a unique master transcription factor (bold letters) in combination with a cytokine-activated signal transducer and activator of transcription (Stat), imposing distinct gene expression profiles. The resulting expression of distinct sets of effector cytokines corresponds to specified roles in immune regulation. This scheme was drawn based on (Schmitt & Ueno, 2015; Vinuesa et al., 2016; Yamane & Paul, 2013).

T cell differentiation in response to different cytokine stimuli has been studied extensively in the mouse system. IL-12/IL12R signaling activates Stat4, which induces the expression of IFN $\gamma$  (Park et al., 2004). IFN $\gamma$  signaling in turn activates Stat1, which is responsible for the induction of the master transcription factor Tbet that drives the characteristic gene expression profile of Th1 cells (Afkarian et al., 2002). By CD40-CD40L interaction in combination with IFN $\gamma$  secretion, Th1 cells are potent activators of macrophages and are in general responsible for regulating the immune response against intracellular bacteria. However, Th1 cells have also been found to be associated with autoimmunity (Janeway, 2001; Yamane & Paul, 2013). Helper cells of the Th2 lineage, by contrast, develop in response to IL-2 and IL-4 signaling, resulting in the activation of Stat5 and Stat6, respectively (Maier et al., 2012). The lineage

determining transcription factor Gata3 induces the secretion of the cytokines IL-4, IL-5 and IL-13, which are effective in inducing plasma cell differentiation and antibody production of B cells. On the other hand, Th2 cells can be the driving force in allergy and asthma (Vinuesa et al., 2016). Th17 cells express the master transcription factor ROR $\gamma$ t and are induced in the mouse system in response to IL-6, IL-21 and TGF- $\beta$  stimulation (Schmitt & Ueno, 2015). IL-6 activates Stat3, which together with Icos signaling enables IL-21 production (Yamane & Paul, 2013). The main characteristic of Th17 cells is the secretion of the cytokine IL-17, along with IL-21 and IL-22. IL-17/IL17R signaling induces gene expression of proinflammatory effector molecules, thereby playing an important role in the clearance of extracellular bacterial infections (Onishi & Gaffen, 2010). Aberrant production of IL-17 is linked to several autoimmune diseases, such as rheumatoid arthritis and systemic lupus erythematosus (Onishi & Gaffen, 2010). In contrast to the differentiation of Th1, Th2 and Th17 cells, T<sub>FH</sub> differentiation is a two-step process. As mentioned before (Chapter 1.2.1.2), initial T cell activation at the T/B boundary induces differentiation into pre-T<sub>FH</sub> cells, while differentiation into mature T<sub>FH</sub> cells takes place in germinal centers of primary lymphoid follicles. GC T<sub>FH</sub> cells express the subset determining transcription factor Bcl-6. By high expression of Icos accompanied by the secretion of IL-21 and IL-4, they are especially potent in inducing affinity maturation of B cells for generation of plasma cells and memory cells (Marine et al., 2012; Tan et al., 2014).

As opposed to the T cell subtypes described so far, regulatory T cells (Tregs) are characterized by the expression of the subset-specifying transcription factor Foxp3 and counteract the immune response by inhibiting effector T cells via multiple mechanisms. These include the secretion of immunosuppressive cytokines such as IL-10 and TGF- $\beta$ , inhibition via cell-to-cell contact e.g. by expressing inhibitory cell surface receptors like CTLA-4 and competition for growth factors such as IL-2 (Sojka et al., 2008). The main population of natural Tregs (nTregs) develops in the thymus, while a subpopulation of induced Tregs (iTregs) differentiate in the periphery from naïve CD4<sup>+</sup> T cells in response to stimulation conditions that can be mimicked in vitro by IL-2 and TGF- $\beta$  signaling (Yamane & Paul, 2013).

While Th1 and Th2 differentiation in response to distinct cytokine signals is generally similar between humans and mice, stronger differences exist in Treg, Th17 and T<sub>FH</sub> differentiation. For instance, human naive T cells do not develop into Th17 cells in response to IL-6, IL-21 and TGF- $\beta$  signaling, but are instead induced upon stimulation

with IL-1 $\beta$  and IL-23 (Schmitt & Ueno, 2015). Moreover, human T<sub>FH</sub> differentiation is initiated primarily by the cytokine IL-12 rather than by IL-6 and IL-21. These differences of human and mouse naïve T cells in responding to different cytokine stimuli are caused by the differential expression of cytokine receptors, and have to be kept in mind when transferring knowledge from animal models to the human system (Schmitt & Ueno, 2015).

T helper cell differentiation in response to distinct cytokine expression profiles is highly complex. Favoring one lineage differentiation program is often accompanied by inhibitory signals for reciprocally developing lineages. For example, Th2-promoting IL-2/Stat5 signaling blocks Th17 differentiation (Yamane & Paul, 2013). In addition to cytokine stimulation, Th cell differentiation is directed by the strength of TCR signaling and costimulatory signals (Zhu & Paul, 2010). The impact of TCR signaling, which is influenced by both antigen dose and TCR affinity, is still highly debated. Overall, weak TCR signaling is believed to promote Th2 or T<sub>FH</sub> differentiation, while intermediate signaling induces Th1- and strong signaling again induces T<sub>FH</sub> cells (Tubo & Jenkins, 2014). Recent research has provided a number of examples of T cell differentiation with a high degree of plasticity. It indicates that the process is far more complex than previously anticipated and differentiation into the one or the other lineage is not as definite as initially thought.

#### **1.2.1.4 The costimulatory receptors CD28 and Icos regulate T<sub>FH</sub> cell differentiation**

Besides cytokine signaling and TCR signal strength, T cell fate decisions are influenced by costimulatory signals. The development of T<sub>FH</sub> cells, which are essential for the generation of a high-affinity antibody response and B cell memory in the germinal center reaction, is critically influenced by the action of two Ig superfamily costimulatory receptors CD28 and Icos. Icos arose from gene duplication of CD28, and both proteins share 39 % amino acid identity and are expressed as homodimeric cell surface proteins (Hutloff et al., 1999). Although structurally similar and equally capable of supporting TCR-induced gene expression, T cell proliferation and cytokine production (Linterman et al., 2009), CD28 and Icos have non-overlapping functions in the induction of an antibody-dependent immune response and show a compartmentalized expression. CD28 is broadly expressed on most T cell subsets and found also on naïve cells, while Icos is only induced on the T cell surface upon activation (Beier et al., 2000; Gross et al., 1992). Icos expression is thus restricted to

CD4<sup>+</sup> effector and memory T cells and found most highly expressed on T<sub>FH</sub> cells within germinal centers (Akiba et al., 2005). Besides, a subset of Foxp3<sup>+</sup> regulatory T cells expresses Icos and is dependent on Icos signaling for proliferation and function (Yong et al., 2009).

The importance of CD28 and Icos for mounting a T cell-dependent antibody response became apparent when studying knockout mice. *CD28*<sup>-/-</sup> mice show impaired T cell proliferation after stimulation, a defect in IL-2 production and impaired antibody class switching (Shahinian et al., 1993). Moreover, germinal centers and T<sub>FH</sub> cells are absent in these mice (Ferguson et al., 1996; Walker et al., 1999), and the numbers of regulatory T cells are drastically reduced (Salomon et al., 2000). *Icos*<sup>-/-</sup> mice phenocopy some of the *CD28*<sup>-/-</sup> phenotypes such as the presence of smaller and fewer GCs, reduced numbers of T<sub>FH</sub> cells and a deficit in antibody class switching (McAdam et al., 2001). Moreover, reactivation of memory T cells is impaired in *Icos*<sup>-/-</sup> mice and differentiated T cells from *Icos*<sup>-/-</sup> mice are unable to produce IL-2 and IL-4 (McAdam et al., 2001). In *CD28*<sup>-/-</sup> *Icos*<sup>-/-</sup> double-deficient mice, antibody production in response to T-dependent antigens as well as viral infection is more severely impaired compared to *CD28*<sup>-/-</sup> animals, indicating that Icos and CD28 fulfill redundant but also diverse roles in the T cell-dependent antibody response (Suh et al., 2004). In humans, loss of function mutations in the *ICOS* gene leading to the absence of ICOS expression on T cells have been identified as a cause of common variable antibody deficiency (CVID). Patients have lower serum levels of IgG and IgA class antibodies indicating a defect in antibody class switching and are susceptible to recurrent respiratory and gastrointestinal infections (Warnatz et al., 2006).

The burning question of how CD28 and Icos signaling influence the development of a T cell-dependent B cell response was recently answered by resolving their role in T<sub>FH</sub> differentiation. Icos ligation leads to a series of intracellular signaling events in T cells, starting with the recruitment of the p50 $\alpha$  regulatory subunit of the phosphatidylinositol 3-kinase (PI3K), which associates with the p110 catalytic subunit to initiate a signaling cascade that results in the phosphorylation and activation of the protein kinase Akt (Fos et al., 2008). Akt phosphorylates and thereby inactivates the transcription factor Foxo1 (Stone et al., 2015), which is responsible for transcriptional induction of Klf2. Klf2 critically determines T<sub>FH</sub> cell homing. A low expression of this transcription factor is important to maintain a T<sub>FH</sub> cell-specific homing factor repertoire (high expression of CXCR5 and low expression of CCR7, CD62L, PSGL-1 and

S1PR1) and to prevent Klf2-induced expression of the Th1- and Th2-promoting transcription factors Tbet and Gata3 (Weber et al., 2015). Besides, Icos signaling can activate the alternative PI3K subunit p85 $\alpha$ , which leads to protection from proteasomal degradation and thus stabilization of the lineage-determining transcription factors Bcl-6 and Ascl2 (Leavenworth et al., 2015) that are responsible for upregulation of CXCR5 and other T<sub>FH</sub> effector molecules such as PD-1, CXCR4, and SAP (Liu et al., 2014). The overall importance of Icos-mediated PI3K signaling for a high-affinity antibody response became clear in a study using conditional PI3K p100 $\delta$  knockout mice. It was found here that the magnitude of Icos signaling via PI3K determines the number of T<sub>FH</sub> cells and consequently also the amount of GC B cells (Rolf et al., 2010). In contrast to ICOS, CD28 has a low affinity for the p110/p50 $\alpha$  isoform of PI3K, resulting in a lower potential of phosphorylating Foxo1 and thereby restricting Klf2 expression (Weber et al., 2015). CD28 is instead necessary for the early events in T<sub>FH</sub> differentiation, including the upregulation of Bcl-6 and CXCR5 (Weber et al., 2015). ICOS and CD28 thus control T<sub>FH</sub> differentiation by acting in different phases: While CD28 regulates early T<sub>FH</sub> differentiation by upregulation of Bcl-6, Icos is important for T<sub>FH</sub> cell maintenance and homing to the B cell zone of the lymphoid follicle (Weber et al., 2015).

### 1.2.2 The CRISPR/Cas system: adaptive immunity in prokaryotes

For a long time it was generally accepted that an adaptive immune response was restricted to higher eukaryotes simply because it appeared to require different cell types. Therefore, the recent discovery of an RNA-based adaptive immune system in bacteria and archaea came as a surprise. Prokaryotes protect themselves against viral re-infection by integrating short fragments of the foreign nucleic acids, called protospacers, into defined loci of their own genome. These loci were named clustered regularly interspaced short palindromic repeats, or short CRISPR (Wiedenheft et al., 2012). In each CRISPR locus a series of identical DNA repeats is interspersed by unique spacer sequences derived from the foreign protospacer motifs (Figure 6).



sequence. tracrRNA and crRNA form a complex with the CRISPR-associated (Cas)-nuclease 9 (Cas9), which recognizes protospacers of foreign DNA sequences by spacer-mediated complementary base pairing. If the protospacer on the target DNA is flanked by a 3' protospacer adjacent motif (PAM), Cas9 performs double strand cleavage of the protospacer sequence, leading to the destruction of the pathogenic DNA (Wiedenheft et al., 2012).

Similar to RNAi (Chapter 1.1.3), the CRISPR system can be harnessed as a biotechnological tool. A breakthrough was achieved when researchers succeeded in combining features of the crRNA and the tracrRNA into a single guide RNA (sgRNA) (Figure 6, dashed box), which was sufficient to guide Cas9 to the intended genomic locus and induce double strand breaks (Jinek et al., 2012). These are repaired either by homology-directed repair (HR) or, more often, by error-prone non-homologous end-joining (NHEJ), which typically results in short stretches of nucleotide insertions or deletions (indels). As a consequence, the reading frame is shifted in 2/3 of all cases, and is likely to produce transcripts with premature stop-codons. These are efficiently removed by NMD. In the remaining 1/3 of all cases indels of DNA lead to mature proteins with a low number of amino acid insertions or deletions. By contrast, homology-directed repair makes use of a homologous repair template and therefore hardly introduces mistakes. One can take advantage of HR to produce tailor-made gene modifications (Zheng et al., 2014) by transferring a specifically designed repair template along with Cas9 and an sgRNA into target cells. Simultaneous presence of Cas9 nuclease and sgRNA in the nucleus are the minimal requirements for CRISPR/Cas-mediated genome editing. Various systems have been developed for efficient delivery of Cas9 into virtually any type of target cell. Cas9-encoding plasmids can be delivered transiently by transfection (Shen et al., 2014) or adenoviral transduction (Maggio et al., 2014), but also stably via lentiviral infection (Shalem et al., 2014). Moreover, Cas9 and sgRNAs can be microinjected either as mRNA or, in the case of Cas9, as recombinant protein (Kalebic et al., 2016; Shen et al., 2014). In combination with lentivirally- or transiently delivered sgRNA-encoding plasmids, the CRISPR/Cas9 system thus provides a versatile tool for the generation of targeted gene modifications (Shalem et al., 2014; Shen et al., 2014).

## 1.3 Post-transcriptional gene regulation in the mammalian immune system

Immune cells have to be able to quickly adapt their cytokine and transcription factor profile in response to pathogen invasion. In mammals, many cytokine and immunomodulatory mRNAs are thus prone to profound post-transcriptional gene regulation and characterized by a short mRNA half-life (Ivanov & Anderson, 2013). Suspension of these control mechanisms can have severe consequences, which I will show exemplarily for two different post-transcriptional regulatory mechanisms in the following two paragraphs. Finally, this chapter will conclude with a detailed illustration of how Roquin proteins mediate peripheral immune tolerance.

### 1.3.1 ARE-mediated decay of cytokine mRNAs

A prominent pathway of post-transcriptional gene regulation is AU-rich element (ARE)-mediated decay, affecting approximately 5 – 10 % of all human mRNAs including many cytokines, chemokines and other proinflammatory proteins (Ivanov & Anderson, 2013). It is conducted by a large number of different ARE-binding proteins that recognize AREs in the 3' UTRs of their target mRNAs and promote or inhibit translation and/or mRNA decay (Ivanov & Anderson, 2013). A well-studied example is an ARE in the *tumor necrosis factor (TNF)* mRNA (Caput et al., 1986) that is targeted by multiple antagonistic ARE-binding proteins including the ZnF RNA-binding protein TTP, which destabilizes *TNF* mRNA (Molle et al., 2013). TNF is a highly potent proinflammatory cytokine, which is produced in abundance by macrophages in response to LPS stimulation (Zhang et al., 1997). Abrogation of TTP-mediated regulation of *TNF* mRNA in *TTP<sup>-/-</sup>* mice leads to excessive TNF production (Carballo et al., 1997) resulting in spontaneous development of a complex inflammatory syndrome characterized by cachexia, myeloid hyperplasia, dermatitis, arthritis and finally autoimmunity including the production of autoantibodies (Taylor et al., 1996). Post-transcriptional regulation of cytokine mRNAs thus seems to be a major mechanism in the prevention of autoimmunity and inflammation.

### 1.3.2 The stem-loop binding proteins Roquin-1, Roquin-2 and Regnase-1 control immunomodulatory mRNAs

Another mechanism of post-transcriptional gene regulation was recently discovered in T cells. Here, the stem-loop binding proteins Roquin-1, Roquin-2 (Chapter 1.1.4.2) and

Regnase-1 (Chapter 1.1.4.3) were found to repress mRNAs encoding cytokines (*Il6*, *TNF*), costimulatory receptors (*Icos*, *Ox40*, *Ctla-4*), transcription factors (*Irf4*, *cRel*) and transcriptional modulators (*Nfkbid*, *Nfkbiz*) (Jeltsch et al., 2014; Uehata et al., 2013; Vogel et al., 2013). Upon T cell activation, both Roquin paralogs and Regnase-1 are cleaved and inactivated by the paracaspase Malt1, which results in the derepression of their target mRNAs (Jeltsch et al., 2014; Uehata et al., 2013).

The majority of mRNAs targeted by Roquin-1 and Regnase-1 code for proteins with crucial roles in the T cell fate decision. The cytokine IL-6 is a potent inducer of Th17 differentiation (Korn et al., 2008), supported by Irf4 (Brustle et al., 2007), cRel (Chen et al., 2011; Reinhard et al., 2011; Ruan et al., 2011), I $\kappa$ B $\zeta$  (Okamoto et al., 2010) and I $\kappa$ BNS (Jeltsch et al., 2014), which operate on the transcriptional level. As described previously (Chapter 1.2.1.4), Icos plays a critical role in T<sub>FH</sub> development. Likewise, costimulatory Ox40 signaling was found to promote upregulation of T<sub>FH</sub> effector proteins on activated and memory CD4<sup>+</sup> T cells (Jacquemin et al., 2015). Moreover, Irf4 is not only essential for Th17, but also for T<sub>FH</sub> differentiation (Bollig et al., 2012; Brustle et al., 2007; Huber et al., 2008). Roquin and Regnase-1 thus primarily regulate mRNAs with a function in Th17 and T<sub>FH</sub> differentiation, and their loss of function should consequently result in a strong imbalance in T cell differentiation. Indeed, mutation of Roquin-1 (M199R, called *sanroque* mutation) or T cell-specific ablation of Roquin-1 and its paralog Roquin-2 in mice leads to the spontaneous activation of CD4<sup>+</sup> and CD8<sup>+</sup> T cells and an accumulation of T<sub>FH</sub> and Th17 cells (Jeltsch et al., 2014; Vinuesa et al., 2005; Vogel et al., 2013). In addition, aberrant production of the Th1 cytokine IFN $\gamma$  was observed in *sanroque* mice (Lee et al., 2012). Strikingly, the bias towards Th1, T<sub>FH</sub> and Th17 cell differentiation upon loss of Roquin function is connected to the development of severe autoimmunity and other pathologies. In *sanroque* mice, enhanced numbers of T<sub>FH</sub> cells are associated with spontaneous germinal center formation and the production of high-affinity anti-nuclear autoantibodies, causing a systemic lupus erythematosus (SLE)-like autoimmune phenotype (Vinuesa et al., 2005). In Roquin-deficient mice, tissue-infiltrating Th17 cells cause lung pathology (Jeltsch et al., 2014). Loss of Regnase-1 has similar severe consequences. Mice with a T cell-specific deletion of the Regnase-1-encoding gene *Zc3h12a* also display an autoimmune phenotype accompanied by spontaneous T cell activation, accumulation of plasma cells and the production of anti-nuclear autoantibodies (Uehata et al., 2013).

### 1.3.3 Roquin proteins mediate peripheral immune tolerance

By restricting unwanted Th1, T<sub>FH</sub> and Th17 differentiation, Roquin proteins thus appear to be essential mediators of peripheral tolerance. While central tolerance operates in the thymus to eliminate self-reactive B and T lymphocytes, peripheral tolerance is a secondary fail-safe mechanism against autoimmunity. An important mechanism in peripheral tolerance is the requirement for costimulation. Many costimulatory receptors, such as the CD28 ligands B7-1 and B7-2, are selectively upregulated on APCs only after pathogen encounter. In the absence of costimulation, self-reactive T cells will become anergic upon activation (Heissmeyer et al., 2005). Some costimulatory receptor ligands however, such as the Icos ligand Icosl, are constitutively expressed on APCs. In this case, expression of the costimulatory receptor, here Icos, has to be restricted in T cells. In addition to the transcriptional program, this is mediated on the post-transcriptional level by Roquin-1, Roquin-2 and Regnase-1. In line with this, it was found that loss of Roquin function uncouples the T cell-dependent antibody response from the requirement for CD28 costimulation (Linterman et al., 2009). Upregulation of Icos due to functional inactivation of Roquin could revert the most prominent phenotypes of CD28-deficient mice, including impaired GC formation and T<sub>FH</sub> differentiation, primary antibody responses and iTreg development (Linterman et al., 2009). This was not the case when Icos signaling was abrogated by additional deletion of Icosl. By post-transcriptional regulation of Icos, Roquin proteins therefore compartmentalize Icos and CD28 function and prevent autoimmunity by making the system dependent on CD28-mediated discrimination between self- and foreign antigens (Linterman et al., 2009). For this reason, upregulation of Icos, together with other Roquin targets, is one of the causative agents of the autoimmune phenotype of *sanroque* mice (Yu et al., 2007).

## 2 Aim of the project

Roquin-1 and its paralog Roquin-2 are RNA-binding proteins with a crucial role in T cell differentiation. They bind to stem-loop structures in the 3' UTRs of their target mRNAs, which are important mediators of Th1, T<sub>FH</sub>, and Th17 differentiation, and induce post-transcriptional repression. Mice where Roquin-1 is mutated (*sanroque* mouse strain) or Roquin-1 and Roquin-2 are missing in T cells develop severe autoimmunity or show lung pathology, respectively. Although Roquin proteins thus appear to be highly important for the maintenance of immunological tolerance, their mechanism of action remains elusive, and especially their regulators and cofactors are largely unknown.

In order to solve this, the aim of this thesis was the development of robust high-throughput screening (HTS) approaches enabling the identification of unknown cofactors of Roquin-mediated post-transcriptional gene regulation. This first of all required the establishment of tailor-made reporter cell lines that allow high-throughput, in the best case genome-wide, screening. Once primary screening was accomplished, hit validation started from a long list of candidate genes. A second milestone of this thesis was therefore the development of a hit validation strategy that potently discriminated true hits from false positives and identified the most promising candidates for functional validation.

The final goal was a detailed functional validation of a so far unknown candidate protein as a new Roquin cofactor. The first question in this context was whether the candidate protein interacts with Roquin-1, which was investigated in protein binding assays. Next, it was important to determine the *cis*-elements on which Roquin can cooperate with its cofactors in a detailed structure-function analysis.

Since Roquin proteins play a critical role in T cells, it furthermore needed to be investigated whether the candidate protein itself is also active in immune cells, and whether it acquires a special function in T cells. Combining the results from the candidate gene validation with the knowledge on potential cofactors of Roquin-1 as suggested by the literature finally enabled us to create a broader picture of the assembly of the mRNP that coordinates Roquin function.



## 3 Material and methods

### 3.1 Material

#### 3.1.1 Mice and MEF cells

Primary immune cells and mouse embryonic fibroblast (MEF) cells used in this study were obtained from wildtype mice unless stated otherwise.

*Rc3h1/2<sup>fl/fl</sup>* MEF cells were generated from *Rc3h1/2<sup>fl/fl</sup>* mice, where exons 4-6 of *Rc3h1* and exon 4 of *Rc3h2* are flanked by loxP sites (Vogel et al., 2013). To produce *Rc3h1/2<sup>-/-</sup>* MEF cells, *Rc3h1/2<sup>fl/fl</sup>* cells were transduced to express Cre recombinase, thereby deleting the respective exons.

*CAG-CAR<sup>STOP-fl</sup>* mice express a signaling-inactive form of the human coxsackie virus and adenovirus receptor (CAR) upon deletion of the loxP-flanked STOP cassette by Cre recombinase (Vogel et al., 2013). Crossing them with *Rc3h1/2<sup>fl/fl</sup>* mice and *Gt(ROSA)26Sor<sup>tm2(cre/ERT2)Brn</sup>* mice provided by Dr. Anton Berns (Hameyer et al., 2007) gave rise to *Rc3h1/2<sup>fl/fl</sup> CAG-CAR<sup>STOP-fl</sup> CreERT2* mice. In MEF cells generated from these mice (*Rc3h1/2<sup>fl/fl</sup> CreERT2* MEF) the Cre recombinase-estrogen receptor fusion protein CreERT2 can be activated *in vitro* by treatment with 4-OH-tamoxifen, leading to the disruption of the floxed exons of *Rc3h1* and *Rc3h2*, while simultaneously inducing expression of the cell surface marker CAR. The single cell *Rc3h1/2<sup>fl/fl</sup> Cre ERT2* MEF clone used in this study was produced by Desiree Argiriou and shows complete ablation of Roquin-1 and Roquin-2 protein expression upon 4-OH-tamoxifen treatment.

All mice were bred on a C57/Bl6 background and housed in a special pathogen-free barrier facility at Helmholtz Zentrum München in accordance with the Helmholtz Zentrum München institutional, state and federal guidelines.

#### 3.1.2 Cell lines and cell culture

HeLa cells were a kind gift from Dr. Helmut Holtmann.

The origin of MEF cells with different genotypes was described above (Chapter 3.1.1).

Jurkat T cells were obtained from ThermoFisher Scientific (Catalog # R762-07).

**MEF cells** and **HeLa cells** were cultured in a cell culture incubator at 37 °C, 10 % CO<sub>2</sub> in DMEM supplemented with 10 % fetal bovine serum (FBS), 1 % penicillin-streptomycin and 1 % HEPES. **Jurkat T cells** were cultured at 37 °C, 5 % CO<sub>2</sub> in RPMI 1640 medium supplemented with 10 % fetal bovine serum, 1 % penicillin-streptomycin, 1 % HEPES, 1 % L-glutamine and 0.1 % β-mercaptoethanol. **Primary mouse T cells** were cultured at 37 °C, 5 % CO<sub>2</sub> in RPMI-1640 medium supplemented with 10 % fetal bovine serum, 1 % HEPES, 1 % penicillin-streptomycin, 1 % non-essential amino acids (NEAA), 1 % sodium pyruvate, 1 % vitamin solution, 1 % L-glutamine and 0.1 % β-mercaptoethanol (Table 2).

**Table 2: Cell culture components**

Component	Supplier
Dulbecco's Modified Eagle Medium (DMEM)	ThermoFisher Scientific
Fetal bovine serum (FBS)	PAN BIOTECH
HEPES pH 7.4 (1 M)	ThermoFisher Scientific
L-Glutamine 200 mM	ThermoFisher Scientific
MEM non-essential amino acids (NEAA) 100x	ThermoFisher Scientific
MEM vitamin solution (100x)	ThermoFisher Scientific
Penicillin-streptomycin (10,000 U/ml)	ThermoFisher Scientific
RPMI 1640, no glutamine	Lonza
Sodium pyruvate (100 mM)	Lonza
Tet-system approved FBS	Clontech Laboratories
β-mercaptoethanol	Sigma-Aldrich

### 3.1.3 Plasmids

Genes of interest were PCR-amplified from cDNA using gene-specific primers (Table 7) and subsequently cloned into Gateway<sup>®</sup> entry vectors by TOPO<sup>®</sup> cloning (Table 3). From entry vectors, genes of interest were recombined into different Gateway<sup>®</sup> destination vectors performing Gateway<sup>®</sup> LR reactions. Transient expression destination vectors (pDest12.2, pLNCX2) were used for calcium phosphate transfection of HEK293T cells (Table 4), while retro- (pKMV IRES GFP, pMSCV-IRES-Thy1.1) and lentiviral (plenti CMV Hygro, plenti PGK Hygro, plentiCMV<sub>tight</sub> Neo) expression destination vectors were used to achieve stable integration of the gene of interest by viral transduction (Table 5).

### 3.1.3.1 Entry vectors

**Table 3: List of Gateway® entry vectors**

Vector backbone	Insert
PCR8/GW TOPO	FBXL14
PCR8/GW TOPO	ICOS 1-600 (coding sequence, CDS)
PCR8/GW TOPO	ICOS CDS-CDE260
PCR8/GW TOPO	ICOS 1-800
PCR8/GW TOPO	ICOS 1-1211
PCR8/GW TOPO	ICOS 1-1811
PCR8/GW TOPO	ICOS 1-2011
PCR8/GW TOPO	ICOS 1-2211 $\Delta$ 700-800
PCR8/GW TOPO	ICOS 1-2271
PCR8/GW TOPO	ICOS 1-2391
PCR8/GW TOPO	ICOS full-length
PCR8/GW TOPO	ICOS SM1
PCR8/GW TOPO	ICOS SM1 SM2
PCR8/GW TOPO	ICOS SM1 SM2R
PCR8/GW TOPO	ICOS SM1R
PCR8/GW TOPO	ICOS SM1R SM2
PCR8/GW TOPO	ICOS SM1R SM2R
PCR8/GW TOPO	ICOS SM2
PCR8/GW TOPO	ICOS SM2R
PCR8/GW TOPO	ICOS $\Delta$ 700-800
PCR8/GW TOPO	ICOS-CDS-GFP-NF $\kappa$ BID 3' UTR
PCR8/GW TOPO	NUFIP2
PCR8/GW TOPO	Rab40c
PCR8/GW TOPO	Regnase-1
PCR8/GW TOPO	RNF222
PCR8/GW TOPO	Roquin-1 (aa 509-1130)-GFP
PCR8/GW TOPO	Roquin-1 full-length
PCR8/GW TOPO	Roquin-1-mCherry
PCR8/GW TOPO	Roquin-1-P2A-mCherry
PCR8/GW TOPO	Roquin-1 (aa 1-509)
PCR8/GW TOPO	Roquin-1 (aa 1-509)-P2A-mCherry
PCR8/GW TOPO	sgRNA-resistant NUFIP2
PCR8/GW TOPO	TRIM6-TRIM34
pENTR11	GFP-NUFIP2
pENTR11	GFP-Roquin-1 full-length
pENTR11	HA-Cas9-GFP
pENTR11	siRNA#2-resistant GFP-NUFIP2
pENTR11	GFP

PCR8/GW TOPO vectors with the inserts Roquin-1 full-length, Roquin-1 (aa 1-509), ICOS full-length, ICOS coding sequence, Roquin-1 (aa 509-1130)-GFP, ICOS 1-1211, ICOS 1-1811, ICOS 1-2011, ICOS 1-2211, ICOS 1-2271, ICOS 1-2391, GFP-Roquin-1 full-length and pENTR11 GFP-Roquin-1 full-length were kindly provided by Dr. Elke Glasmacher and Dr. Katharina Vogel and are described in (Glasmacher et al., 2010) and in (Vogel, 2012).

PCR8/GW TOPO ICOS 1-2211  $\Delta$ 700-800 was provided by Dr. Gitta Heinz, PCR8/GW TOPO ICOS CDS-CDE260 and ICOS-CDS-GFP-NF $\kappa$ BID 3' UTR were cloned by Dr. Sven Brenner and PCR8/GW TOPO ICOS 1-800 and ICOS  $\Delta$ 700-800 were generated by Claudia Lohs using primer sequences listed in Table 7.

HA-Cas9-GFP was cloned into PE11 via restriction digest of pMJ920, which was a kind gift from Dr. Jennifer Doudna (Addgene #42234) (Jinek et al., 2013).

### 3.1.3.2 Transient transfection destination vectors

**Table 4: Gateway® destination vectors for transient transfection**

Vector backbone	Insert
pDest12.2	GFP
pDest12.2	Roquin-1-mCherry
pDest12.2	Roquin-1 (aa 509-1130)-GFP
pLNCX2	Roquin-1-GFP
pLNCX2	Roquin-1 (aa 1-509)-GFP

pLNCX2 Roquin-1 (aa 1-509)-GFP and Roquin-1-GFP were provided by Dr. Elke Glasmacher. All other transient transfection destination vectors (Table 4) were cloned by Gateway® LR recombination from entry clones listed in Table 3. pDest12.2 (ThermoFisher Scientific) contains a CMV promoter for transient expression and a neomycin resistance gene as a selectable marker, while pLNCX2 (Clontech) is a retroviral vector that enables either transient or stable expression of a gene of interest from the CMV promoter.

### 3.1.3.3 Retro- and lentiviral destination vectors

Genes of interest were cloned into retro- and lentiviral Gateway® destination vectors by LR recombination from entry vectors listed in Table 3.

**Table 5: Retro- and lentiviral Gateway® destination vectors**

<b>Destination vector</b>	<b>Insert</b>
pKMV IRES GFP	ICOS 1-600 (coding sequence, CDS)
pKMV IRES GFP	ICOS CDS-CDE260
pKMV IRES GFP	ICOS 1-800
pKMV IRES GFP	ICOS 1-1211
pKMV IRES GFP	ICOS 1-1811
pKMV IRES GFP	ICOS 1-2011
pKMV IRES GFP	ICOS 1-2211
pKMV IRES GFP	ICOS 1-2211 $\Delta$ 700-800
pKMV IRES GFP	ICOS 1-2271
pKMV IRES GFP	ICOS 1-2391
pKMV IRES GFP	ICOS full-length (FL)
pKMV IRES GFP	ICOS SM1
pKMV IRES GFP	ICOS SM1 SM2
pKMV IRES GFP	ICOS SM1 SM2R
pKMV IRES GFP	ICOS SM1R
pKMV IRES GFP	ICOS SM1R SM2
pKMV IRES GFP	ICOS SM1R SM2R
pKMV IRES GFP	ICOS SM2
pKMV IRES GFP	ICOS SM2R
pKMV IRES GFP	ICOS $\Delta$ 700-800
plenti CMV Hygro	HA-Cas9-GFP
plenti PGK Hygro	ICOS 1-600 (coding sequence, CDS)
plenti PGK Hygro	ICOS full-length (FL)
plentiCMV <sub>tight</sub> Neo	Roquin-1-mCherry
plentiCMV <sub>tight</sub> Neo	Roquin-1-P2A-mCherry
plentiCMV <sub>tight</sub> Neo	Roquin-1 (aa 1-509)-P2A-mCherry
pMSCV-IRES-Thy1.1	FBXL14
pMSCV-IRES-Thy1.1	GFP
pMSCV-IRES-Thy1.1	GFP-NUFIP2
pMSCV-IRES-Thy1.1	ICOS-CDS-GFP-NF $\kappa$ BID 3' UTR
pMSCV-IRES-Thy1.1	NUFIP2
pMSCV-IRES-Thy1.1	Rab40c
pMSCV-IRES-Thy1.1	Regnase-1
pMSCV-IRES-Thy1.1	RNF222
pMSCV-IRES-Thy1.1	Roquin-1 full-length
pMSCV-IRES-Thy1.1	Roquin-1 (aa 1-509)
pMSCV-IRES-Thy1.1	sgRNA-resistant NUFIP2
pMSCV-IRES-Thy1.1	siRNA#2-resistant GFP-NUFIP2
pMSCV-IRES-Thy1.1	TRIM6-TRIM34

plentiCMV<sub>tight</sub> Neo DEST was a kind gift from Dr. Eric Campeau (Addgene plasmid #26432) and allows doxycycline-inducible gene expression from the CMV<sub>tight</sub> promoter, while including a neomycin resistance as a selectable marker gene.

plenti PGK Hygro DEST and plenti CMV Hygro DEST were donated by Dr. Eric Campeau (Addgene plasmids #19066 and #17454) (Campeau et al., 2009) and serve for stable lentiviral expression of a gene of interest from the PGK or CMV promoter, respectively, while including a hygromycin resistance gene as a selectable marker.

pMSCV-IRES-Thy1.1 DEST was a kind gift from Dr. Anjana Rao and allows stable retroviral expression of a gene of interest from retroviral LTRs with bicistronic expression of the surface marker Thy1.1.

pKMV IRES GFP allows stable retroviral expression of a gene of interest with an IRES-GFP fluorescence reporter.

#### **3.1.3.4 Non-Gateway® expression vectors**

The pOPINS3C vector was employed by Elena Davydova for expression of recombinant NUFIP2 (aa 255-411) in bacteria.

For doxycycline-inducible lentiviral gene expression from the plentiCMV<sub>tight</sub> Neo DEST vector (Table 5), cells need to be cotransduced with the TET-ON transactivator rtTA3. The rtTA3-encoding vector plenti CMV rtTA3 Blast was a kind gift from Dr. Eric Campeau (Addgene plasmid #26429).

The genome-scale lentiviral mouse GeCKO v2 Library (2 plasmid system) was purchased from Addgene (Addgene #1000000053) (Sanjana et al., 2014).

plentiCRISPR v1 was a kind gift from Dr. Feng Zhang (Addgene, now available as plentiCRISPR v2 #52961) (Shalem et al., 2014). plentiCRISPR EFS GFP was deposited by Dr. Benjamin Ebert (Addgene plasmid #57818) (Heckl et al., 2014).

Mouse and human Nufip2-targeting sgRNAs were designed using the 'optimized CRISPR tool' (<http://crispr.mit.edu>) provided by the Zhang lab and cloned into plentiCRISPR v1 or plentiCRISPR EFS GFP by annealing of oligonucleotides with *BsmBI* overhangs (Table 11) and ligation into *BsmBI*-digested vectors. Sequences for non-targeting controls (NT1, NT2) were taken from the mouse GeCKO v2 library.

**Table 6: lentiCRISPR vectors**

Vector backbone	Insert	Species
plentiCRISPR EFS GFP	mNUFIP2#1 sgRNA	Mouse
plentiCRISPR EFS GFP	mNUFIP2#2 sgRNA	Mouse
plentiCRISPR EFS GFP	mNUFIP2#3 sgRNA	Mouse
plentiCRISPR EFS GFP	mNUFIP2#4 sgRNA	Mouse
plentiCRISPR EFS GFP	NT1 sgRNA	-
plentiCRISPR EFS GFP	NT2 sgRNA	-
plentiCRISPR v1	hNUFIP2#3 sgRNA	Human

Retrovirus production was performed with ecotropic (eco-pac) or amphotropic (gag-pol and amphi-env) packaging vectors.

Lentivirus production was performed with second generation (pMD2.G VSVG and psPAX2 ) or third generation (pMD2.G VSVG, pRSV-Rev and pMDLg/pRRE) packaging plasmids, depending on the backbone of the lentiviral transfer vector (Chapter 3.2.3.4).

### 3.1.4 Oligonucleotides

#### 3.1.4.1 DNA oligonucleotides

DNA oligonucleotides were purchased from Metabion (Planegg, Germany) or Eurofins DNA (Ebersberg, Germany).

**Table 7: Primers for cDNA cloning**

Name	Sequence	cDNA
CDE260 for	CTCGAGGGAAGGCCGGGTGTCC	ICOS CDS CDE260
CDE260 rev	CTCGAGCTCTCAATGACCCGTAGGG	ICOS CDS CDE260
hFBXL14 for	GTCGACCATGGAGACCCACATCTCATGC	FBXL14
hFBXL14 rev	GCGGCCGCTCACCTTCTGGAGCTTCCC	FBXL14
hICOS_ATGfor	ATGAAGTCAGGCCTCTGGTATTTT	ICOS 1-800, ICOS Δ700-800
hICOS 1-700Xholrev	GAGACTCGAGTAAGTCAGACTCTCCGTGGTCC	ICOS Δ700-800
hICOS 1-800Xholrev	GAGACTCGAGAGAGGACTCGGCAGTACCAAG	ICOS 1-800
hTRIM6_TRIM34 for	GTCGACCATGTGCGGGTCAGAGAGGA	TRIM6_TRIM34
hTRIM6_TRIM34 rev	GCGGCCGCTCAAGAGCTTGGTGGGCATAG	TRIM6_TRIM34
ICOS-700-end Sall rev	GTCGACTACTACTGTAAAATCTTTTGATAAGTG	ICOS Δ700-800
ICOS Xhol 800-end for	CTCGAGCAAACAACACCCTCTTGCAAC	ICOS Δ700-800
mRab40c for	GTCGACCATGGGCACCCAGGGCAGT	Rab40c
mRab40c rev	GCGGCCGCTAGGAGATCTTGCAAGTCT	Rab40c
mRnf222 for	GTCGACCATGTGAGAAGGAGGAAGCAAG	Rnf222

Name	Sequence	cDNA
mRnf222 rev	GCGGCCGCTCAGGCCTGCTTCTCACCAG	Rnf222
Nfkbid-UTR_fo_Sal1_Cla1	GTCGACAAAAAATCGATGCGGCCGCCAGTGTGATG	ICOS CDS GFP NFkBID UTR
Nfkbid-UTR_re_Sfi1	GGCCTTAATGGCCTGAGGCCAAATTGAGTTTAATT	ICOS CDS GFP NFkBID UTR
NotI-Linker-P2A-mCherry rev	GCGGCCGCTACTTATAAAGCTCATCCATTCC	Roquin-1-P2A-mCherry
NotI-Linker-P2A-mCherry fw	GCGGCCGCTCAGGTTCCGGAGCCACG	Roquin-1-P2A-mCherry
NotI-mCherry-NotI fw	GCGGCCGCATGGTGAGCAAAGGCGAGG	Roquin-1-mCherry
NotI-mCherry-NotI rev	GCGGCCGCTACTTATAAAGCTCATCCATTCC	Roquin-1-mCherry
Nufip2 255-411 for	AAGTTCTGTTTCAGGGCCCGAAACAGGGACTTGAA	NUFIP2 255-411
Nufip2 255-411 rev	ATGGTCTAGAAAGCTTTAAGAAGTAACAGATTTTCAG	NUFIP2 255-411
NUFIP2 for	GTCGACCATGGAGGAGAAGCCCGGC	NUFIP2
NUFIP2 rev	GCGGCCGCTCATTGATCTGGACTATCCATGG	NUFIP2
Roquin-1 DeltaPro rev 2	GCGGCCGCTGGAATCAGTTGTGCTACTGTGC	Roquin-1 (aa 1-509)-P2A-mCherry
Roquin-1DeltaPro for	ATGCCTGTACAAGCTCCACAATG	Roquin-1 (aa 1-509)-P2A-mCherry

Primers for site-directed mutagenesis (Table 8) were designed with the QuikChange *Primer Design Tool* from Agilent's Technologies (<http://www.genomics.agilent.com/primerDesignProgram>).

**Table 8: Primers for site-directed mutagenesis**

Name	Sequence	Mutation
QC_miR101_mut_for	TACTAGATTCAAATTACAAGTTCAGATCTGACTGTACACATCCA GCATTAC	ICOS SM1
QC_miR101_mut_rev	GTAATGCTGGATGTGTACAGTACAGATCTGAACTTGTAATTTGA ATCTAGTA	ICOS SM1
QC_miR101_backmut_for	CATACTAGATTCAAATTACAAGTTCAGATCTGATCTGTACACATC CAGCATTACACATGCT	ICOS SM1R
QC_miR101_backmut_rev	AGCATGTGTAATGCTGGATGTGTACAGATCAGATCTGAACTTGT AATTTGAATCTAGTATG	ICOS SM1R
ICOS SM3 fw	CTGTTAAAATCCCCATTGACTGATAGTGTCAATCTTCCAGATTGA ACAAAAC	ICOS SM2
ICOS SM3 rev	GTTTTGTCAATCTGGAAGAATGACACTATCAGTCAATGGGGAT TTTAACAG	ICOS SM2
ICOS SM4 fw	GCAGTCTGTTAAAATCCCCATTGACACATAGTGTCAATCTTCCAG ATTGAACAAAA	ICOS SM2R
ICOS SM4 rev	GTTTTGTCAATCTGGAAGAATGACACTATGTGTCAATGGGGAT TTTAACAGACTGC	ICOS SM2R
QC_NUFIP2_rescue_for	TTGCTGCTCACACCAGGTTTACTATCAGATGACTTCTAAGCATA TCACCCACAGCAGGTTTTTC	siNUFIP2#2-res. NUFIP2
QC_NUFIP2_rescue_rev	GAAAACCTGCTGTGGGTGATATGCTTAGGAAGTCATCTGATAG TAAACCTGGTGTGAGCAGCAA	siNUFIP2#2-res. NUFIP2

Name	Sequence	Mutation
QC_sgRNAres_NUFIP2_fw	GTCTGCTTCAGGCTAGTGTCCACCACCTGTTGATTGCCATTGAG GACCCTGGAA	sgRNA#4-res. NUFIP2
QC_sgRNAres_NUFIP2_rev	TTCCAGGGTCCTCAATGGCAATCAACAGGTGGTGGACACTAGC CTGAAGCAGAC	sgRNA#4-res. NUFIP2

Intron-spanning qPCR primers (Table 9) were designed using the *Universal ProbeLibrary Assay Design Center* from Roche (<https://lifescience.roche.com>).

**Table 9: Primers for qPCR**

Target	Forward primer	Reverse primer	Probe
ATP2A1	CCGAGACAGCACTCACCAC	GGTGAATTCCTTCTTCATTAGCTG	42
CERK	TGGCACCAGTTCACCTTA	CCTTGGCCTGATTAGCATGT	9
CNOT1	TTGGAGGACTTTCATCACAGC	GAGCACCAGTTCCTATACCAGTC	27
CSTF3	AGTGCGCACGTTGTAATCAG	TCCGCTTCTTCACCTTCTC	27
HPRT	TCCTCCTCAGACCGCTTTT	CCTGGTTCATCATCGTAATC	95
ICOS	GGATGCATACTTATTTGTTGGCTTA	TGTATTCACCGTTAGGGTCGT	47
MARCH5	CCGCCTCTCAGTGCTATTGT	ACAAACCCAGCAACTTCTGTC	60
NUFIP2	CGCTGAAACATGAGCAGAAA	TCCAGCATTACCGTTTAGTTCA	67
PI4KA	AAGGCCAGCTCCGTTGTAT	TCACTGCCAGGGAGCAAT	83
PTBP2	GCTCAACAAGCAAACTAGCC	CACAAGTTTGGAAAAATCAATCC	40
STAU1	ATGGTATCGGCAAGGATGTG	TGGTCCAACCTCAGACAGCAA	46
STK38	GGATTGGAAGATTTTGAGTCCTT	TTCTTCTGAACAAGCCGTACCT	13
TES	AGCGAGAAACCCCGATGT	GCCTGGGTATACTCATTGCTG	76
TNRC6A	TGGTCCACAAGCATTAAAGCA	TCCTCTTCCCAGCCAGTG	5
TNRC6B	CCTGCTGGTGATAGCTGGTT	ATGGCACTCCTGGTTGGA	22
TNRC6C	ACTCACAGACATGGGCTTCC	GCCTGATCAAGATTCATATTGTTACTC	73
TRUB1	TCCGGATGTAAGCCTCTCT	TCCGGATGTAAGCCTCTCT	42
TYW5	CCAGAATTCTCAAAGAGGAACA	GACTGAAGAGTACAACACGCTTTT	47
YTHDC2	TTCAGACTCCGGAACCTTTGA	AGAAAATCAGCAATGGGACAA	45
YWHAZ	CGCTAATAATGCAGTACTGAGAGA	TTGGAAGCCGGTTAATTTT	2
ZYX	TCCACATGAAGTGTACAAGTGTG	GTGTGGCACTTCCGACAGA	38

In the CRISPR/Cas9 screen, genome-integrated sgRNA sequences were amplified by nested PCR. The first PCR amplifies a 317 nt fragment, including the integrated sgRNA sequence. A second PCR on the first PCR product creates libraries for next generation sequencing by adding sequences for flow cell annealing, sequencing and indexing primer annealing and barcoding to produce a 352 nt amplicon. Primer sequences for the first PCR were taken from (Shalem et al., 2014):

F1: AATGGACTATCATATGCTTACCGTAACTTGAAAGTATTTCCG  
R1: CTTTAGTTGTATGTCTGTTGCTATTATGTCTACTATTCTTTCC

Primers for the second PCR were assembled from (Shalem et al., 2014) and taking into account recommendations from Dr. Stefan Krebs, who actually performed the NGS (Genzentrum, LMU München). These included a variable length sequence to increase library complexity (labeled in red in fw primers) and barcodes for multiplexing (NEBNext Index 1-12 Primers for Illumina, NEB) (labeled in red in rev primers). Primer sequences that are needed to amplify the product of the first PCR are shown in blue (Table 10).

**Table 10: Primers for the second CRISPR PCR**

Primer sequence	Name
AATGATACGGCGACCACCGAGATCTACACTCTTTCCCTACACGACGCTCTCCGATCTATCTTGTGGAAA GGACGAAACACCG	1 fw
CAAGCAGAAGACGGCATAACGAGATACATCGGTGACTGGAGTTCAGACGTGTGCTCTCCGATCTTCTAC TATTCTTTCCCTGCACTGT	1 rev
AATGATACGGCGACCACCGAGATCTACACTCTTTCCCTACACGACGCTCTCCGATCTGATCTTGTGGAA AGGACGAAACACCG	2 fw
CAAGCAGAAGACGGCATAACGAGATTGGTCAGTGACTGGAGTTCAGACGTGTGCTCTCCGATCTTCTAC TATTCTTTCCCTGCACTGT	2 rev
AATGATACGGCGACCACCGAGATCTACACTCTTTCCCTACACGACGCTCTCCGATCTCTATCTTGTGGAA AGGACGAAACACCG	3 fw
CAAGCAGAAGACGGCATAACGAGATCACTGTGTGACTGGAGTTCAGACGTGTGCTCTCCGATCTTCTAC TATTCTTTCCCTGCACTGT	3 rev
AATGATACGGCGACCACCGAGATCTACACTCTTTCCCTACACGACGCTCTCCGATCTTCGATCTTGTGG AAAGGACGAAACACCG	4 fw
CAAGCAGAAGACGGCATAACGAGATATTGGCGTGACTGGAGTTCAGACGTGTGCTCTCCGATCTTCTAC TATTCTTTCCCTGCACTGT	4 rev
AATGATACGGCGACCACCGAGATCTACACTCTTTCCCTACACGACGCTCTCCGATCTAGCGTTCTAGCG TGAAAGGACGAAACACCG	5 fw
CAAGCAGAAGACGGCATAACGAGATGATCTGGTGACTGGAGTTCAGACGTGTGCTCTCCGATCTTCTAC TATTCTTTCCCTGCACTGT	5 rev
AATGATACGGCGACCACCGAGATCTACACTCTTTCCCTACACGACGCTCTCCGATCTACTGCTCTAGCG TGAAAGGACGAAACACCG	6 fw
CAAGCAGAAGACGGCATAACGAGATTACAAGGTGACTGGAGTTCAGACGTGTGCTCTCCGATCTTCTAC TATTCTTTCCCTGCACTGT	6 rev

To produce plasmids with gene editing potential (Table 6), sgRNAs were cloned into lentiCRISPR vectors by annealing of reverse complementary oligonucleotides (Table 11). CACC and AAAC are 5' overhangs on the sense and antisense strand, respectively, which allow cloning into *BsmBI* restriction sites. In the case that the 20 nt sgRNA sequence does not start with a guanine, an additional 'G' is added to the 5' end, which marks the transcription start site downstream of the U6 promoter.

**Table 11: Oligonucleotides for cloning of sgRNAs into lentiCRISPR vectors**

Name	Sequence	Target
mNUFIP2#1 for	CACC GCATGTTTCAGCGGCTTGGGC	Mouse Nufip2
mNUFIP2#1 rev	AAAC GCCCAAGCCGCTGAAACATGC	Mouse Nufip2
mNUFIP2#2 for	CACC GCGGCTCCATGCTGCAGGTAT	Mouse Nufip2
mNUFIP2#2 rev	AAAC ATACCTGCAGCATGGAGCCGC	Mouse Nufip2
mNUFIP2#3 for	CACC GGTGAAATAAACGGTAATGC	Mouse Nufip2
mNUFIP2#3 rev	AAAC GCATTACCGTTTATTTACC	Mouse Nufip2
mNUFIP2#4 for	CACC GGCTTGTCTACAACCTGC	Mouse Nufip2
mNUFIP2#4 rev	AAAC GCAAGTTGTAGAAACAAGCC	Mouse Nufip2
NT1 for	CACC GCGAGGTATTCGGCTCCGCG	Non-targeting
NT1 rev	AAAC CGCGGAGCCGAATACCTCGC	Non-targeting
NT2 for	CACC GCCGAGAGGCGTAAGCGCGA	Non-targeting
NT2 rev	AAAC TCGCGCTTACGCCTCTCGGC	Non-targeting
hNUFIP2#3 for	CACC GTACCTGCAGCATGGAGCCGA	Human NUFIP2
hNUFIP2#3 rev	AAAC TCGGCTCCATGCTGCAGGTAC	Human NUFIP2

### 3.1.4.2 siRNA duplexes

siGENOME siRNA duplexes were ordered from GE Healthcare Dharmacon, Lafayette, CO, USA (Table 12).

**Table 12: siRNA duplexes**

Name	Sequence	Catalog#	Species
siATP2A1#1	GAAAGUCCAUGUCUGUCUA	D-006113-01	Human
siATP2A1#2	GCAAGAUGUUUAUCAUUGA	D-006113-02	Human
siATP2A1#3	CCAAAGGUGUCUAUGAGAA	D-006113-03	Human
siATP2A1#4	GCACCGAGAUUGGAAGAU	D-006113-04	Human
siCERK#1	GAUCAUCGCCGUUGAGGAA	D-004061-01	Human
siCERK#2	CAACGGACUGCGUGUGUUA	D-004061-02	Human
siCERK#3	CCACUGACAUCAUCGUUAC	D-004061-03	Human
siCERK#4	CAAGGCAAGCGGAUUAUUG	D-004061-04	Human
siCNOT1#1	AUAAGUGGCUCACAGAUAA	D-015369-01	Human
siCNOT1#2	CAAGUUAGCACUAUGGUAA	D-015369-02	Human
siCNOT1#3	GAGUGUGCGUUGCUGAUUA	D-015369-03	Human
siCNOT1#4	GCAAUAUAAUCGUCAGUU	D-015369-04	Human
siCSTF3#1	CUGAGUAUGUCCCAGAGAA	D-011247-21	Human
siCSTF3#2	CUAUAGACAAAGCACGGAA	D-011247-22	Human
siCSTF3#3	GAAACUGUACAUUGAAGCA	D-011247-23	Human
siCSTF3#4	GCGGAAAAGAAUUAGAAG	D-011247-24	Human
siMARCH5#1	UCAAACAGCAGCAAUUUU	D-007001-01	Human
siMARCH5#2	GGACAGCUGUGACUUAUGG	D-007001-02	Human

Name	Sequence	Catalog#	Species
siMARCH5#3	GUAAAUUGAUGUUCAGUAG	D-007001-03	Human
siMARCH5#4	GACAGAAGUUGCUGGGUUU	D-007001-04	Human
siNUFIP2#1	GUAGAU AAGUCUGAUACUA	D-021280-01	Human
siNUFIP2#2	CGGAAAAGCUCAGAUAGUA	D-021280-03	Human
siNUFIP2#3	GGUCAGCCACUGCUAACUA	D-021280-04	Human
siNUFIP2#4	AGGAAAGCUAGGCGCAAUA	D-021280-17	Human
siPTBP2#1	GAGAGGAUCUGACGAACUA	D-021323-01	Human
siPTBP2#2	GAAAGACAGCGCUCUAAUA	D-021323-02	Human
siPTBP2#3	UAAGAAACCUUGGAUCCAAA	D-021323-03	Human
siPTBP2#4	GGAAGCAGCUAUUACUAUG	D-021323-04	Human
siSTAU1#1	AAACGGAACUUGCCUGUGA	D-011894-01	Human
siSTAU1#2	GAACGAAUUUGUAUCUCUU	D-011894-02	Human
siSTAU1#3	GCAAUUUAAUGGCAAAGGA	D-011894-03	Human
siSTAU1#4	CACGGUAACUGCCAUGAUA	D-011894-04	Human
siTES#1	CGAAAGGGCUGGCUAUGAU	D-013026-01	Human
siTES#2	GUUAUGAUUUGACGAAUC	D-013026-02	Human
siTES#3	CGGGUGACCUUAACAAUU	D-013026-03	Human
siTES#4	CCUGCUAUGUGAAGAAUCA	D-013026-04	Human
siTNRC6A#1	GAAAUGCUCUGGUCCGCUA	D-014107-01	Human
siTNRC6A#2	GCCUAAAUAUUGGUGAUUA	D-014107-02	Human
siTNRC6A#3	GAUCUGCUGUUAAGGUGUU	D-014107-03	Human
siTNRC6A#4	GAACAAUGGACUUGCCUA	D-014107-04	Human
siTRUB1#1	GAAAGCUACUGAUACACUA	D-016391-01	Human
siTRUB1#2	CAGAAUGGACCAAGAGGAA	D-016391-03	Human
siTRUB1#3	CUGAAUCGGUUGAAGGAGA	D-016391-04	Human
siTRUB1#4	GAAGAGAGGUGAAGUCGUA	D-016391-17	Human
siTYW5#1	GGUGAUGUAUUUAUCAUUC	D-016468-01	Human
siTYW5#2	GGACUUCUAUGCACGACGA	D-016468-02	Human
siTYW5#3	CGAGAUGCCAGUAUUUAU	D-016468-03	Human
siTYW5#4	CCGAGUUACCAGAGGAAUA	D-016468-04	Human
siYTHDC2#1	GCAAUAGAUACCUAACUG	D-014220-01	Human
siYTHDC2#1	CAGCAUAGUUUACUUGGUA	D-014220-02	Human
siYTHDC2#1	GCAAGCAUGUAUCCUAAUU	D-014220-03	Human
siYTHDC2#1	GGACUAGGAGGAGUAUUUA	D-014220-04	Human
siZYX#1	GACAAGAACUCCACAUGA	D-016734-01	Human
siZYX#2	GAAUGUGGCUGUCAACGAA	D-016734-02	Human
siZYX#3	GACCAAGAAUGAUCCUUUC	D-016734-03	Human
siZYX#4	GGUGAGCAGUAUUGAUUUG	D-016734-04	Human
Nufip2 siRNA pool :			
#1	UAAGACCGAUACCAUAGCA	M-063890-01	Mouse
#2	UAACAAGUAGUUCAGGCUA	M-063890-01	Mouse
#3	GGAUUUAACCUCCUAAAA	M-063890-01	Mouse
#4	AGGAAAGCUAGGCGCAAUA	M-063890-01	Mouse

Name	Sequence	Catalog#	Species
Non-targeting siRNA #1	UAGCGACUAAACACAUCAA	D-001210-01	Mouse
Non-targeting siRNA #2	UAAGGCUAUGAAGAGAUAC	D-001210-02	Mouse
Rc3h1 siRNA pool:			
#1	GUACGGUAGUGCAUGGAUU	M-044230-01	Mouse
#2	GAACAUGACUCCCAGAUAG	M-044230-01	Mouse
#3	UCUCAUAUGCAGUCUAUUA	M-044230-01	Mouse
#4	GAAUUUGAACCGACUAAGA	M-044230-01	Mouse

### 3.1.5 Artificially synthesized DNA sequences

A mammalian codon-optimized sequence encoding an SGSG-linker followed by P2A-mCherry (798 nts) was synthesized by Entechelon GmbH (now Eurofins Genomics).

ICOS-GFP CDS was synthesized by GeneArt Gene Synthesis (ThermoFisher Scientific).

### 3.1.6 cDNA clones

For cloning of NUFIP2, FBXL14, TRIM6-TRIM34, Rab40c and RNF222 full-length cDNA sequences, IMAGE cDNA clones were ordered from Source BioScience LifeSciences (Nottingham) (Table 13).

**Table 13: IMAGE cDNA clones**

Name	Image #	Code	Species
FBXL14	IMAGE:5205284	RATp970D0949D	Human
LOC643904 (RNF222)	IMAGE:100016331	OCACo5052D077D	Mouse
NUFIP2	IMAGE:40128910	IRCMp5012G0838D	Human
Rab40c	IMAGE:5364768	IRAVp968G0665D	Mouse
TRIM6-TRIM34	IMAGE:9021590	IRCBp5005G2410Q	Human

### 3.1.7 Antibodies and fluorescent dyes

Antibodies employed for flow cytometry (FC), tissue culture (TC), immunofluorescence (IF), immunoblotting (IB) or immunoprecipitation (IP) and fluorescent dyes used for fluorescent cell barcoding (FCB) are listed in Table 14.

**Table 14: Antibodies and fluorescent dyes**

Name	Conjugation	Dilution	Supplier	Application
Alexa Fluor® 488 Carboxylic Acid, Succinimidyl Ester, Mixed Isomers		5 mg/ml stock	Life Technologies	FCB
Anti-Ago (Pan, 11G1)	-	1:10	In-house production	IB
Anti-CD3 (145-2C11)	-	2.5 µg/ml	In-house production	TC
Anti-Mouse Cd4 (Rm4-5)	APC	1:200	eBioscience	FC
Anti-CD8	eFluor450	1:200	eBioscience	FC
Anti-CD28 (37N)	-	0.25 µg/ml	In-house production	TC
Anti-Mouse Cd45r (B220)	PeCy7	1:200	eBioscience	FC
Anti-Cd90.1 (Thy1.1)	PerCP	1:5000	eBioscience	FC
Anti-Cd90.1 (Thy1.1)	PE	1:5000	eBioscience	FC
Anti-CD125	-	1:200	eBioscience	FC
Anti-CD278 (Human ICOS) Clone ISA-3	Biotin	1:400	eBioscience	FC
Anti-FMRP	-	1:1000	Cell Signaling Technologies	IB
Anti-GAPDH	-	1:10,000	Calbiochem	IB
Anti G3BP1	-	1:100	Santa Cruz Biotechnology	IF
Anti-GFP	-	1:1000	ThermoFisher Scientific	IB
Anti-HA (12CA5)	-	1:10	In-house production	IB
Anti-IL4 (11B11)	-	10 µg/ml	In-house production	TC
Anti-IkBNS	-	1:5000	In-house production	IB
Anti-Mouse IgG	HRP	1:3000	Cell Signaling Technologies	IB
Anti-NUFIP2	-	1:1000	BETHYL Laboratories	IB
Anti-Rabbit IgG	HRP	1:3000	Cell Signaling Technologies	IB
Anti-Rat IgG	HRP	1:3000	Cell Signaling Technologies	IB
Anti-Renase-1 (15D11)	-	1:10	In-house production	IB
Anti-Roquin-1	-	1:500	BETHYL Laboratories	IB
Anti-Roquin-1 (Q4-2)	-	1:10	In-house production	IP
Anti-Roquin-1/-2 (3F12)	-	1:10	In-house production	FC, IB
Anti-Tubulin	-	1:2000	Santa Cruz Technologies	IB
Pacific Blue™ Succinimidyl Ester		5 mg/ml stock	Life Technologies	FCB
Streptavidin	Allophycocyanin	1:600	eBioscience	FC

### 3.1.8 Cytokines

Recombinant cytokines were used for stimulation of primary mouse CD4<sup>+</sup> T cells (Table 15).

**Table 15: Cytokines**

Name	Species	Dilution	Supplier	Application
IL-2	human	20 U/ml	Novartis	TC
IL-12	mouse	10 ng/ml	BD Biosciences	TC

### 3.1.9 Chemicals, enzymes and kits

**Table 16: Chemicals**

Compound	Supplier
2-Propanol	Merck
2log DNA ladder	New England Biolabs
Acrylamide 4K solution	AppliChem
Amersham™ ECL™ Prime	GE Healthcare
Ammonium persulfate (APS)	Serva
Ampicillin	Roche
Bio-rad protein assay (Bradford assay)	Bio-rad
Biozym LE agarose	Biozym
Blasticidin S HCl (10 mg/ml)	ThermoFisher Scientific
Boric acid	Calbiochem
Bovine serum albumin (BSA)	Carl Roth
Calcium chloride	Sigma-Aldrich
Chloroform	Sigma-Aldrich
Chloroquine diphosphate salt	Sigma-Aldrich
DEPC	Carl Roth
Dimethyl sulfoxide	Sigma-Aldrich
Dithiothreitol (DTT)	AppliChem
dNTP set	ThermoFisher Scientific
Doxycycline	AppliChem
Dynabeads® MyOne™ Tosylactivated	ThermoFisher Scientific
Dynabeads® Protein G for immunoprecipitation	ThermoFisher Scientific
Ethanol	Merck Millipore
Ethidium bromide (0.07%)	AppliChem
Ethylendiamin-tetraessigsäure Dinatriumsalz Dihydrat	Carl Roth
Formaldehyde solution 36.5-38 %	Sigma-Aldrich
Geneticin® selective antibiotic (G418) 50 mg/ml	ThermoFisher Scientific
GlycoBlue™ coprecipitant	Ambion
HiPerFect® transfection reagent	Qiagen
Hygromycin B	ThermoFisher Scientific
Ionomycin, free acid, <i>Streptomyces conglobatus</i>	Merck Millipore
Kanamycin	Carl Roth
Methanol	Merck Millipore

Compound	Supplier
Nonfat dry milk powder	AppliChem
Nonident P40	Sigma-Aldrich
Phorbol-12-myristate-13-acetate (PMA)	Merck Millipore
Polybrene	Sigma-Aldrich
Protease inhibitor tablets, cOmplete™ Mini EDTA-free	Roche diagnostics
Protein Marker VI (10 - 245) prestained	AppliChem
Saponin GPR RECTAPUR®	VWR
Sodium dodecylsulfate, pellets	Serva Electrophoresis
Spectinomycin	AppliChem
4-OH-tamoxifen	Sigma-Aldrich
TEMED	AppliChem
TRI reagent® solution	Ambion
Trypsin-EDTA	ThermoFisher Scientific
Tween 20	AppliChem

**Table 17: Enzymes**

Enzyme	Supplier
<i>BsmBI</i>	New England Biolabs
FastAP™ thermosensitive alkaline phosphatase	ThermoFisher Scientific
Gateway® LR Clonase® II enzyme mix	ThermoFisher Scientific
Herculase II Fusion DNA polymerase	Agilent Technologies
<i>NotI</i> -HF®	New England Biolabs
Proteinase K	Roche
<i>Sall</i> -HF®	New England Biolabs
T4 DNA ligase	New England Biolabs
T4 polynucleotide kinase	New England Biolabs
T4 RNA ligase	New England Biolabs
<i>Taq</i> DNA polymerase	ThermoFisher Scientific
Vent® polymerase	New England Biolabs
<i>XhoI</i>	New England Biolabs

**Table 18: Kits**

Kits	Supplier
DNeasy® Blood & Tissue Kit	QIAGEN
EasySep™ Mouse CD4 <sup>+</sup> T Cell Isolation Kit	Stemcell Technologies
Gateway® LR Clonase® II enzyme mix	ThermoFisher Scientific
LightCycler® 480 Probes Master	Roche
Universal probe library	
NucleoBond® Xtra Maxi	MACHERY-NAGEL

<b>Kits</b>	<b>Supplier</b>
OneStep RT-PCR Kit	QIAGEN
pCR™8/GW/TOPO® TA Cloning® Kit	ThermoFisher Scientific
pGEM®-T Easy Vector System	Promega
PureYield™ Plasmid Miniprep System	Promega
QIAquick® Gel Extraction Kit	QIAGEN
QIAquick® PCR Purification Kit	QIAGEN
QuantiTect® Reverse Transcription Kit	QIAGEN
Qubit® dsDNA BR Assay Kit	ThermoFisher Scientific
QuikChange® II XL Site-Directed Mutagenesis Kit	Agilent Technologies
RNeasy® Mini Kit	QIAGEN

### 3.1.10 Buffers

**Table 19: Buffers**

<b>Buffer name</b>	<b>Composition</b>
Blotting buffer	25 mM Tris 192 mM glycine 20 % methanol
ECL solution 1	100 mM Tris-HCl pH 8.8 1.25 mM Luminol 200 nM p-Coumaric-acid
ECL solution 2	3 % H <sub>2</sub> O <sub>2</sub>
FACS staining buffer	PBS 2 % FCS 2 mM EDTA
HBS (2x)	274 mM NaCl 10 mM KCl 1.4 mM Na <sub>2</sub> HPO <sub>4</sub> , pH 7.0
Laemmli SDS sample buffer (4x)	200 mM Tris-HCl, pH 6.8 8 % SDS 40 % glycerol 0.1 % bromophenol blue 10 % β-mercaptoethanol
Lysis buffer	20 mM Tris-HCl pH 7.5 150 mM NaCl 0.25 % NP-40 1.5 mM MgCl <sub>2</sub>
PBS	137 mM NaCl 10 mM Na <sub>2</sub> HPO <sub>4</sub> , pH 7.4 2.7 mM KCl
Saponin buffer	PBS 0.5 % saponin 1 % BSA

Buffer name	Composition
SDS PAGE buffer	25 mM Tris 250 mM glycine 0.1 % SDS
TAC lysis buffer	13 mM Tris 140 mM NaH <sub>4</sub> Cl, pH 7.2
TE	10 mM Tris-HCl pH 7.5 1 mM EDTA pH 8
TBE (1x)	89 mM Tris-borate 2 mM EDTA, pH 8
TBS	10 mM Tris-HCl pH 8 150 mM NaCl
TBST	10 mM Tris-HCl pH 8 150 mM NaCl 0.05 % Tween-20

**Table 20: Consumables**

Name	Supplier
1.5 ml, 2 ml centrifuge tubes	Eppendorf
15 ml, 50 ml tubes	Falcon
96-well reaction plate (qPCR)	4titude
Cell culture plates	Thermo Scientific
Cell scraper	Sarstedt
Clear seal foils for qPCR	4titude
Cryotubes	Thermo Scientific
Cuvettes	Brand
Disposable pipetting reservoirs	VWR
Filter paper Whatman, 3 mm	VWR
Gloves	ShieldSkin™ orange Nitril
Immobilon® Nitrocellulose membrane	Merck
Pipette tips	Sorenson
Surgical disposable scalpels	Braun
X-ray films	Agfa health Care

### 3.1.11 Instruments

**Table 21: Instruments**

Instrument Name	Supplier
Agarose gel chambers	Peqlab
Bacterial incubator	Brutschrank BINDER BF 53 (Binder Labortechnik) Innova 4400 incubator shaker (New Brunswick Scientific GmbH)
Balances	KERN ABJ-220-4M (Kern und Söhne GmbH) KERN EW 220-3NM (Kern und Söhne GmbH)

<b>Instrument Name</b>	<b>Supplier</b>
BD FACS Ariall cellsorter	BD Biosciences
BD LSRFortessa cell analyzer	BD Biosciences
Benchtop working rack 1.5 ml	Stratagene
Cell freezing container	CoolCell® (Biocision)
Blotting chamber	Bio-Rad
Centrifuges and rotors	Beckman Coulter Avanti-J-26XP (Beckman Coulter); JA-10 Rotor, Fixed Angle (Beckman Coulter)
	Allegra®X-12R Centrifuge (Beckman Coulter); Rotor SX 4750 (Beckman Coulter)
	Eppendorf Centrifuge 5810R (Eppendorf); Rotor A-4-62 and F-34-6-38
Confocal microscope	Leica TCS SP5
CO <sub>2</sub> incubator	Forma Direct Heat CO <sub>2</sub> Incubator HEPA Class 100 (Thermo Electron Corporation)
Gel documentation system	Quantum ST4 (Vilber)
High-throughout sampler	BD Biosciences
Ice machine	Scotsman AF 200 (Scotsman Icesystem)
Magnet stirrer	RCT basic safety control (IKA)
Microscope	Axiovert 40C (Zeiss)
Microwave	Bosch
Neubauer improved hemocytometer	Marienfeld
pH meter	pH-Meter inoLab® pH 720 (W TW)
Pipettor	Pipetboy acu (IBS)
Power supplies	Stromgeber EC105 (Thermo Electron Corporation) Power Pac200 (Bio-Rad)
Sterile-working bench	BDK, Luft und Reinraumtechnik
Spectrophotometer	NanoDrop™ 1000 Spectrophotometer (ThermoFisher Scientific)
Table centrifuge	Centrifuge 5415D (Eppendorf)
	Centrifuge 5417R (Eppendorf)
Thermocycler	DNA Engine 48/48 Dual Alpha Unit (Bio-Rad) Light Cycler 480II (Roche)
Thermo mixer	Thermomixer comfort (Eppendorf)
Vacuum pump	Diaphragm Vacuum Pump MZ 2C (Vacuubrand)
Vertical electrophoresis chamber	Bio-Rad
	Eppendorf BioPhotometers (Eppendorf)
Vortex MS2 mini shaker	IKA
Waterbath	WB7 (Memmert)

### 3.1.12 Software

**Table 22: Software**

Name	Application
Adobe Illustrator CS5	Image processing
Adobe Photoshop CS5	Image processing
ApE	Analysis of DNA sequences
Endnote X7	Literature organization
FlowJo 3	Flow cytometry data analysis
GraphPad Prism	Graphs, statistics
Light Cycler 480 software release 1.5.1	qPCR data analysis
Microsoft Office for Mac 2011	Writing in Word, data analysis in Excel

## 3.2 Methods

### 3.2.1 Cloning of cDNA and amplification of DNA plasmids

#### 3.2.1.1 Polymerase chain reaction and TOPO cloning

DNA fragments were amplified in standard polymerase chain reactions (PCR) with gene-specific 3' and 5' flanking oligonucleotides (primers) (Table 7). The set up of a standard PCR reaction is shown in Table 23, left. A mixture of Taq- and Vent<sup>®</sup>-polymerase was employed for DNA amplification in order to combine critical features, such as 3' adenine overhangs and proofreading activity. Cycling conditions are shown in Table 23, right. The annealing temperature is adjusted according to the calculated melting temperature ( $T_m$ ) of the primers. For TOPO<sup>®</sup> cloning, a final step for 5 min at 72°C is added to ensure the synthesis of 3' adenosine overhangs.

**Table 23: PCR composition and cycling conditions**

Amount	Reagent	Step	Temp	Duration	
0.3 µl	Taq polymerase	Activation	95°C	2 min	} 32x
0.2 µl	Vent Polymerase	Denaturation	95°C	15 sec	
2.5 µl	10x reaction buffer	Annealing	~ $T_m$ - 5°C	30 sec	
1 µl	MgCl <sub>2</sub> (50 mM)	Elongation	72°C	1 min/kb cDNA	
0.5 µl	dNTP 10 mM each				
0.5 µl	Forward primer (10 pM)				
0.5 µl	Reverse primer (10 pM)				
20 ng	Template cDNA				
Up to 25 µl	H <sub>2</sub> O				

Following PCR amplification, DNA was separated on 0.8 % agarose gels containing 1 droplet of 0.07 % ethidium bromide solution per 75 ml gel in TBE buffer at 100 – 120 V. The PCR product of the desired size was excised under 254 nm UV light and purified using the QIAquick® Gel Extraction Kit (Qiagen) according to the manufacturer's instructions.

After gel elution, PCR products were subcloned into linearized TOPO® vectors, which possess 3' thymine overhangs and covalently linked topoisomerase enzymes.

### **3.2.1.2 Bacterial culture and plasmid preparation**

Plasmids were propagated in chemically competent *E. coli* DH5α bacteria (in-house production). 50 µl of bacterial suspension were transformed with ~100 ng of the desired plasmid by heat shock transformation (20 min on ice, 30 s 42°C, 2 min on ice). Subsequently, 250 µl glucose-containing SOC medium was added and cells were shaken at 600 rpm, 37 °C for 1 h in a Thermo mixer. 50 - 200 µl of the amplified suspension was spread onto LB-agar plates containing the respective antibiotics and incubated in a bacterial incubator for 18 h at 37 °C. 5 ml bacterial cultures („mini cultures“) were inoculated from single colonies and subjected to plasmid isolation with PureYield™ Plasmid Miniprep kit according to the manufacturer's protocol. 300 ml cultures (“maxi cultures“) were inoculated from mini cultures, and plasmid DNA was isolated with the NucleoBond® Xtra Maxi kit (Macherey Nagel) according to the manufacturer's instructions. LB media and LB agar were prepared with LB medium powder (SERVA), supplemented with ampicillin (100 µg/ml), spectinomycin (50 µg/ml), kanamycin (30 µg/ml) or chloramphenicol (170 µg/ml) depending on the plasmid-encoded antibiotic resistance gene.

### **3.2.1.3 Restriction enzyme digestion and ligation of DNA fragments**

Enzymatic digestion of plasmid DNA was performed in 30 µl reactions containing 2 µg of plasmid DNA, 3 µl of the appropriate 10x buffer, and 0.2 µl of the desired restriction enzyme(s). Digestion was performed for 1.5 h at the appropriate temperature. Restriction digest products were separated by agarose gel electrophoresis and eluted from the gel as described above (Chapter 3.2.1.3).

For the ligation of digested DNA fragments into the desired vector backbones, 20 µl ligation reactions were set up including 2 µl 10x T4 DNA ligase buffer, 1 µl T4 DNA ligase, 3 - 5 µl (~300 ng) of purified insert DNA, 1 – 2 µl (~100 ng) of purified vector

DNA and H<sub>2</sub>O. Ligation was performed overnight at 16 °C. Ligation reactions were heat-inactivated for 10 min at 65 °C, and 6 µl of each reaction were used for bacterial transformation.

#### **3.2.1.4 Site-directed mutagenesis**

Targeted mutations were introduced into plasmid DNA using the QuikChange® II XL Site-Directed Mutagenesis Kit according to the manufacturer's instructions. Primer sequences are listed in Table 8.

### **3.2.2 Extraction of RNA and qPCR**

#### **3.2.2.1 Isolation of RNA**

TRI reagent® (Ambion) was employed for isolation of RNA from varying amounts of cells. Cells were centrifuged at 300 x g for 5 min and the resulting cell pellet was resuspended in 1 ml TRI reagent® and lysed for 5 min at room temperature (RT). Lysed reactions were either stored at -80 °C, or subjected to instant RNA isolation according to the manufacturer's protocol. The resulting RNA concentration was determined spectrophotometrically using the NanoDrop device. In the case of phenol contaminations, samples were subjected to additional purification using the RNeasy® Mini Kit according to the manufacturer's instructions.

#### **3.2.2.2 Reverse transcription**

RNA was reverse transcribed into cDNA with the QuantiTect® Reverse Transcription Kit, according to the manufacturer's instructions. The resulting cDNA was diluted with H<sub>2</sub>O to 100 µl and stored at -20 °C.

#### **3.2.2.3 Quantitative PCR**

Following reverse transcription, quantitative PCR assays (qPCR) were run on a Light Cycler 480II machine using the Roche Universal Probe Library. Primers and universal probes are listed in Table 9. Relative gene expression was determined with the Light Cycler 480 SW 1.5.1 software, and normalized to the expression of a housekeeping gene (YWHAZ or Hprt).

### **3.2.3 Cell culture**

#### **3.2.3.1 Cultivation of cell lines**

Cells were cultured in the appropriate medium as described in chapter 3.1.2 and split every 2 - 3 days when reaching confluency. For storage, at least  $3 \times 10^6$  cells were centrifuged, resuspended in 1.8 ml cell freezing medium (10 % DMSO, 90 % FCS) and transferred into cryotubes. Multiple cell aliquots were subsequently frozen in a CoolCell® Cell Freezing Container cooling down at a rate of  $-1 \text{ }^\circ\text{C}/\text{min}$ . After a short period at  $-80 \text{ }^\circ\text{C}$ , cells were transferred to a liquid nitrogen tank for long-term storage.

#### **3.2.3.2 Isolation of genomic DNA**

Genomic DNA (gDNA) was isolated from  $3.5 - 5 \times 10^6$  MEF cells with the DNeasy Blood & Tissue Kit according to the manufacturer's protocol and resolved in 200 - 800  $\mu\text{l}$   $\text{H}_2\text{O}$ . The resulting gDNA concentration was determined with the Qubit® dsDNA BR Assay Kit, according to the manufacturer's instructions.

#### **3.2.3.3 Preparation and stimulation of primary mouse $\text{CD4}^+$ T cells**

Cell suspensions were generated from spleen and lymph nodes obtained from C57/Bl6 mice by mashing the organs through a  $150 \text{ }\mu\text{m}$  mesh. Splenocytes were centrifuged for 5 min,  $300 \times g$  at  $4 \text{ }^\circ\text{C}$  and the cell pellet was resuspended in 3 ml TAC lysis buffer. TAC lysis was performed for 5 min at RT, resulting in erythrocyte lysis. The remaining leucocytes were filtered and combined with the cell suspension obtained from lymph nodes for T cell purification.  $\text{CD4}^+$  T cells were isolated by depletion of all non- $\text{CD4}^+$  T cells using the EasySep™ Mouse  $\text{CD4}^+$  T Cell negative selection kit, according to the manufacturer's instructions. Purified  $\text{CD4}^+$  T cells were stimulated on goat-anti-hamster coated plates with anti-CD3 and anti-CD28 antibodies and skewed towards Th1 differentiation in RPMI complete medium (Chapter 3.1.2) by addition of IL-12 and anti-IL-4. Following 48 h of activation, Th1 cells were amplified in the presence of IL-2.

#### **3.2.3.4 Retro- and lentivirus production**

Retro- and lentiviral supernatants were produced by calcium-phosphate transfection of HEK293T cells with the retro- or lentiviral expression plasmid and the corresponding packaging vectors (Chapter 3.1.3.3).  $8-14 \times 10^6$  HEK293T cells were seeded onto 14 cm plates 18 h prior to transfection. Starting transfection, cells were incubated with fresh DMEM medium containing  $25 \text{ }\mu\text{M}$  chloroquine for 1 h.

Meanwhile, transfection mixes were prepared by dropwise addition of the DNA mix (Table 24) to the same amount (1250  $\mu$ l) of 2x HBS buffer, while constantly vortexing. Transfection mixes were incubated at 37 °C for 20 min and finally added to the cells. The medium was replaced 8-10 h later. After 48 h, the virus-containing supernatant was harvested, filtered (0.45  $\mu$ m) and frozen at -80 °C or directly used for transduction of recipient cells.

**Table 24: Composition of the DNA mix for calcium-phosphate transfection.**

Lentivirus 2 <sup>nd</sup> generation vector	Lentivirus 3 <sup>rd</sup> generation vector	Retrovirus ecotropic	Retrovirus amphotropic
25 $\mu$ g transfer vector	21 $\mu$ g transfer vector	50 $\mu$ g transfer vector	50 $\mu$ g transfer vector
12.5 $\mu$ g pspax2	14 $\mu$ g pMDLg/pRRE	5 $\mu$ g Ecopac	5 $\mu$ g env
12.5 $\mu$ g pMD2.VSVG	7 $\mu$ g pMD2.VSVG		5 $\mu$ g gag/pol
	7 $\mu$ g pRSV-Rev		
125 $\mu$ l CaCl <sub>2</sub> (2.5 M)	125 $\mu$ l CaCl <sub>2</sub> (2.5 M)	125 $\mu$ l CaCl <sub>2</sub> (2.5 M)	125 $\mu$ l CaCl <sub>2</sub> (2.5 M)
add H <sub>2</sub> O to 1250 $\mu$ l			

In addition to the transfer plasmid encoding the gene of interest, lentivirus production requires the genes *gag*, *pol*, *rev* and *env*. Second generation lentiviral transfer vectors additionally require the *tat* protein, which is encoded on the vector pspax2 together with *gag*, *pol*, and *rev*. Second generation lentivirus production is therefore achieved with pspax2 in addition to pMD2.VSVG encoding *env*. Third generation-lentiviral vector backbones are *tat*-independent, and therefore only require *gag*, *pol*, *rev* and *env*. For safety reasons, the *gag*, *pol* and *rev* genes have been split onto two vectors: pMDLg/pRRE encodes *gag* and *pol* and pRSV-Rev delivers *rev*.

### 3.2.3.5 Virus transduction

MEF or HeLa cells were transduced with lenti- or retroviral supernatants by spin-infection. Therefore, 100,000 cells were plated onto each well of a six-well plate 18 h prior to transduction. The medium was replaced by the desired amount of viral supernatant (100  $\mu$ l to 2.5 ml), and filled up to a total of 5 ml using the appropriate medium. Infection was performed by centrifugation for 2 h at 32 °C, 300 x g in the presence of 8  $\mu$ g/ml polybrene. 8 – 10 h after transduction, the supernatant was replaced by fresh medium.

### 3.2.3.6 Lentiviral doxycycline-inducible overexpression system

A lentiviral tet-ON expression system was employed to achieve stable, doxycycline-inducible overexpression of genes of interest. cDNAs were ligated into the plentiCMV<sub>tight</sub> Neo Dest vector downstream of the CMV<sub>tight</sub> promoter by LR recombination (Chapter 3.1.3.3) The CMV<sub>tight</sub> promoter consists of a tet-response element (TRE) that is located upstream of a minimal CMV promoter (Gossen et al., 1995). The minimal CMV promoter by itself cannot induce transgene expression and is consequently silent in the absence of TRE activation. It is therefore required to either sequentially or to cotransduce cells with a second plasmid, encoding the transactivator rtTA3. rtTA3 is inactive in the absence of the tetracycline derivative doxycycline, and activated upon doxycycline binding. An activation-induced conformational change allows binding to the TRE and a subsequent activation of the CMV<sub>tight</sub> promoter, leading to inducible overexpression of the gene of interest (Figure 7).

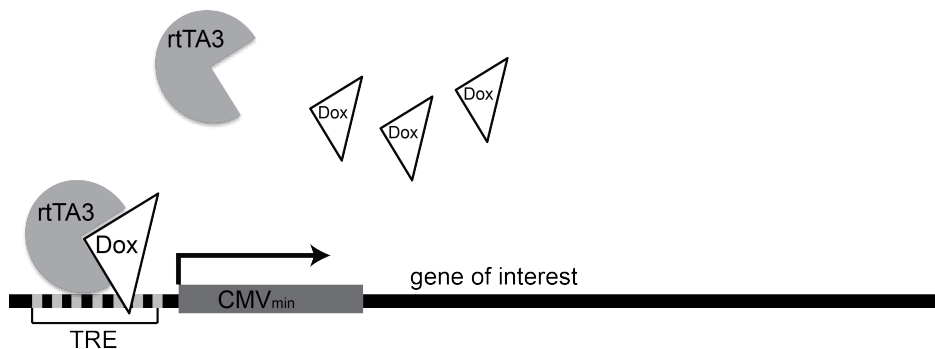


**Figure 7: Tet-ON inducible gene expression system.**

The CMV<sub>tight</sub> promoter upstream of the gene of interest consists of a tet-response element (TRE) of seven identical sequence repeats followed by a minimal CMV promoter (CMV<sub>min</sub>). When activated by doxycycline (dox), the transactivator rtTA3 can bind to the TRE and induce gene expression.

Cells were transduced with CMV<sub>tight</sub> Neo +gene of interest and rtTA3 Blast lentiviruses on two consecutive days by spin-infection as described in chapter 3.2.3.5. Starting 48 h after the second transduction, cells were cultured in medium supplemented with 500 µg/ml Geneticin (Neomycin) and 2.85 µg/ml Blasticidin S HCl for 7 days to select for stably infected cells.

### 3.2.3.7 siRNA transfection of HeLa cells

Reverse transfection of HeLa cells with siGENOME siRNAs (Table 12) was performed with the lipid-based HiPerFect transfection reagent according to the manufacturer's

instructions. The original 96-well reverse transfection protocol was scaled up to a 24-well format to allow simultaneous generation of samples for qPCR and flow cytometry. The HiPerFect transfection reagent was pre-diluted 32-fold in Opti-MEM serum-reduced medium. 125  $\mu$ l of the pre-diluted transfection reagent were pipetted into one well of a 24-well plate, followed by the addition of 6  $\mu$ l of a 2  $\mu$ M siRNA stock. Samples were incubated for 10 min to allow the formation of siRNA-lipid complexes, followed by the addition of 25,000 HeLa cells in 475  $\mu$ l of complete DMEM medium. Plates were incubated for 48 h and subsequently the medium was replaced by fresh medium containing 1  $\mu$ g/ml doxycycline. After 18 h, ICOS surface staining was carried out as described in chapter 3.2.7.1.

### 3.2.4 Confocal microscopy

HEK293T cells were transfected with pDest12.2 GFP-Nufip2 and pDest12.2 Roquin-mCherry by calcium-phosphate transfection as described in chapter 3.2.3.4. 200,000 cells were seeded onto glass cover slips and incubated overnight at 37 °C to allow adherence. Before staining, cells were subjected to oxidative stress with 0.5 mM sodium arsenite for 1 h at 37 °C or left untreated. Next, cells were rinsed once with PBS, and fixed in 2 % formaldehyde for 10 min. After washing twice with PBS + 0.5 % Triton and twice with plain PBS, primary antibody staining with anti-G3bp1 was performed for 1 h at RT. After washing, the secondary antibody staining was performed with anti-mouse Cy5 for 45 min. All washing and incubation steps were performed at room temperature. Images of mCherry, GFP and Cy5 signals were captured with a Leica TCS SP5 confocal microscope, and analyzed with the Leica confocal LAS AF software.

### 3.2.5 Expression and purification of recombinant proteins

Expression and purification of recombinant Roquin and NUFIP2 proteins was performed by Elena Davydova from Prof. Dr. Dierk Niessing's group. The Roquin fragment (amino acids 2-441), which was inserted into pETM11, was expressed as an N-terminal His<sub>6</sub>-fusion protein in *E.coli* BL21(DE3)Star. The cells were grown at 37 °C in LB medium with 50  $\mu$ g/mL kanamycin, 34  $\mu$ g/mL chloramphenicol and 100  $\mu$ M ZnCl<sub>2</sub>. After reaching an OD<sub>600</sub> of 0.9, the cell cultures were induced by adding 0.5 mM IPTG and overnight growing conditions changed to 20 °C. Afterwards, the cells were harvested, resuspended in lysis buffer (500 mM NaCl, 2 mM DTT, 15 mM imidazole, 1 mg/mL lysozyme, 10  $\mu$ g/mL DNase I, protease inhibitors, 50 mM Tris, pH 8) and

sonicated at 4 °C. After centrifugation, the cleared lysates were applied to a HisTrap FF column (GE Healthcare) and subsequently size exclusion chromatography was performed using a HighLoad 16/60 Superdex 200 column (Amersham Pharmacia Biosciences) in buffer containing 500 mM NaCl, 2 mM DTT, 20 mM Tris, pH 7.0.

The NUFIP2 fragment (amino acids 255-411) was inserted into the pOPINS3C and expressed as N-terminal His<sub>6</sub>-SUMO-fusion protein in *E.coli* BL21(DE3)pRIL. Cells were grown at 37 °C in LB medium with 100 µg/mL ampicillin and 34 µg/mL chloramphenicol. At OD<sub>600</sub> = 0.7, the cell cultures were induced by adding 0.5 mM IPTG and overnight growing conditions changed to 20 °C. Next, the cells were harvested and resuspended in lysis buffer (500 mM NaCl, 20 mM imidazole, 0.1 % Tween, 10 µg/mL DNase I, protease inhibitors, 50 mM HEPES, pH 7.5) and sonicated at 4 °C. After centrifugation, the cleared lysates were applied to a HisTrap FF column (GE Healthcare). The His<sub>6</sub>-SUMO tag was cut off by applying the PreScission Protease at 4 °C overnight and then removed using a HisTrap FF column (GE Healthcare). The protein, which did not bind to the HisTrap FF column, was concentrated and gel filtrated using a Superdex 75 10/300 GL column (Amersham Pharmacia Biosciences) in 200 mM NaCl and 50 mM HEPES pH 7.5.

### 3.2.6 Surface plasmon resonance

Surface plasmon resonance experiments were performed by Elena Davydova from Prof. Dr. Dierk Niessing's group. A BIACORE 3000 instrument (Biacore Inc.) was used to perform Roquin-NUFIP2 binding experiments. Roquin (amino acids 2-441) was immobilized to the CM5 sensor chip with amine coupling (Biacore Inc.) at a concentration of 50 µg/ml in 10 mM Na-phosphate buffer pH 5.7. NUFIP2 (amino acids 255-411) was injected onto the sensor chip using the concentrations 0.063 µM, 0.125 µM, 0.25 µM, 0.5 µM, 1 µM, 2 µM and 4 µM at 30 µL/min at 20 °C in running buffer (150 mM NaCl, 0.05% Tween20, 10 mM HEPES). The experiment was performed three times and the injection of 0.5 µM NUFIP2 was performed twice within each experiment. The equilibrium dissociation constant  $K_D$  was calculated from steady-state measurements using the BIAevaluation program (Biacore Inc.).

### **3.2.7 Flow cytometry**

#### **3.2.7.1 Surface staining**

For staining of ICOS on adherent cells (MEF, HeLa), cells were trypsinized and cell suspensions were incubated with biotinylated anti-human ICOS antibody in FACS staining buffer. Antibody staining was performed for 20 min at 4 °C. Cells were washed once, and subsequently incubated with Streptavidin-Allophycocyanin in a second staining step. After washing twice, sample readouts were acquired on a flow cytometer.

#### **3.2.7.2 Intracellular staining**

For intracellular staining of Roquin-1/-2, MEF cells were trypsinized and cell suspensions were fixed with 2 % formaldehyde for 20 min at room temperature. Following fixation, cells were permeabilized by washing in saponin buffer. Primary antibody staining was performed with anti-Roquin 3F12 for 1 h at RT, followed by a staining with the secondary antibody anti-mouse Alexa647. After washing twice, sample readouts were acquired on a flow cytometer.

### **3.2.8 Coimmunoprecipitation and immunoblotting**

For GFP-immunoprecipitation, a polyclonal anti-GFP antibody was coupled to protein G dynabeads, whereas pulldown of endogenous Roquin-1/2 from MEF cells was performed with anti-Roquin-1/2 (Q4-2)-coupled tosylactivated MyOne Dynabeads. Antibody coupling was performed according to the manufacturer's instructions. For preparation of the protein lysates, MEF or HEK293T cells growing on large tissue culture plates were rinsed once with cold PBS, detached with cell scrapers and centrifuged (300 x g, 5 min, 4 °C). Cell pellets were shock frozen in liquid nitrogen, thawed and resuspended in varying amounts of lysis buffer depending on the size of the cell pellet (Table 19). Lysis was performed for 20 min on ice, followed by clearance of the lysate via centrifugation (10,000 x g, 4 °C, 10 min). The protein concentration was determined with the Bio Rad protein assay (Bradford assay). Antibody-coupled beads were subsequently incubated with 2 mg of protein lysate for 4 h at 4 °C in the presence or absence of RNase. After washing three times with lysis buffer the beads were resuspended in Laemmli SDS sample buffer and boiled for 5 min at 95 °C for protein elution. The supernatant was subjected to immunoblotting.

For immunoblotting, protein lysates were generated as described above. After determination of the protein concentration, the desired amount of lysate (usually 50 µg protein/ slot for detection of endogenous proteins) was diluted with H<sub>2</sub>O and Laemmli SDS sample buffer and samples were subsequently boiled for 5 min at 95 °C. Denatured samples were loaded into the slots of an SDS-polyacrylamide gel consisting of an upper stacking gel and a lower running gel (Table 25). Gels with an acrylamide content of 10 % were used for detection of smaller proteins, such as Nufip2 (75 kDa), while 8 % gels were employed for detection of larger proteins, such as Roquin (130 kDa). The stacking gel serves to line up the proteins in the samples, which are subsequently separated according to size in the running gel. A prestained protein size marker was used as a reference. Electrophoresis was performed at 50 V for 20 min, followed by 120 V for 1.5 h. Separated proteins were blotted onto methanol-activated PVDF membranes at 40 V overnight in a wet gel blotting chamber filled with blotting buffer. After blotting, membranes were blocked in TBS + 5 % milk for two hours at RT. After a 10 min washing step with TBST, primary antibody dilutions in TBST + 1 % milk or 5 % were applied for incubation overnight at 4 °C. Afterwards membranes were washed three times with TBST + 1 % milk, and incubated with HRP-conjugated secondary antibody dilutions for 1 h at RT. Following three more washing steps with TBST + 1 % milk, TBST and TBS, blots were developed with self-made ECL solution.

**Table 25: Composition of SDS PAGE gels**

<b>Stacking gel</b>	<b>Separating gel (8% or 10%)</b>
5% Polyacrylamide	8 % or 10 % Polyacrylamide
125 mM Tris-HCl pH 6.8	375 mM Tris-HCl pH 8.8
0.1 % SDS	0.2 % SDS
0.1 % APS	0.2 % APS
0.1 % TEMED	0.06 % TEMED
up to 5 ml with H <sub>2</sub> O	up to 10 ml with H <sub>2</sub> O

### **3.2.9 High-throughput siRNA screen**

#### **3.2.9.1 siRNA Transfection**

High-throughput siRNA screening in HeLa cells was performed by reverse transfection of siRNAs in 96-wells similar to the protocol described in chapter 3.2.3.7 for the 24-well format. The high-throughput transfection protocol included transfection in duplicates and automated delivery of the siRNA reagents and the cells. 40 µl of the pre-diluted HiPerFect transfection reagent was dispensed manually into each well of a

96-well U-bottom plate (plate A) using a multichannel pipette. 8  $\mu$ l of 1 mM siRNA library stocks and 32  $\mu$ l of H<sub>2</sub>O were subsequently added by a robot, and after mixing, the robot dispensed half of the solution (40  $\mu$ l) into a replicate plate (plate B). 8  $\mu$ l of 1 mM control siRNAs in 32  $\mu$ l H<sub>2</sub>O (siRoquin, siCtrl) had been added manually before addition of the library stocks. Following an incubation time of 10 min to allow complex formation, 4,000 HeLa cells were added in 160  $\mu$ l of complete DMEM medium to each well. Plates were incubated for 48 h and subsequently the medium was replaced by fresh medium containing 1  $\mu$ g/ml doxycycline. After 18 h the cells were subjected to fluorescent cell barcoding and antibody staining.

### **3.2.9.2 Fluorescent cell surface barcoding and ICOS staining**

Before ICOS staining, cells were subjected to fluorescent cell barcoding, which allows multiplexing of different samples for combined antibody staining and data acquisition (Krutzik et al., 2011; Krutzik & Nolan, 2006). Fluorescent cell barcoding was in principal performed as described in (Krutzik et al., 2011), however, the protocol was adapted to label cell surface proteins only. HeLa cells were washed once with PBS, trypsinized and transferred to U-bottom 96-well plates. Washing steps were now carried out by resuspension, centrifugation at 400 x g and 4 °C for 5 min followed by aspiration of the supernatant with a vacuum pump containing an 8-channel adaptor. Cells were washed once with PBS, while dilutions of the amine-reactive fluorescent dyes Pacific blue Succinimidyl Ester and Alexa Fluor 488 Succinimidyl Ester were simultaneously prepared from 5 mg/ml stock solutions in PBS. Four different barcoding solutions were generated by employing both dyes in either a low (0.2  $\mu$ g/ml) or a high (4  $\mu$ g/ml) concentration. Cell pellets of each 96-well plate were resuspended in 50  $\mu$ l of one of the four distinct barcoding solutions, and plates were sealed, vortexed and incubated at 4 °C for 30 min. After washing twice with FACS buffer, four plates with differential barcoding signatures were pooled into one. After spinning for 5 min at 400 x g, 4°C, cells were resuspended in 50  $\mu$ l of the biotinylated anti-ICOS antibody dilution in FACS buffer. Antibody staining was performed for 20 min at 4 °C. After washing once with PBS, cells were stained with a dilution of Streptavidin-Allophycocyanin. After a final washing step, cells were resuspended in 100  $\mu$ l FACS buffer and analyzed on a LSRII Fortessa flow cytometer with the help of a high-throughput sampler.

### **3.2.10 Pooled CRISPR/Cas9 screen**

A pooled CRISPR/Cas9 screen was performed to identify genes that are involved in Roquin-induced cell death (Figure 39).

#### **3.2.10.1 Library amplification**

The mouse Gecko v2 library is delivered as two half-libraries (A and B), each containing one half of the sgRNAs targeting genes and miRNAs. Library amplification was performed as described in the data sheet provided by Addgene. In brief, four aliquots of electrocompetent bacteria were electroporated with 100 ng of the Gecko library each. All batches were pooled, and plated onto two 24.5 cm<sup>2</sup> agar plates containing ampicillin. Cells were grown at 32°C for 14 h. All colonies were scraped off the plate with a cell scraper, and plasmid DNA was prepared from the total amount of bacteria using the maxiprep kit (Chapter 3.2.1.2).

#### **3.2.10.2 Lentivirus production and virus transduction**

Lentiviral particles were produced as described for second-generation lentiviral vectors in chapter 3.2.3.4. One plate of HEK293T cells each was transfected with 25 µg of library A and B together with the corresponding packaging plasmids. The lentiviral supernatant was harvested as described in chapter 3.2.3.4, frozen and directly used for transduction. Virus titration was performed as described in (Shalem et al., 2014). Transduction was performed via spin infection as described in chapter 3.2.3.5. After spinning, the medium was replaced by fresh medium, and cells were incubated for 20 h at 37 °C. After trypsinizing and pooling of all cells, 5 x 10<sup>7</sup> cells were frozen for isolation of genomic DNA as described in chapter 3.2.3.2. The remaining cells were cultured in the presence of 2 µg/ml puromycin for seven days. Following puromycin selection, maintenance of 5 x 10<sup>6</sup> cells was sufficient to maintain the complexity of the library. Cells were passaged every other day for the duration of the experiment, and 5 x 10<sup>6</sup> cells were harvested for genomic DNA on the indicated days (Figure 40A).

#### **3.2.10.3 Amplification of sgRNA sequences from genomic DNA**

Following isolation of genomic DNA as described in chapter 3.2.3.2, integrated sgRNA sequences were amplified in a two-step PCR reaction using Herculase II Fusion DNA polymerase. For the first PCR, the required amount of input genomic DNA was calculated in order to achieve 300-fold coverage over the GECKO library, which resulted in 280 µg DNA per sample (assuming 7 pg of genomic DNA per cell). For each

sample, a PCR master mix (Table 26) was prepared to contain the 280 µg template DNA. The master mix was distributed to 28 wells of a 96-well plate (100 µl/well) and run on a Lightcycler (cycling conditions: 2 min at 95 °C, 18 x (20 s at 95 °C, 45 s at 61 °C, 30 s at 72 °C), 72 °C for 3 min).

**Table 26: Master mix for the first CRISPR/Cas9 PCR**

Amount	Reagent
560 µl	5x buffer
28 µl	dNTP 10mM each
70 µl	Forward primer (10 µM)
70 µl	Reverse primer (10 µM)
28 µl	Herculase
280 µg	Genomic DNA
Up to 2800 µl	H <sub>2</sub> O

Following amplification, the reactions of all 28 wells were pooled and 5 µl of the pooled amplicons were amplified in a single 100 µl reaction using the primers of the second CRISPR/Cas9 PCR (Table 10) (2 min at 95 °C, 24 x (20 s at 95 °C, 45 s at 60 °C, 30 s at 72 °C), 72 °C for 3 min). The resulting PCR products were gel-purified as described in chapter 3.2.1.3 and subjected to next-generation sequencing (NGS), which was performed by Dr. Stefan Krebs in the laboratory of Dr. Helmut Blum, Gene Center Munich.

## 4 Results

### 4.1 Targeted siRNA screen for cofactors of Roquin-1 in post-transcriptional gene regulation

Roquin family proteins (Chapter 1.1.4.2) bind to stem-loop structures in the 3' untranslated region (3' UTR) of their target mRNAs and inhibit gene expression (Jeltsch & Heissmeyer, 2016). However, the mechanism, which is employed by the highly homologous proteins Roquin-1 and Roquin-2 to induce post-transcriptional gene regulation, is still elusive. Roquin-1 was initially shown to interact with the RNA helicase Rck (also known as Ddx6) and the enhancer of mRNA decapping Edc4 (also known as Hedls or Ge-1), supporting a model in which Roquin-1 inhibits its target mRNA expression through decapping and subsequent 5' to 3' degradation (Glasmacher et al., 2010). More recent studies primarily found interactions of mouse and human ROQUIN-1 with subunits of the CCR4-CAF1-NOT deadenylation complex, in particular with the scaffolding subunit CNOT1 and the deadenylases CNOT7 and CNOT8 (Leppek et al., 2013; Murakawa et al., 2015). Therefore, in Roquin-1-mediated mRNA degradation deadenylation may precede decapping. Additionally, it was demonstrated that Roquin-1 can cooperate with the endonuclease Regnase-1 (Chapter 1.1.4.3) on the 3' terminal 260 nucleotides (nts) of the *TNF* 3' UTR to induce post-transcriptional repression (Jeltsch et al., 2014). Obviously, Roquin-1-mediated repression of its target mRNAs is highly complex and our understanding of the underlying principles is still sketchy at best. Consequently, crucial cofactors and collaborating RNA-binding proteins (RBPs) are likely missing in current models.

The inducible T cell co-stimulator *ICOS* (Chapter 1.2.1.4) was the first identified mRNA targeted by Roquin-1 (Vinuesa et al., 2005). Its long 3' UTR of ~2000 nucleotides (nts) would allow for a multitude of cooperative interactions with different post-transcriptional regulators, such as miRNAs and RBPs, but only miR-101-, miR-146-, Regnase-1- and Roquin-1-mediated repression have been described thus far (Glasmacher, 2010; Jeltsch et al., 2014; Srivastava et al., 2015; Yu et al., 2007). In *sanroque* mice, where Roquin-1 function is impaired due to a single point mutation, all T cells show enhanced *Icos* expression (Vinuesa et al., 2005) and dysregulated *Icos* can take over CD28 functions in initiating T cell help (Linterman et al., 2009). Uncoupling of the T cell-dependent antibody response from the requirement for CD28

costimulation to discriminate between foreign and self is thought to contribute to the development of the severe autoimmune phenotype of *sanroque* mice (Chapter 1.3.3) (Linterman et al., 2009). Insights into the principles of post-transcriptional *ICOS* regulation would consequently be of considerable interest and may also be transferred to other transcripts targeted by Roquin-1. On the basis of these considerations, we decided to perform a high-throughput RNAi screen for cofactors of Roquin-1-mediated *ICOS* regulation.

#### 4.1.1 Generating a reporter cell line

I started out to produce a reporter cell line, which would enable the quantification of post-transcriptional regulation of *ICOS* by Roquin-1 with flow cytometry. Recently, up to 20-fold downregulation of exogenously expressed *ICOS* surface protein was observed in response to retroviral overexpression of Roquin-1 in mouse embryonic fibroblast (MEF) cells (Glasmacher et al., 2010). Therefore, I decided to also use this system for the development of my reporter cell line. I adopted the flow cytometric readout of *ICOS* surface expression after antibody staining. Avoiding cell toxicity due to constitutive Roquin-1-IRES-Thy1.1 expression, I decided to generate a clonal cell line with stable *ICOS*- and inducible Roquin-1 overexpression.

To circumvent the need for intracellular FACS staining, Roquin-1 was cloned in frame with the fluorescence marker mCherry. The two genes were separated by the sequence of a self-cleaving peptide from porcine teschovirus-1 (P2A), which causes defined stopping and reinitiation events of the ribosome during translation, thereby allowing the expression of stoichiometric amounts of two separate proteins from one mRNA (Figure 8A) (Kim et al., 2011). A fusion construct lacking the P2A peptide (Roquin-1-mCherry) was cloned as a control. The lentiviral tet-on system (Chapter 3.2.3.6) was used to achieve doxycycline-inducible gene expression. Specifically, wildtype MEF cells were transduced with the transactivator rtTA3 and a second lentivirus encoding Roquin-1-P2A-mCherry or Roquin-1-mCherry expressed from the doxycycline-inducible  $CMV_{\text{tight}}$  promoter. After 24 h of doxycycline treatment, Roquin-1 expression levels were analyzed by immunoblotting (Figure 8B) showing strong induction after doxycycline treatment. Comparing cells transduced with Roquin-1-P2A-mCherry versus Roquin-1-mCherry revealed that only a small amount of protein from the Roquin-1-P2A-mCherry construct was not separated (Figure 8B), second lane, highest band), leading to the expression of relatively small amounts of a Roquin-1-mCherry fusion protein.

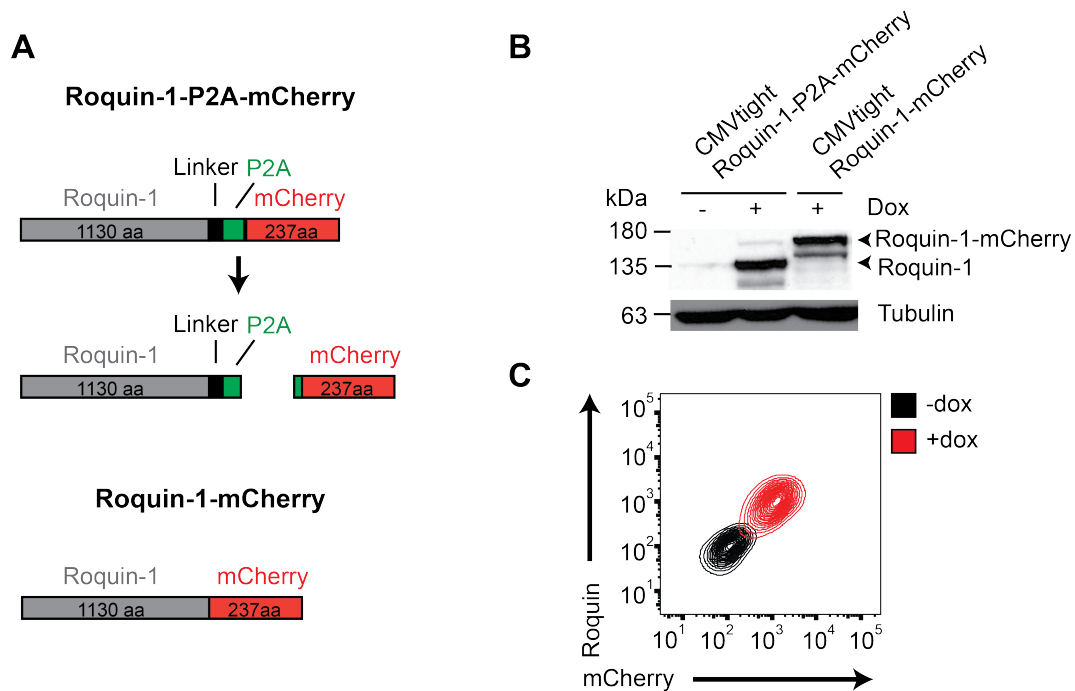


**Figure 8: Evaluation of dox-inducible overexpression of Roquin-1-P2A-mCherry.**

**(A)** Schematic representation of Roquin-1-P2A-mCherry and Roquin-1-mCherry expression constructs. In the upper construct, Roquin-1 and mCherry are separated by a 7-amino acid linker and a porcine techovirus-1 2A (P2A) peptide of 19 amino acids (aa). The C-terminus of the 2A peptide is “cleaved” by ribosome skipping, resulting in the separation of the proteins Roquin-1 and mCherry. The linker and the N-terminal 18 amino acids of the 2A peptide stay attached to the C-terminus of Roquin-1, while a single proline residue of P2A is added to the N-terminus of mCherry. The lower construct (Roquin-1-mCherry) results in the generation of a Roquin-1-mCherry fusion protein. **(B)** Immunoblot analysis of Roquin-1 expression in whole cell lysates from wt MEF cells transduced lentivirally with doxycycline (dox)-inducible Roquin-1-P2A-mCherry or Roquin-1-mCherry. Cells were cultured in the presence of dox for 24 h or left untreated as indicated. **(C)** Flow cytometric analysis of intracellular Roquin-1- and mCherry expression in a clonal Rc3h1/2<sup>-/-</sup> cell line with dox-inducible Roquin-1-P2A-mCherry. Cells were cultured in the presence of dox for 24 h (+dox) or left untreated (-dox). Intracellular Roquin was stained with an antibody recognizing Roquin-1 and Roquin-2.

In order to achieve maximal changes of Roquin-1 levels after doxycycline-induction, we used Rc3h1/2<sup>-/-</sup> MEF cells, in which the genes encoding Roquin-1 and Roquin-2 (Rc3h1 and Rc3h2, respectively) were deleted. These cells were transduced with doxycycline-inducible Roquin-1-P2A-mCherry, and single clones were generated. Flow cytometric analysis of the clone with highest induction revealed a full correlation between intracellular Roquin-1 and mCherry expression, validating the use of mCherry as a fluorescent marker for Roquin-1 overexpression for the course of this study (Figure 8C).

After establishing the inducible Roquin-1 overexpression system, the reporter, ICOS, was stably integrated into the genome of the cells via lentiviral transduction. In order

to find physiologic cofactors with an impact on Roquin-1-mediated mRNA repression of ICOS, the protein coding sequence (CDS) and the whole ~2 kb 3' untranslated region (3' UTR) of *ICOS* mRNA were used as a reporter. Another step of single cell cloning eventually resulted in the successful generation of a reporter cell line, which was suitable for the intended screening experiment. This cell line showed high expression of ICOS in the absence of Roquin (Figure 9A, cells in black), but enabled a strong downregulation of ICOS surface expression in response to doxycycline-induced overexpression of Roquin-1 (Figure 9A, cells in red). Supporting specificity of this assay, there was no repression of the CDS of *ICOS* without the 3' UTR after Roquin-1-induction, and similarly the *ICOS* full-length mRNA was not regulated by a truncated, inactive version of Roquin-1, (Roquin-1 aa 1-509) (Glasmacher, 2010) (Figure 9B, C).

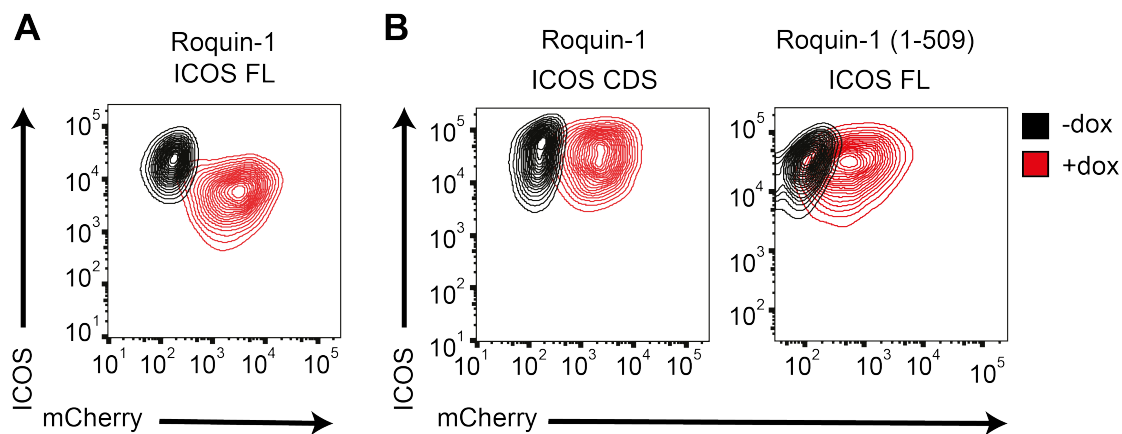


**Figure 9: Validation of the reporter system for Roquin-1-mediated post-transcriptional gene regulation.**

**(A)** Flow cytometric analysis of ICOS and mCherry expression in a clone of *Rc3h1/2<sup>-/-</sup>* MEF cells that were lentivirally transduced with doxycycline (dox)-inducible Roquin-1-P2A-mCherry and ICOS full-length (ICOS FL). Cells were treated with dox for 24 h (+dox) or left untreated (-dox). **(B)** Flow cytometric analysis of ICOS and mCherry expression of MEF cell clones that were transduced with dox-inducible Roquin-1-P2A-mCherry or Roquin-1 (aa 1-509)-P2A-mCherry constructs and superinfected with vectors encoding only the coding sequence of ICOS mRNA (CDS) or ICOS CDS followed by its 3' UTR (full-length, FL), respectively. Cells were treated with dox for 24 h (+dox) or left untreated (-dox).

#### 4.1.2 Characterization of Roquin-1-induced post-transcriptional regulation of ICOS

The newly established *Rc3h1/2<sup>-/-</sup>* MEF reporter cell line for Roquin-dependent *ICOS* repression (Figure 9A) was characterized in a time course of ICOS regulation after doxycycline-induction of Roquin-1 (Figure 10).

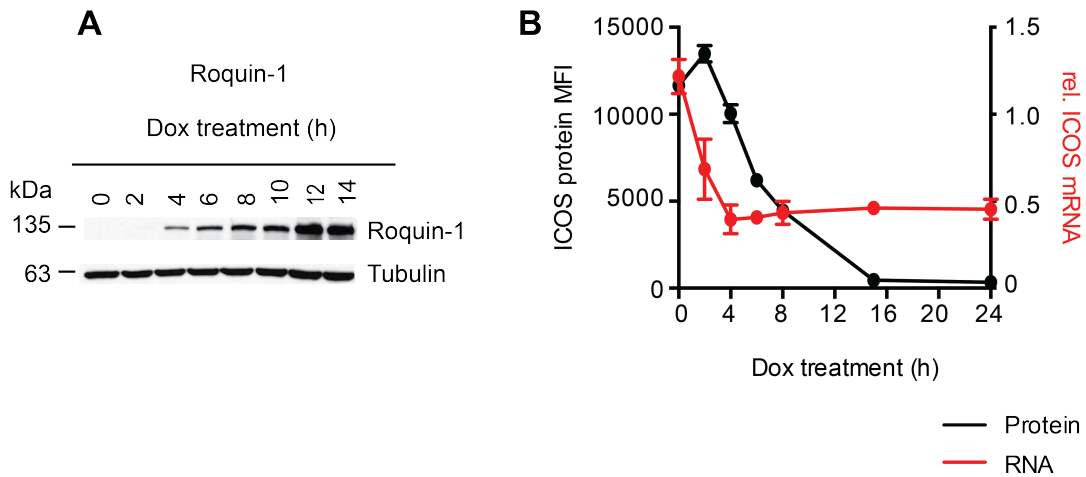


**Figure 10: Time course of Roquin-1-dependent ICOS regulation.**

**(A)** Immunoblot analysis of Roquin-1 expression in whole cell lysates from *Rc3h1/2<sup>-/-</sup>* MEF cells with doxycycline-inducible Roquin-1-P2A-mCherry and stable ICOS expression. Cells were treated with doxycycline (dox) for the indicated times. **(B)** Quantified protein and mRNA expression of ICOS in *Rc3h1/2<sup>-/-</sup>* MEF cells with dox-inducible Roquin-1-P2A-mCherry and stable ICOS expression. Cells were treated with dox for the indicated times. Mean Fluorescence Intensity (MFI) of ICOS surface expression was quantified by flow cytometry and ICOS mRNA expression was measured by qPCR relative to Hprt.

Roquin-1 overexpression was detectable in immunoblots as early as 4 h after doxycycline-induction (Figure 10A). At that time ICOS mRNA was also maximally repressed, while full regulation of ICOS surface expression did not occur until 15 h after doxycycline treatment (Figure 10B). Interestingly, *Rc3h1/2<sup>-/-</sup>* MEF cells showed a high downregulation of ICOS expression on the protein level (30-fold), while ICOS mRNA was only 2-fold reduced. This finding suggests that mRNA decay is not the only mechanism by which Roquin-1 controls ICOS expression. These data would be consistent with Roquin-1 mediating mRNA decay early on, and, in addition, causing translational inhibition at later time points. Starting from these findings another project in our lab is currently investigating Roquin-mediated translational inhibition, which is not addressed further in this study. As maximal downregulation of ICOS surface expression required at > 15 h of doxycycline stimulation (Figure 10), 18 h of doxycycline treatment was chosen for read out during the following pilot experiments and the actual screen.

#### 4.1.3 Pilot experiments to prepare the screen

After successful generation and characterization of the reporter system, pilot experiments were run in order to prepare for the high-throughput screen. In this chapter, I will first describe how assay robustness was assessed by calculating the Z'

factor. This was first performed in a 24-well format without siRNAs and then in the 96-well screening format with positive and negative control siRNAs. Finally, fluorescent cell barcoding was incorporated into the screening protocol to minimize consumable costs on the one hand and sample handling and data acquisition time on the other.

#### 4.1.3.1 Calculation of the Z' factor

The *Rc3h1/2<sup>-/-</sup>* MEF reporter cells showed strong downregulation of ICOS surface proteins in response to doxycycline-induced Roquin-1 expression, however, it was unclear whether it would be possible to achieve high siRNA knockdown efficiencies in MEF cells. As this was already proven for HeLa cells, which are widely used in RNAi screens (Badertscher et al., 2015; Henderson & Azorsa, 2013; Simpson et al., 2012), a second reporter cell line was also set up in HeLa cells using the same system of dox-inducible Roquin-1-P2A-mCherry and stable ICOS expression as described in chapter 4.1.1. In order to choose one of the two reporter cell lines, Z' factors were calculated for both. The Z factor assesses the quality of a high-throughput screening assay, taking both the dynamic range and the data variation into account, which are calculated from mean and standard deviation of sample versus control data (Figure 11). The Z' factor is usually calculated during the pre-screening pilot experiments with multiple measurements of a known positive control versus a negative control (Zhang et al., 1999).

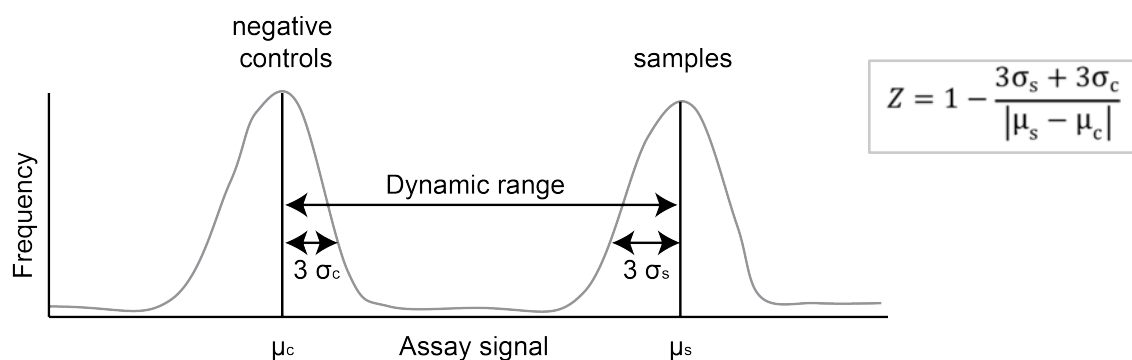


**Figure 11: Schematic representation of data variation and dynamic range of a high-throughput screen (adapted from (Zhang et al., 1999)).**

This graphic illustrates normally distributed sample and control data of a high-throughput screen. The dynamic range is defined as the difference between the mean of sample data ( $\mu_s$ ) and the mean of the control data ( $\mu_c$ ). The standard deviation (SD) of sample ( $\sigma_s$ ) and control data ( $\sigma_c$ ) defines the variation of the assay. In normally distributed populations, 95 % of the data points lie within 3 SDs from the mean.

The equation for calculating the Z factor is shown in Figure 11. For low standard deviations (SDs) of positive ( $\sigma_s$ ) and negative controls ( $\sigma_c$ ), the numerator approaches 0 and in consequence Z approaches 1. Likewise, a high difference between the means of positive and negative controls will drive the denominator towards infinity; therefore Z will again approach 1. Thus, the ideal assay with no SD or an infinitely high difference between positive and negative controls would have a Z factor of 1. In practice, assays with a Z factor between 0.5 and 1 are considered excellent and show a good separation between positive and negative controls (Zhang et al., 1999).

In our screen, doxycycline-inducible Roquin-1-P2A-mCherry overexpression causes post-transcriptional repression of stably expressed ICOS, which will be inhibited after knockdown of a Roquin-1 cofactor. Hits are therefore characterized by increased ICOS expression, and the maximal signal is expected to reach the level of ICOS expression in the absence of Roquin-1, which can be mimicked by non-induced reporter cells. In contrast, doxycycline-induced samples with fully downregulated ICOS surface expression represent the minimal screening signal. To calculate the Z' factors of Roquin-1-mediated ICOS repression in *Rc3h1/2<sup>-/-</sup>* MEF and HeLa reporter cell lines, the dynamic range and data variation of untreated versus doxycycline-treated cells were analyzed in a 24-well format.

The MEF cell line showed higher expression of mCherry and stronger downregulation of ICOS than the HeLa cell line (Figure 12A). Immunoblot analysis confirmed the absence of endogenous Roquin-1 and -2 in *Rc3h1/2<sup>-/-</sup>* MEF cells without doxycycline and a higher overexpression of Roquin-1 in response to doxycycline treatment than in HeLa cells, where endogenous *Rc3h1* and -2 were present in untreated cells due to their wildtype background (Figure 12B). Both cell lines showed only small amounts of the "uncleaved" Roquin-1-mCherry fusion protein. Calculating the mean and standard deviation of 12 treated and 12 untreated samples, MEF cells showed a larger screening window (30-fold difference between  $\mu_s$  and  $\mu_c$ ), but also a much higher variance between equally treated samples (Figure 12C). For HeLa cells, the screening window was smaller, with a 3-fold difference between  $\mu_s$  and  $\mu_c$ , but due to the lower variation this assay proved to be more robust and with a Z score of 0.65 better suitable for high-throughput screening. The HeLa cell line was therefore chosen as a reporter cell line for the RNAi screen.

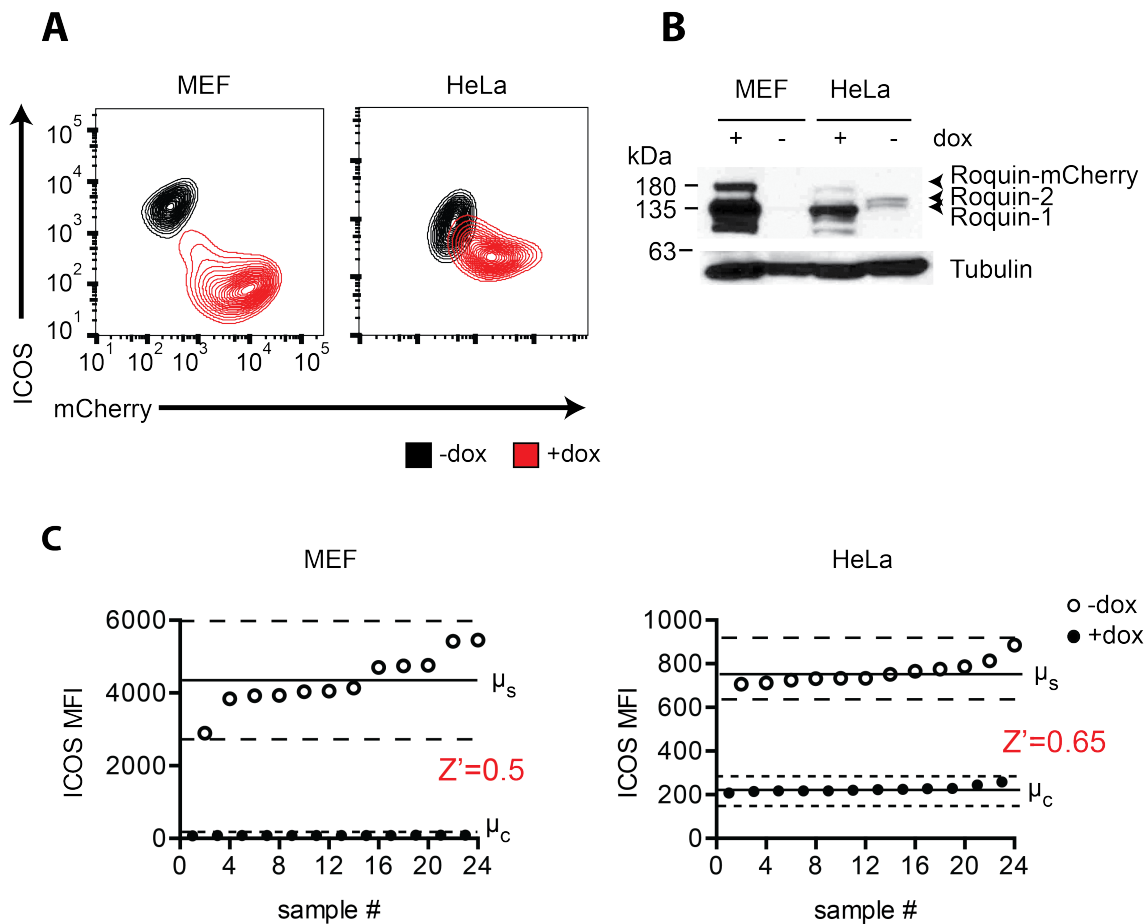


**Figure 12: Calculation of the  $Z'$  factor in induced versus non-induced  $Rc3h1/2^{-/-}$  MEF and HeLa reporter cell lines.**

**(A)** Representative flow cytometric analysis of ICOS and mCherry expression in  $Rc3h1/2^{-/-}$  MEF and HeLa reporter cells with stable ICOS and doxycycline (dox)-inducible Roquin-1-P2A-mCherry expression. Cells were induced with dox for 18 h (+dox) or left untreated (-dox). **(B)** Immunoblot analysis of  $Rc3h1$  and -2 expression in whole cell lysates from  $Rc3h1/2^{-/-}$  MEF and HeLa reporter cells. Cells were induced with dox for 18 h (+dox) or left untreated (-dox). **(C)** Quantified ICOS expression from 24 wells of MEF or HeLa reporter cells that were treated with dox for 18 h (+dox) or left untreated (-dox). ICOS mean fluorescence intensity (MFI) was determined by flow cytometry. Solid lines show the means of positive (-dox,  $\mu_s$ ) and negative control (+dox,  $\mu_c$ ) data, dashed lines display 3 SDs from the mean of each data set.

After choosing the desired reporter cell line, the next important step was the development of a robust high-throughput RNAi screening protocol. Therefore, a procedure was established to include siRNA transfection and doxycycline-induced expression of Roquin-1 after 48 h, in order to provide enough time for the knockdown to become effective in HeLa reporter cells (Figure 13A). ICOS surface expression was then analyzed 18 h after Roquin-1-induction, in a 96-well format and using a flow cytometer in combination with a high-throughput sampler. In this set up the reporter cell line was routinely transfected with siGENOME siRNA pools. In each pool four

different siRNAs target the same gene. In each well of a 96-well plate, one pool of siRNAs leads to the knockdown of the expression of a different candidate gene. To investigate whether a robust Z factor could be reached in the 96-well screening format and with siRNA transfection, 2 x 36 wells with reporter cells were treated with Roquin-1-targeting (siRoquin-1) or non-targeting siRNAs (siCtrl) as positive and negative controls, respectively. Knockdown of Roquin-1 resulted repeatedly and uniformly in an effective derepression of ICOS, while its expression was unaffected by non-targeting control siRNAs. The protocol above was optimized until a Z' factor of 0.7 was reached to make it highly suitable for high-throughput screening (Figure 13B).

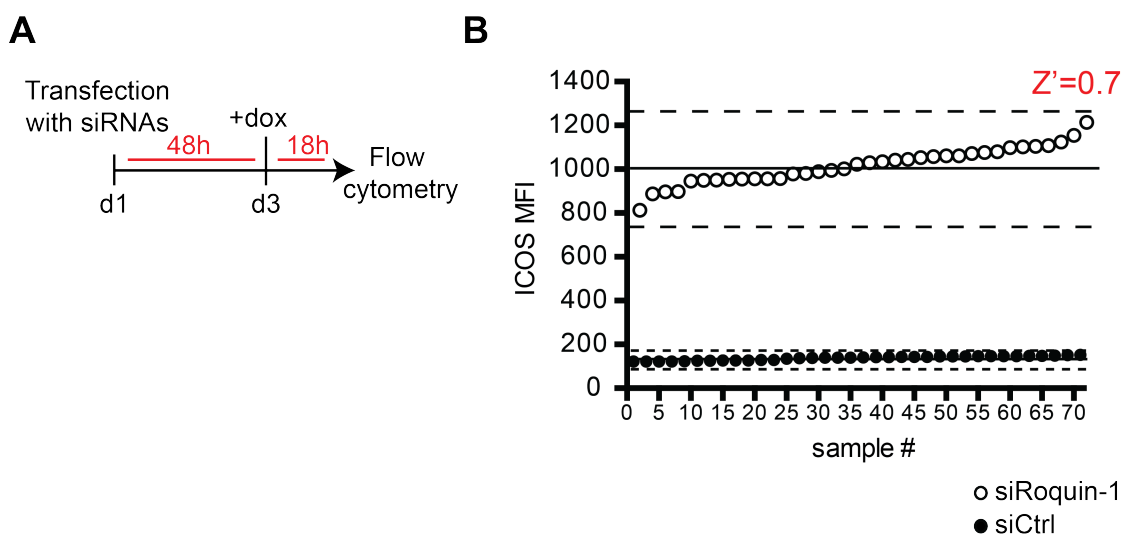


**Figure 13: Calculation of the Z' factor after siRNA knockdown of Roquin-1 in HeLa reporter cells.**

**(A)** Schematic representation of the screen workflow. HeLa reporter cells were transfected with siRNA pools targeting different genes in each well of a 96-well plate. 48 h after transfection, Roquin-1 overexpression was induced with doxycycline (dox). After 18 h, ICOS and mCherry expression were quantified by flow cytometry. **(B)** Distribution of ICOS expression in HeLa reporter cells after siRNA transfection. HeLa reporter cells were transfected with Roquin-1-targeting siGENOME siRNA pools (siRoquin-1) or a non-targeting control siRNA (siCtrl) in a 96-well plate as described in **(A)**. The Z' factor was calculated from mean and SDs of positive (siRoquin-1) and negative (siCtrl) control data. Solid lines show the means of positive (siRoquin-1) and negative control (siCtrl) data, dashed lines indicate three SDs from the mean of each data set.

#### 4.1.3.2 Establishing fluorescent cell surface barcoding

In order to enhance the screening throughput, I established fluorescent cell barcoding as a technique of multiplexing different samples for combined antibody staining and data acquisition. First described in 2006, fluorescent cell barcoding employs chemically activated fluorescent dyes for labeling of amino acid side chains of cellular proteins. Incubation with different concentrations of the fluorescent barcoding dyes

results in a unique fluorescence signature of each individual sample. After combined data acquisition, samples can be deconvoluted based on their fluorescence fingerprint (Krutzik et al., 2011; Krutzik & Nolan, 2006) (Figure 14A). Eventually four distinct barcoding signatures were created by combination of two fluorescent dyes in two different concentrations. Alexa Fluor 488 and Pacific blue were chosen as barcoding dyes in order to minimize spillover into the mCherry or ICOS (Allophycocyanin) channel of the flow cytometer.

0

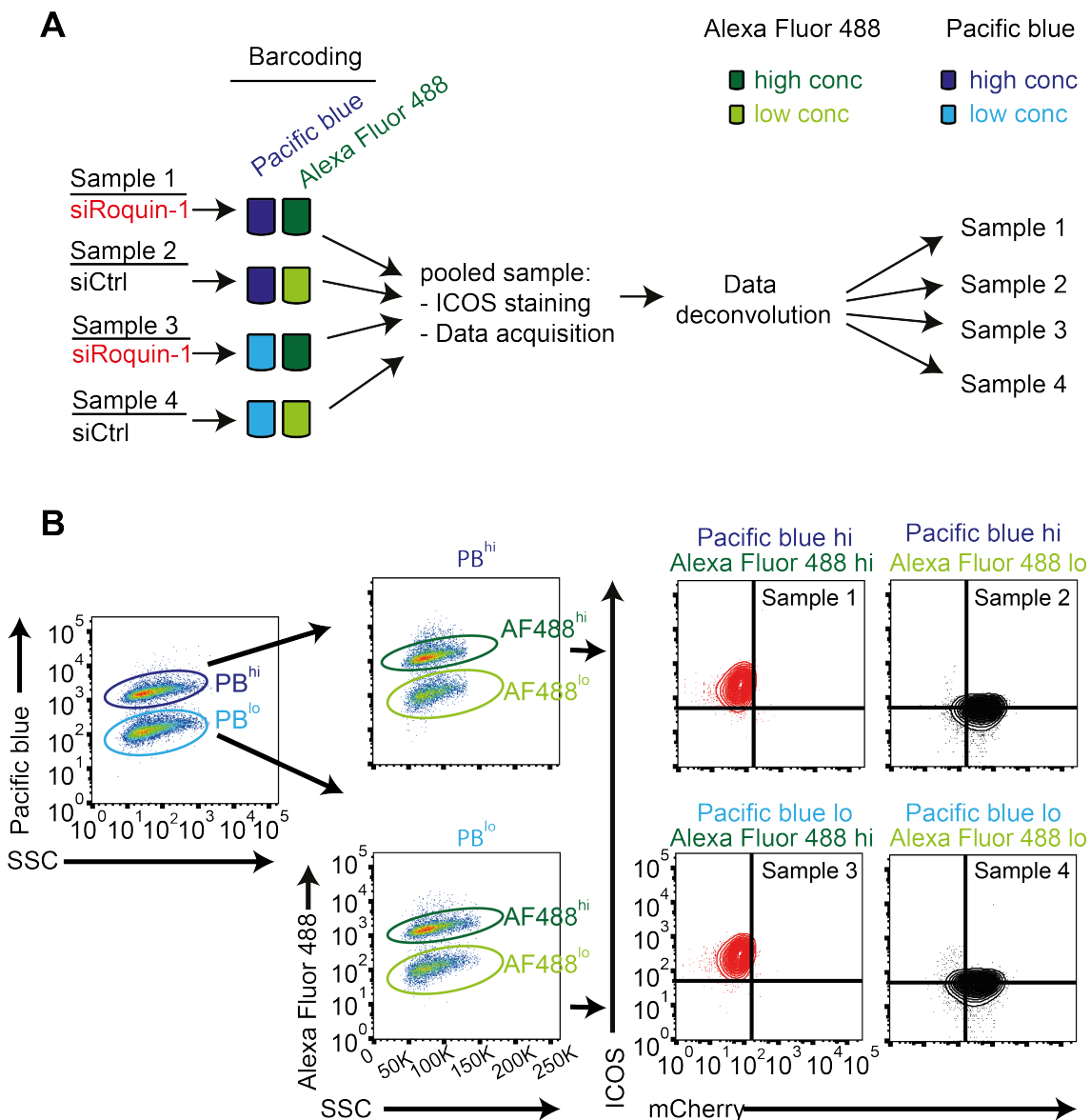


**Figure 14: Fluorescent cell surface barcoding allows multiplexing of different samples for antibody staining and data acquisition.**

**(A)** Schematic representation of the transfection, barcoding and data acquisition workflow. **(B)** Deconvolution of barcoded samples. Samples from **(A)** were first deconvoluted based on their Pacific blue (PB) fluorescence intensity into high (PB<sup>hi</sup>) and low (PB<sup>lo</sup>)-expressing cells. Second, Alexa fluor

*488 high (AF488<sup>hi</sup>) and low (AF488<sup>lo</sup>)-expressing cells were separated, leading to the deconvolution into the four original samples. ICOS and mCherry expression was plotted for each sample.*

At this point all requirements had been met to perform a high-throughput RNAi screen.

#### **4.1.4 Arrayed RNAi screening**

RNAi screening was performed at *the Functional Genomics Center of La Jolla Institute for Allergy and Immunology (LJI)* under the supervision of Dr. Sonia Sharma and in collaboration with Dr. Anjana Rao's lab. Prior to using an expensive customized siRNA library, we wanted to test our assay in the high-throughput RNAi screening mode. We therefore started by screening six arrayed Dharmacon siGENOME subset libraries (GPCR, Ion Channels, Proteases, Phosphatases, Kinases and Ubiquitin Conjugation) that were instantly available at the Functional Genomics Center. Screening these protein subset libraries also had a second purpose: Since possible cofactors of Roquin-1-mediated ICOS regulation are not necessarily restricted to RNA-binding proteins, interesting hits might also arise from one of these subset libraries.

After conclusion of the protein subset screens, we set our focus on the identification of targets involved in known steps of *ICOS* post-transcriptional regulation: RNA binding, localization into P bodies or stress granules, and finally mRNA decay. Therefore, a cherry-picked, customized siRNA library was assembled of ~1500 candidates. This list comprised:

- All RBPs bound to polyadenylated mRNA in HeLa cells (Castello et al., 2012) as well as all proteins that were annotated as "RNA-binding" in gene ontology ([www.geneontology.org](http://www.geneontology.org))
- Factors that are involved in P body and stress granule assembly (Ohn et al., 2008)
- Proteins involved in deadenylation- and decapping-dependent mRNA decay (Braun et al., 2012; Chen & Shyu, 2011; Cooke et al., 2010)

##### **4.1.4.1 Screening of arrayed subset libraries**

ICOS regulation in HeLa cells transfected with siRNA pools targeting the protein families of GPCR, ion channels, phosphatases, proteases, kinases and the ubiquitin conjugation system was assessed with the 96-well screening protocol including barcoding as described before (Figure 13A, Figure 14A). After data deconvolution,

average ICOS mean fluorescence intensity (MFI) of each duplicate sample was normalized into a Z score using the following equation:

$$Z = \frac{ICOS\ MFI_{sample} - ICOS\ MFI_{plate\ average}}{SD\ plate}$$

Ranked Z scores were plotted for each subset library (Figure 15), and every data point with a Z score > 2 was considered a hit. Hit rates lay constantly between 5 and 6.5 %, with the subset of phosphatases showing the lowest hit rate. Strikingly, positive Z scores reached from zero up to a maximum of 16, while negative Z scores never fell below -2 in any of the protein subset screens (Figure 15). This is explained by the nature of the reporter cell line: The HeLa cell line is characterized by a rather low level of ICOS overexpression, which is completely reduced to background levels after doxycycline-induced Roquin overexpression (Figure 12). Our assay did thus not allow the identification of Roquin antagonists, which is an aspect that was not part of this research project.

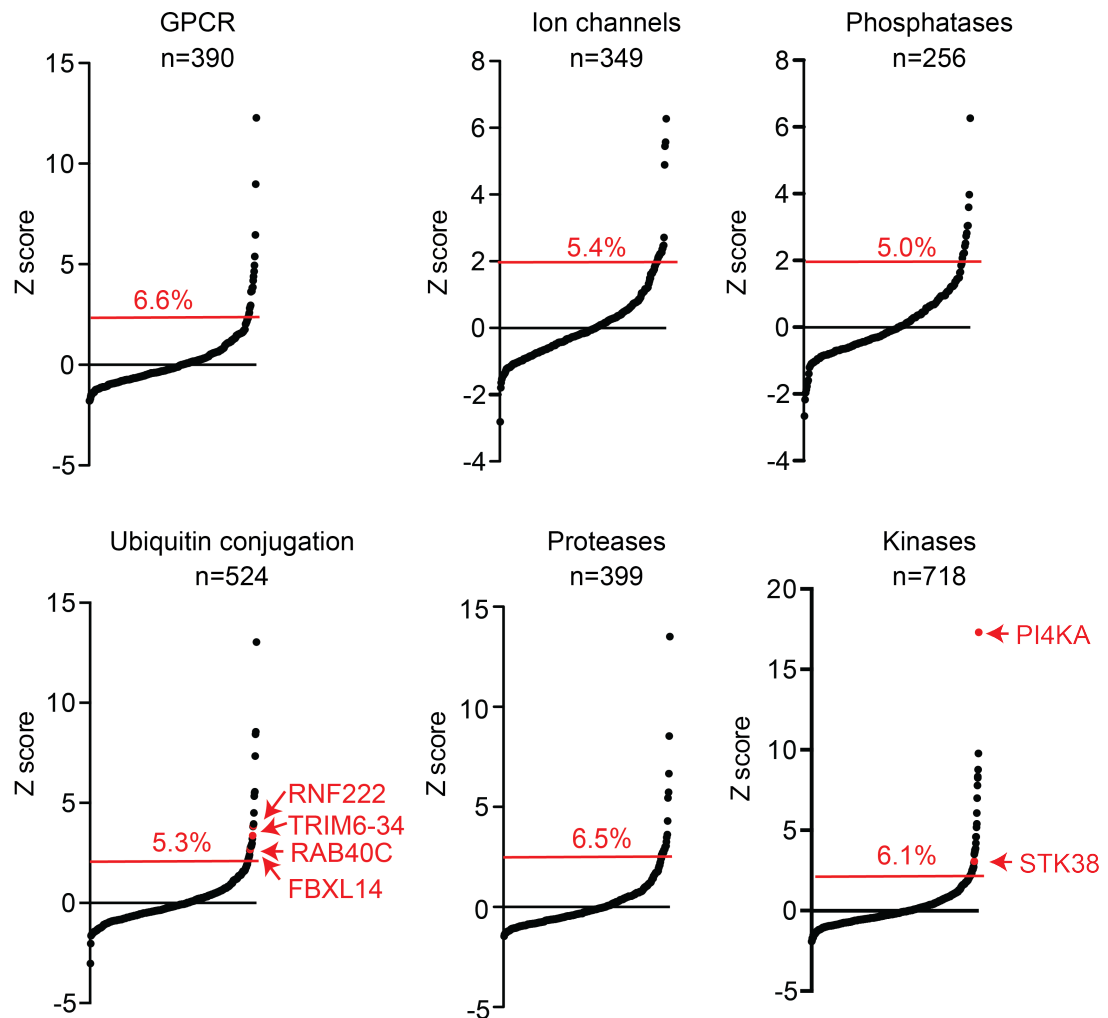


**Figure 15: Screening of six siGENOME arrayed subset libraries.**

Normalized data from screening six subset libraries. HeLa reporter cells were transfected with siRNA pools targeting all members of each subset library in duplicates. 48 h after transfection, Roquin-1 overexpression was induced with doxycycline for 18 h. Cells were harvested, barcoded and 4 wells were combined into one for ICOS staining and data acquisition. After deconvolution, average ICOS MFI of each sample was normalized into a Z score with the plate mean and SD. Ranked Z scores are shown for each library. Each data point with an average Z score > 2 was considered a hit, and hit rates are indicated in red as percentages. Candidates that were chosen for further validation are labeled in red.

Since Roquin-1 is a putative E3 ubiquitin ligase and contains a RING finger at its N-terminus (Vinuesa et al., 2005), candidates from the ubiquitin conjugation subset were initially chosen for further validation.

#### 4.1.4.2 Overexpression of individual candidates of the ubiquitin conjugation system in MEF reporter cell lines

Of the 28 candidates that scored positively in the primary screen of proteins involved in ubiquitin conjugation, seven showed reduced mCherry expression (> 25 %) as compared to siCtrl. This indicates off-target effects on Roquin-1-P2A-mCherry overexpression and the respective candidates were excluded from further analysis.

In contrast, four promising candidates showed unaffected mCherry and strongly increased ICOS expression after siRNA knockdown (Figure 16A, red versus black populations) and thus were chosen for further validation. Since the knockdown of FBXL14, RAB40C, TRIM6-TRIM34 and RNF222 caused a derepression of ICOS, we reasoned that their overexpression should reciprocally lead to lower ICOS expression. The reporter system of our screen is based on the system published by Glasmacher and colleagues (Glasmacher et al., 2010), and likewise employs mouse Roquin in combination with human ICOS. Since we have thus far not observed any species-specific differences using mouse or human proteins, the pathway of Roquin-mediated ICOS repression seems to be generally conserved between the two species. For overexpression of potential Roquin cofactors we therefore employed human or mouse cDNA clones whichever was available. The mouse or human cDNAs were cloned into a retroviral expression vector, which contained the surface marker Thy1.1. The candidate proteins were subsequently overexpressed in *Rc3h1/2<sup>-/-</sup>* or wildtype MEF cells with inducible Roquin-1-P2A-mCherry that stably expressed ICOS, in order to assess whether overexpression of the candidate itself, or only in combination with overexpressed Roquin-1, can repress ICOS expression. In *Rc3h1/2<sup>-/-</sup>* MEF cells, none of the candidates and only Roquin-1 overexpression led to downregulation of ICOS expression in cells that were positive for the infection marker Thy1.1 (Figure 16B). In wildtype MEF cells with doxycycline-induced Roquin-1 overexpression, ICOS levels were already strongly reduced in non-infected Thy1.1<sup>-</sup> cells, and were not further repressed by additional retroviral overexpression of Roquin-1 (Thy1.1<sup>+</sup> cells) (Figure 16C upper panel). Again, none of the candidates further downregulated ICOS (Figure 16C lower panel).

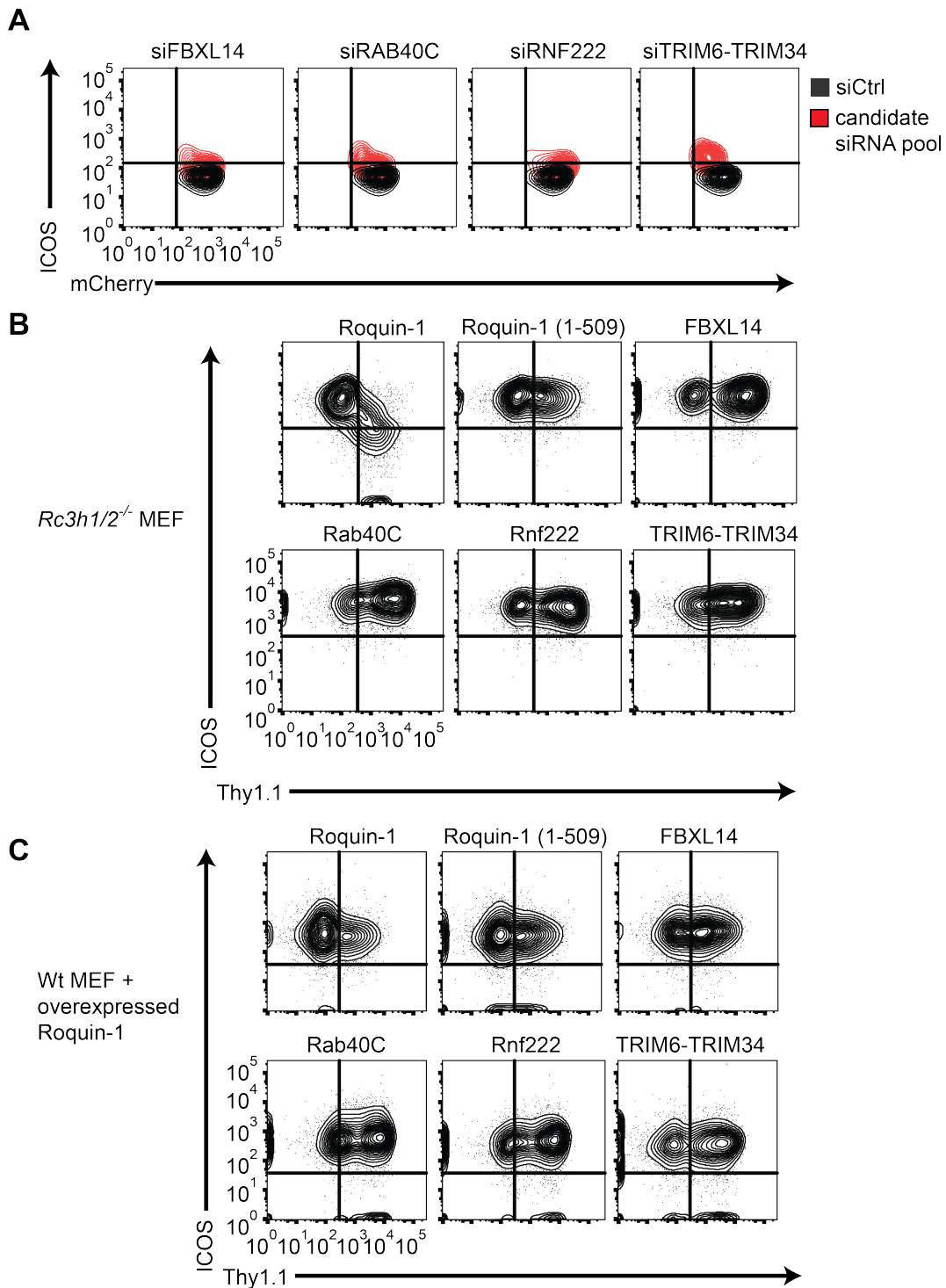


**Figure 16: Validation of four candidates from the ubiquitin conjugation system by overexpression.**

**(A)** Flow cytometric analysis of ICOS and mCherry expression in doxycycline-induced HeLa reporter cells after siRNA knockdown of FBXL14, RAB40C, RNF222 or TRIM6-TRIM34 (red population) compared to a non-targeting siRNA (black population). **(B)** Flow cytometric analysis of ICOS and Thy1.1 expression in Rc3h1/2<sup>-/-</sup> MEF cells upon overexpression of FBXL14, Rab40C, Rnf222 or TRIM6-TRIM34. Thy1.1 was used as a marker for retroviral transduction with the overexpression constructs. **(C)** Overexpression of candidates was performed as in **(B)**. Instead of Rc3h1/2<sup>-/-</sup> MEF cells, wt MEF cells with doxycycline-induced overexpression of Roquin-1 were used in order to assess the impact of candidate overexpression in the presence of Roquin-1.

Due to failure of the candidates to repress ICOS upon overexpression in our initial validation approach, the analysis was not further pursued. Instead, we proceeded with the customized RNAi screen.

#### 4.1.4.3 Screening of RBPs, P body-, stress granule- and mRNA decay-factors

Screening of the customized siRNA library targeting RBPs, P body-, stress granule- and mRNA decay-factors arrived at a hit rate of 5.5 %, similar to the smaller protein subset screens performed previously (Figure 17). In the resulting list of candidates, already established Roquin-1 interacting proteins were identified by eye and additional literature searches were aimed to select for further interesting hits. Two well-known candidates that are part of the mRNA decapping- and deadenylation pathways, the enhancer of decapping EDC4 and the scaffolding subunit of the deadenylation complex CNOT1, scored positively, thereby confirming that the screen was able to identify candidates in the pathway of Roquin-mediated post-transcriptional gene regulation (Glasmacher et al., 2010; Leppek et al., 2013). Yet, the RNase REGNASE-1, the only RBP that has been described as a cofactor of Roquin-1 in the literature so far (Jeltsch et al., 2014) was not identified.

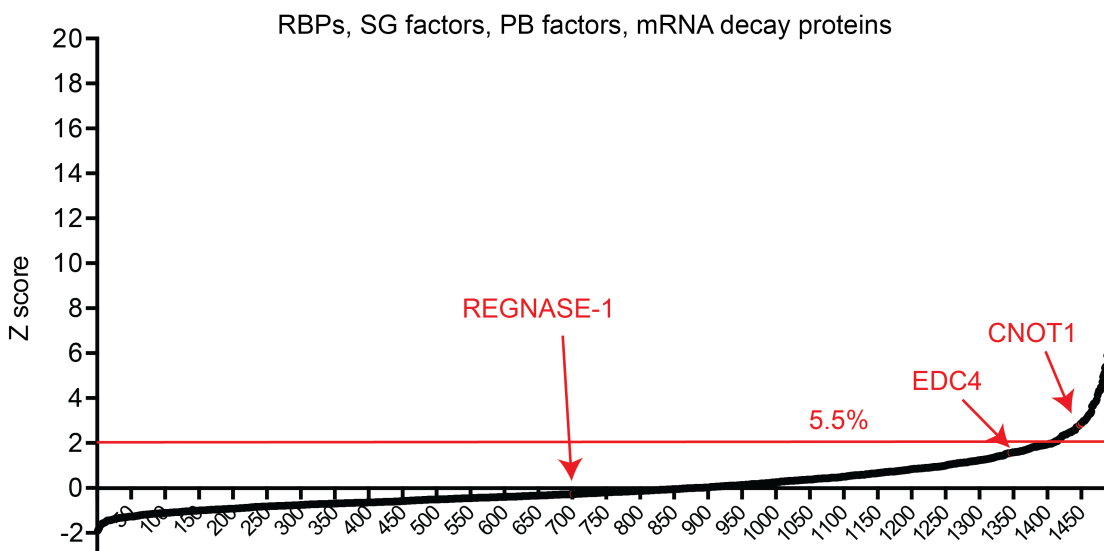


**Figure 17: Screening of a customized siRNA library targeting RBPs and factors of mRNA decay.**

Normalized screen data of the customized siRNA library for Roquin-1 cofactors. HeLa reporter cells were transfected with siRNA pools in duplicates. 48 h after transfection, Roquin-1-overexpression was induced with doxycycline for 18 h. Cells were harvested, barcoded and four wells were combined into one for ICOS staining and data acquisition. After deconvolution, average ICOS MFI of each sample was normalized into a Z score based on plate mean and SD. Ranked Z scores are shown for each siRNA pool. Each data point with an average Z score > 2 was considered a hit. Known cofactors of Roquin-1 are indicated in red.

Regnase-1 was recently shown to be indispensable for Roquin-1-mediated repression of a minimal response element from *TNF*, the most 3' 260 nts of its 3' UTR (termed CDE260) (Figure 18A). Moreover, Regnase-1 overexpression in MEF cells downregulated *ICOS* suggesting a cooperation of both proteins also on this 3'UTR (Jeltsch et al., 2014).

#### **4.1.5 Regnase-1 is dispensable for Roquin-1-mediated regulation of *ICOS***

We investigated whether Regnase-1 is similarly important for Roquin-1-mediated repression of *ICOS* as it is for *TNF* mRNA. Specifically, *Rc3h1/2<sup>-/-</sup>* MEF cells and MEF cells, which are deficient for Regnase-1 (*Zc3h12a<sup>-/-</sup>* MEF cells), were transduced with reporter constructs consisting of the *ICOS* CDS followed by either the *TNF* CDE260 or the complete 3' UTR of *ICOS* (Figure 18A and B) as used in the RNAi screen. Subsequently, the cells were superinfected with retroviruses encoding Roquin-1 or Regnase-1. Reporter expression was measured using flow cytometry. The *ICOS* mean fluorescence intensity (MFI) was normalized to the MFI of the uninfected control cells (Figure 18C). Regnase-1-mediated regulation of the CDE260 reporter was almost completely abolished in *Rc3h1/2<sup>-/-</sup>* MEF cells, while reconstitution with Roquin-1 led to a 10-fold repression of reporter expression (Figure 18C). Vice versa, overexpressed Roquin-1 was unable to repress the CDE260 reporter in the absence of endogenous Regnase-1 in *Zc3h12a<sup>-/-</sup>* MEF cells, while reconstitution with Regnase-1 led to a rescue of reporter regulation. Thus, overexpressed Regnase-1 and Roquin-1 require endogenous amounts of each other for the repression of the CDE260 reporter from the *TNF* 3' UTR.

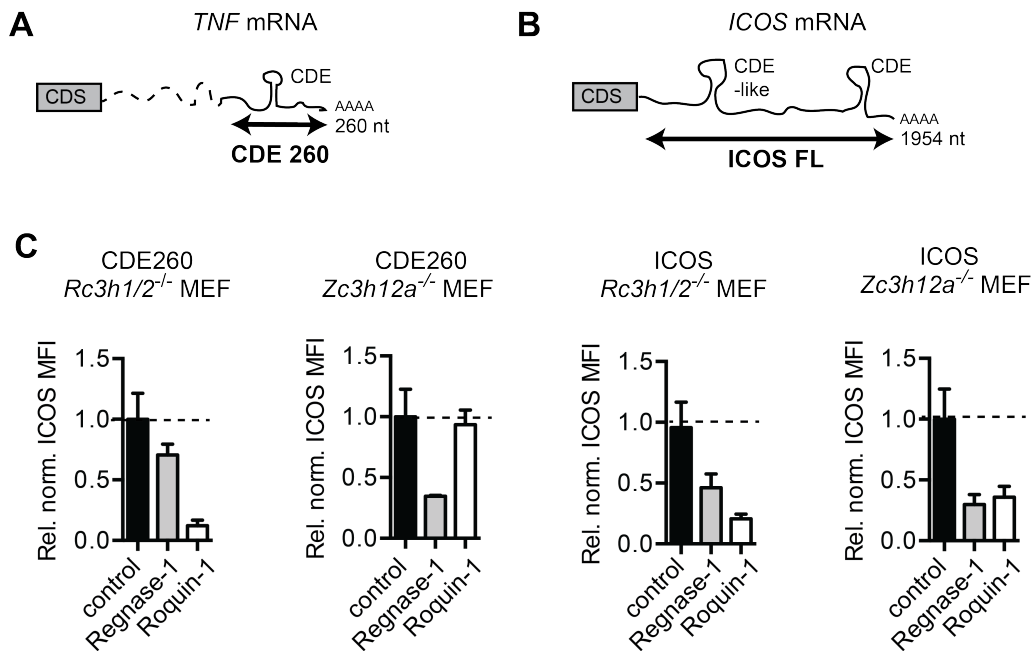


**Figure 18: Analysis of post-transcriptional regulation of the TNF CDE260 or full-length ICOS by Roquin-1 and Regnase-1.**

**(A)** Schematic representation of the TNF mRNA. The CDE260 reporter element comprises the most 3' 260 nts of the TNF 3' UTR, including the constitutive decay element (CDE) stem-loop that is recognized by Roquin-1. **(B)** Schematic representation of ICOS mRNA used as a reporter in the RNAi screen including the ~2 kb long 3' UTR. **(C)** *Rc3h1/2<sup>-/-</sup>* or *Zc3h12a<sup>-/-</sup>* MEF cells were transduced with the CDE260 or ICOS 3' UTR reporters that were cloned downstream of the CDS of ICOS. The cells were superinfected with Roquin-1 or Regnase-1 encoding retroviruses and ICOS expression was analyzed by flow cytometry after 48 h. ICOS MFI of each sample was normalized to the average of the uninfected control. This data set was provided by Dr. Sven Brenner.

Analyzing the 3' UTR of ICOS on the other hand showed that the respective reporter could be repressed by Regnase-1 in *Rc3h1/2<sup>-/-</sup>* MEF cells to at least twofold. Most importantly however, Roquin-1 was able to strongly repress ICOS in *Zc3h12a<sup>-/-</sup>* MEF cells in the absence of Regnase-1, indicating that Roquin-1 and Regnase-1 can also work independently of each other on certain target transcripts, such as ICOS. This result clearly demonstrates that Regnase-1 is unlikely to be an essential cofactor of Roquin-1 under the conditions used in the screen and hence cannot be expected among the candidate genes of the target list.

#### 4.1.6 Establishment of a target list of candidate genes

29 candidates arising from the primary customized screen (Figure 17) with a Z score > 2 and with an mCherry expression that was not more than threefold reduced as compared to the non-targeting control are listed in Table 27. Within each group of genes (indicated by different shades of gray) candidates were ranked according to the

increase in ICOS expression (ICOS MFI) that was observed upon siRNA knockdown. Known regulators (CNOT1, EDC4) as well as positive (Rc3h1) and negative (Ctrl) controls were included as references.

**Table 27: Ranked candidate list of the customized siRNA screen.**

Gene name	Gene ID	Gene subset	ICOS MFI
YTHDC2	64848	RNA-binding protein	275
TRUB1	142940	RNA-binding protein	228
STAU1	6780	RNA-binding protein	182.5
TES	26136	RNA-binding protein	167.5
SF1	7536	RNA-binding protein	166
ZC3H10	84872	RNA-binding protein	160
GTF2E2	2961	RNA-binding protein	159
NUFIP2	57532	RNA-binding protein	157.5
RPGR	6103	RNA-binding protein	154.8
TNRC6A	27327	RNA-binding protein	154.5
PTBP2	58155	RNA-binding protein	149
ZYX	7791	RNA-binding protein	125
DYNC1H1	1778	RNA-binding protein	113.5
WDR6	11180	RNA-binding protein	110
SARS	6301	RNA-binding protein	103.65
CSTF3	1479	RNA-binding protein	216.5
GTF2H3	2967	RNA-binding protein	173
C2orf60	129450	RNA-binding protein	166.5
SNRPN	6638	RNA-binding protein	164.5
DHFR	1719	RNA-binding protein	129
HEXIM2	124790	RNA-binding protein	127
SF4	57794	RNA-binding protein	118.5
DDX11	1663	RNA-binding protein	97.2
AGL	178	P body formation	99.2
ATP2A1	487	Stress granule formation	291
C9ORF115	138428	Stress granule formation	136.5
PLAUR	5329	Stress granule formation	127
SFRS2B	10929	Stress granule formation	117
EIF3S7	8664	Stress granule formation	106.6
Roquin-1		Positive control	279.5
CNOT1	23019	Validated cofactor	136.5
EDC4	23644	Validated cofactor	108
Ctrl	-	Non-targeting control	38.1

23 proteins were derived from the subset of RNA-binding proteins, whereas only one P body factor and five stress granule factors made it into the list of new potential cofactors of Roquin-1-mediated *ICOS* repression.

#### **4.1.7 Deconvolution of siRNA pools identifies false positive hits**

For further validation 14 RNA-binding candidates with a high derepression of *ICOS* were chosen from Table 27. As already performed for candidates arising from the ubiquitin conjugation screen (Chapter 4.1.4.2), our primary validation approach was cloning and overexpression of the selected candidates in an *ICOS* reporter cell line, expecting further downregulation of *ICOS* after candidate overexpression. 12 RBP candidates were successfully cloned and overexpressed in the exact HeLa reporter cell line of the screen. However, as observed before (Figure 16), none of the candidates could downregulate *ICOS* (Appendix I). This approach was consequently dropped for multiple reasons. First of all, although Thy1.1 was used as a marker for retroviral infection, this does not guarantee that the candidate protein is likewise expressed and functional. For confirmation, one would have to establish immunoblotting assays for each single candidate, which is both expensive and time-consuming. Furthermore, even if candidate overexpression was successfully accomplished, it is not guaranteed that increased levels of Roquin cofactors will lead to further downregulation of *ICOS*. When a candidate protein is highly expressed at endogenous levels, Roquin might already be saturated with this cofactor, so that its overexpression would not further contribute to *ICOS* repression. Overall, since cloning of multiple candidates demands high efforts, but the outcome of overexpression is rather uncertain, this method appeared to be not particularly suited for validation of primary screen candidates.

Since overexpression experiments had been unsuccessful, I decided to rather validate candidates by deconvoluting all siRNA pools and compare phenotypic effects with knockdown efficiencies for the individual siRNAs. This approach allows to discriminate between genuine hits and false positive results, since sequence-specific off-target effects are often caused by one individual siRNA in the pool, which can be identified by a low knockdown efficiency of the target mRNA in combination with an inexplicably strong phenotypic effect. The known cofactor *CNOT1* was included to serve as an internal positive control.

For *CNOT1* a clear correlation between knockdown efficiency and derepression of the *ICOS* reporter was observed. Each single siRNA of the pool led to a derepression of

*ICOS*, and the decrease of *CNOT1* mRNA correlated inversely with *ICOS* levels (Figure 19). This confirmed that *CNOT1* was indeed a positive control in the screen.

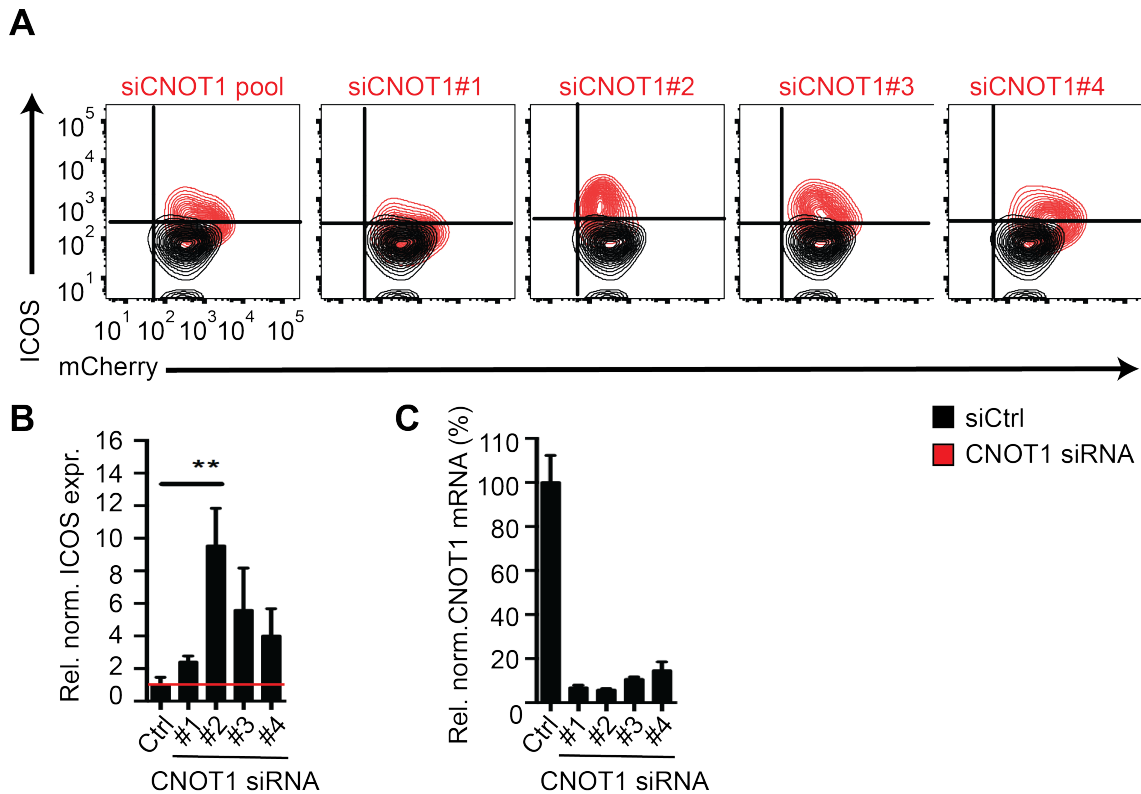


**Figure 19: Deconvolution of the *CNOT1* siRNA pool confirms its role as an internal positive control of the siRNA screen.**

**(A)** Flow cytometric analysis of *ICOS* and *mCherry* expression in HeLa reporter cells after doxycycline-induction of *Roquin-1*. Cells were treated with the *CNOT1*-targeting siGENOME siRNA pool used in the screen or the four individual siRNAs as indicated (red population). For comparison, cells treated with a non-targeting control siRNA are shown in black. **(B)** Quantified *ICOS* MFI shown in **(A)**. Expression was normalized to the average of the non-targeting control, which was set to 1. **(C)** qPCR analysis of *CNOT1* mRNA expression in cells from **(A)**. Expression was calculated relative to the housekeeping gene *YWHAZ* and normalized to the average of the non-targeting control. Shown is one representative of three independent experiments **(A)** or mean and standard deviation of three independent experiments **(B, C)**. Statistical significance in **(B)** was calculated with one-way Anova Kruskal-Wallis test followed by Dunn's multiple comparisons test (\*\* $p < 0.01$ ).

Of the remaining 13 candidates, surprisingly, 12 did not pass this primary validation step. Regularly, one single siRNA was identified to dominate the performance of the siRNA pool, which potentially reflects the result of an off-target effect (Appendix II). For five candidates, two out of four individual siRNAs were phenotypically effective, but their knockdown efficiency did not correlate well with the effect on *ICOS* expression (Appendix III). One representative of this group was the mammalian *TNRC6A*, also known as *GW182*. The mammalian *TNRC6A* and its paralogs *TNRC6B*

and TNRC6C play an important role in miRNA-induced gene repression (Chapter 1.1.3). They are recruited to target mRNAs to induce translational inhibition and deadenylation-dependent mRNA decay (Chapter 1.1.1)(Lazzaretti et al., 2009). It was recently reported that Roquin-1 directly interacts with the RISC component Ago2 on the mouse *Icos* 3' UTR (Srivastava et al., 2015), proposing that Roquin-1 might induce deadenylation-dependent mRNA decay via the miRNA pathway of gene silencing. These findings make TNRC6A an attractive potential cofactor of Roquin-1, warranting further investigations.

HeLa reporter cells were treated either with the TNRC6A-targeting pool of four siRNAs or with each individual siRNA prior to induction of Roquin-1-overexpression (Figure 20A). Flow cytometric analysis of ICOS and mCherry expression clearly showed that the derepression of ICOS in response to TNRC6A knockdown with the siRNA pool was mediated by two individual siRNAs, siTNRC6A#2 and siTNRC6A#3, with #3 causing the strongest increase in ICOS levels (Figure 20A, B). However, mCherry expression, which was only slightly reduced after knockdown with the siRNA pool, was strongly reduced in response to treatment with siRNA#3, indicating decreased expression of Roquin-1-P2A-mCherry. This effect was obviously masked in the pool by the two other, non-responsive siRNAs. qPCR analysis of TNRC6A mRNA expression revealed a strong knockdown of TNRC6A expression with siRNA#2 and siRNA#4, while the functionally most effective siRNA#3 showed no reduction of mRNA expression at all (Figure 20C). Since TNRC6A, -B and -C are closely related, we wondered whether the strong phenotypic effect of siTNRC6A#3 could be explained by an off-target knockdown of TNRC6B and TNRC6C. This has been observed before for the septin protein family (Sharma et al., 2013). Before examining off-target effects of TNRC6A-targeting siRNAs on other family members, the expression levels of TNRC6A, TNRC6B and TNRC6C were determined in HeLa cells (Figure 20D). TNRC6A was most prominently expressed, followed by TNRC6B. Since TNRC6C showed a 10-fold lower expression as compared to its family members, we evaluated off-target effects of TNRC6A knockdown on TNRC6B only. Of note, none of the TNRC6A-targeting siRNAs caused a decrease in TNRC6B expression. In line with this, sequence alignment of the TNRC6A-targeting siRNAs showed frequent seed-sequence matching, but no full complementarity of any individual TNRC6A-targeting siRNA with TNRC6B mRNA. This experiment clearly indicates that TNRC6A-targeting siRNAs are well designed and cause no off-target knockdown of the paralog TNRC6B. Since the results of siRNA deconvolution were inconclusive at best, TNRC6A was not evaluated any further.

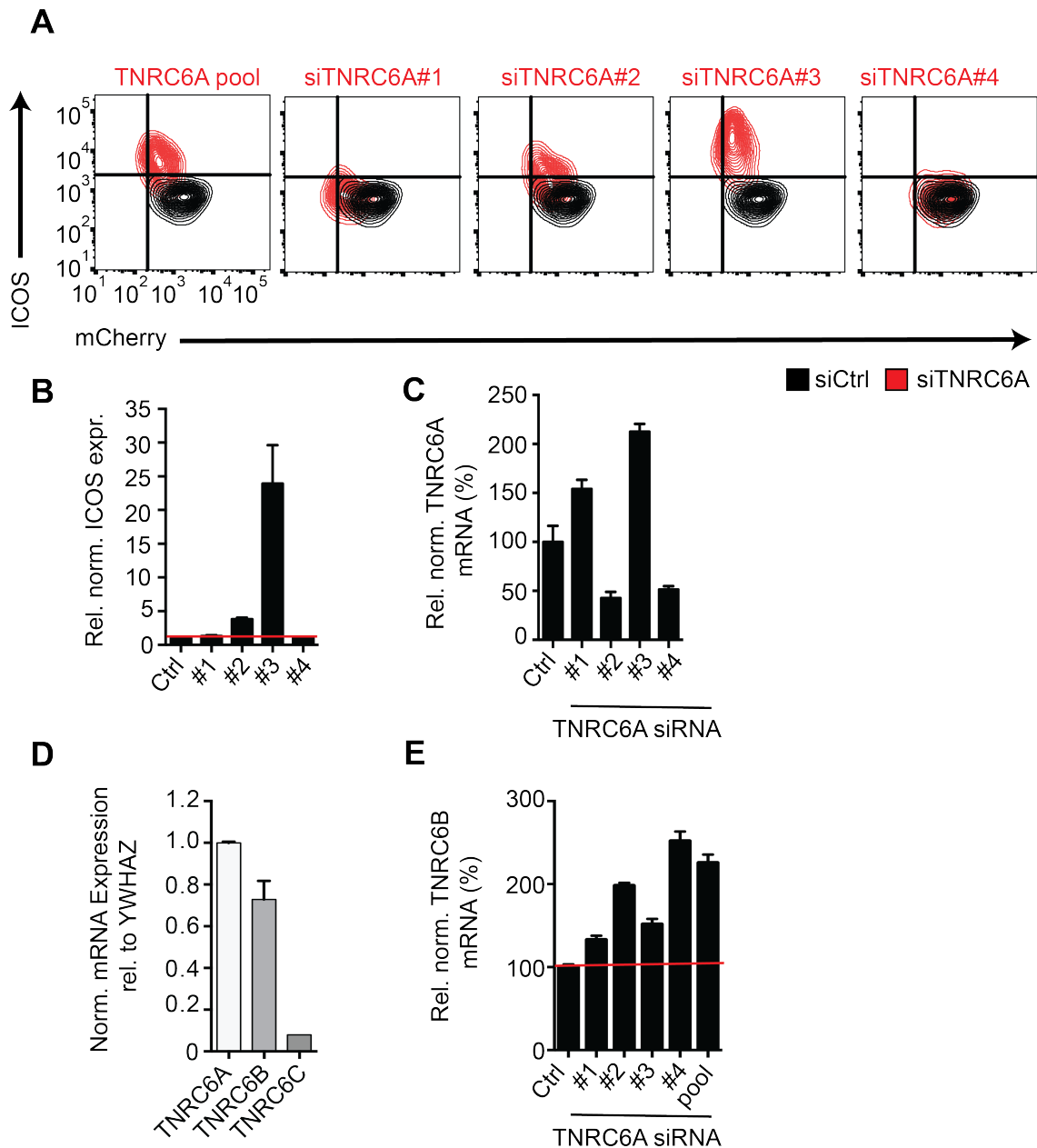


**Figure 20: Deconvolution of siRNA pools identifies TNRC6A as a false positive hit.**

**(A)** Flow cytometric analysis of ICOS and mCherry expression in HeLa reporter cells after doxycycline-induction of Roquin-1. Cells were treated with the TNRC6A-targeting siRNA pool used in the screen or the four individual siRNAs as indicated (red population). Cells treated with a non-targeting control siRNA are shown in black. **(B)** Quantified ICOS MFI shown in **(A)**. Expression was normalized to the average of the non-targeting control, which was set to 1. **(C)** qPCR analysis of TNRC6A mRNA expression in cells from **(A)**. Expression was calculated relative to the housekeeping gene YWHAZ and normalized to the average of the non-targeting control. **(D)** qPCR analysis of TNRC6A, TNRC6B and TNRC6C mRNA expression in wt HeLa cells. mRNA expression relative to YWHAZ was calculated with the  $\Delta\Delta C_t$  method using the primer efficiencies determined with standard curves. **(E)** qPCR analysis of TNRC6B mRNA expression in cells from **(A)**. Error bars show standard deviation of two **(B, C)** independent experiments or two technical replicates **(D, E)**.

Apart from CNOT1, flawless results for four individual siRNAs were only obtained for one more candidate: the NUFIP2 protein. Similar to CNOT1, most individual NUFIP2-targeting siRNAs caused strongly derepressed ICOS, except for siRNA#3, which however also showed the lowest knockdown efficiency (Figure 21).

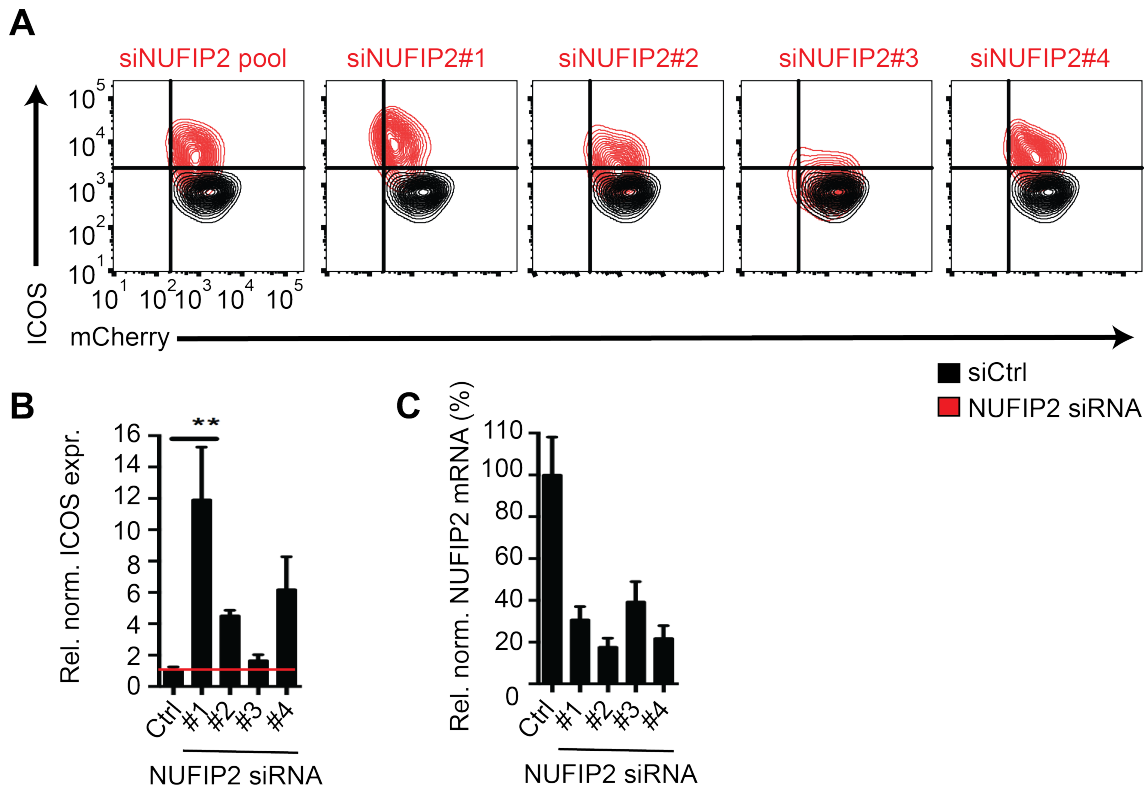


**Figure 21: Deconvolution of the NUFIP2 siRNA pool shows a strong correlation between ICOS derepression and knockdown of NUFIP2 mRNA.**

**(A)** Flow cytometric analysis of ICOS and mCherry expression in HeLa reporter cells after doxycycline-induction of Roquin-1. Cells were treated with the NUFIP2-targeting siGENOME siRNA pool used in the screen or the four individual siRNAs as indicated (red population). For comparison, cells treated with a non-targeting control siRNA are shown in black. **(B)** Quantified ICOS MFI shown in **(A)**. Expression was normalized to the average of the non-targeting control, which was set to 1. **(C)** qPCR analysis of NUFIP2 mRNA expression in cells from **(A)**. Expression was calculated relative to the housekeeping gene YWHAZ and normalized to the average of the non-targeting control. Shown is one representative of three independent experiments **(A)** or mean and standard deviation of three independent experiments **(B, C)**. Statistical significance in **(B)** was calculated with one-way Anova Kruskal-Wallis test followed by Dunn's multiple comparisons test (\*\*p < 0.01).

ICOS derepression caused by knockdown of NUFIP2 with the siRNA pool was highly significant and even outperformed the effect of CNOT1 (Figure 22A). The knockdown efficiency of the NUFIP2 siRNA pool was close to 90 % on the mRNA level (Figure 22B). For validation of NUFIP2 protein knockdown, a NUFIP2 immunoblotting assay was established using a commercially available polyclonal anti-NUFIP2 antibody.

Immunoblotting confirmed the decrease of protein expression in agreement with the qPCR analysis (Figure 22C).

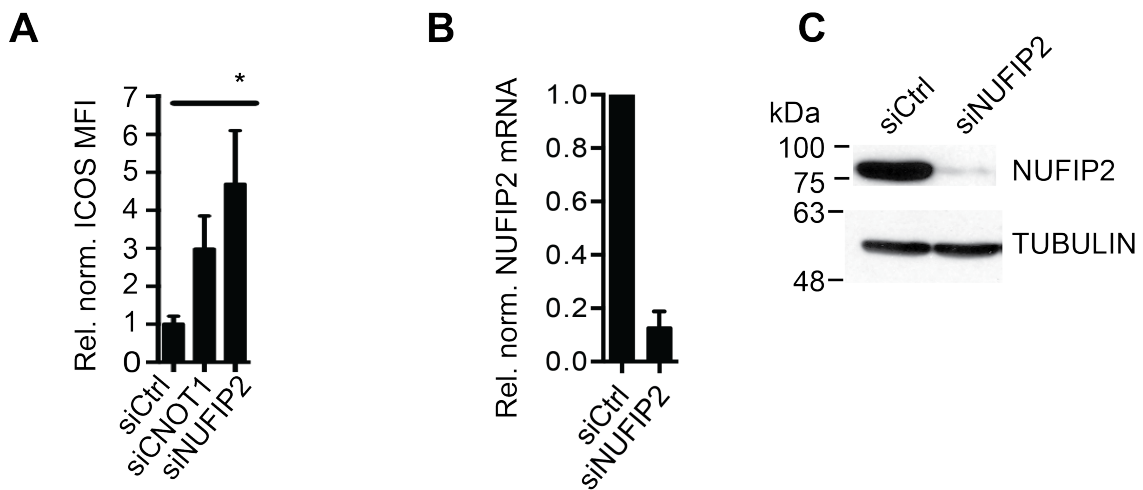


**Figure 22: Knockdown of NUFIP2 leads to a strong derepression of ICOS.**

**(A)** Quantified mean fluorescence intensity (MFI) of ICOS expression after siRNA knockdown of NUFIP2 and CNOT1 in HeLa reporter cells. Cells were treated with siGENOME siRNA pools, and ICOS expression was determined by flow cytometry. **(B)** qPCR analysis of NUFIP2 mRNA expression in HeLa reporter cells after treatment with the siGENOME NUFIP2 siRNA pool. Expression relative to the housekeeping gene YWHAZ was normalized to the non-targeting control **(C)** Immunoblot analysis of NUFIP2 expression in HeLa reporter cells upon NUFIP2 knockdown. Error bars represent mean and SD of three **(A)** and two **(B)** independent experiments. In **(C)** one representative of two independent experiments is shown. Statistical significance in **(A)** was calculated with one-way Anova Kruskal-Wallis test followed by Dunn's multiple comparisons test ( $*p < 0.05$ ).

Overall, siRNA deconvolution allowed the discrimination between true hits and off-target effects and identified NUFIP2 as the sole remaining RNA-binding candidate from our customized RNAi screen. For validation of candidates from one of the six protein subset screens performed before, siRNA deconvolution should therefore be the method of choice. Employing it on selective candidates arising from the protein kinase screen identified two kinases, PI4KA and STK38, for which a strong positive correlation between knockdown efficiency and the phenotypic effect is seen with multiple individual siRNAs (Appendix IV). This confirms that siRNA deconvolution is the best way of identifying promising candidates for follow-up validation. NUFIP2 from the RBP subset was subsequently chosen for functional validation. The strong ICOS derepression after NUFIP2 knockdown and the fact that it is an RNA-binding of unknown function with only three references in the literature made it a perfect candidate for further exploration.

## 4.1.8 Functional validation of NUFIP2 as a cofactor of Roquin

### 4.1.8.1 Rescue through expression of siRNA-resistant NUFIP2

In order to unambiguously prove that the strong derepression of *ICOS* in response to *NUFIP2* knockdown in HeLa cells was indeed caused by a loss of NUFIP2 function, a NUFIP2 expression construct was designed to contain six silent mutations rendering it immune to siRNA (siNUFIP2#2) targeting (Figure 23).

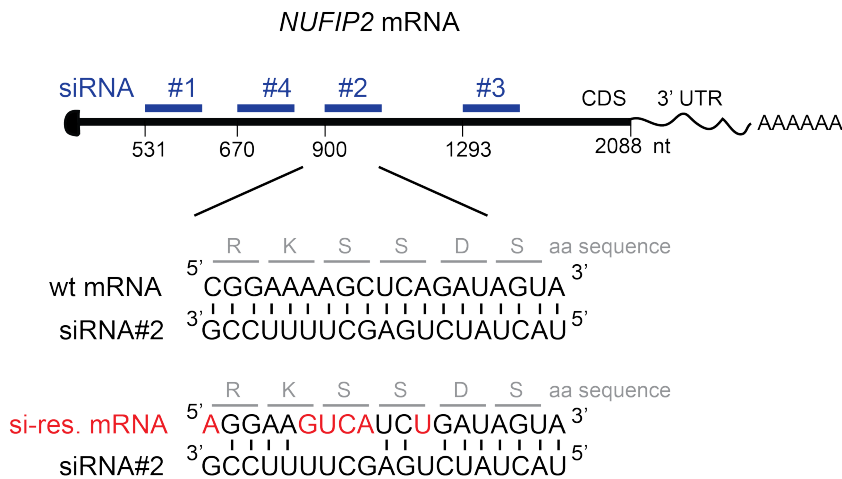


**Figure 23: Generation of *NUFIP2*-targeting siRNA#2 resistant *NUFIP2* cDNA.**

Schematic representation of the target sites of *NUFIP2*-targeting siRNAs #1-4 (blue) in the coding sequence (CDS) of *NUFIP2* mRNA. Six silent mutations (red) were inserted into the *NUFIP2* cDNA sequence to create an siRNA#2-resistant (si-res.) *NUFIP2* overexpression construct. The amino acid (aa) sequence was not altered (shown in grey).

HeLa reporter cells with stable *ICOS*- and doxycycline-inducible Roquin-1-P2A-mCherry expression were retrovirally transduced to express siNUFIP2#2-resistant GFP-NUFIP2 or GFP as a control. Immunoblot analysis of NUFIP2 levels confirmed overexpression of GFP-NUFIP2 as well as the presence of endogenous NUFIP2 (Figure 24A). GFP- or GFP-NUFIP2-overexpressing cells were subsequently treated with siNUFIP2#2, siNUFIP2#4 or non-targeting control siRNAs, and *ICOS* and GFP expression were measured by flow cytometry after doxycycline-induced Roquin-1 overexpression. *ICOS* expression was analyzed after gating on populations of low, intermediate and high GFP expression for each sample (Figure 24B). *ICOS* MFI's of siNUFIP2-treated samples were normalized to the MFI's of samples treated with non-targeting controls (Figure 24C, D). A 4-fold increase of *ICOS* expression was observed after NUFIP2 knockdown with siRNA#2, which was rescued by the overexpression of siRNA#2-resistant GFP-NUFIP2 (Figure 24C).

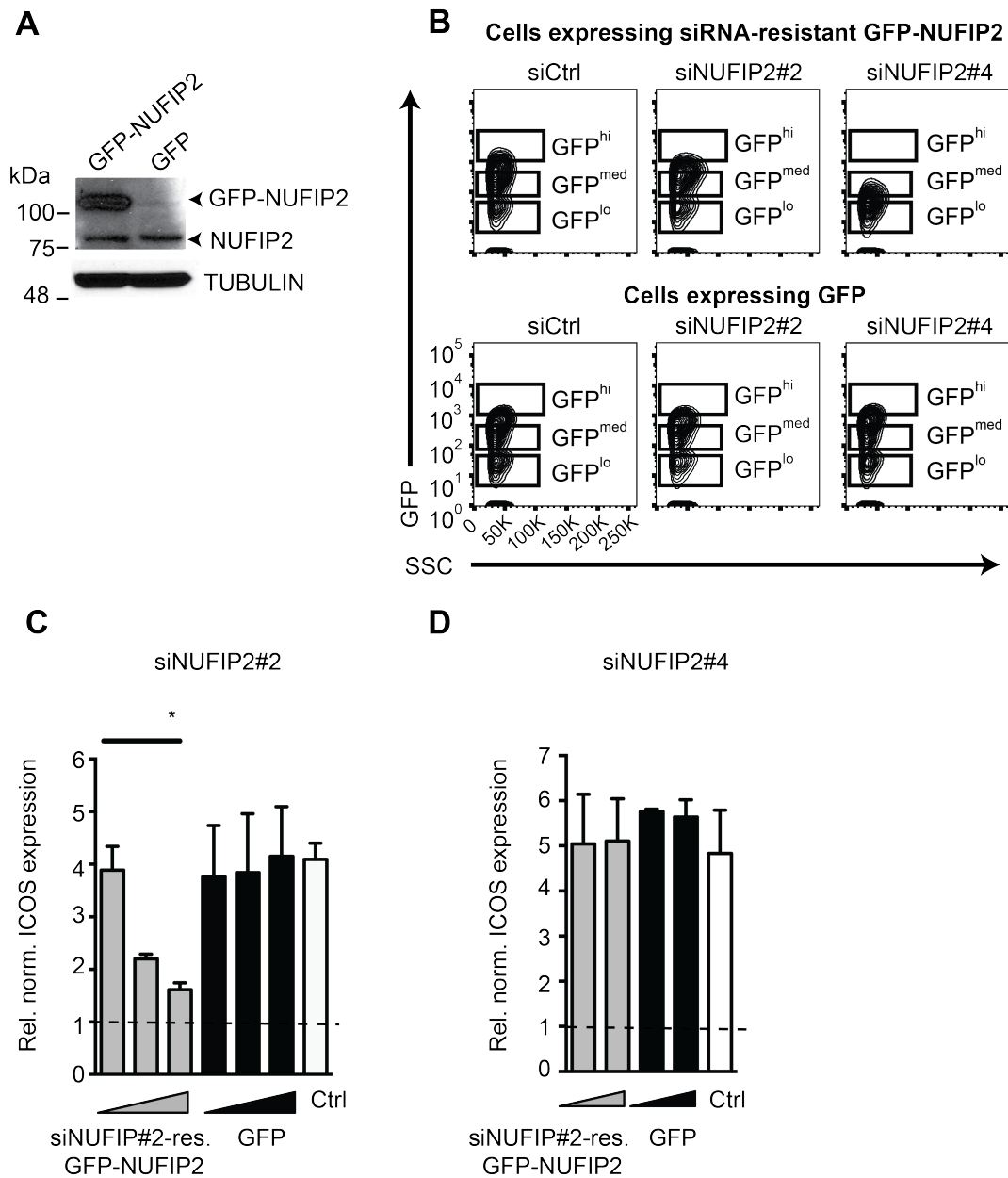


**Figure 24: Overexpression of siRNA-resistant NUFIP2 rescues ICOS repression.**

**(A)** Immunoblot analysis of NUFIP2 expression in whole cell lysates from HeLa cells retrovirally transduced to express siNUFIP2#2-resistant NUFIP2 or GFP. Analysis was performed using bulk populations prior to siRNA knockdown. **(B)** Flow cytometric analysis of GFP expression in HeLa reporter cells with stable ICOS and doxycycline-inducible Roquin-1-P2A-mCherry expression after retroviral overexpression of siNUFIP2#2-resistant GFP-NUFIP2 or GFP. Gates for GFP-high (GFP<sup>hi</sup>), -intermediate (GFP<sup>int</sup>) or -low (GFP<sup>lo</sup>) expressing cells are indicated. **(C)** Quantified ICOS expression of siNUFIP2#2 targeted GFP<sup>lo</sup>, GFP<sup>int</sup> and GFP<sup>hi</sup> populations from **(B)**. ICOS MFI of each GFP-expressing population of NUFIP2-siRNA#2 treated cells was normalized to ICOS MFI in the same population of cells treated with a non-targeting control (siCtrl), which was set to 1. **(D)** Quantified ICOS expression of siNUFIP2#4 targeted GFP<sup>lo</sup> and GFP<sup>med</sup> populations from **(B)**. ICOS MFI of each GFP-expressing population of NUFIP2-siRNA#4 treated cells was normalized to ICOS MFI in the same population of cells treated with a non-targeting control (siCtrl), which was set to 1. **(B)** shows one representative of three independent experiments, **(C)** and **(D)** show mean and standard deviation of three independent experiments. Statistical significance in **(C)** was calculated with one-way Anova Kruskal-Wallis test followed by Dunn's multiple comparisons test (\* $p < 0.05$ ).

The rescue effect occurred in a concentration-dependent manner. In the cells with the strongest GFP-NUFIP2 expression, ICOS expression almost reached the level of the non-targeting control, indicating that Roquin-1-dependent post-transcriptional regulation of ICOS was completely restored. Overexpression of GFP alone did not rescue ICOS regulation, even at high expression levels. When NUFIP2 knockdown was performed with siRNA#4 instead of siRNA#2, overexpressed siNUFIP2#2-resistant GFP-NUFIP2 was obviously silenced, resulting in a loss of GFP<sup>hi</sup>-expressing cells (Figure 24B, upper right). Quantification of ICOS expression in the remaining GFP-low and -intermediate expressing populations showed no impact of GFP-NUFIP2 on derepressed ICOS levels (Figure 24D) neither did GFP in the cells transduced with the GFP-control.

#### 4.1.8.2 Rescue of Roquin-1-mediated ICOS repression in *Nufip2*<sup>-/-</sup> MEF cells

As a final proof that loss of *Nufip2* leads to inhibition of ICOS repression, the CRISPR/Cas9 gene editing system was employed to generate a pool of *Nufip2* knockout cells. The CRISPR/Cas9 system makes use of single guide RNAs (sgRNAs) to direct the endonuclease Cas9 to a genomic locus of interest, where it induces double strand breaks (Chapter 1.2.2). These are usually repaired by non-homologous end-joining (NHEJ), an error-prone mechanism that often causes untemplated insertions or deletions (indels) of nucleotides and consequently the disruption of the reading frame of the target gene (Jinek et al., 2013). It is thus a useful tool to generate *Nufip2*-deficient MEF cells.

Four different sgRNAs were designed to target the second exon of the *Nufip2* gene locus. Along with two non-targeting sgRNAs, the four *Nufip2*-targeting sgRNAs were cloned into the lentiCRISPR vector, which additionally contains an open reading frame to express a humanized, nuclear localization signal (NLS)-bearing Cas9 gene. The knockout efficiency of each sgRNA was first tested in wildtype MEF cells (Figure 25A). All sgRNAs caused a reduction in *Nufip2* protein expression as analyzed by immunoblot analysis, with sgRNA#4 causing the most efficient knockout of *Nufip2* expression (Figure 25A). Figure 25B shows the targeting strategy of sgRNA#4.

In a second step *Rc3h1/2*<sup>fl/fl</sup> *Cre* *ERT2* MEF cells, a cell line in which endogenous Roquin-1 and -2 can be deleted by 4-OH-tamoxifen-induced nuclear translocation of a Cre recombinase, were lentivirally transduced to transcribe the mouse *Nufip2*-targeting sgRNA#4 and Cas9. Disruption of the *Nufip2* coding sequence resulted in an

approximately 70-80 % reduction of Nufip2 protein levels in the bulk cell populations, as judged by immunoblotting (Figure 25C). It should be mentioned here that the results of Nufip2 knockdown (Figure 22C) and -knockout (Figure 25C) may appear similar while they are not. siRNA-mediated knockdowns usually reduce the levels of the targeted protein in all cells similarly. This may not be sufficient to detect the anticipated phenotype, because the cellular mechanism of interest might also work with decreased protein levels. However, if the knockdown was sufficient to cause a phenotypic effect, this should equally affect all cells in the pool. In contrast, sgRNAs either lead to double strand breaks or do not. This means that in the cells in which the sgRNA was effective to generate a knockout, the anticipated phenotype can definitely be observed if present, but wildtype cells in the bulk population may mask the effect.

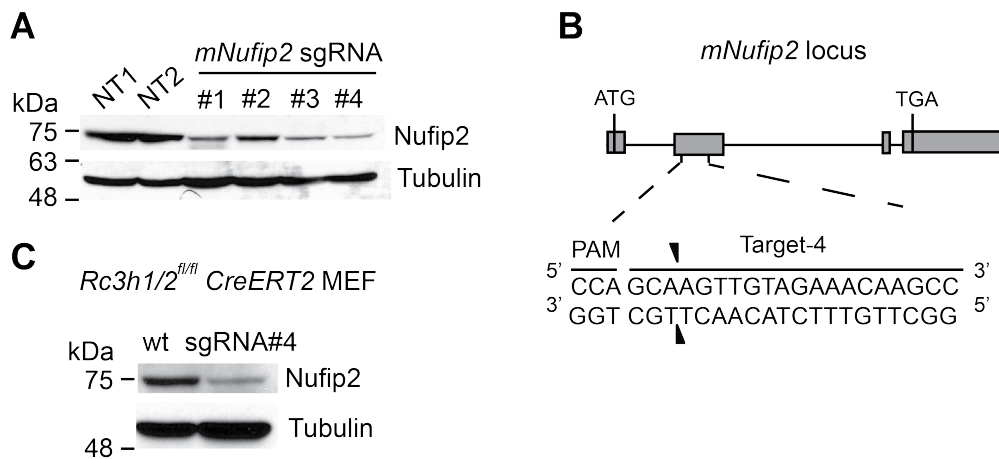


**Figure 25: Generating Nufip2 knockout MEF cells using the CRISPR/Cas9 system.**

**(A)** Immunoblot analysis of Nufip2 expression in whole cell lysates from wildtype MEF cells after transduction with lentiCRISPR-encoded Cas9 nuclease and different Nufip2-targeting sgRNAs or non-targeting controls (NT1, NT2). Whole cell lysates were prepared 10 days after transduction to provide time for the gene editing process to take place. **(B)** Schematic representation of mNufip2 sgRNA#4 targeting its complementary genomic sequence in the second exon of Nufip2. Cas9 nuclease binds the sgRNA and subsequently cleaves both strands of the genomic DNA, leading to NHEJ, indels and finally gene inactivation (Mali et al., 2013). Exons are depicted as grey boxes, whereas introns are indicated by black lines. **(C)** Immunoblot analysis of Nufip2 expression in whole cell lysates from Rc3h1/2<sup>fl/fl</sup> CreERT2 MEF cells that were transduced with lentiCRISPR mNufip2 sgRNA#4 or left untransduced.

In order to perform rescue experiments with this pool of Nufip2 knockout cells, I cloned an sgRNA-resistant NUFIP2 cDNA. Since the lentiCRISPR vector sequence stably integrates into host genomes, the cell pool will maintain sgRNA- and Cas9 expression throughout the whole experiment, thereby cleaving any Nufip2 DNA sequence that resembles the genomic target sequence. To circumvent this problem,

the human NUFIP2 cDNA was used as a basis for the rescue construct, since it already contains natural mismatches to the mouse genomic sequence. Further silent mutations were introduced as depicted in Figure 26A to render the site immune against sgRNA#4/Cas9 recognition.

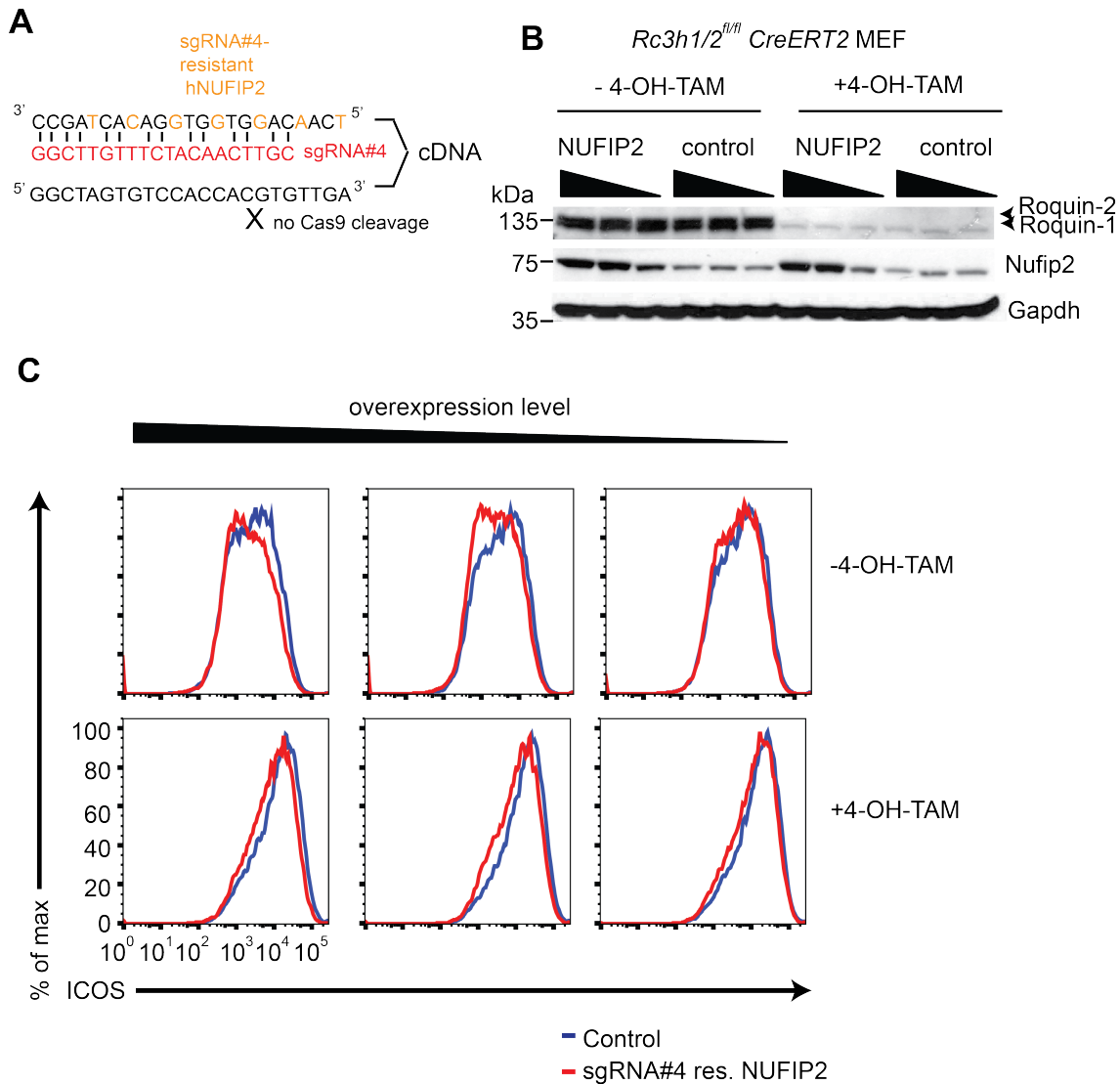


**Figure 26: Rescue of Roquin-1-mediated ICOS repression in Nufip2 knockout cells.**

**(A)** Schematic representation of mouse *Nufip2*-sgRNA#4-resistant human NUFIP2 cDNA sequence. Several mutations were introduced in order to prevent base pairing with sgRNA#4 and to protect the human cDNA sequence from Cas9 cleavage. Differences to the wildtype sequence are shown in orange. **(B)** Immunoblot analysis of Nufip2 and Roquin-1 expression in *Rc3h1/2<sup>fl/fl</sup> Cre ERT2* MEF cells that were first transduced with lentiCRISPR mNufip2 sgRNA#4 to knock out Nufip2 expression and then superinfected with different amounts of sgRNA#4-resistant NUFIP2 cDNA or an empty control vector. Cells were subsequently treated with 4-OH-tamoxifen (+4-OH-TAM) for 6 days to delete endogenous Roquin-1 and -2 expression or left untreated (-4-OH-TAM). **(C)** Flow cytometric analysis of ICOS expression in cells from **(B)**.

Bulk *Rc3h1/2<sup>fl/fl</sup> Cre ERT2* MEF cells transduced with lentiCRISPR mNufip2#4 as in Figure 25C were transduced with the complete sequence of *ICOS* mRNA as a reporter. Once stable *ICOS* expression was achieved, cells were superinfected with a retroviral vector encoding the sgRNA#4-resistant NUFIP2 or an empty control vector. Cells from each transduction were split into two pools, and were either left untreated or were treated with 4-OH-tamoxifen to induce deletion of *Rc3h1* and -2. Immunoblot analysis confirmed deletion of Roquin-1 and -2 in response to 4-OH-tamoxifen, as well as overexpression of NUFIP2 (Figure 26B). Flow cytometric analysis of *ICOS* expression in untreated cells showed a clear downshift of *ICOS* expression in response to overexpression of increasing amounts of NUFIP2, which was not seen for the empty vector control (Figure 26C). In cells where *Roquin-1* and -2 were deleted with 4-OH-tamoxifen, rescue of Nufip2 expression by overexpression of sgRNA-resistant NUFIP2 cDNA did not enhance post-transcriptional regulation of *ICOS*. These findings show that the effect of Nufip2 is dependent on the presence of Roquin-1, indicating that it is a true cofactor of Roquin-1 and not a regulator of *ICOS* that works independent of Roquin-1 function. The question whether the inhibitory effect of endogenous Roquin on *ICOS* is similarly dependent on Nufip2 could not be solved in this experiment. In Nufip2 knockout cells without the rescue construct (Figure 26C blue curves) *ICOS* was clearly upregulated in 4-OH-tamoxifen-treated cells compared to untreated cells, indicating that endogenous Roquin might still be able to repress *ICOS* in the absence of Nufip2. The Nufip2 knockout cell pool did, however, also contain cells where the CRISPR/Cas9 deletion of Nufip2 was not effective, as observed by detection of residual Nufip2 in protein lysates (Figure 25C), which might be responsible for Roquin being still able to regulate *ICOS* here. To solve this, we will use the pool to generate a clonal cell line where both Nufip2 alleles were deleted and repeat the experiment under complete knockout conditions.

The downshifts of *ICOS* expression upon re-expression of Nufip2 that were achieved with the CRISPR/Cas9 system were considerably smaller than observed in the RNAi rescue approach. In addition to the dependency of the repression on endogenous instead of overexpressed Roquin, this might as well be caused by those cells in the pool where Nufip2 was not deleted, and repetition of the experiment in a Nufip2 knockout clone might result in a stronger signal. Still, these findings confirmed Nufip2 as a Roquin cofactor because the rescue effect could also be achieved in a different species (mouse) and with a different method for Nufip2 depletion (CRISPR/Cas9 knockout versus siRNA knockdown).

#### 4.1.9 Characterization of the Roquin-1/Nufip2 interaction

Knowing that Nufip2 was important for Roquin-1-mediated repression of *ICOS* mRNA, we set out to explore its function in this pathway in more detail. Nufip2 is a hardly investigated protein, with only few references in the literature. It was identified in 2003 in a screening approach for interactors of the RNA-binding protein FMRP (Chapter 1.1.4.1), whose loss causes a severe mental retardation syndrome (Bardoni et al., 2003). As an unknown protein that interacted specifically with FMRP, but not with the highly homologous family members FXR1 and FXR2, and furthermore displayed the characteristic nuclear-/cytoplasmic expression pattern of FMRP, it was termed Nuclear FMRP Interaction Partner (NUFIP2).

RNA-binding ability was attributed to NUFIP2 due to its capability of binding polyadenylated RNA and its detection in polysomal fractions of sucrose gradients, which indicated an association with mRNA in polyribosomal ribonucleoprotein complexes (Bardoni et al., 2003). However, no RNA-binding domain or any other known functional protein domain was predicted from the primary amino acid sequence of NUFIP2 so far. Using the DisEMBL server (<http://dis.embl.de>) the prediction for NUFIP2 showed that large areas of the protein have a high probability of being intrinsically disordered (personal communication with Prof. Dr. Dierk Niessing), which is probably why no stable protein domains were identified so far. Our knowledge about the domain organization of NUFIP2 thus consists of an annotated histidine-rich region in the N-terminus and a serine-rich region in the middle of the protein ([www.uniprot.org](http://www.uniprot.org)). Additionally, the interaction with FMRP has been mapped to amino acid 255-411 of NUFIP2 (Figure 27) (Bardoni et al., 2003).

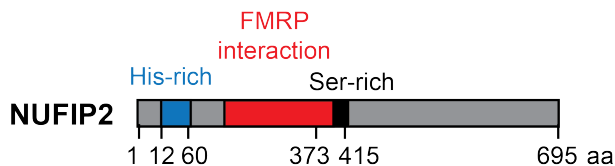


**Figure 27: Domain organization of NUFIP2.**

The domain organization of NUFIP2 is mostly unknown except for a histidine-rich (*his-rich*) region in the N-terminal part and a serine-rich region (*ser-rich*) in the middle of the protein. The amino acids 255-411 of NUFIP2 have been demonstrated to be crucial in its interaction with FMRP (Bardoni et al., 2003; Ramos et al., 2006).

#### 4.1.9.1 Investigating protein/protein interactions of Roquin-1 and Nufip2

We wanted to find out whether or not Nufip2 binds Roquin-1. For this purpose, NUFIP2 and GFP-Roquin-1 were overexpressed in HEK293T cells. In these experiments, NUFIP2 could be co-immunoprecipitated with GFP-Roquin-1 from cell lysates using anti-GFP antibodies (Figure 28A). The interaction was not sensitive to RNase treatment, indicating an RNA-independent protein/protein interaction. Yet, although unlikely, it cannot be excluded that both proteins recognize the same *cis*-element of one mRNA or two different *cis*-elements in close proximity to each other that may protect this short stretch of RNA from RNase activity.

In order to find out which domain in Roquin-1 mediates the interaction with NUFIP2, HEK293T cells were transfected with NUFIP2 and GFP-tagged Roquin-1 constructs that were either Roquin-1 full-length (FL), an N-terminal (aa 1-509) or a C-terminal (aa 509-1130) fragment of Roquin-1 (Figure 28B). Interestingly, only the N-terminal part of Roquin-1 was able to pull-down NUFIP2 (Figure 28C). It can thus be concluded that the interaction between Roquin-1 and Nufip2 is mediated by the RING finger, the ROQ/HEPN domain or the Zinc finger of Roquin-1. So far only the binding of the enhancer of mRNA decapping 4 (Edc4) has been mapped to the N-terminus of Roquin-1 (Glasmacher et al., 2010).

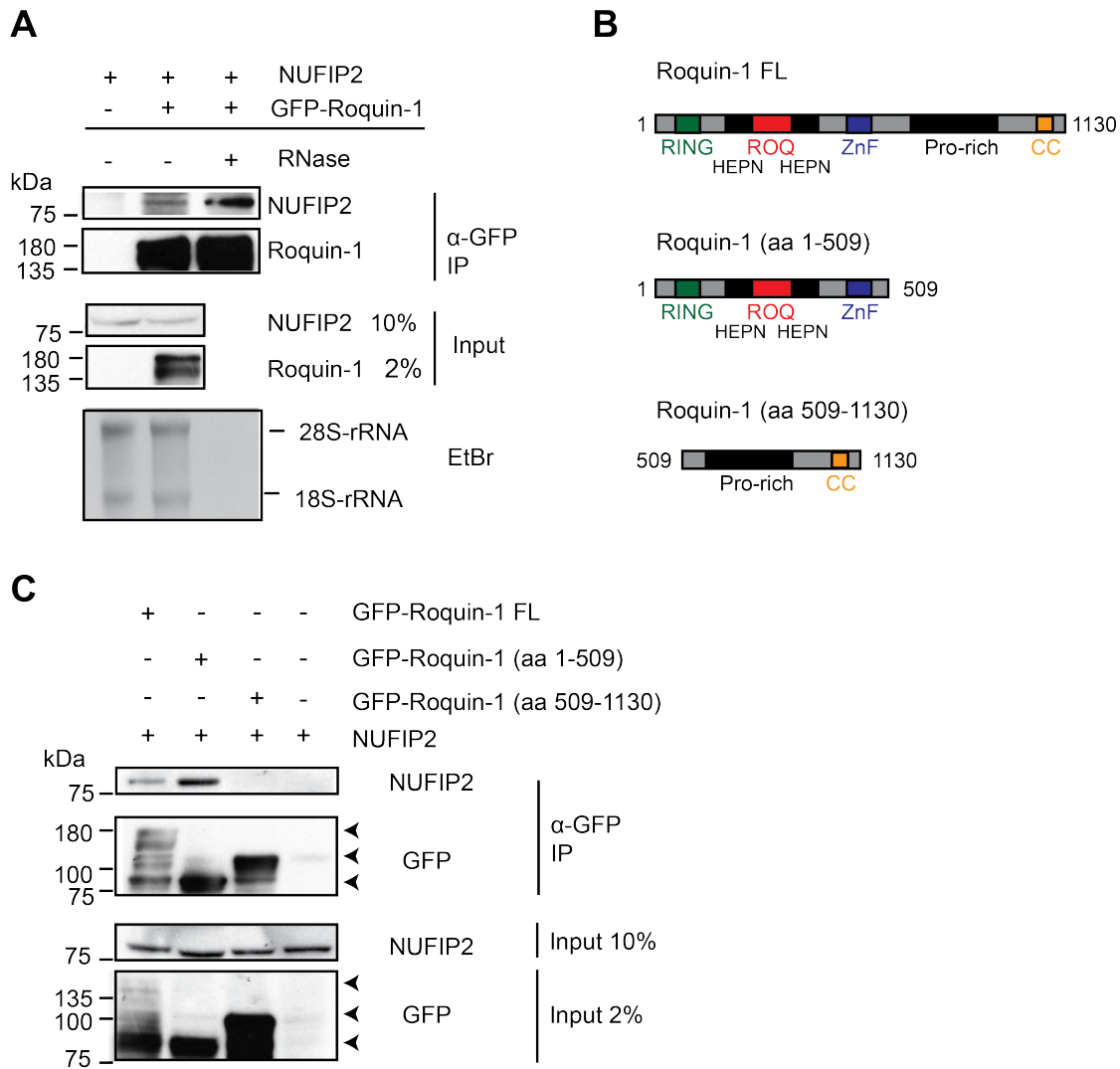


**Figure 28: NUFIP2 and Roquin-1 interact in an RNase-independent manner.**

**(A)** HEK293T cells overexpressing GFP-Roquin-1 and human NUFIP2 were lysed and the Roquin-1 fusion protein was immunoprecipitated using polyclonal anti-GFP antibodies. Immunoblot analysis of NUFIP2 and Roquin-1 after anti-GFP immunoprecipitation (IP) is shown. Samples were treated during immunoprecipitation with or without RNase as indicated. Efficient degradation of rRNA by RNase treatment was confirmed by Ethidium bromide staining of RNA extracts from IP supernatants. **(B)** Schematic representation of mouse Roquin-1 protein domains. Roquin-1 contains a RING finger with putative E3 ubiquitin ligase activity, the RNA-binding ROQ domain embedded in an amino- and a carboxy-terminal part of a HEPN domain, a CCCH-type Zinc finger (ZnF) with potential RNA-binding activity, and the proline-rich (pro-rich) and coiled-coil (CC) regions at the C-terminus, which may be involved in the protein/protein interactions with CCR4-NOT complexes (Schlundt et al., 2016). **(C)** Immunoblot analysis of NUFIP2 and GFP expression after immunoprecipitation of protein lysates with polyclonal anti-GFP from HEK293T cells overexpressing human NUFIP2 and GFP-Roquin-1 FL, GFP-Roquin-1-N-term (aa 1-509) or GFP-Roquin-1-C-term (aa 509-1130). One representative of three independent experiments is shown in **(A)** and **(C)**.

A single point mutation in the ROQ domain of Roquin-1 (M199R) is responsible for the severe autoimmune phenotype of the *sanroque* mouse, which is caused by derepression of several Roquin-1 target mRNAs in response to Roquin-1 dysfunction

(Vinuesa et al., 2005). Although this mutation is located in the RNA-binding ROQ-domain, it does neither disrupt the structure of the RNA-binding domain nor interfere with RNA-binding (Srivastava et al., 2015). It also does not seem to play a major role in selecting RNA binders (Janowski et al., 2016). It can therefore be assumed that the *sanroque* mutation abolishes an unknown protein/protein interaction that is essential for Roquin-1 function. To find out whether this unknown factor might be Nufip2, endogenous Roquin-1 was precipitated from MEF cell extracts in which Roquin-1 and -2 were present (wt), deleted (*Rc3h1/2<sup>-/-</sup>*) or Roquin-1 was carrying the *sanroque* mutation (*Rc3h1<sup>san/san</sup>*) by Aicha Jeridi in our lab (Figure 29). Immunoprecipitated Roquin-1 protein was strongly enriched over input levels in wildtype and *Rc3h1/2<sup>san/san</sup>* MEF cells, while no Roquin-1 was detected in *Rc3h1/2<sup>-/-</sup>* MEF cells, which served as negative control. Co-immunoprecipitated Nufip2 levels derived from wildtype and *Rc3h1/2<sup>san/san</sup>* lysates were also similarly enriched over input levels. Although the antibody was able to equally well immunoprecipitate Roquin-1 and -2, the co-immunoprecipitated amount of Nufip2 was unchanged when comparing extracts of wildtype or *sanroque* MEF cells. This suggested that the *sanroque* mutation did not abolish Roquin-1 interaction. Strikingly, Roquin-1 and Nufip2 showed almost the same enrichment over input, indicating that most Roquin-1 protein that was pulled down was bound to Nufip2.

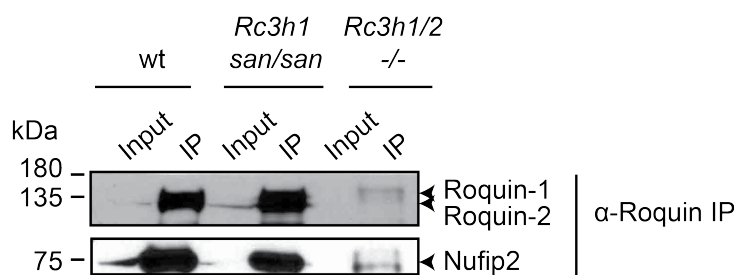


**Figure 29: Co-immunoprecipitation of endogenous Roquin-1 or Roquin-1<sup>san</sup> with Nufip2.**

Immunoblot analysis of Nufip2 and Roquin-1 expression after immunoprecipitation of endogenous Roquin-1 from wt MEF cells, *Rc3h1/2<sup>-/-</sup>* MEF cells and *Rc3h1<sup>san/san</sup>* MEF cells. This immunoprecipitation was performed by Aicha Jeridi using a monoclonal pan-Roquin-1/2 antibody. One representative of three independent experiments is shown here.

To address whether the observed interaction between Nufip2 and the Roquin-1-N-terminus was direct, recombinant proteins were produced in bacteria as N-terminal His<sub>6</sub>-SUMO-fusion proteins, purified by HisTrap™ and size exclusion chromatography (Chapter 3.2.5) and tested in *in-vitro* binding assays by Elena Davydova from Prof. Dr. Dierk Niessing's group. An N-terminal fragment (aa 2-441) of mouse Roquin-1 was

purified first, while an internal protein fragment (aa 255-411) was chosen for Nufip2. Successful expression of Nufip2 (aa 255-411) has already been reported in the literature, where it was stable enough for use in protein binding assays (Ramos et al., 2006).

A direct interaction between mouse Roquin-1 (aa 2-441) and human NUFIP2 (aa 255-411) was demonstrated in surface plasmon resonance (SPR) experiments. Roquin-1 was coupled to the sensor chip of a Biacore SPR system, followed by injection of different concentrations of NUFIP2. Direct binding of NUFIP2 to Roquin-1 caused changes in the refractivity of the sensor chip surface, which was measured as resonance units by the SPR instrument.

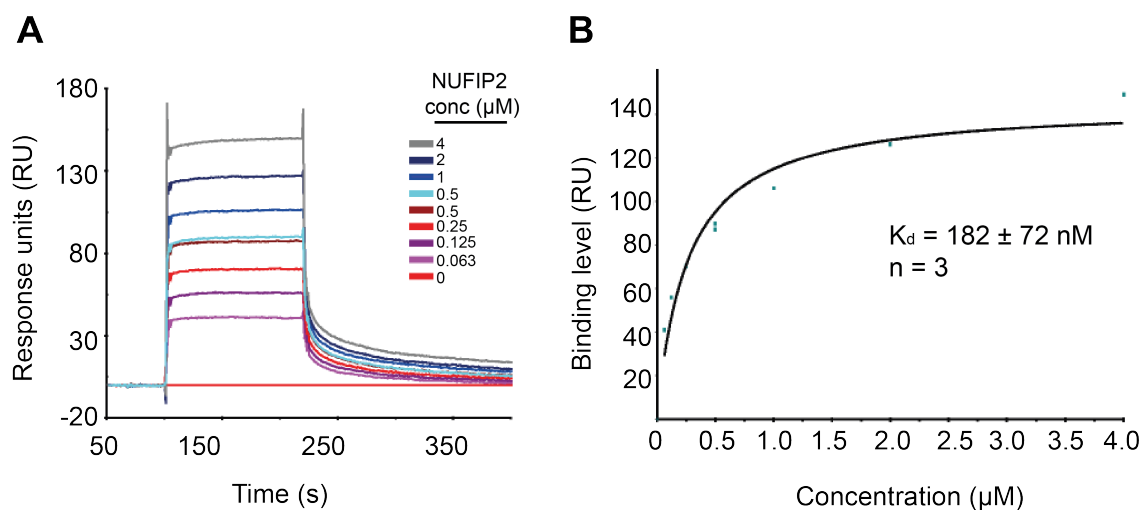


**Figure 30: Binary interaction of NUFIP2 and Roquin-1 fragments.**

**(A, B)** Surface plasmon resonance study of the binding of NUFIP2 (aa 255-411) to immobilized Roquin-1 (aa 2-441). **(A)** Biacore sensograms recording the binding of NUFIP2 (aa 255-411) injected at twofold serial dilutions ranging from 4-0.063 μM to Roquin-1 (aa 2-441). After the highest concentration, the 0.5 μM sample dilution was re-injected in order to ensure that the increase in resonance units (RUs) was caused by increasing concentrations of NUFIP2 and not by background signals adding up after each concentration. **(B)** Steady state affinity analysis of the binding level in RUs against the Nufip2 (aa 255-411) protein concentration. One representative of three independent experiments are shown in both **(A)** and **(B)**. The  $K_d$  was calculated from mean and SD of three independent experiments. This experiment was performed and analyzed by Elena Davydova.

The Biacore sensogram clearly showed a concentration-dependent increase in resonance units in response to injection of NUFIP2 (aa 255-411) (Figure 30A). Steady state affinity analysis depicted the binding level in resonance units that is reached at equilibrium (saturation points of the curves in Figure 30A) for each NUFIP2 concentration. The dissociation constant  $K_d$  of the Roquin-1-NUFIP2 complex at equilibrium is defined as the NUFIP2 concentration where half of the NUFIP2 protein

is engaged in a complex with Roquin-1. As deduced from the steady state affinity plot a  $K_d$  of 182 nM was calculated indicating a strong, direct interaction between Roquin-1 2-441 and NUFIP2 (aa 255-411).

#### 4.1.9.2 Subcellular localization of Nufip2

Having learnt that Roquin-1 and NUFIP2 directly interact, we asked whether they also colocalized within cells. Nufip2 has originally been described as a protein that shuttles to nucleo-cytoplasmic localizations in different phases of the cell cycle (Bardoni et al., 2003). In the cytoplasm, NUFIP2 was described to localize diffusely, without showing colocalization with RCK in P bodies (Chapter 1.1.2) (Bish et al., 2015). However, NUFIP2 was observed to localize to stress granules in response to arsenite-induced oxidative stress (Bish et al., 2015). Roquin-1 also localizes to stress granules upon arsenite treatment (Glasmacher et al., 2010; Vinuesa et al., 2005; Yu et al., 2007). We therefore addressed whether Nufip2 and Roquin-1 colocalize in stress granules when cells are exposed to oxidative stress.

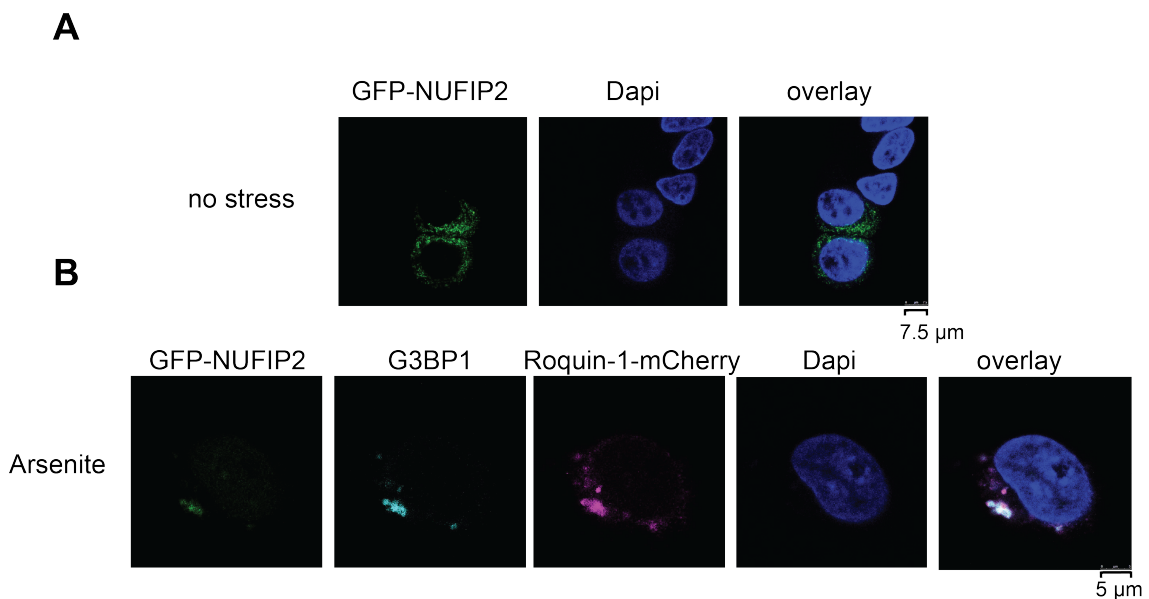


**Figure 31: NUFIP2 and Roquin-1 colocalize in stress granules upon arsenite treatment.**

**(A)** Confocal microscopy of the localization of GFP-NUFIP2 (green) in HEK293T cells upon overexpression of GFP-NUFIP2 without arsenite treatment (no stress). **(B)** Confocal microscopy of the localization of GFP-NUFIP2 (green), G3BP1 (light blue) and Roquin-1-mCherry (pink) in HEK293T cells upon overexpression of GFP-NUFIP2 and Roquin-1-mCherry after arsenite-induced stress. Since the Roquin-1/Nufip2 interaction was mapped to the N-terminus of Roquin-1, a C-terminal fusion of the fluorescent reporter mCherry was used here in order to prevent disturbance of the interaction with N-terminally GFP-tagged NUFIP2.

First, I reconfirmed the findings by Bish et al., 2015, that overexpressed GFP-NUFIP2 showed a diffuse, primarily cytoplasmic localization in HEK293T cells in the absence of stress (Figure 31A). Upon arsenite treatment, almost all GFP-NUFIP2 signal relocated to stress granules, where it colocalized with overexpressed Roquin-1-mCherry protein (Figure 31B).

Both Roquin-1 and Nufip2 have been reported to possess amino acid stretches with a higher frequency of glutamine and asparagine residues (Bish et al., 2015; Glasmacher et al., 2010). These so-called Q/N rich regions, originally discovered as protein aggregation sequences of prion proteins, were found to be involved in the assembly of stress granules (Chapter 1.1.2) (Gilks et al., 2004). Nufip2 and Roquin-1 might thus be important mediators of the cellular stress response by binding to translationally arrested mRNAs and inducing stress granule assembly via their Q/N rich protein aggregation domains.

Nufip2 has been described as a cell-cycle dependent nucleo-cytoplasmic shuttle protein, showing high nuclear localization in G1, both cytoplasmic and nuclear localization in S and predominantly cytoplasmic localization in the G2/M phase of the cell cycle (Bardoni et al., 2003). These studies were performed in NIH3T3 fibroblasts and fibroblast-like COS cells with endogenous Nufip2. However, we did not observe significant nuclear expression of overexpressed GFP-NUFIP2 in HEK293T cells during our confocal microscopy experiments, a finding which was supported by a recent publication showing a predominantly cytoplasmic expression of endogenous NUFIP2 in HEK293T cells (Bish et al., 2015).

#### **4.1.10 Expression of Nufip2 in immune cells**

Since the functional role of Nufip2 is mostly unclear, we wondered whether Nufip2 expression was ubiquitous, similar to that of Roquin-1, or restricted to certain cell types, which might provide important clues with respect to its function. Publicly available gene expression data ([www.biogps.org](http://www.biogps.org), [www.immgen.org](http://www.immgen.org)) pointed towards a constant mRNA expression over a wide range of different tissues and cells types. In order to assess whether this was indeed also the case for Nufip2 protein, we evaluated Nufip2 expression in different cell types using immunoblots. Due to its low sensitivity, the commercially available polyclonal antibody proved unsuitable. Therefore, a high-affinity monoclonal antibody was generated against recombinant NUFIP2 protein in collaboration with the in-house monoclonal antibody service facility (Dr. Elisabeth

Kremmer/Dr. Regina Feederle). Rats were immunized with recombinant human NUFIP2 protein and splenocytes from these rats were fused with a myeloma cell line. After clonal expansion of antibody-secreting cells, several dozens of supernatants were screened. We selected one hybridoma supernatant showing the highest signal for endogenous mouse and human Nufip2 for future applications. This antibody appeared to bind to an epitope near the N-terminus of Nufip2 (between aa 1-255), and specifically recognized Nufip2 with a molecular weight of 75 kDa. Specific recognition was confirmed in immunoblotting experiments with different Nufip2-knockout and overexpression cell lines (Appendix V).

#### 4.1.10.1 Analysis of Nufip2 protein expression in different mouse tissues

The newly established monoclonal Nufip2 antibody was employed for immunoblot analysis of Nufip2 expression in lysates from different mouse organs (Figure 32A). Nufip2 expression peaked in the brain, which is in agreement with the literature where Nufip2 was shown to be highly expressed in neurons (Bardoni et al., 2003). Apart from the brain, Nufip2 was more abundant in lymphoid tissues, with a high expression in the thymus but also in the lung, and intermediate levels found in the spleen and in lymph nodes. These results indicate that, apart from its known role as an interactor of FMRP in the brain, Nufip2 potentially carries out specific functions in immune cells.

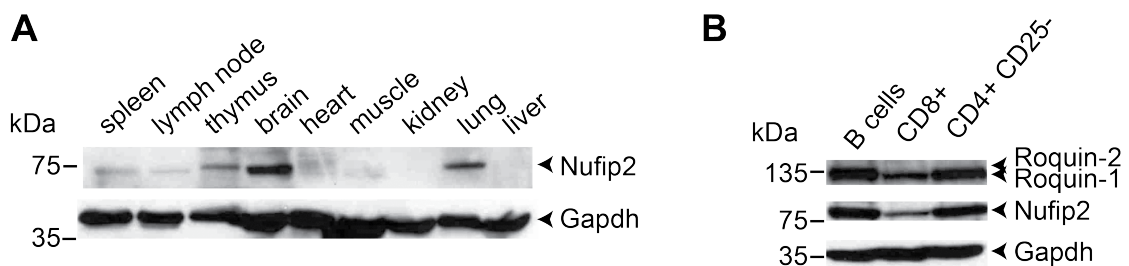


**Figure 32: Nufip2 is strongly expressed in the brain and in lymphoid tissues.**

**(A)** Immunoblot analysis of Nufip2 protein expression in different mouse tissues with GAPDH as a loading control. **(B)** Immunoblot analysis of Roquin-1 and Nufip2 expression in sorted B and T cells.

In order to determine which types of immune cells showed the highest expression of Nufip2, whole cell lysates from FACS-sorted mouse B cells, CD8<sup>+</sup> T cells and CD4<sup>+</sup> CD25<sup>-</sup> (non-regulatory T cells) T cells were analyzed for Nufip2 expression. Similar to Roquin-1, Nufip2 showed a high expression in B cells and CD4<sup>+</sup> T cells, with a lower expression in CD8<sup>+</sup> T cells (Figure 32B).

#### **4.1.10.2 Correlating expression levels of ICOS, Roquin-1 and potential Roquin-1 cofactors in a time course of T cell activation**

We focused on CD4<sup>+</sup> T cells to study the control of Nufip2 expression in more detail. Upon activation of CD4<sup>+</sup> T cells, Roquin-1 is cleaved into its inactive form by the paracaspase Malt1 (Jeltsch et al., 2014). We therefore wondered how Nufip2 expression levels would develop in the course of T cell activation and differentiation in comparison to Roquin-1 itself and other known and potential Roquin-1 cofactors. Therefore, the expression levels of Nufip2, Fmrp, Fxr1, Ago 1-4, Regnase-1 and Roquin-1 were analyzed in a time course of T cell activation and IL-2 culture, followed by restimulation with anti-CD3/CD28 antibodies and secondary IL-2 culture and correlated with their common target Icos (Figure 33A).

Stimulation of naïve T cells with anti-CD3/CD28 antibodies induces Malt1-mediated cleavage of Roquin-1 as early as three hours after stimulation (Jeltsch et al., 2014). In line with this, we observed an accumulation of the cleavage product (50 - 60 kDa) on the first day after T cell activation (d1) (Figure 33B). During IL-2 culture, the cleavage product as well as full-length Roquin-1 became less abundant, indicating that both post-transcriptional cleavage and transcriptional induction of Roquin-1 decreased over time. After restimulation on day 7, expression of both full-length Roquin-1 and the cleavage product was strongly induced and their expression remained constant for two days, before declining again (Figure 33B). Strikingly, Nufip2 was strongly induced 24 h after stimulation of naive T cells with anti-CD3/CD28 (d1) (Figure 33B). Nufip2 expression stayed maximal for 3 days and then constantly declined from day 4 till day 7. A similar expression pattern was observed after restimulation.

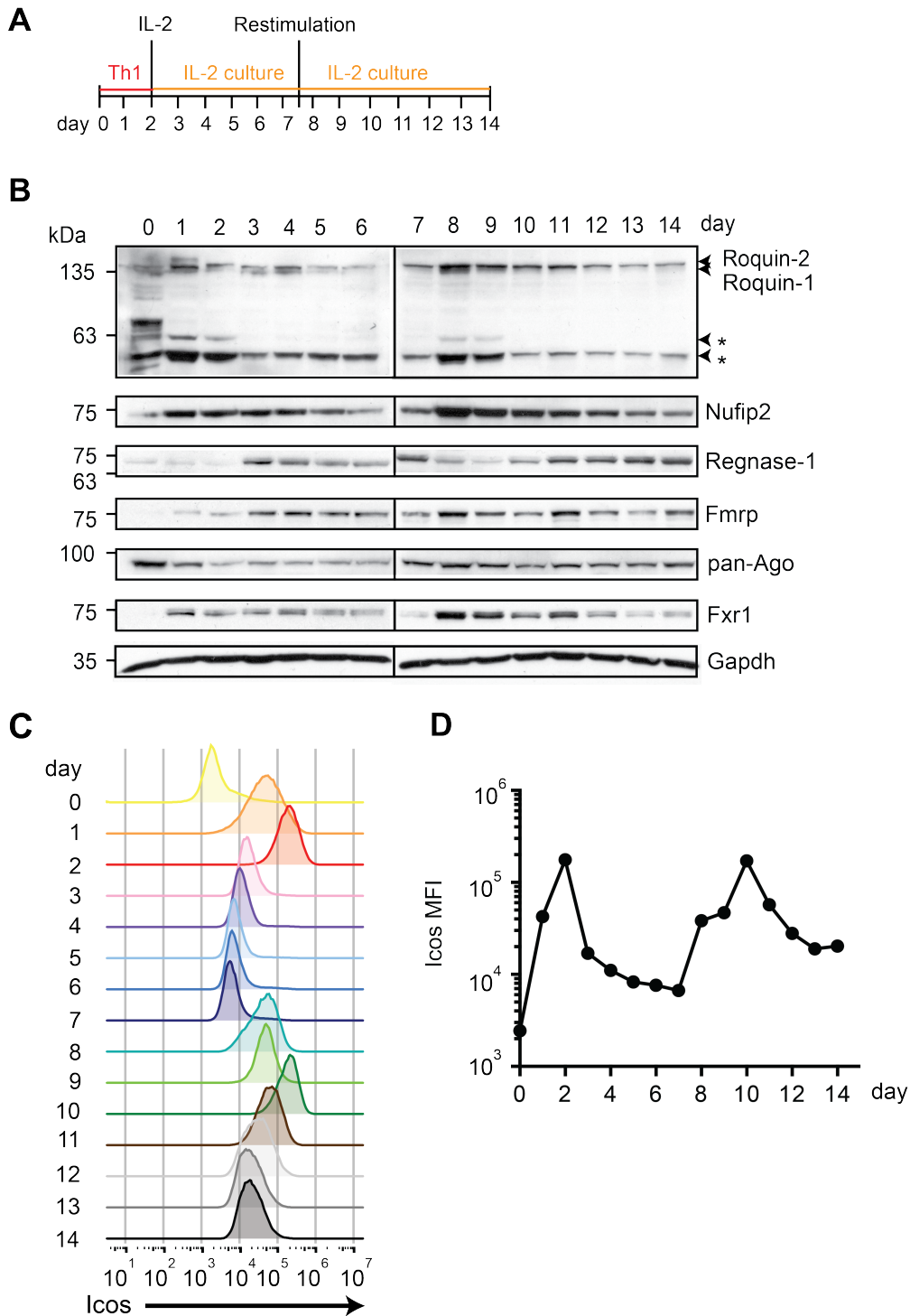


**Figure 33: Correlating Icos levels with the expression of different trans-acting factors.**

**(A)** Schematic representation of the performed time course of T cell activation. Primary mouse CD4<sup>+</sup> T cells were stimulated with anti-CD3 and anti-CD28 antibodies under Th1 differentiating conditions for 48 h, and then cultured in IL2-containing medium for five days. After restimulation with anti-CD3 and anti-CD28 antibodies, cells were rested in IL-2 medium for another four days. Cells for flow cytometry and immunoblotting experiments were harvested daily. **(B)** Immunoblot analysis of Roquin-1, Regnase-1, Nufip2, Fxr1, Ago and Fmrp expression levels in whole cell lysates derived from the time course of T cell activation as described in **(A)**. **(C)** Flow cytometric analysis of Icos surface expression on mouse CD4<sup>+</sup> T cells during the time course described in **(A)**. **(D)** Quantified mean fluorescence intensity (MFI) of ICOS expression in **(C)**.

The RNase Regnase-1 can work in concert with Roquin-1 in the regulation of certain mRNA targets and is equally subject to Malt1-induced cleavage after T cell activation (Uehata et al., 2013). In line with this, expression of full-length Regnase-1 was low on day 1 and day 2 after T cell activation and was restored between day 2 and day 3 (Figure 33B). This was similarly observed after T cell restimulation on day 7. Fmrp, which was included in this experiment due to its function as a direct interaction partner of Nufip2 (Bardoni et al., 2003; Ramos et al., 2006), was induced upon T cell activation similar to Nufip2. However, there appeared to be a time delay, resulting in Fmrp expression peaks occurring 3 - 4 days after T cell activation. Fmrp can form homodimers, but also heterodimers with its family member Fxr1 (Dolzhanskaya et al., 2006). Fxr1 was, however, induced early upon T cell activation, thereby mimicking the expression pattern of Nufip2 (Figure 33B). Finally, Ago proteins were investigated due to a potential collaboration of Roquin-1 with the miRNA pathway, which has been proposed for certain Roquin-1 targets (Pratama et al., 2015; Srivastava et al., 2015). Ago 1-4 were detected with a pan-Ago antibody and showed a time-delayed downregulation upon T cell activation (Figure 33B). This is in concert with the literature, where a strong downregulation of Ago proteins between 24 h and 48 h after T cell activation accompanied by a general reduction of overall miRNA expression were observed in a similar time course (Bronevetsky et al., 2013). In their experiments, loss of Ago2 was found to be mediated by ubiquitin-dependent proteasomal degradation of Ago2 proteins. Although the first part of our T cell activation time course confirmed a loss of Ago expression upon T cell activation, this was not the case after T cell restimulation on day 7. How Ago proteins behave upon secondary T cell stimulation has, however, never been investigated before, and might thus be different from initial priming.

While Roquin-1 and Regnase-1 were cleaved and inactivated upon anti-CD3/CD28 stimulation, their target Icos was strongly induced on the T cell surface between the first and second day after T cell activation (Figure 33C, D). It remained at its upper limit for two days and suddenly declined between the second and the third day and then stayed low until restimulation. After restimulation of resting T cells on the seventh day, high ICOS levels were reached again for 48 h, followed by a slower decline between day 10 and day 12. How the observed expression pattern of Icos during T cell activation, resting and restimulation might relate to the differential expression patterns of Roquin-1 and its cofactors will be discussed later in this work (Chapter 5.3.3).

#### 4.1.11 Analysis of cis-elements in the human *ICOS* 3' UTR

Roquin-1 directly binds to stem-loops in the 3' UTR of *ICOS* mRNA (Schlundt et al., 2014; Srivastava et al., 2015) and in turn Nufip2 directly binds Roquin-1, which has been clearly demonstrated during the work of this thesis. Knockdown and knockout of Nufip2 in combination with the respective rescue experiments showed that this protein is a player in Roquin-1-dependent *ICOS* repression. Although Nufip2 was initially chosen as a candidate for the Roquin-1 cofactor screen because of its annotation as an RNA-binding protein, it is still elusive whether it binds to *ICOS* mRNA in addition to its interaction with Roquin-1. To answer that question, a first step would be to find out if Nufip2 and Roquin-1 bind to the same *cis*-elements of the *ICOS* 3' UTR. Unfortunately, a complete list of the sites and motifs bound by Roquin-1 in this 3' UTR does not exist. Therefore, in the last part of this study, we performed a comprehensive mutation analysis of the human *ICOS* 3' UTR sequence to find the sites with the highest impact on *ICOS* repression.

##### 4.1.11.1 Identification of the main regulatory regions of human *ICOS* mRNA

Several Roquin-1 *cis*-elements have been described in the literature for the human *ICOS* 3' UTR (Figure 34A). The first to be identified was a target sequence of miR-101, close to the 3' end of *ICOS* mRNA. Inversion of two nucleotides in the sequence targeted by miR-101 caused impaired Roquin-1-dependent post-transcriptional gene regulation in reporter assays (Yu et al., 2007). A potential direct binding site for Roquin-1 on *ICOS* mRNA was subsequently mapped immediately upstream of the miR-101 target site (Athanasopoulos et al., 2010). Next, the *ICOS* constitutive decay element (CDE) close to the 3' end was inferred from the *TNF* CDE sequence (Leppek et al., 2013). Finally, Glasmacher et al. could demonstrate (Glasmacher et al., 2010) in gel shift assays that Roquin-1 strongly binds to a region close to the coding sequence of human *ICOS* mRNA (nt 700-800). Within this region a stem-loop of high similarity to the previously described CDE was identified as the crucial *cis*-acting element and called 'CDE-like' (Schlundt et al., 2014). While several binding sites of Roquin-1 in the *ICOS* 3' UTR have been described thus far, the functional impact of these elements has not been analyzed systematically.

For a comprehensive investigation of Roquin-1 *cis*-elements in the *ICOS* 3' UTR, I employed a set of 3' UTR deletion constructs, which were fused to the *ICOS* coding sequence as a reporter. Those constructs were evaluated in two different cell lines. On the one hand, *Rc3h1/2*<sup>-/-</sup> MEF cells with doxycycline-inducible expression of Roquin-1-

P2A-mCherry allowed the quantification of reporter expression in the presence and absence of high amounts of Roquin-1. Advantages of this system lie in the high dynamic range, since overexpressed Roquin-1 can cause up to 20-fold downregulation of ICOS expression (Chapter 4.1.1). However, the high expression of a protein may potentially lead to unphysiologic regulation. Therefore, *Rc3h1/2<sup>fl/fl</sup> Cre ERT2* MEF cells were employed as a second cell line, where changes in reporter expression in response to the presence or absence of endogenous Roquin-1 and Roquin-2 can be monitored. However, in this kind of experiment the dynamic range is much reduced as compared to overexpression. In a best-case scenario the results obtained from both approaches support the same conclusion(s).

It has been shown previously that serial shortening of the human *ICOS* UTR from the 3' end leads to a stepwise decrease in the degree of regulation by overexpressed Roquin-1 (Glasmacher et al., 2010). We could confirm this finding with our doxycycline-inducible Roquin-1 overexpression system (Figure 34B). The 1-2271 construct still exhibited full regulation, but regulation strongly decreased with further shortening of the mRNA (Figure 34B). Testing the same deletion constructs in the presence or absence of endogenous Roquin-1 arrived at different results. Now repression was either on or off, with no intermediate phenotype (Figure 33C). However, similar to the first "boundary" in overexpression, loss of regulation occurred when the 3' UTR constructs were 2011 nts or shorter, while constructs of 2271 nts or longer were fully repressed.

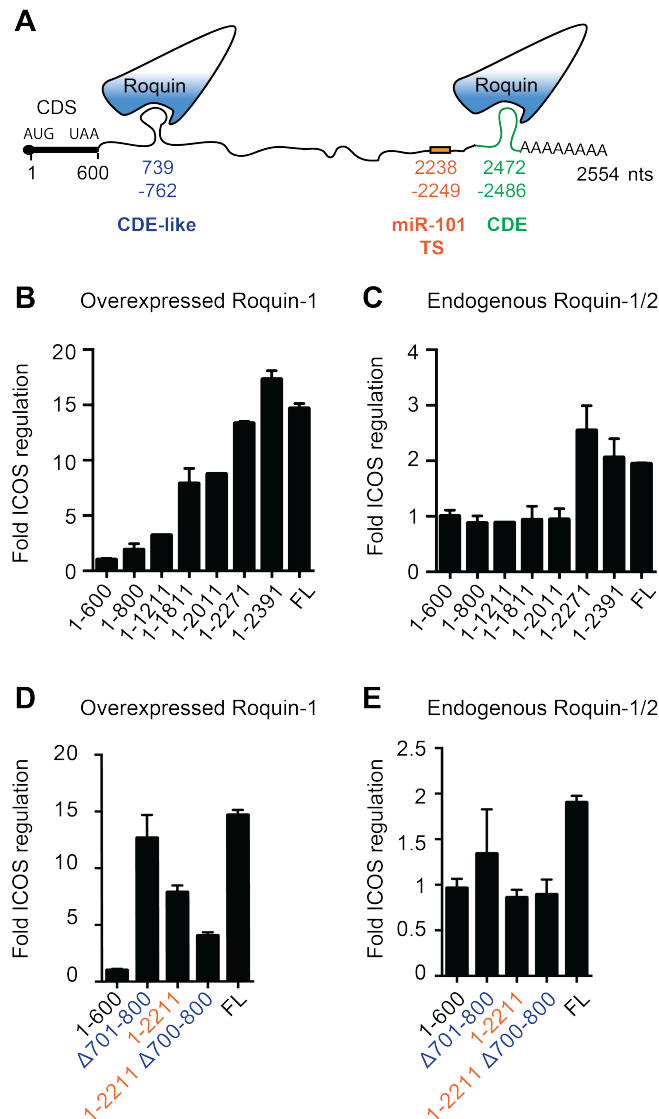


**Figure 34: Identification of Roquin-1 cis-elements present in the 3' UTR of human ICOS mRNA.**

**(A)** Schematic representation of known and suspected cis-elements in the human ICOS 3' UTR. **(B)** Reporter regulation of gradually shortened ICOS 3' UTR fragments in response to overexpressed Roquin-1 in Rc3h1/2<sup>-/-</sup>MEF cells + doxycycline (dox)-inducible Roquin-1-P2A-mCherry. ICOS expression of reporter constructs consisting of ICOS CDS fused to different fragments of ICOS 3' UTR as indicated was measured by flow cytometry in cells with and without induction of Roquin-1 overexpression with dox for 18 h. Fold regulation was quantified by dividing (ICOS MFI -dox)/(ICOS MFI +dox) and normalized to the regulation of ICOS CDS, which was set to 1. **(C)** Reporter regulation of gradually shortened ICOS 3' UTR fragments in response to deletion of endogenous Roquin-1 in Rc3h1/2<sup>fl/fl</sup> CreERT2 MEF cells. Fold regulation was determined by dividing (ICOS MFI -4-OH-TAM)/(ICOS MFI +4-OH-TAM) and normalized to the regulation of ICOS CDS, which was set to 1. **(D)** Reporter regulation of ICOS 3' UTR deletion constructs in response to overexpressed Roquin-1 in Rc3h1/2<sup>-/-</sup> MEF cells +dox-inducible Roquin-1-P2A-mCherry. Fold regulation was calculated as described in **(A)**. Constructs missing the miR-101 TS are labeled in orange and lack of the CDE-like element is indicated in blue. **(E)** Reporter regulation of ICOS 3' UTR deletion constructs in response to deletion of endogenous Roquin-1 in Rc3h1/2<sup>fl/fl</sup> Cre ERT2 MEF cells. Fold regulation was calculated as described in **(B)**. Error bars indicate mean and SD of two independent experiments for **(A)** to **(C)**. In **(D)**, mean and SD are calculated from two or three independent experiments depending on the construct.

Considering these results in the context of the three described *cis*-elements, there was a strong indication towards an important *cis*-element being present between nucleotide 2011 and 2271, the region where the miR-101 target site had been mapped (Yu et al., 2007). Noteworthy, the 1-2391 and the 1-2271 constructs, both lacking the *ICOS* CDE at the very 3' end of the 3' UTR, showed unimpaired regulation in the context of Roquin-1 overexpression (Schlundt et al., 2014) and after deletion of endogenous Roquin-1. Therefore, in the biological context and under the conditions of these experiments the canonical CDE in the *ICOS* 3' UTR is not a major *cis*-element. This finding is particularly surprising since the isolated CDE sequence was shown to induce Roquin-1-mediated mRNA decay *in vitro* (Leppek et al., 2013). Yet, Stöcklin and colleagues never deleted or mutated the CDE in the context of the full-length *ICOS* 3' UTR. Moreover, while I determined post-transcriptional gene regulation by quantifying *ICOS* protein expression as a final output of mRNA stability and translation efficiency, Stöcklin and colleagues solely investigated mRNA decay, thereby excluding other post-transcriptional mechanisms that can influence the output, such as translational inhibition. The discrepancy between the results of their and my analysis of the importance of the CDE highlights the different outcomes that can result from the application of different methods for studying *cis*-elements, and underlines the need for a comprehensive analysis of *ICOS* *cis*-elements in their native context.

The impact of the remaining two *cis*-elements was investigated more precisely through the additional trimming of the existing deletion constructs. In the context of Roquin-1 overexpression the deletion of the CDE-like stem-loop region ( $\Delta$ 700-800) surprisingly did not interfere with Roquin-1-dependent regulation, although the isolated sequence was previously reported to be bound by Roquin-1 *in vitro* (Glasmacher et al., 2010; Schlundt et al., 2014) (Figure 33D). In contrast, a construct ending directly 5' of the miR-101 target site (1-2211) showed already impaired repression, which was even more compromised upon additional deletion of the CDE-like stem-loop region (1-2211  $\Delta$ 700-800). This result suggests that both *cis*-elements work redundantly, with the miR-101 target sequence playing a dominant role. This was confirmed by studies relying on endogenous Roquin-1 levels (Figure 33E). Repression of a construct lacking the CDE-like element ( $\Delta$ 700-800) was partially impaired, and additional deletion of the miR-101 target site completely abolished regulation. However, no contributive effect could be seen for additional deletion of the CDE-like element in the shorter compared to the full-length construct. This might be

explained by the small dynamic range of the assay (on/off type), which possibly did not allow for the detection of intermediate states.

#### **4.1.11.2 A new stem-loop structure in the miR-101 target site is a putative *cis*-element targeted by Roquin-1**

miR-101 was initially described as the *cis*-element-recognizing *trans*-acting factor in Roquin-1-dependent post-transcriptional gene regulation of *ICOS* mRNA (Yu et al., 2007). Since Roquin-1 binding sites were mapped immediately upstream of the predicted miR-101 target site, it has been proposed that Roquin-1 binding enables miR-101 targeting by changing the secondary structure of *ICOS* 3' UTR (Athanasopoulos et al., 2010). However, the contribution of miR-101 to Roquin-1-mediated post-transcriptional repression is still controversial, since it was shown later that overexpression of Roquin-1-induced *ICOS* regulation independent of the miRNA pathway (Glasmacher et al., 2010). Instead, Roquin-1 itself was demonstrated to be an RNA-binding protein (Athanasopoulos et al., 2010; Glasmacher et al., 2010), and as a *trans*-acting factor it recognizes specific tri-loop and hexa-loop or U-rich hairpin structures with different loop sizes (Codutti et al., 2015; Janowski et al., 2016; Leppek et al., 2013; Murakawa et al., 2015; Schlundt et al., 2014; Tan et al., 2014). Therefore, we asked whether a secondary structure was buried within the sequence predicted to be recognized by miR-101 and regulated by Roquin-1. In the group of Dr. Jörg Hackermüller and Dr. Kristin Reiche, Anne Hoffmann generated a model of the secondary structure of the *ICOS* 3' UTR. She used the LocARNA software (Will et al., 2012; Will et al., 2007), which employs structure-based alignments of sequences from different species to identify evolutionary conserved structured motifs. This algorithm first calculates for each nucleotide the probability for base pairing with other nucleotides within the same RNA molecule (i.e. the probability to form a structure), then aligns multiple sequences based on sequence and structure, and finally predicts the secondary structure of the alignment (Hoffmann, 2015). The consensus secondary structure was predicted for the 3' UTR of *ICOS* in the context of its preceding protein coding sequence (CDS) to ensure proper folding of the most 5' part of the 3' UTR and the sequence around the stop codon. Since the CDE had no impact on Roquin-1-dependent regulation of *ICOS* mRNA in the experiments presented above, we focused on the miR-101 target site and the CDE-like stem-loop in the 5' end of the 3' UTR. As suspected, a highly conserved tri-loop structure was identified in the region of the miR-101 target sequence (Figure 35A, B). For the CDE-like stem-loop, the locARNA

sequence alignment predicted the same structure as previously published (Schlundt et al., 2014). However, as compared to the stem-loop buried within the miR-101 target site, the degree of structural conservation of this sequence was less evident.

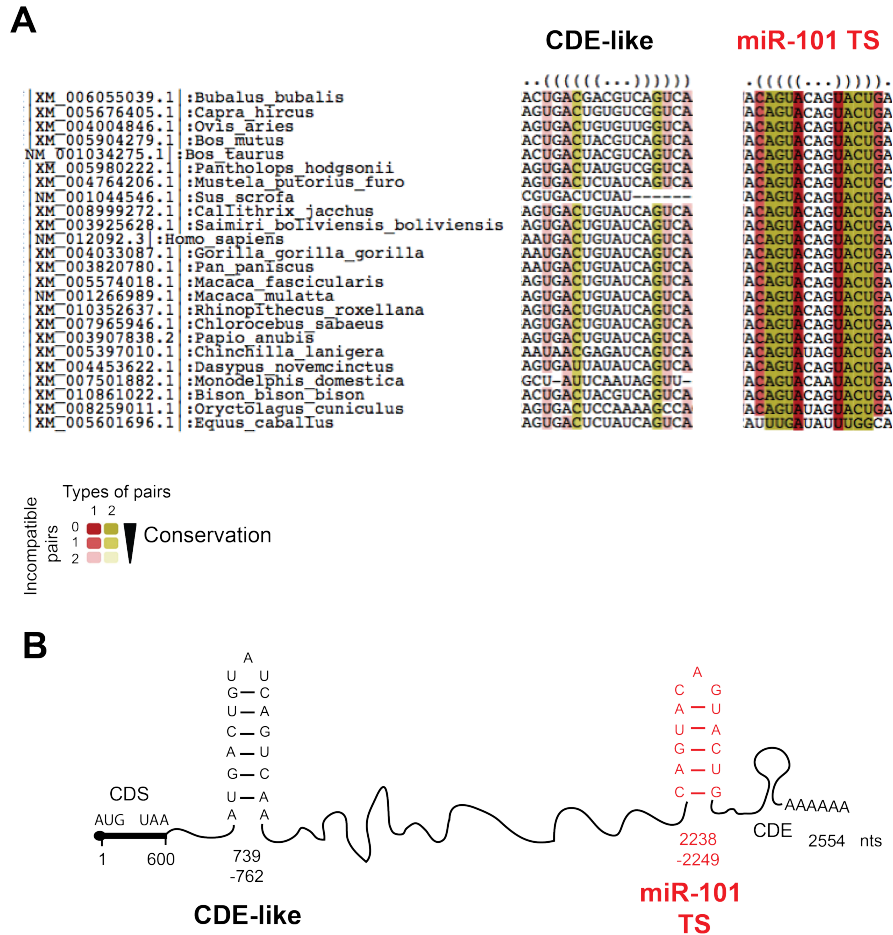


**Figure 35: Multiple sequence and structure alignments for the CDE-like stem-loop and the miR-101 target site stem-loop.**

**(A)** LocARNA multiple sequence and structure alignment of the CDE-like stem-loop and the newly identified stem-loop in the region targeted by miR-101 of human ICOS mRNA. Structural alignment was performed with ICOS coding sequence and the complete 3' UTR sequences from 24 species. The color code indicates the degree of secondary structure conservation across species. Compensatory mutations (types of pairs) are indicated by different colors, while the number of incompatible base pairs is reflected in the saturation. Saturated colors indicate a low number of incompatible base pairs and thus high structural conservation. Opposing brackets indicate base pairing nucleotides, while dots represent flexible loops. **(B)** Schematic representation of the CDE-like stem-loop and the miR-101 target site stem-loop secondary structures as identified in **(A)** and their relative position on ICOS mRNA. LocARNA sequence alignment was performed by Anne Hoffmann.

After modeling of the secondary structure, we set out to validate the predicted structure elements by functional assays. Interestingly, the mutations that were formerly introduced by Prof. Carola Vinuesa's group (Yu et al., 2007) to mutate the

region that is targeted by the seed sequence of miR-101 overlapped with the position of the closing base pair and the next base pair in the upper stem of the predicted stem-loop (SM1 in Figure 36). It is thus possible that the mutations, which were previously thought to ablate miR-101 binding, actually destroyed a stem-loop structure located at the very same position.

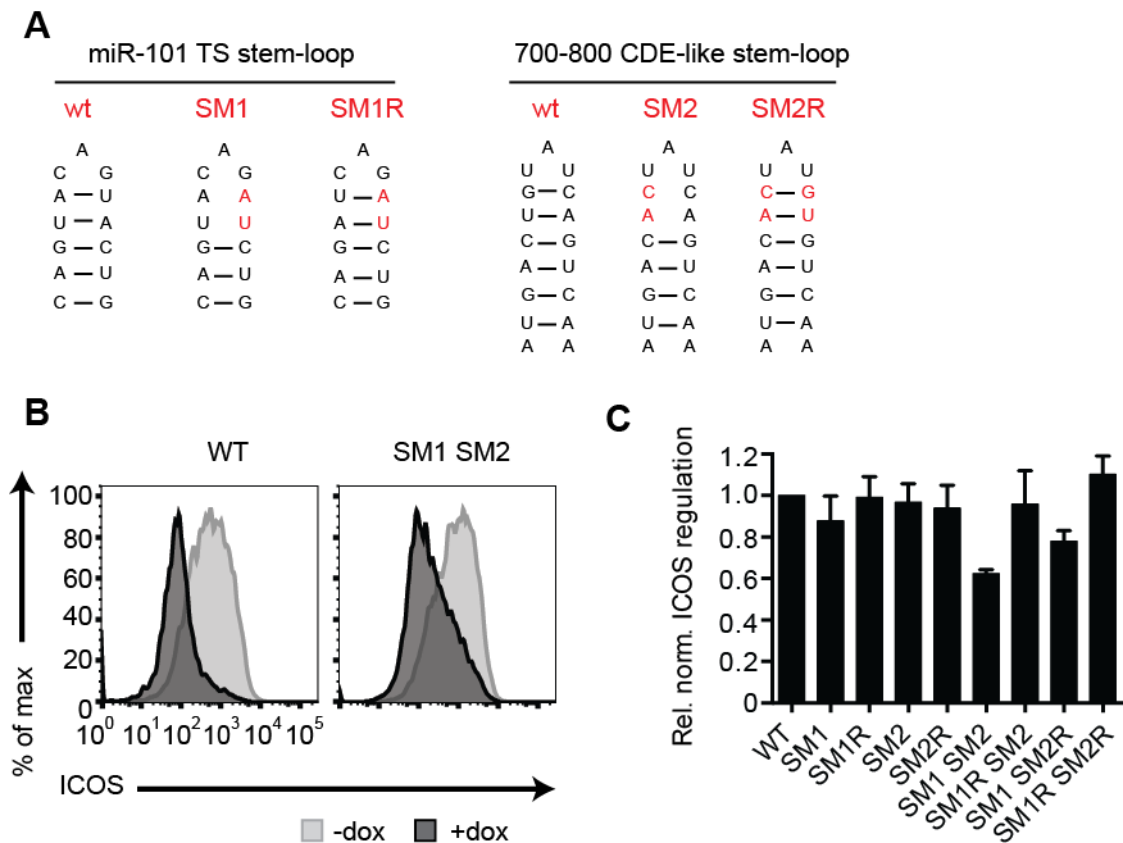


**Figure 36: Two stem-loop structures contribute to Roquin-1-dependent regulation of ICOS mRNA.**

**(A)** Schematic representation of the miR-101 target site stem-loop structure and the CDE-like stem-loop together with stem-loop mutants affecting the closing base pair and the upper stem (SM1, SM2) and stem-restoring mutants (SM1R, SM2R). Mutated nucleotides are labeled in red. **(B)** Flow cytometric analysis of ICOS wt and ICOS SM1 SM2 expression in Rc3h1/2<sup>-/-</sup> MEF cells with doxycycline (dox)-inducible Roquin-1-P2A-mCherry overexpression +/-dox. Cells were transduced with reporter constructs of ICOS CDS and the wt 3' UTR or a 3' UTR carrying the SM1 and SM2 stem-loop mutation. **(C)** Quantified ICOS regulation of ICOS stem-loop mutation constructs in Rc3h1/2<sup>-/-</sup> MEF cells with dox-inducible Roquin-1-P2A-mCherry overexpression. Fold regulation was quantified by dividing (ICOS MFI -dox)/(ICOS MFI +dox) and normalized to the regulation of ICOS wt, which was set to 1. **(B)** shows representative examples of two independent experiments, while mean and standard deviation from two independent experiments are shown in **(C)**.

To find out if the *cis*-element at this position conveys function through its secondary stem-loop structure, we introduced the SM1 mutation (similar to (Yu et al., 2007)) or a reverse mutation that restored the stem by additional mutation of the opposite base

pairs (SM1R) into *ICOS* mRNA (Figure 36A). Since our previous experiments had indicated a cooperation between a *cis*-element located at the miR-101 TS and the CDE-like stem-loop structure in the 5' end of the 3' UTR, we also designed a mutation destroying the closing base pair and the upper stem of the CDE-like stem-loop (SM2) as well as a reverse mutation that restored the stem-loop structure (SM2R) (Figure 36A).

*ICOS* reporter mRNAs with the different stem-loop mutations were overexpressed in *Rc3h1/2<sup>-/-</sup>* MEF cells with doxycycline-inducible Roquin-1-P2A-mCherry, and *ICOS* expression was analyzed in the presence and absence of Roquin-1. Mutating the miR-101 TS stem-loop alone had a mild effect on *ICOS* repression, which however was restored by the reverse mutation SM1R. In good accordance with our previous results (Figure 36 D and E) the SM2 mutation by itself had no impact on *ICOS* regulation. In the double mutant SM1 SM2, where both the miR-101 TS stem-loop as well as the CDE-like stem-loop were disrupted, *ICOS* downregulation in response to Roquin-1 overexpression was considerably impaired (Figure 36B), leading to about half of repression observed for the *ICOS* wildtype 3' UTR (Figure 36C). Most importantly, this effect could be fully restored with the reverse mutations SM1R SM2R. The results support a model in which RNA-binding factors bind to the two investigated stem-loop structures and act cooperatively in *ICOS* repression. Based on our mutagenesis we propose that the conserved stem-loop structure and not the miR-101 target sequence is the actual *cis*-element that contributes to *ICOS* repression in the context of the mapped region (nt 2011-2271) (Athanasopoulos et al., 2010).

To sum up, a comprehensive analysis of Roquin-1 *cis*-elements in the 3' UTR of *ICOS* revealed exciting new insights. The CDE at the very end of the *ICOS* 3' UTR, which is considered the bona fide Roquin-1 target sequence, appeared to be of no regulatory impact in the context of the whole *ICOS* mRNA sequence in the fibroblast cells that we analyzed. Instead, a close-by region (nt 2011-2271) that was initially described as being targeted by Roquin-1 via a miR-101 target sequence emerged as the most important *cis*-element. Advanced structure predictions led to the surprising discovery of a so far overlooked but highly conserved stem-loop structure in the same region that was previously assumed to be a miR-101 target site. The findings presented above provide a start point for future experiments that shall dissect the structural aspects for the cooperation on the RNA and elucidate the individual and combined contributions of Roquin-1 and Nufip2 to the post-transcriptional regulation of *ICOS*.

## 4.2 Genome-wide CRISPR/Cas9 screen for cofactors of Roquin-1-induced cell death

Initially, it was unclear whether or not a promising candidate would arise from the Roquin-1 cofactor screen central to the first part of this study (Chapter 4.1.1). While preparing the reporter cell lines for the screen, I made a striking observation: Cells seemed to suffer in response to long-term doxycycline-induced overexpression of Roquin-1-P2A-mCherry, such that all cells were dying from a not yet defined type of cell death upon > 48 h of doxycycline stimulation. Since this function of Roquin-1 was completely new to the field, we wanted to shed light on it by exploring which cellular factors were critically involved in the pathway of Roquin-1-induced cell death. We therefore decided to employ one of the new publicly available CRISPR/Cas9 gene knockout libraries (Koike-Yusa et al., 2013; Shalem et al., 2014; Wang et al., 2014) and performed a genome-wide pooled positive selection screen for cofactors of Roquin-1-induced cell death. This screen was performed parallel to the functional validation of Nufip2 (Chapter 4.1.8-4.1.10), which had emerged as a promising candidate from the Roquin-1 cofactor screen.

### 4.2.1 Overexpression of Roquin-1 induces cell death

The observed cell death in response to Roquin-1 overexpression could either be linked to a specific function of Roquin-1, or arise from general toxicity of the high overexpression levels reached with the lentiviral doxycycline-inducible expression system. To discriminate between the two possibilities, we compared cell survival upon overexpression of Roquin-1 full-length and the N-terminal fragment Roquin-1 (aa 1-509), which lacks Roquin-1 effector functions (Glasmacher et al., 2010). MEF cell clones overexpressing Roquin-1-P2A-mCherry or Roquin-1 (aa 1-509)-P2A-mCherry to equal levels upon doxycycline treatment were chosen for a time course experiment (Figure 37A). Already after 48 h of doxycycline treatment the percentage of living cells was considerably reduced when Roquin-1 full-length (FL) was expressed, whereas Roquin-1 (aa 1-509)-overexpressing cells showed similar frequencies of live cells as non-induced control cells (Figure 37B). Counting viable cells in a time course of doxycycline treatment revealed normal exponential cell growth for cells expressing the truncated Roquin-1 (aa 1-509), while cells overexpressing full-length Roquin-1 were dying (Figure 37C).

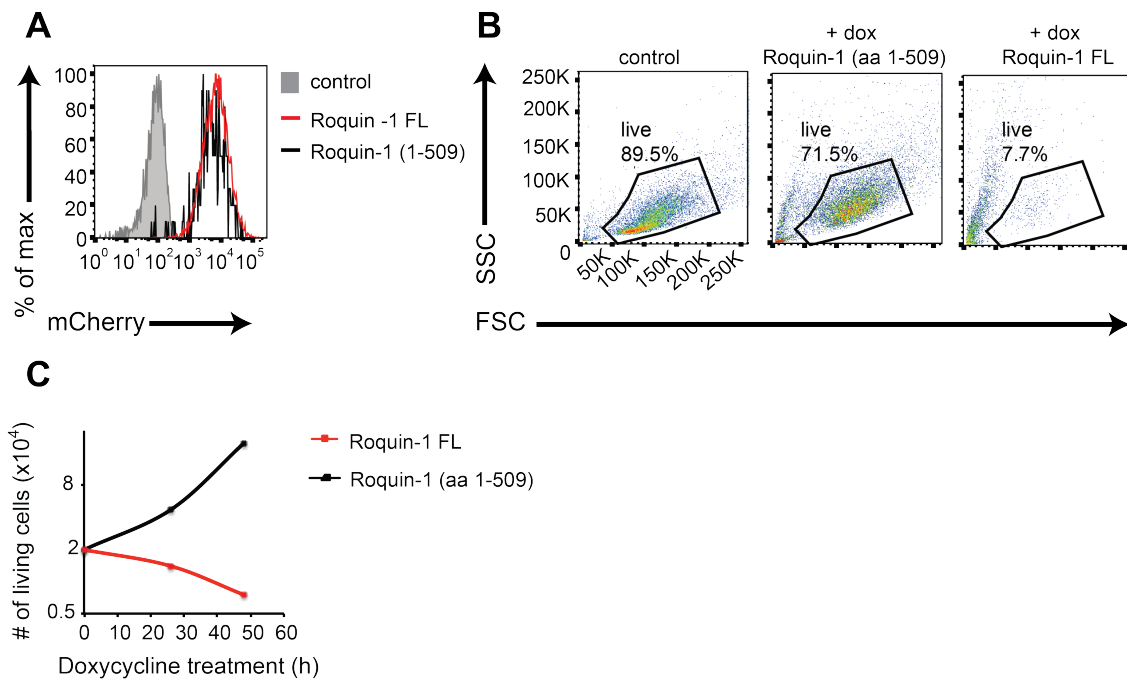


**Figure 37: Long-term overexpression of full-length Roquin-1 in MEF cells interferes with cell survival.**

**(A)** Flow cytometric analysis of mCherry expression in MEF cells overexpressing doxycycline (dox)-inducible Roquin-1-P2A-mCherry (FL) or Roquin-1 (aa 1-509)-P2A-mCherry. Cells were treated with dox for 48 h or left untreated (control). **(B)** Percentage of living cells as determined by flow cytometric analysis of size (FSC) and granularity (SSC) of cells in **(A)**. **(C)** Growth curves of MEF cells overexpressing dox-inducible Roquin-1-P2A-mCherry (FL) or Roquin-1 (aa 1-509)-P2A-mCherry. Cells were counted 24 h and 48 h after dox-addition.

Thus, the observed cell death phenotype upon overexpression of Roquin-1 was specific to Roquin-1 function and required the C-terminal part of Roquin-1 (proline-rich region, coiled-coil) in addition to the N-terminal part, which contains motifs involved in RNA-binding (ROQ domain, Zn finger) and putative ubiquitination function (RING finger).

#### 4.2.2 Genome-wide CRISPR/Cas9 screen

To identify the signaling pathways involved in Roquin-1-mediated cell death, which might ultimately guide us towards a yet unidentified form of cell death, we made use of a genome-wide pooled CRISPR/Cas9 knockout library. The CRISPR/Cas9 genome-editing technology (Chapter 1.2.2) opened up a new dimension in loss-of-function screening by providing easily accessible tools for rapid and inexpensive generation of targeted gene knockouts. Researchers recently employed this technology to create pooled sgRNA libraries capable of inactivating every single gene of the mouse or human genome on the DNA level (Koike-Yusa et al., 2013; Shalem et al., 2014; Wang et

al., 2014). In contrast to arrayed RNAi screening where RNAi reagents targeting different genes are delivered into separate wells of a 96- or 384-well plate (Chapter 4.1), pooled CRISPR/Cas9 screening involves the delivery of genome-covering sgRNA pools with multiple perturbations per gene simultaneously to a large number of cells. Following positive or negative selection for a desired phenotype, the responsible sgRNA sequences are identified by deep sequencing (Chapter 3.2.10) (Sims et al., 2011). A positive selection screen aims at the identification of sgRNAs that are enriched in the pool after selection, thereby identifying genes that were essential for the selected phenotype, while a negative selection screen identifies sgRNAs that were inhibitory for the selected phenotype and are thus underrepresented in the final pool. Being interested in sgRNAs that enabled cells to survive Roquin-1-overexpression due to specific inactivation of Roquin-1 cofactors, we performed a positive selection screen. Two different mouse Genome-scale CRISPR/Cas9 Knockout (GeCKO) Gecko libraries provided by the lab of Dr. Feng Zhang (MIT, Boston, USA) were available at Addgene: a one vector system, where sgRNAs and Cas9 nuclease are encoded on one vector, and a two-vector system, where Cas9 is provided from a separate vector. Since higher virus titers can be reached without Cas9 being present on the library vector (Sanjana et al., 2014), we decided to use the two-vector system. The first step of our screen workflow thus involved the generation of a reporter cell line with stable Cas9 expression.

#### **4.2.2.1 Producing a stable Cas9-GFP-expressing reporter cell line**

First, the MEF cell clone with doxycycline-inducible overexpression of Roquin-1-P2A-mCherry used for pre-screening experiments in chapter 4.2.1 was stably transduced with Cas9-GFP (Figure 38A). After a second round of single cell cloning, the clone showing the highest expression of HA-tagged Cas9-GFP (Figure 38B, C) was chosen as a reporter cell line (clone 8).

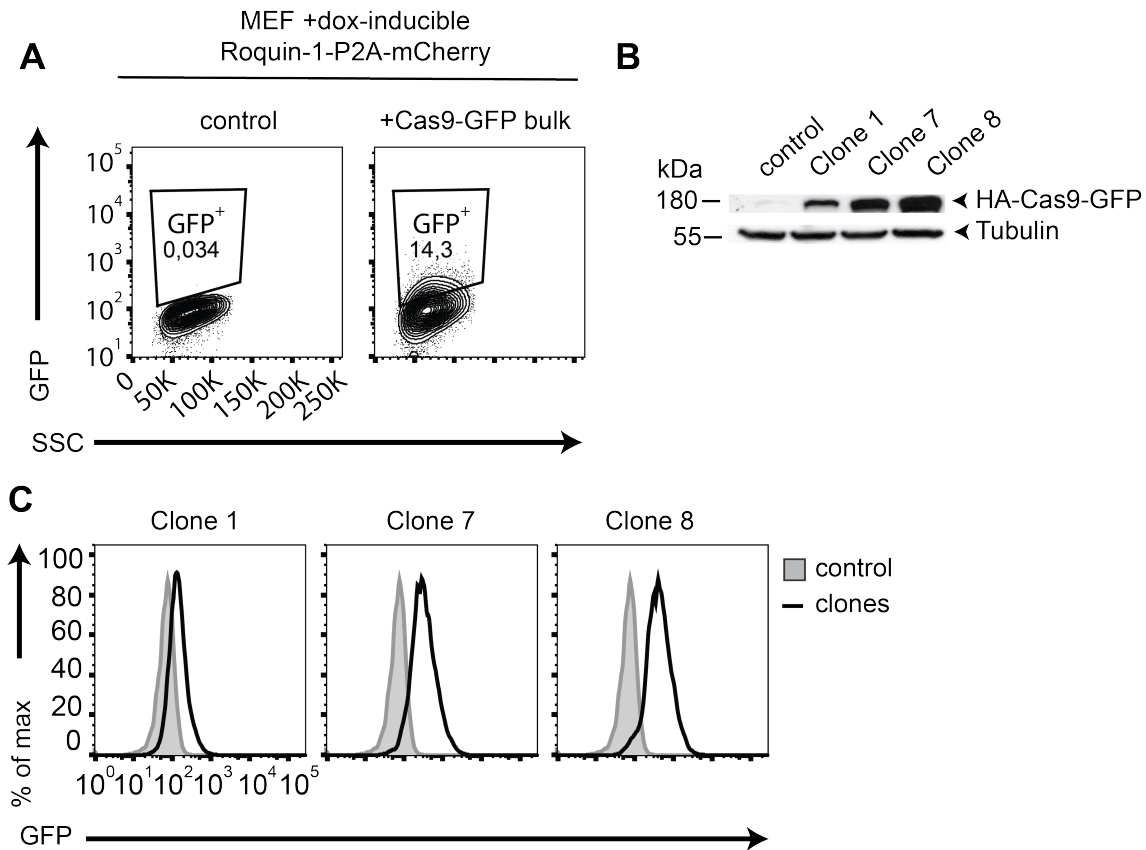


**Figure 38: Producing a stable Cas9-GFP-expressing reporter cell line.**

**(A)** Flow cytometric analysis of GFP expression of doxycycline (dox)-inducible Roquin-1-P2A-mCherry-expressing MEF cells upon stable transduction with Cas9-GFP. Cells were transduced with Cas9-GFP expressing lentivirus (bulk) or left untransduced (control). **(B)** Immunoblot analysis of HA-Cas9-GFP expression on whole cell extracts from single cell clones of Cas9-GFP expressing bulk cells in **(A)**. HA-Cas9-GFP expression is shown in comparison to untransduced control cells. **(C)** Flow cytometric analysis of GFP expression of single cell clones in **(B)**. GFP expression is shown in comparison to untransduced control cells (grey).

#### 4.2.2.2 Primary CRISPR/Cas9 screen and data analysis

Once pre-screening preparations including establishment of the reporter cell line, puromycin titration, lentiviral library production and -titration were completed (Chapter 3.2.10), the genome-wide CRISPR/Cas9 screen was initiated (Figure 39).

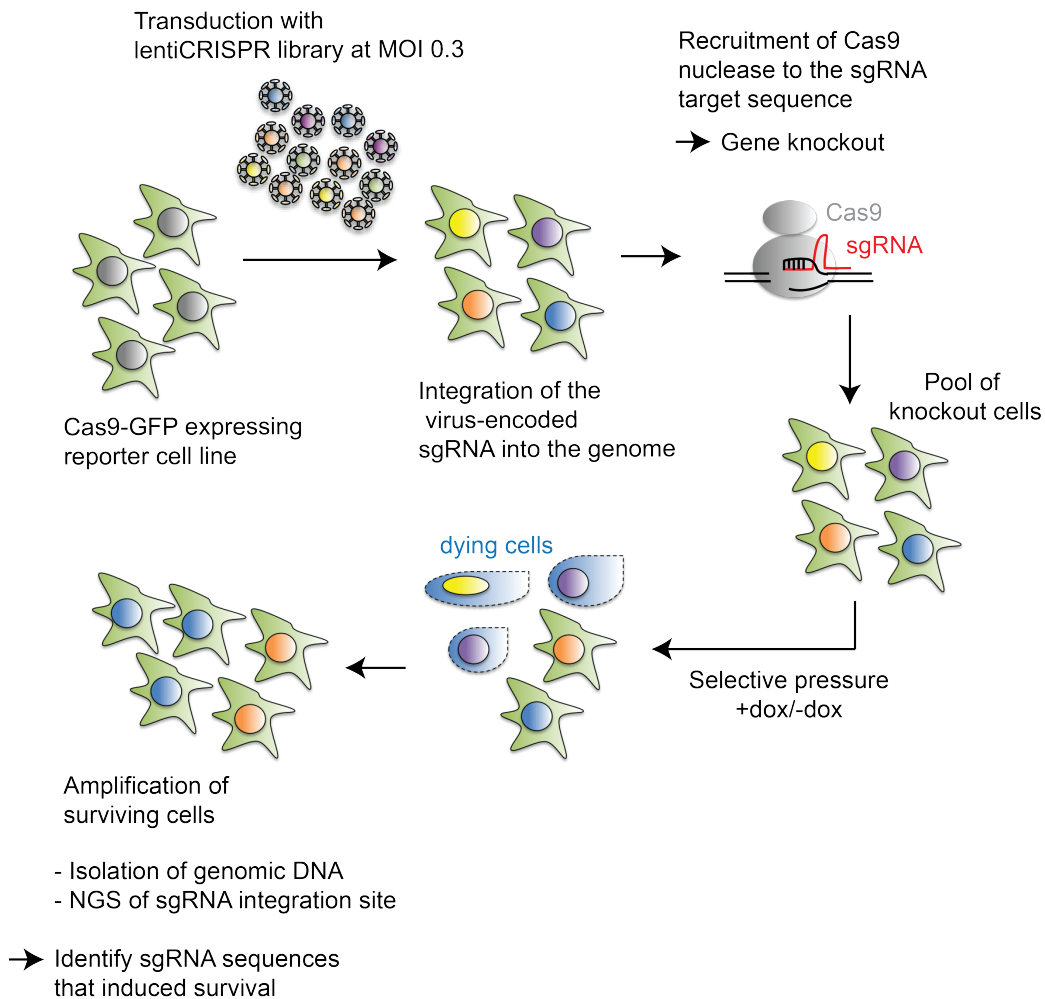


**Figure 39: Positive selection CRISPR/Cas9 screen.**

Schematic representation of the screen workflow. Stable Cas9-GFP expressing MEF reporter cells with doxycycline (dox)-inducible Roquin-1-P2A-mCherry expression were transduced with the two plasmid system Mouse GeCKO v2 Library (Addgene). The library contains 130,209 sgRNA sequences cloned into the lentiGuide vector. 20,611 genes of the mouse genome are targeted with 6 sgRNAs each, 1175 miRNAs are targeted by 4 sgRNAs each, and 1000 non-targeting controls were included. Reporter cells were infected at a low MOI to ensure single copy sgRNA integration, and infected cells were selected with puromycin. Upon expression of Cas9 and sgRNA, double strand breaks were created at the sgRNA target sites, leading to disruption of a different protein-coding gene in each cell. After seven days of selection, one pool of knockout cells was treated with dox to induce Roquin-1-mediated cell death and a second pool of knockout cells is left untreated. Cells that survived due to deletion of a gene that is indispensable for Roquin-1-induced cell death were proliferating and thereby amplifying the sgRNA sequence, which was lentivirally, integrated into the genome. Isolation of genomic DNA and deep sequencing of sgRNA integration sites revealed which sgRNA, i.e. deletion of which gene was responsible for the rescue phenotype.

The screen and all follow-up experiments were performed in collaboration with Dr. Kai Höfig. To ensure single copy sgRNA integration, we aimed at a multiplicity of infection (MOI) of 0.3, meaning that each cell was infected on average with 0.3 viruses. According to the Poisson distribution, only 3 % of cells are predicted to contain more

than one lentiviral integration at MOI 0.3, while 74 % of cells contain no integration.  $1.8 \times 10^8$  reporter cells were infected with the lentiviral library to ensure full library coverage with 300 infected cells per sgRNA.  $5.0 \times 10^7$  cells were harvested for genomic DNA (gDNA) extraction 24 h after infection for evaluation of the initial library complexity and coverage. After elimination of uninfected cells by puromycin selection, maintenance of a pool of  $5.0 \times 10^7$  cells was sufficient to ensure the initial complexity of the library. The timeline of the screening procedure is shown in Figure 40A.

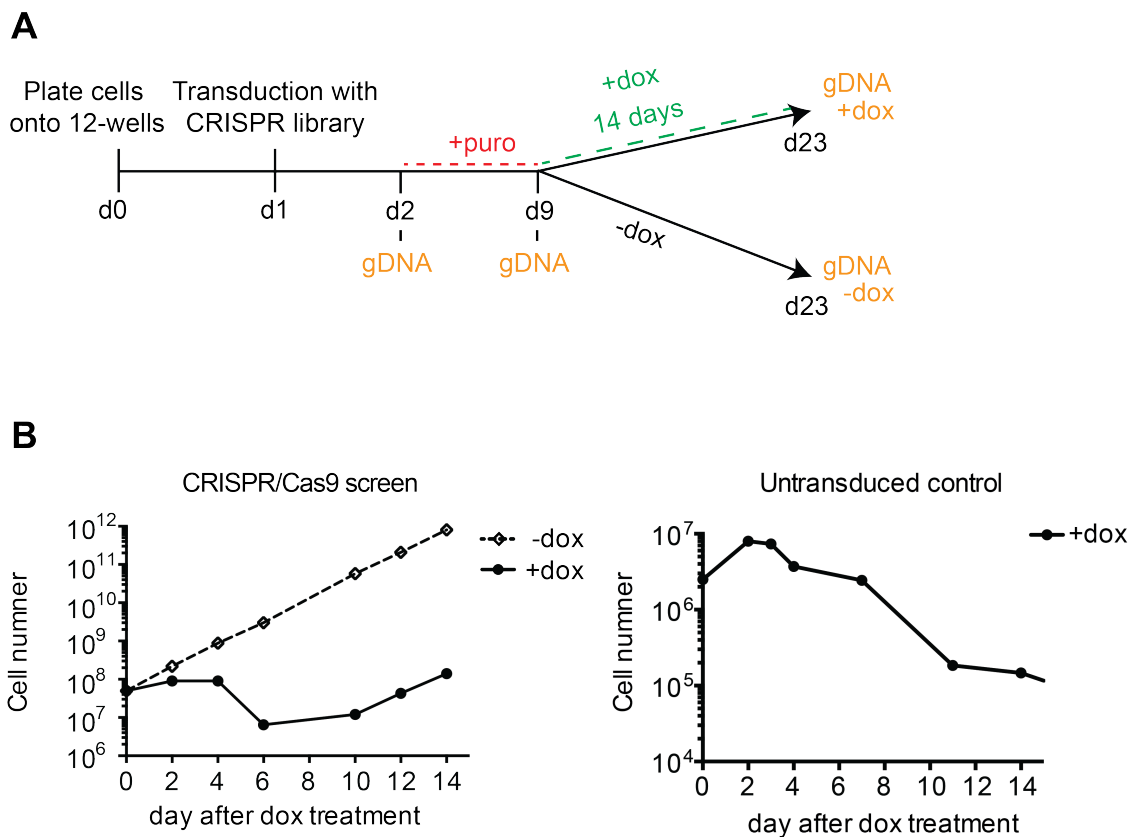


**Figure 40: Genome-wide CRISPR/Cas9 screen for mediators of Roquin-1-induced cell death.**

**(A)** Schematic representation of the screen workflow. On d0,  $9.0 \times 10^7$  reporter cells were seeded into 30 12-well plates with 250,000 cells per well. 24 h later, cells were transduced with the lentiCRISPR library at MOI 0.3. Starting 30 h after transduction, cells were cultured in the presence of  $2 \mu\text{g/ml}$  puromycin. After 7 days of puromycin selection, cells were split into two cultures and  $5.0 \times 10^7$  cells each were treated with  $1 \mu\text{g/ml}$  doxycycline (dox) to induce Roquin-1 overexpression (+dox) or were left untreated (-dox). Dox treatment was continued for 14 days. Genomic DNA was isolated from  $5.0 \times 10^7$  cells (d2, d9) or  $3.5 \times 10^7$  cells (d23+dox, d23-dox) on the indicated days. **(B)** Growth curves of dox-treated (+dox) and untreated cells (-dox) from the CRISPR screen versus dox-treated untransduced reporter cells (untransduced control). The CRISPR/Cas9 screen was performed in collaboration with Dr. Kai Höfig.

Following doxycycline treatment of half of the cell pool on day 9, cells started dying in response to overexpression of Roquin-1 as expected (Figure 40B), while the untreated

half showed normal exponential cell growth. The cell number of the doxycycline-treated sample declined drastically ( $> 1$  log-level) until day 6 of treatment, however, starting from day 8, surviving cells started to grow out, reaching normal exponential growth on day 10. Cell survival was clearly caused as a consequence of infection with the CRISPR library, since untransduced control reporter cells did neither start to grow eight days after Roquin-1 overexpression was induced, nor at later time points (Figure 40B). Genomic DNA was extracted from the cell pool on d2 and d9 before doxycycline stimulation and from the untreated sample on d23 in order to assess how the initial library complexity changed over time without selective pressure (Chapter 3.2.3.2). On the other hand, gDNA extracted from the doxycycline-surviving cell pool on d23 contained the information which sgRNAs were responsible for the rescue from Roquin-1-induced cell death. Integrated sgRNA sequences were amplified from genomic DNA in a two-step PCR reaction as described in chapter 3.2.10 and final PCR products were subjected to NGS in the laboratory of Dr. Helmut Blum, Gene Center Munich.

Analysis of deep sequencing data was performed by Dr. Dirk Repsilber and Dr. Brynjar Bjarnason, Örebro Universitet, Sweden. Evaluation of raw counts for each sgRNA confirmed a fairly even distribution of the library in the sample taken 24 h after infection (d2) (Figure 41, upper left). At this time point, 98.5 % of all sgRNA sequences were identified in the genomes of the MEF cell pool, indicating that the library amplification, virus production and MEF infection had maintained the original complexity of the library. Uniform sgRNA distribution hardly changed over 7 days of puromycin selection (d8) (Figure 41, upper right). At the end of the screen on day 23, in the sample that was not treated with doxycycline (d23-dox) some sgRNA sequences were overrepresented up to 12-fold, while others were depleted (Figure 41, lower left). This was expected, since cells carrying sgRNAs that negatively affect cell survival are outgrown by those where the sgRNA has no effect or even a positive influence on cell proliferation. This sample served as a very good negative control, because it allowed us to differentiate between Roquin-1-specific candidates and factors that have a general function in cell death or related pathways. After doxycycline-induced Roquin-1 overexpression (d23+dox) some sgRNA sequences were massively enriched (up to 2000-fold), but most had disappeared completely (Figure 41, lower right). This indicates a successful outcome of our positive selection screen.

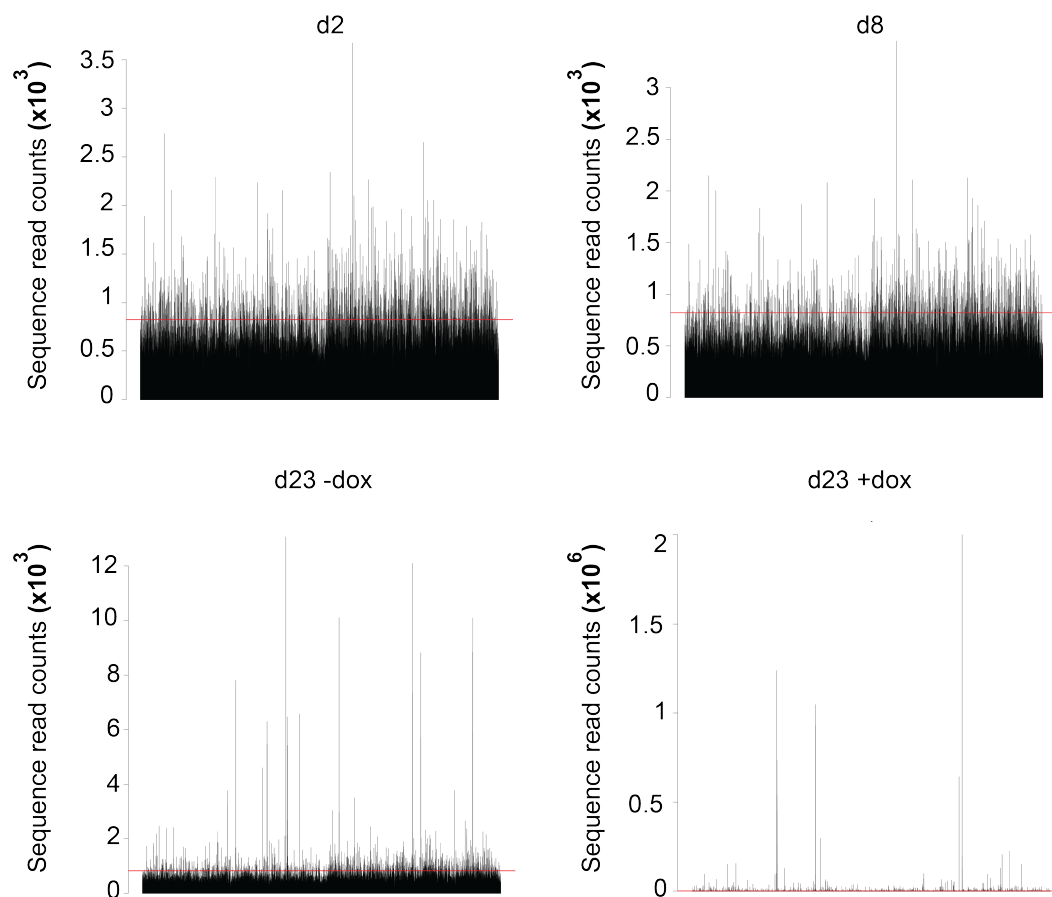


**Figure 41: Raw counts of individual sgRNA sequences.**

Raw counts of concatenated sgRNA sequences as obtained by deep sequencing of final PCR products. Obtained sequences were demultiplexed, trimmed and aligned to the concatenated sequences of all ~130,000 sgRNAs by Dr. Dirk Repsilber.

#### 4.2.2.3 Identification of candidates using MAGeCK

Dirk Repsilber and Brynjar Bjarnason employed Model- based Analysis of Genome-wide CRISPR/Cas9 Knockout (MAGeCK) in order to identify those genes where sgRNA-mediated gene knockout induced survival of Roquin-1-overexpression (Li et al., 2014a). The MAGeCK algorithm consists of four steps: First, sgRNA read counts in each sample are median-normalized in order to correct for differences in sequencing depths between different samples. Next, sgRNAs are ranked according to the number of read counts. sgRNAs that are not involved in the rescue phenotype should show a uniform distribution across treated and untreated samples. sgRNAs, however, that rank significantly higher in the treated than in control samples, are prioritized. Significance is calculated with the mean variance model, i.e. considering mean and variance of sgRNA read counts over several replicate samples. Finally, the list of significantly enriched sgRNAs is assembled and genes are ranked based on how many

sgRNAs targeting the same gene are significantly enriched (Li et al., 2014a). In our screen, MAGeCK analysis resulted in the identification of 31 protein-coding genes where multiple of the six gene-targeting sgRNAs from the library were significantly enriched in the doxycycline-surviving cell pool as compared to the untreated cell pool at the end of the screen (d23) (Table 28). Although 1,175 miRNAs were likewise targeted by 4 sgRNAs each, none was found enriched in the doxycycline-surviving cell pool.

**Table 28: Ranked list of candidates resulting from MAGeCK analysis comparing the sample d23-dox with sample d23+dox.**

Rank	Gene name	q-value	Fold change	Rank	Gene name	q-value	Fold change
1	Rc3h1	4.42E-10	2,697.6	17	Extl1	3.38E-02	73.4
2	Med24	4.42E-10	2,151.0	18	Cxxc1	9.54E-02	69.1
3	Med25	2.18E-12	1,478.7	19	Ext1	4.22E-04	65.8
4	Med17	5.83E-05	1,342.7	20	Usp7	2.27E-04	59.8
5	Med16	1.52E-02	1,255.2	21	Trim29	3.90E-02	51.2
6	Med26	4.22E-04	885.9	22	Cacybp	5.98E-02	50.2
7	Rc3h2	1.76E-02	470.8	23	B3galt6	3.22E-04	44.3
8	Kmt2b/Wbp7	3.48E-03	440.2	24	Pcbp1	8.71E-02	26.7
9	Rhoh	8.75E-02	344.0	25	Nxf1	8.44E-03	23.0
10	Snw1	2.50E-02	198.6	26	Rbm33	4.87E-02	17.5
11	Ext2	5.73E-02	162.5	27	Trim28	3.48E-03	15.2
12	Extl3	1.08E-06	123.5	28	Kpna6	1.93E-05	10.3
13	Slc35b2	5.21E-05	98.7	29	Tada2b	2.51E-03	10.3
14	Kmt2a/ Mll1	3.65E-03	92.3	30	Phip	2.27E-04	5.1
15	Usp8	5.16E-02	92.3	31	Leprel2	5.98E-02	2.7
16	Cacul1	1.51E-04	85.3				

The fold change indicates the extent of enrichment in the doxycycline-treated sample and determines the rank, while the q-value shows the significance. Identification of Rc3h1 as the top gene necessary for Roquin-1-induced cell death (> 2000-fold enriched) was an expected positive control, since targeting sgRNAs will prevent overexpression of Roquin-1-P2A-mCherry, thereby providing the cell with the opportunity to circumvent Roquin-1-induced cell death. To help classify the remaining candidates, the STRING protein interaction database was consulted in order to identify known and predicted protein-interactions among the candidates (<http://string-db.org>). Five clusters of protein interactions were discovered. Ubiquitin-specific peptidase 7 (Usp7) and Usp8 are **deubiquitinating enzymes** involved in the removal of ubiquitin residues from proteins that were previously transferred by E3 protein ligases (Komander et al., 2009). Since Roquin-1, Roquin-2, Trim28 and Trim29 all

possess predicted or proven E3 ligase function (Vinuesa et al., 2005), this group of genes is highly interesting and may represent a network of ubiquitination/deubiquitination events to promote Roquin-1-mediated cell death signaling. Another striking protein-interaction cluster comprised several members of the **heparan sulfate synthesis pathway**. Four of five members of the Exostosin protein family (Ext1, Ext2, Extl3, Extl1) were found among the screen candidates, as well as two other proteins (Slc35b2, B3galt6) that are involved in protein glycosylation. Other interactions suggested by STRING involved the **nuclear import/export pathway** (Kpna6/Nxf1), a cluster involved in **histone methylation** (Cxxc1, Mll1, Wbp7) and interactions between subunits of the **mediator complex** (Med16, Med17, Med24, Med25, Med26).

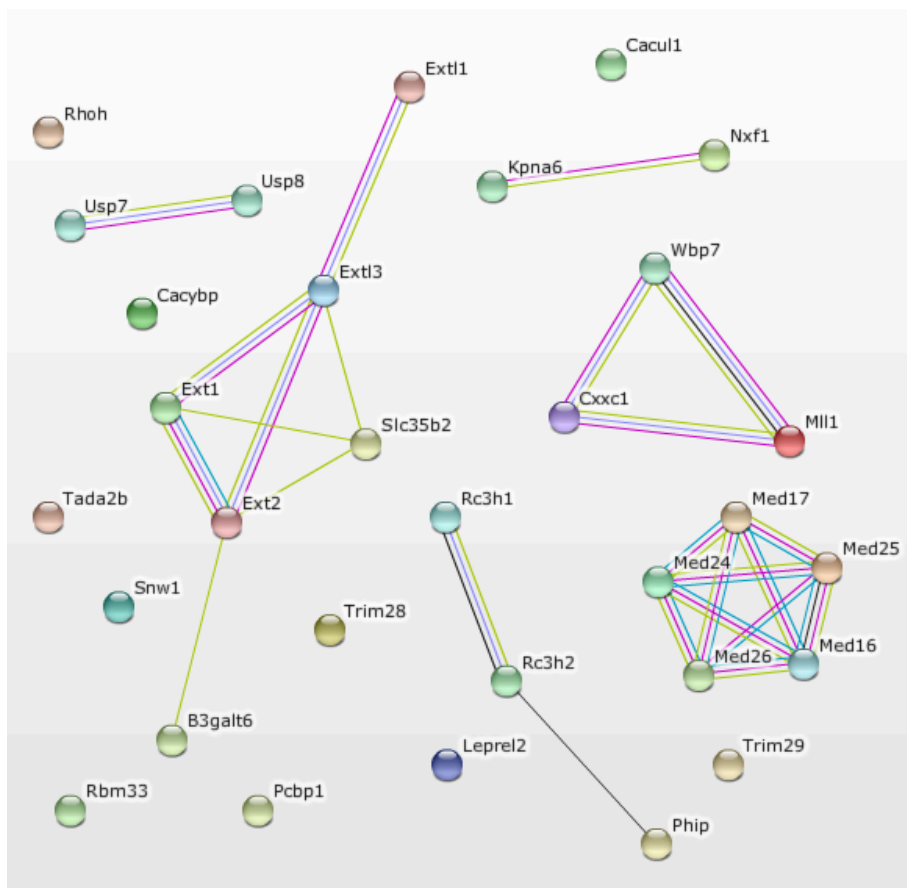


**Figure 42: Clustering of screen candidates according to known and predicted protein interactions.**

The list of screen candidates was evaluated using the STRING protein interaction database (<http://string-db.org>). Predicted protein interactions are based on coexpression (black lines), experimental protein-interaction data (pink), occurrence in databases (turquoise), homology (purple) or text mining (green).

In addition to Rc3h1, five subunits of the mediator complex were the highest-scoring candidates in the screen. The large mediator complex consists of 26 core proteins and is recruited to DNA by transcription factors to induce polymerase-II-dependent transcription of protein-coding genes (Allen & Taatjes, 2015). Thus, we had a sneaking suspicion that transcription of Roquin-1-P2A-mCherry rather than effector functions associated with Roquin-1 overexpression seemed to be affected by the knockout of these candidate genes. This could also be true for other candidates with known transcription promoting functions, such as histone methyltransferases. In order to discriminate between true Roquin-1 effector proteins and transcriptional regulators required to express Roquin-1, we decided to repeat the screen with an additional sorting step for mCherry expression at the end, which would allow us to focus only on those cells with intact Roquin-1-P2A-mCherry overexpression.

#### **4.2.2.4 Secondary CRISPR/Cas9 screen**

For the cell sorting approach, frozen cell aliquots of library-transduced reporter cells after puromycin selection (d8) from the first CRISPR/Cas9 screen were thawed and treated with doxycycline or left untreated. Cells were cultured in the presence of doxycycline for 18 instead of 14 days in order to reach to the cell number required for cell sorting and downstream processing. 14.5 % of doxycycline-treated cells were mCherry<sup>+</sup> on day 18 of doxycycline treatment as compared to uninduced control cells, indicating that indeed a large number of sgRNAs in this pool interfered with Roquin-1-P2A-mCherry overexpression. Alternatively, cells may have adapted to counteract the strong overexpression, or both. Next, cells were sorted using a BD FACSAria cell sorting machine to separate mCherry<sup>+</sup> from mCherry<sup>-</sup> cells (Figure 43). The purity of the cell populations was > 99 % for mCherry<sup>-</sup> cells, but only 67 % for the mCherry<sup>+</sup> population. This result might be due to the tendency of MEF cells to adhere to each other, or due to a loss of the mCherry fluorescence signal due to photobleaching (Shaner et al., 2005).

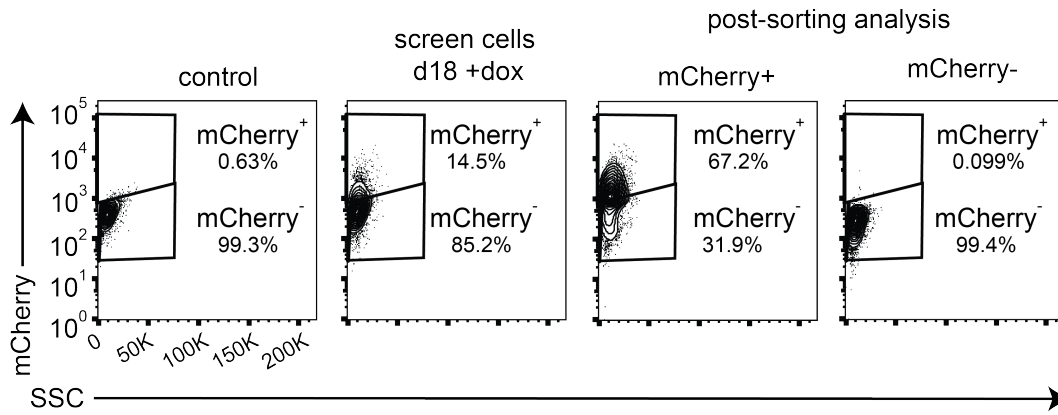


**Figure 43: Sorting of mCherry<sup>+</sup> cells from the Roquin-1-overexpression-surviving cell pool.**

Flow cytometric analysis of mCherry expression in reporter MEF cells of our secondary CRISPR/Cas9 screen, after 18 days of doxycycline treatment. Cells were sorted into mCherry<sup>+</sup> and mCherry<sup>-</sup> populations using uninduced cells as a negative reference.

After PCR-amplification of the integrated sgRNA sequences from genomic DNA obtained from both cell populations, high-throughput sequencing and data analysis were performed. In the analysis, Dirk Repsilber focused on the 31 candidates identified in the first screen, and asked whether these hits were significantly enriched in the genomes of mCherry<sup>+</sup> cells as compared to mCherry<sup>-</sup> cells and vice versa. From normalized sgRNA sequence counts the fold changes were calculated for each candidate (Table 29). A fold change < 1 means that more sgRNA counts were observed in mCherry<sup>-</sup> cells than in mCherry<sup>+</sup> cells, while a fold change > 1 points towards an enrichment in mCherry<sup>+</sup> cells. Additionally, false discovery rates (FDR) for sgRNA enrichment were calculated, with a FDR < 0.05 indicating significant enrichment (shown in red in Table 29).

The most prominent result of our secondary CRISPR/Cas9 screen was that sgRNA sequences targeting mediator complex proteins were strongly and significantly enriched in the mCherry<sup>-</sup> sample. Since the mediator complex functions as a general transcriptional co-activator, it might be concluded that sgRNA-mediated knockout of some of its components represses overexpression of Roquin-1-P2A-mCherry. Surprisingly, Rc3h1 was not found enriched in mCherry<sup>-</sup> samples. This might mean that in addition to overexpressed Roquin-1, which is coexpressed with mCherry, a certain amount of endogenous Roquin-1 may be required to induce cell death.

**Table 29: MAGeCK analysis of candidate enrichment in mCherry<sup>+</sup> and mCherry<sup>-</sup> cells.**

Gene name	Fold change	FDR mCherry <sup>-</sup>	FDR mCherry <sup>+</sup>	
Med24	0.35	6.07E-06	1.00E+00	Mediator complex
Med25	0.35	6.07E-06	1.00E+00	Ubiquitin conjugation / Deubiquitination
Med17	0.14	3.45E-04	7.40E-01	Heparan sulfate biosynthesis
Med16	0.18	1.19E-03	7.40E-01	Histonmethyltransferases
Med26	0.36	1.03E-02	1.00E+00	Nuclear import/export
Rc3h1	4.14	1.00E+00	1.22E-01	others
Rc3h2	5.78	1.00E+00	3.65E-01	
Usp8	2.41	1.00E+00	1.00E+00	
Usp7	3.11	1.00E+00	6.95E-01	
Trim29	0.41	3.83E-02	1.00E+00	
Cacybp	62.16	1.00E+00	1.47E-03	
Trim28	0.90	6.97E-01	1.00E+00	
Ext2	22.76	1.00E+00	4.77E-02	
Extl3	6.58	1.00E+00	2.49E-02	
Ext1	51.79	1.00E+00	5.89E-03	
Extl1	10.63	1.00E+00	6.73E-01	
Slc35b2	16.76	1.00E+00	2.19E-03	
B3galt6	3.45	1.00E+00	1.57E-02	
Kmt2b	2.05	1.00E+00	1.00E+00	
Kmt2a	2.98	1.00E+00	6.86E-01	
Nxf1	5.07	1.00E+00	1.43E-01	
Kpna6	102.92	1.00E+00	6.07E-06	
Rbm33	3.40	1.00E+00	6.73E-01	
Tada2b	3.26	1.00E+00	1.43E-01	
Phip	2.12	7.91E-01	1.00E+00	
Cacul1	128.31	1.00E+00	6.07E-06	

Despite the surprising result for Roquin-1-targeting sgRNAs, this approach served to successfully weed out factors that generally interfere with transcription such as the mediator complex and increased our confidence in the remaining candidates.

#### 4.2.2.5 Identification of promising candidates

Of the eight candidates that were significantly enriched in mCherry<sup>+</sup> cells, five turned out to be highly interesting due to their function in a shared pathway. Ext1, Ext2 and Extl3 belong to the Exostosin protein family. Moreover, the family member Extl1 was identified in the primary screen and also enriched in mCherry<sup>+</sup> cells, though not significantly. Together with the similarly enriched candidates Slc35b2 and B3galt6, EXT family proteins are involved in the biosynthesis of heparan sulfate proteoglycans (Duncan et al., 2001). Heparan sulfates are negatively charged oligosaccharide chains

that are covalently linked to selective serine residues on core proteins via the action of EXT glycosyl transferases. The resulting heparan sulfate proteoglycans are transported to the outer surface of the cell, where they mediate cell migration and cell-to-cell contact (Simon Davis & Parish, 2013). Looking at the normalized counts of each individual sgRNA in mCherry<sup>+</sup> versus mCherry<sup>-</sup> cells, it was obvious that for all three Ext family members as well as for Slc35b2 and B3galt6, three or even four individual sgRNAs were identified by deep sequencing, and most importantly, all of them occurred prevalently in mCherry<sup>+</sup> cells (Figure 44).

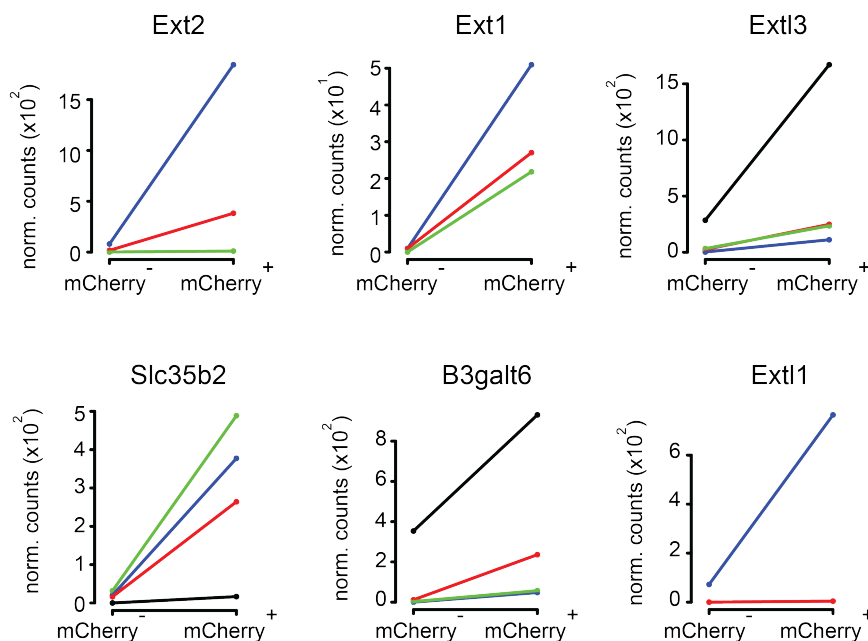


**Figure 44: sgRNA sequence representation in mCherry<sup>+</sup> and mCherry<sup>-</sup> cells for candidates of the heparan sulfate biosynthesis pathway.**

Normalized sgRNA sequence counts derived from genomes of mCherry<sup>+</sup> and mCherry<sup>-</sup> cell populations shown for six candidates involved in heparan sulfate synthesis. Colors represent different sgRNAs targeting the same gene. Each candidate gene was targeted by six sgRNAs, but sgRNA sequences that were neither present in mCherry<sup>+</sup> nor in mCherry<sup>-</sup> samples were not depicted. This data set was provided by Dr. Dirk Repsilber.

Even for Extl1, where enrichment in mCherry<sup>+</sup> cells was not significant, one sgRNA showed a strong overrepresentation in mCherry<sup>+</sup> cells. Discovery of several critical players of one pathway, which are represented by multiple sgRNAs per gene, is the ideal outcome of a genome-wide screen. It now remains to be solved how the heparan sulfate proteoglycan synthesis pathway is linked to Roquin-1-induced cell death. Interestingly, EXT family proteins have been described as tumor suppressor genes in the literature (Busse-Wicher et al., 2014). Mutations of either EXT1 or EXT2, but not of their paralogs EXTL1, EXTL2 or EXTL3, lead to the hereditary multiple

osteochondromas (HMO) disease in humans, which is characterized by the formation of multiple bone tumors (Jennes et al., 2009). How exactly EXT1 and EXT2 elicit their role as tumor suppressors is still unknown. Their loss might prevent the generation of certain proteoglycan(s) that restrict aberrant cell growth, which might equally be responsible for Roquin-1-induced cell death. Identifying these unknown factors will be a central aim of future studies. Other interesting candidates that emerged from the screen were proteins linked to the E3 ligase function of Roquin-1. *Rc3h2*, encoding the Roquin paralog Roquin-2, was > 400-fold increased in the primary screen and showed a strong, but non-significant enrichment in mCherry<sup>+</sup> cells, represented by two sgRNAs (Figure 45). Roquin-1 and Roquin-2 might function as heterodimers here, as it is often observed among members of RBP families (e.g. the FMR family chapter 1.1.4.1). Alternatively, Roquin-2 might act as an E3 ligase downstream of Roquin-1, ubiquitinating the apoptosis-signal regulating kinase 1 (ASK-1) (Maruyama et al., 2014). Other highly interesting, ubiquitination-related candidates were Cacybp, a bridging factor of calcium-dependent ubiquitination, and the deubiquitinases Usp7 and Usp8. These candidates will be central to the discussion (Chapter 5.2).

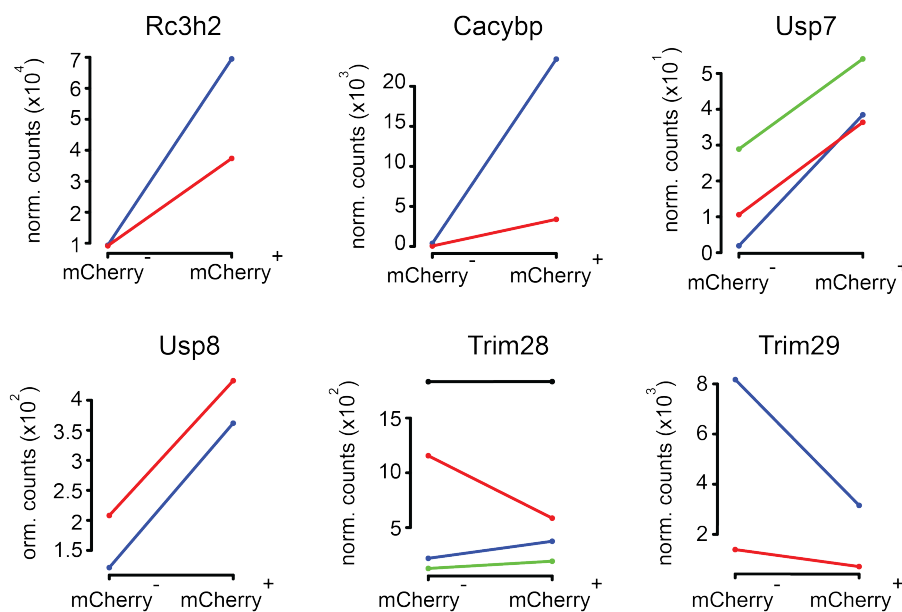


**Figure 45: sgRNA sequence representation in mCherry<sup>+</sup> and mCherry<sup>-</sup> cells for candidates of the ubiquitin conjugation and deubiquitination pathway.**

Normalized sgRNA counts derived from genomes of mCherry<sup>+</sup> and mCherry<sup>-</sup> cell populations shown for six candidates involved in ubiquitination/deubiquitination of proteins. Colors represent different sgRNAs targeting the same gene. Each candidate gene was targeted by six sgRNAs, but sgRNA sequences that were neither present in mCherry<sup>+</sup> nor in mCherry<sup>-</sup> samples were not depicted. This data set was provided by Dr. Dirk Repsilber.

---

To conclude, our genome-wide CRISPR/Cas9 screen led to the identification of promising candidates with a possible role in Roquin-1-induced cell death. Further evaluation of target proteins involved in ubiquitin conjugation will likely reveal exciting new insights into Roquin-1's putative role as an E3 ligase. Finding several essential members of the heparan sulfate synthesis pathway among our top candidates enormously strengthened our confidence in the performance of the CRISPR/Cas9 technology as applied in this whole-genome screening approach. As unexpected as it was to uncover a potential role for heparan sulfates in Roquin-1-mediated cell death, it bears the potential to cast light on a Roquin-1 function that until now is entirely unknown.

## 5 Discussion

In this research project, two different high-throughput screening technologies were applied in order to identify cofactors of Roquin-1-mediated post-transcriptional gene regulation. In a targeted siRNA screen, we screened for cofactors of Roquin-1 in post-transcriptional repression of the inducible T cell costimulator ICOS, while a genome-wide CRISPR/Cas9 screen aimed at the discovery of gene products required for Roquin-1-induced cell death. In this discussion, I will first compare the accomplishment and results of both screening approaches, emphasizing the particular challenges faced within each screen. After developing hit validation strategies for both screening approaches, I will then focus on the uncharacterized protein Nufip2, which arose as a promising candidate from the RNAi screen. Based on the functional validation of Nufip2 as a cofactor of Roquin-1 that was part of this research work, I will discuss the burning question for the function of Nufip2 in Roquin-1-mediated post-transcriptional gene regulation, and how this can be solved experimentally.

### 5.1 Accomplishment and data analysis of two high-throughput screens

#### 5.1.1 Targeted siRNA screen for cofactors of Roquin-1-mediated ICOS regulation

When this research project was started, loss-of function screening in mammalian cells was restricted to the RNA-interference technology (Chapter 1.1.3). In collaboration with the Functional Genomics Center at La Jolla Institute for Allergy and Immunology, we decided to set up an arrayed reporter-based siRNA screen for Roquin-1 function. I generated a HeLa reporter cell line where downregulation of an ICOS reporter in response to doxycycline-inducible Roquin-1-P2A-mCherry overexpression was quantified in a flow cytometric assay. The suitability of the cell line for high-throughput screening was confirmed in pilot assays without siRNAs (Figure 12) and after transfection with control siRNAs (Figure 13). To increase the screening throughput, I established fluorescent cell barcoding with a 2x2 barcoding matrix that was capable of enhancing the screening throughput 4-fold (Figure 14). However, due to the complexity of the screening assay we were unable to perform a genome-scale screen, and decided for a targeted screen instead. We thus screened six preassembled protein subset libraries (Figure 15) and a customized siRNA library of RBPs, stress

granule-, P body- and mRNA decay factors (Figure 17). Screening of the customized siRNA library resulted in the assembly of a primary target list of candidate genes (Table 27). This list included several, but not all proteins being referred to as Roquin-1 cofactors in the literature. Two validated cofactors of Roquin-1, the enhancer of mRNA decapping Edc4 (Glasmacher, 2010) and the scaffolding subunit of the Ccr4-Caf1-Not deadenylation complex Cnot1 (Leppek et al., 2013; Murakawa et al., 2015) were identified in the screen. However, considering the fact that both proteins are part of large multi-protein complexes, (Figure 1) one would have expected to find more than just one representative protein of each complex. Next to Edc4, an interaction with Roquin-1 has been shown for the RNA helicase Rck, which is also part of the mRNA decapping complex (Glasmacher et al., 2010). Moreover, Roquin-1 has been reported to be co-immunoprecipitated with several more proteins of the Ccr4-Caf1-Not complex including the catalytic subunits Cnot7 and Cnot8 (Leppek et al., 2013; Murakawa et al., 2015). The nonappearance of Edc4, Rck, Cnot7 and Cnot8 in the target list can have multiple reasons. First of all, knockdown of one protein might be compensated by a paralog. In line with this, it has been shown that the deadenylases Cnot7 and Cnot8 can largely compensate for each other's function (Aslam et al., 2009). Furthermore, the impact of certain cofactors might be target-specific, as in the case of Regnase-1. Regnase-1 was shown to be indispensable for Roquin-1-mediated repression of the CDE260 minimal response element from the *TNF* mRNA (Jeltsch et al., 2014), and was therefore expected to be likewise required for Roquin-1 dependent *ICOS* regulation. However, our overexpression analysis of Roquin-1 and Regnase-1 in knockout MEF cells revealed that both proteins could work independently of each other on *ICOS* (Figure 18), which explains why Regnase-1 was missing in the target list. The last, most prominent reason for the lack of certain known cofactors in the list of candidate genes may be insufficient protein knockdown. siRNAs interfere with their target gene expression at the transcript level, leading to incomplete gene knockdown since some transcripts naturally escape the silencing mechanism (Chapter 1.1.3). This characteristic of RNAi-based screening approaches is responsible for a large number of false negatives in primary hit lists (Booker et al., 2011).

Besides false negatives, the identification of false positives is a major challenge when analyzing RNAi screening data. Screening the six preassembled siRNA libraries as well as the customized siRNA library arrived at hit rates of approximately 5 to 7 % (Figure 15). Whether this is high or low compared to other siRNA screens is hard to judge, since the definition of a hit is different for individual researchers. Primary hit rates

range from 2 – 3 % up to 17 %, depending on the chosen threshold (Said et al., 2014). While the threshold of genome-wide screens is often set to  $Z > 3$  due to limited follow-up capacities (Sharma & Rao, 2009), targeted screens start with a much lower number of siRNAs to be screened and can thus afford to include all candidates with  $Z > 2$ . Since the former option bears the risk of false negatives, we decided to use  $Z > 2$  as the cutoff, thus taking higher rates of false positives into account.

For validation, I deconvoluted the siRNA pools to determine phenotypic effect as well as the knockdown efficiency for each individual siRNA. To our big surprise, only two of 14 candidates passed this first step of validation (Figure 19, Figure 21, Appendix II, Appendix III). Interestingly, the fact that false positive candidates dominate hit lists of primary RNAi screens has been more and more acknowledged (personal communication at the screening conference “Discovery on Target”, Boston, September 2015). Already a decade ago, it has been described that siRNAs can cause off-target knockdowns, which is thought to be due to miRNA-like repression of mRNAs that harbor seed-region complementarity (Birmingham et al., 2006). In principle, 19-nt-long siRNAs are carefully designed to show perfect and exclusive complementarity to one RNA of the whole transcriptome, but nonetheless, their 5' ends can mimic the 6 - 8 nt long seed regions of endogenous miRNAs, resulting in hundreds of potential target sites bearing seed-region complementarity. Recently, researchers realized the magnitude of this phenomenon and its impact on RNAi screens (Marine et al., 2012; Sudbery et al., 2010). Marine and colleagues performed a Wnt/ $\beta$ -catenin-Luc siRNA screen using a library in which one gene is targeted by multiple individual duplexes. Disturbingly, they saw almost no correlation between the results of different siRNA duplexes targeting the same gene, but a stronger correlation for individual duplexes sharing the same seed sequence but designed to target different genes (Marine et al., 2012). In their screen, the seed sequence appeared to be the main determinant of siRNA performance. This led to the conclusion that primary hit lists are dominated by false-positives, resulting from seed-based off-target effects (Marine et al., 2012). Based on this finding it appears logical that of 14 RNA-binding proteins identified in my primary screen only two emerged as true cofactors of Roquin-1.

Several improvements in the set-up of an RNAi screen can help to avoid false positives, some of which had already been considered in our approach. First of all, a gain-of-function screen was favored over a loss-of-function screen. When looking for the loss of a certain phenotype, false positives can arise from all proteins with functions in

general cellular processes, such as cell viability, transcription or translation. Such proteins can inhibit reporter expression regardless of the pathway that is supposed to be screened. Moreover, upon advice of Dr. Sonia Sharma from the Functional Genomics Center at *La Jolla Institute for Allergy and Immunology*, we administered the siRNA pools at a low concentration (20 nM total), which limits off-target effects due to low individual siRNA concentrations. However, since our primary hit list still included  $\approx 85\%$  false positive candidates, I propose these additional changes to reduce this number in future screening assays:

- Use of second-generation siRNA libraries such as Dharmacon ON-TARGET*plus* instead of siGENOME. siRNA duplexes consist of a sense and an antisense strand, whereby only the antisense strand is intended to be incorporated into the RISC complex for cleavage of perfectly complementary target sequences (Chapter 1.1.3). Off-target effects can, however, arise from unwanted RISC loading of the sense strand (Schwarz et al., 2003). In the ON-TARGET*plus* library, chemical modifications of the siRNA duplexes bias strand loading towards the antisense strand (Dharmacon; Vaish et al., 2011). Moreover, seed sequences from known mammalian microRNAs are avoided in second generation siRNA libraries (Dharmacon).
- Take all positively scoring candidates arising from a primary screen with siRNA pools into a secondary screen with a custom-arrayed library of 4 - 6 individual duplexes per gene.
- Designing “C9-11 controls” for all hits arising from the secondary screen. Here, bases 9-11 of the siRNA duplex are exchanged by their complementary bases, thereby prohibiting endonucleolytic cleavage of the perfectly complementary target mRNA, while seed-based off-target knockdowns are unimpaired. For true candidates, exchanging bases 9-11 should abrogate the phenotypic effect, while its persistence indicates a false positive candidate (Buehler et al., 2012a).
- For large data sets screened with individual duplexes, two different publicly available software tools, Genome-wide Enrichment for Seed Sequence match (GESS) (Sigoillot et al., 2012) and Haystack (Buehler et al., 2012b), can help to identify seed sequence-caused off-target effects of primary screen data prior to candidate validation.

### 5.1.2 CRISPR/Cas9 screen for cofactors of Roquin-1-induced cell death

While the targeted siRNA screen was ongoing, pooled lentiviral CRISPR/Cas9 libraries (Chapter 1.2.2) were developed as an alternative to RNAi based screens. Here, genome-covering single guide RNAs (sgRNAs) are delivered simultaneously to a large cell pool together with the Cas9 nuclease, and initiate targeted gene knockouts (Koike-Yusa et al., 2013; Shalem et al., 2014; Wang et al., 2014; Zhou et al., 2014). By targeting the genomic loci rather than the transcript level, the CRISPR/Cas9 technology overcomes one of the big challenges of RNAi: the incomplete gene knockdown leading to a high frequency of false negatives in a screen. Due to the advantages that this system offers, we decided to employ a CRISPR/Cas9 rather than an RNAi screen for our second screening approach searching for cofactors of Roquin-1-induced cell death.

I found out that Roquin-1-induced cell death was elicited when a reporter cell line with doxycycline-inducible Roquin-1-P2A-mCherry was stimulated with doxycycline for >24 h (Figure 37). This aspect was not part of the first screen, where a shorter doxycycline treatment (18 h) was employed that was insufficient to induce cell death. As the readout of our screen was cell death, no  $Z'$  factors needed to be calculated beforehand. Instead, the most important pre-experiment was the titration of the lentiviral library to ensure single copy integration of the sgRNA cassette into each cell (Chapter 3.2.10.2). When starting the screen, multiple pooled lentiviral CRISPR/Cas9 libraries were available at Addgene. Having a MEF reporter cell line at hand, we decided to employ the mouse GeCKO v2.0 library designed by the lab of Dr. Feng Zhang (MIT, Boston, USA). The mouse GeCKO library contains  $\approx 130,000$  individual sgRNA lentiviral plasmids, with 6 sgRNAs targeting each of the 20,611 genes of the mouse genome (Sanjana et al., 2014). 24 h after transduction of reporter cells with the CRISPR/Cas9 library, deep sequencing of reporter cells revealed that >98% of sgRNAs were represented in the cell pool in more or less similar frequencies, indicating successful library propagation and almost unbiased transduction of the MEF cell line (Figure 41). This analysis required bioinformatics assistance, which is a major drawback of pooled screening. After culturing library-infected cells for 14 days with or without doxycycline (+/-dox), deep sequencing and subsequent statistical data analysis revealed which sgRNAs were selectively enriched in the cells that had survived Roquin-1 overexpression (+dox) compared to those that were left untreated (-dox) (Table 28).

Since no screening results have been published for the mouse Gecko library yet, our findings can only be compared to screening data obtained with different CRISPR libraries. The first Gecko library expressed both Cas9 and the sgRNA from one vector to target  $\approx 18,000$  genes of the human genome containing 3 - 4 sgRNAs per gene (Shalem et al., 2014). This library was successfully applied in a protein kinase inhibitor screen and led to the identification of several known, but also unknown factors that conferred inhibitor resistance. However, sgRNA cleavage efficiencies and off-target hits were not addressed in this publication. The CRISPR library designed by Eric Lander's group, by contrast, was evaluated in more detail. When screening a haploid cell line for essential factors of the DNA mismatch repair (MMR) pathway, the 20 most abundant sgRNAs were directed against the four known components of the MMR pathway, while only few other sgRNAs scored positively (Wang et al., 2014). In combination with a low number of off-target effects found for the investigated sgRNAs, this result suggested that in contrast to RNAi, CRISPR screens are characterized by a low false discovery rate. For the identified candidates, at least 4 out of 10 sgRNAs scored positively, indicating that for some candidates up to 50 % of sgRNAs worked efficiently. This is in good accordance with the results of our CRISPR screen. For the only known positive control Roquin-1 itself as well as candidates of the ubiquitin conjugation and the glycosylation pathway (Figure 44, Figure 45), two to four out of the six provided sgRNAs were represented in the final cell pool. The mouse Gecko library has only been available for two years, and the six sgRNAs targeting each gene were randomly distributed over 3 - 4 coding exons (Sanjana et al., 2014). It can therefore be anticipated that with increasing knowledge on sgRNA performance, better design of CRISPR/Cas9 libraries with higher cleavage efficiencies will be possible in the future. However, the outcome of our screen, identifying Roquin-1 as the top candidate as well as complete networks of proteins, demonstrates that usage of early CRISPR/Cas9 libraries can as well lead to a successful result.

### 5.1.3 Comparison of both screening approaches

Comparing both screening approaches (Table 30), the arrayed siRNA screen was the method of choice for a reporter-based screen to investigate Roquin-1- induced post-transcriptional gene regulation. Pooled screening would have required repeated sorting steps for cells with the desired reporter expression, which is both time-consuming and expensive and therefore disadvantageous. A pooled CRISPR/Cas9 screen was, however, chosen to investigate Roquin-1-induced cell death, since positive

selection could easily be achieved by application of doxycycline in this case. The arrayed siRNA screen included processing hundreds of plates, thereby restricting the assay to a targeted screen. By contrast, all genes of the mouse genome were targeted in the CRISPR/Cas9 screen. This higher depth of information did, however, require bioinformatics and statistical data analysis for the CRISPR screen, while results were instantly available in the RNAi screen. One of the major differences between both screening approaches is the method of target gene inactivation. While siRNAs achieve transient and incomplete gene knockdown by targeting the mRNA, sgRNAs cause an irreversible knockout of the gene of interest, leading to complete ablation of protein expression. The CRISPR/Cas9 system might thus overcome the challenge of accumulating false negatives resulting from insufficient protein knockdown, which is a big issue in siRNA screens.

**Table 30: Comparison of high-throughput screening methods.**

Type of screen	siRNA	CRISPR/Cas9
Screening format	arrayed	pooled
Delivery method	transfection	lentiviral
Genome-scale	(+)	++
Loss of gene expression	transient knockdown	knockout
Reporter-based screen	++	(+)
Positive selection screen	(+)	++
Ease of data analysis	++	(+)
Off-target effects	+++	(+)
Primary validation	deconvolution of siRNA pools	-

On the other hand, gene knockout can lead to another kind of false negatives. Recently, the CRISPR/Cas9 technology was employed in order to identify the whole set of essential human genes in a whole-genome negative selection screen (Wang et al., 2015). Essential genes, represented by sgRNAs that were depleted in the final population of cells after 14 population doublings, made up 9.2% of the entire genome. These would consequently never be identified in a CRISPR/Cas9 positive selection screen, and are likely to be missing in our target list. When performing a positive selection screen expecting essential genes in the target list, RNAi rather than CRISPR might thus be the method of choice. False positives arising from siRNA off-target effects were prevailing in the primary hit list arising from our RNAi screen. Separating true hits from false positives emerged as a major challenge in RNAi screening, and was addressed by deconvolution of siRNA pools in this research work. Although this

technique readily identified false positives, it is expensive and cumbersome. This primary validation was unnecessary in the CRISPR/Cas9 screen. Each gene was targeted by 6 individual sgRNAs in the pool, and only those genes where more than one individual sgRNA was enriched in the doxycycline-surviving cell pool as identified by statistical analysis were considered as candidates.

Overall, both screening approaches have advantages and disadvantages and the appropriate technique has to be selected carefully with respect to the biological question. For a reporter-based screen, RNAi is the method of choice, while a positive selection screen can highly benefit from the CRISPR/Cas9 technology.

## **5.2 Candidates arising from the CRISPR screen: Towards a pathway of Roquin-1-induced cell death?**

A total of 30 candidate proteins arose from our primary screen for cofactors of Roquin-1-induced cell death (Table 28), comprising whole networks of proteins involved in protein deubiquitination, the heparan sulfate synthesis pathway, nucleocytoplasmic transport, histone methylation and the mediator complex. However, a network of proteins involved in one of the common pathways of cell death was missing, and also individual candidates did not help to shed light on the question why cells were dying in response to Roquin-1 overexpression. In the following, I will therefore discuss which forms of cell death are possible considering the morphological changes that occur during Roquin-1-induced cell death, and how they can be confirmed experimentally.

### **5.2.1 Possible cell death pathways and their validation**

After inducing Roquin-1 overexpression, MEF cells changed their morphology, transforming from large plasmacytoid and adherent cells into smaller, more elongated and barely attached cells, which were rounding up, detaching and finally fragmenting in solution (Figure 46). This process was strikingly accompanied by the conversion of small, irregularly shaped black structures into larger, light round vesicular structures, which accumulated in the cytoplasm over time.

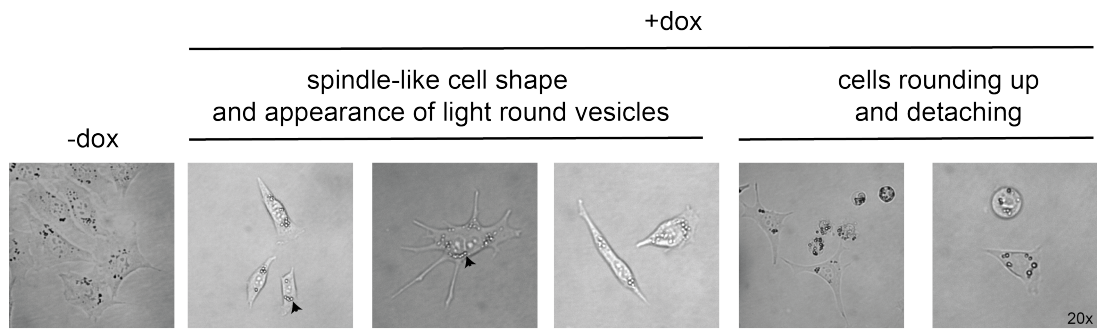


**Figure 46: Morphological changes of MEF cells undergoing Roquin-1-induced cell death.**

Phase-contrast images of cells overexpressing doxycycline (dox)-inducible Roquin-1-P2A-mcherry were captured under a Zeiss microscope using a 20x magnification objective. Cells were treated with doxycycline for 48 h (+dox) or left untreated (-dox).

Determining the responsible cell death pathway, the first question is whether it is an active (regulated) or a passive form of cell death. While regulated cell death is actively induced by certain signaling pathways and requires energy, passive cell death occurs upon extracellular stress and results in uncontrolled cell rupture called necrosis (Labbé & Saleh, 2011). Roquin-1-induced cell death specifically occurred after overexpression of full-length Roquin-1 and required the C-terminal part of Roquin-1 (proline-rich region, coiled-coil) in addition to the N-terminal part (Figure 37). It can thus be assumed that Roquin-1 overexpression elicits a regulated form of cell death involving specific signaling pathways rather than inducing unspecific cell stress due to high protein overexpression. Five different pathways of regulated cell death are discriminated in the literature: Apoptosis, necroptosis, autophagy, pyroptosis and ferroptosis. Their morphological characteristics are compared in Table 31. Apoptosis is the most prominent cell death pathway (Nikoletopoulou et al., 2013). It can be induced intrinsically by intracellular stress signals, or extrinsically in response to stimulation of cell surface death receptors (Duprez et al., 2009). Both pathways lead to the activation of caspases, the central players of apoptosis, which are responsible for DNA fragmentation. In the course of apoptosis, cells are rounding up, while large vacuoles form in the cytoplasm. Apoptotic cells can be identified by characteristic morphological changes such as shrinkage of nuclei and membrane blebbing, the latter of which should be easily detectable by light microscopy as round structures emerging from the plasma membrane that are finally released into the extracellular space (Schwarzer et al., 2014). These were clearly absent in cells dying from Roquin-1 overexpression (Figure 46), thereby decreasing the likelihood that Roquin-1-overexpressing cells underwent apoptosis.

Another option is necroptosis, a programmed form of necrotic cell death. Necroptosis is induced by death receptor signaling, and crucially depends on activation of the kinase RIP-1, which forms a pro-necrotic protein complex with RIP-3 that activates downstream effector proteins. Morphologically, necroptotic cells can be recognized by cytoplasmic and organelle swelling, which is noticeable by cells growing in size. Finally, the cell membrane is ruptured and the cytoplasmic content is released into the extracellular space (Duprez et al., 2009). Since cells undergoing Roquin-1-dependent cell death did not grow in size and finally “explode”, but rather shrunk and rounded up, necroptosis is unlikely to be the mechanism searched for. The same holds true for pyroptosis, which displays similar morphological characteristics. Pyroptosis works via activation of caspase-1, which initiates DNA fragmentation by other caspases as well as nuclear condensation as observed in apoptosis (Fernandes-Alnemri et al., 2007). This is followed by the formation of pores in the plasma membrane, leading to cell swelling and membrane rupture similar to necrosis (Duprez et al., 2009).

Considering the prominent accumulation of vesicular structures in cells dying from Roquin-1 overexpression (Figure 46), I find it likely that autophagy is involved in the pathway of Roquin-1-induced cell death. Autophagy is a cell-intrinsic recycling pathway, where cellular components are engulfed by specialized cytoplasmic vesicles called autophagosomes and finally digested after fusion with lysosomes (Jiang et al., 2011). Although autophagy is generally believed to support cell survival, massive autophagic activity can induce programmed cell death leading to “self-engulfment” of a dying cell by autophagosomes (Fernandes-Alnemri et al., 2007). Autophagy is negatively regulated by the serine/threonine kinase mTOR, and consequently initiated by mTOR inhibition e.g. in response to starvation (Fullgrabe et al., 2014). The ULK-Atg13-FIP200 protein complex is activated in turn, and initiates the formation of autophagosomes (Jung et al., 2009). Vesicle nucleation requires the activation of a phosphatidylinositol 3-kinase (PI3K) complex for generation of phosphatidylinositol-3-phosphate (Fullgrabe et al., 2014). The following step of vesicle elongation is mediated by two ubiquitin-like conjugation systems. In this context, conjugation of LC3 (LC3-I) with phosphatidylethanolamine (PE) to LC3-PE (also-called LC3-II), which stays attached to the autophagic membrane, is a characteristic marker of autophagy.

Roquin-1-induced cell death also shows some morphological characteristics of ferroptosis. Ferroptosis was identified in 2012 as a new form of non-apoptotic cell death being unaffected by inhibitors of apoptosis, necrosis, necroptosis and autophagy

(Dixon et al., 2012). Moreover, it showed prominently different morphological characteristics, such as mitochondrial condensation and rupture of the outer mitochondrial membrane. The execution of ferroptosis was found to depend on the iron metabolisms, with an accumulation of reactive oxygen species. Inhibitors and inducers of ferroptosis have readily been identified, however, it is still unclear which factors control ferroptosis cell-intrinsically. Cells undergoing ferroptosis were found to round up and detach, which is also a characteristic of Roquin-1-induced cell death (Xie et al., 2016). This is, however, also observed during apoptosis. The comparison of characteristic morphological features of the different kinds of cell death is summarized in Table 31.

**Table 31: Comparison of morphological features of different types of regulated cell death (adapted from (Xie et al., 2016)).**

Type of cell death	Apoptosis	Necroptosis	Autophagy	Ferroptosis	Pyroptosis
Cell membrane	Plasma membrane blebbing	Rupture of the plasma membrane	No changes	No changes	Rupture of the plasma membrane
Cytoplasm	Reduction of cellular volume, rounding up	Cytoplasmic swelling, swelling of organelles	Accumulation of cytoplasmic vacuoles	Condensation of mitochondria, outer mitochondrial membrane rupture, rounding up	Cytoplasmic swelling, swelling of organelles
Nucleus	Nuclear shrinkage and fragmentation, chromatin condensation	Intermediate chromatin condensation	Lack of chromatin condensation	No changes	Nuclear shrinkage and fragmentation, chromatin condensation

In future experiments, we will first test whether autophagy is involved in Roquin-1-induced cell death. The standard assay demonstrating autophagy is the detection of enhanced LC3-II, the lipidated form of LC3-I, in immunoblotting assays. This experiment is often carried out in the presence and absence of Bafilomycin A1, an inhibitor of the autophagosomal-lysosomal fusion (Gammoh et al., 2012; Jiang et al., 2011). Since LC3-II is degraded in lysosomes in the course of autophagy, autophagic cells should accumulate LC3-II upon Bafilomycin A1 treatment when exhibiting the full autophagy pathway including the formation of an autolysosome. The functionality of autolysosomes can be proven by determining the expression of p62. P62 is subject to strong degradation in autolysosomes, and should consequently be reduced in protein lysates of autophagic cells (Gammoh et al., 2012; Jiang et al., 2011). All three assays

can be performed easily by preparing protein extracts from doxycycline-treated and untreated MEF reporter cells. Employing the mTOR inhibitor rapamycin as a positive control, these three immunoblotting assays will finally clarify whether or not autophagy is a central aspect of Roquin-1-induced cell death. A final proof would be provided if Roquin-1-induced cell death was suspended upon application of autophagy inhibitors, such as the PI3K inhibitor 3-Methyladenine (Seglen & Gordon, 1982).

If autophagic cell death is not involved, assays for detection of the other types of cell death will follow. The multitude of different methods existing to discriminate different cell death pathways are summarized and compared in (Galluzzi et al., 2009). In general, a combination of different approaches should be employed to unambiguously prove a certain type of cell death. The Nomenclature Committee on Cell Death (NCCD) has recently released recommendations on the classification of cell death (Galluzzi et al., 2012), which might provide help in the matter of choosing the right assays.

For a final diagnosis of Roquin-1-induced cell death, it would be beneficial to obtain electron microscopy images of dying cells in collaboration with an experienced research group. This would enable the visualization of morphological changes that are too small to be seen by light microscopy, such as plasma membrane rupture, mitochondrial changes as occurring during ferroptosis or chromatin condensation and nuclear shrinkage, which are hallmarks of apoptosis and pyroptosis (Galluzzi et al., 2009).

### **5.2.2 Ubiquitin conjugation as a potential pathway linked to Roquin-1 effector functions**

A total of 30 candidate proteins arose from our primary screen for cofactors of Roquin-1-induced cell death (Table 28). Surprisingly, this primary candidate list did not contain any central players of common cell death pathways. To narrow the candidate list down to downstream effector proteins of Roquin-1, we first of all aimed at eliminating all sgRNAs that interfered with Roquin-1-P2A-mCherry overexpression. A secondary screen was therefore performed with an additional sorting step at the end of the cell culture, separating mCherry<sup>+</sup> from mCherry<sup>-</sup> cells using flow cytometry. In future hit validation experiments, we will concentrate on candidate genes, which were targeted by sgRNAs that did not have a negative impact on Roquin-1-P2A-mCherry expression (Table 29). This final list of proteins whose sgRNAs were enriched in mCherry<sup>+</sup> cells was dominated by six proteins of the ubiquitin conjugation

system (Figure 44, Figure 45). Even without knowing how Roquin-1 overexpression induces cell death, this suggests that Roquin-1-induced cell death might be connected to its as yet barely investigated function as an E3 ubiquitin ligase. Yet, contradicting evidence is provided by my initial finding that the truncated Roquin-1 (aa 1-509) protein containing the RING finger and hence the putative E3 ligase function is unable to induce cell death (Figure 37). However, since protein/protein interaction domains are contained in the C-terminal part of the Roquin-1 protein, it might be possible that in addition to an E3 ligase function Roquin-1 is required to interact with other factors (e. g. Roquin-2) in order to induce cell death. To clarify whether the RING finger domain is required to induce Roquin-1-mediated cell death, we will generate a reporter cell line with doxycycline-inducible overexpression of Roquin-1 where the structure of the RING finger is destroyed by point mutations. If this mutant is, similar to Roquin-1 (aa 1-509), unable to induce cell death, this would be a final proof that the RING domain in combination with the C-terminal part of Roquin-1 mediates Roquin-1-induced cell death.

Among the final candidates whose cellular function is related to protein ubiquitination, the deubiquitination (DUB) enzyme Usp7 is especially interesting. Usp7 is strongly expressed in regulatory T cells and was found to be associated with the transcription factor Foxp3 in the nucleus of Tregs. Here, Usp7 stabilizes Foxp3 expression through deubiquitination and protection from proteasomal degradation. Therefore, Usp7 strongly contributes to the maintenance of the Treg-specific transcription program (van Loosdregt et al., 2013) and consequently to immunological tolerance. It thus complements the action of Roquin-1, which confers peripheral tolerance by restricting aberrant Th1, T<sub>FH</sub> and Th17 differentiation.

Interestingly, Usp7 can be a mediator of cell death by deubiquitination of p53. P53 is a transcription factor that is induced upon cellular stress signals such as DNA damage or starvation and a potent initiator of cell-cycle arrest and apoptosis (Chen, 2016). Usp7 can stabilize both p53 and the ubiquitin ligase Mdm2, which induces proteasomal degradation of p53 (Sheng et al., 2006). In normal cycling cells, Mdm2 is its primary target, and Usp7 thus restricts p53 levels (Vucic et al., 2011). In line with this, loss of Usp7 has been reported to result in enhanced p53 expression and thus increased apoptosis (Fan et al., 2013; Kon et al., 2010). Overexpression of Roquin-1, however, might bias Usp7 towards deubiquitination of p53, resulting in high p53 expression levels and cell death. Whether enhanced p53 expression is responsible for Roquin-1-

induced cell death shall be easily evaluated by p53 immunoblotting of doxycycline-treated versus untreated reporter cells. Another possible function of Usp7 in Roquin-1-induced cell death is direct interaction and stabilization of Roquin-1. DUBs are commonly found associated with E3 ubiquitin ligases to protect them from autoubiquitination and thus proteasomal degradation (Wilkinson, 2009). Following the steps of the original publication describing such a relationship for Usp7 and Mdm2 (Li et al., 2004), we will determine whether this is also the case for Roquin-1 by performing three main experiments. Pulldown of Roquin-1 from doxycycline-induced reporter cells and subsequent detection of Usp7 in immunoblotting assays will reveal whether Roquin-1 forms a complex with Usp7 to induce cell death. Secondly, we will determine the protein half-life of Roquin-1 with the protein synthesis inhibitor cycloheximide, and evaluate whether it is prolonged when Usp7 is overexpressed. Finally, *in vitro* ubiquitination assays will prove whether ubiquitinated Roquin-1 is deubiquitinated by Usp7. These approaches will finally clarify whether Usp7 is a Roquin-1-stabilizing DUB during Roquin-1-induced cell death.

Overall, the future validation strategy for the candidates arising from our CRISPR/Cas9 screen for cofactors of Roquin-1-induced cell death will first of all focus on the determination of the type of cell death. Once this is accomplished, literature search will identify which of the identified networks of candidate proteins is most likely involved in the particular type of cell death, and CRISPR/Cas9 gene knockout can easily be employed in order to show whether loss of the respective candidates interferes with the determined type of cell death. In parallel, we will dissect the role of Roquin's function as an E3 ligase in Roquin-1-induced cell death, and evaluate whether the promising candidate Usp7 is a Roquin-1-stabilizing DUB and inducer of cell death via p53.

### **5.3 Nufip2 as a new cofactor of Roquin-1-mediated ICOS repression**

The Nufip2 protein arose as a promising candidate from the targeted siRNA screen for cofactors of Roquin-1-mediated ICOS repression. Except for the known cofactor CNOT1 (Figure 19), NUFIP2 was the only RBP that passed the primary validation by siRNA deconvolution (Figure 21). I subsequently confirmed the significance of Nufip2 for Roquin-1-induced ICOS repression in two rescue experiments employing reconstitution of Nufip2-knockdown HeLa cells (Figure 24) and CRISPR/Cas9 Nufip2

knockout MEF cells with siRNA- or sgRNA-resistant Nufip2 cDNA, respectively (Figure 26). Based on the functional validation of Nufip2 that was performed in this study, I will now discuss possible functions of Nufip2 in the pathway of *ICOS* regulation and develop strategies for future experimental approaches helping to shed light on the burning question how Nufip2 supports Roquin-1 function. Starting with the analysis of *cis*-elements in *ICOS* mRNA where Roquin-1 binds and Nufip2 might operate as a cofactor, the interaction partners of Nufip2 and Roquin-1 will be discussed building a potential network of post-transcriptional regulators on target mRNAs. Finally, I will suggest a model for a temporal compartmentalization of *ICOS* regulation based on the differential expression of Roquin-1 and its cofactors in the T cell activation time course.

### **5.3.1 Molecular analysis of Roquin-1 *cis*-elements in human *ICOS* mRNA**

It has been shown that Roquin-1 binds to a highly conserved CDE tri-loop structure in the *TNF* 3' UTR, and induces deadenylation-dependent mRNA decay by interaction with the CCR4-CAF1-NOT deadenylase complex (Leppek et al., 2013). An identical CDE was found at the 3' end of *ICOS* mRNA. Since overexpressed Roquin-1 was able to shorten the half-life of a reporter mRNA that contained the isolated *ICOS* CDE sequence, it was anticipated that Roquin-1 would induce post-transcriptional regulation of *ICOS* mRNA in a CDE-dependent manner (Leppek et al., 2013). Nonetheless, our comprehensive analysis of Roquin-1 *cis*-elements in the 3' UTR of *ICOS* mRNA revealed in agreement with (Schlundt et al., 2014) that the perfect CDE is negligible for Roquin-1-dependent *ICOS* regulation in the context of a reporter system employing full-length *ICOS* mRNA (Figure 34B, C). Instead, *ICOS* regulation depended on a region that was formerly assumed to be a target of miR-101. It has been shown in previous work that overexpression of Roquin-1 is able to repress *ICOS* in miRNA-deficient cells or in cells that lack argonaute proteins (Glasmacher, 2010). Consistently, we could now show that a potential new tri-loop structure folding at the same position as the miR-101 binding site is involved in Roquin-1-induced *ICOS* regulation (Figure 36). Our mutational analysis allowed to rule out Roquin-1 cooperation with miR-101 regulation and instead involved Roquin-1 interaction with a novel stem-loop structure. Specifically, we involved the previously published mutation that changed the sequence complementary to the seed sequence of miR-101 in the *ICOS* 3' UTR dissolving into a stem-loop structure. Most importantly, we

demonstrated a functional rescue by introducing additional mutations that restored the base pairing of the stem-loop. Additionally, we saw a contributive effect of a CDE-like stem-loop in the 5' part of *ICOS* 3' UTR. In the following paragraph, I will discuss how these findings can be reconciled with the published canonical and alternative Roquin-1-bound stem-loop structures.

### 5.3.1.1 Experimentally determined *ICOS* cis-elements compared to the CDE

Based on crystal structures obtained from the RNA-binding ROQ domain of Roquin-1 in complex with the *TNF* CDE and mutational analyses (Codutti et al., 2015; Schlundt et al., 2014; Tan et al., 2014), Codutti and colleagues developed a consensus sequence for Roquin-1-bound and regulated tri-loop structures (Codutti et al., 2015) (Figure 47). The consensus motif predicted high-affinity Roquin-1 binding to stem-loop structures with a 5-7 nt stem and a tri-loop where the first nucleotide of the loop is a pyrimidine, followed by a central purine, with no restrictions for the third nucleotide (Y-R-N loop). Additionally, nucleotide identity of bases in the upper (apical) part of the stem-loop seemed to be an important determinant of the loop conformation by allowing purine stacking interactions between the central loop purine and further purine residues in the 3' part of the stem. The resulting major groove conformation of the RNA was found to be essential for Roquin-1 binding (Codutti et al., 2015). Comparing the former and newly identified *ICOS* cis-elements (the CDE-, CDE-like- and miR-101 TS stem-loop) (Figure 47) with the consensus sequence, the CDE is a near perfect match. It deviates from the CDE consensus only in its lack of the basal G-C base pair, while all four required purine residues in the apical 3' part of the stem are present and allow purine stacking (Figure 47B) (Leppek et al., 2013).

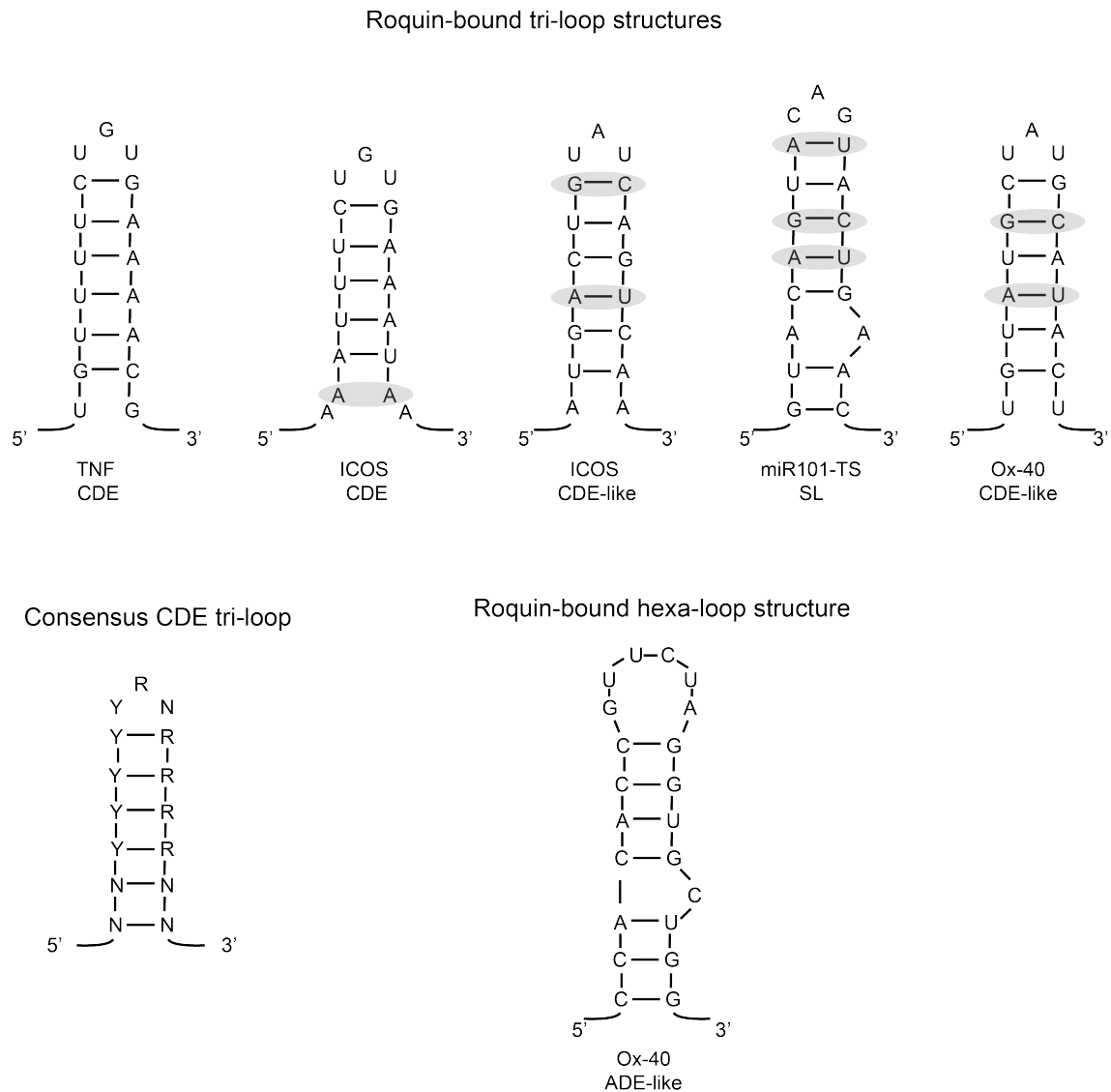


**Figure 47: Roquin-1-bound stem-loop structures.**

*Schematic representation of stem-loop structures targeted by Roquin-1 and the deduced CDE consensus sequence for Roquin-1-bound tri-loops. Y = pyrimidine, R = purine, N = pyrimidine or purine. Deviations from the consensus CDE tri-loop are highlighted in grey.*

For the CDE-like element located at the 5' end of *ICOS* 3' UTR, however, the situation is different (Figure 47). Although fulfilling the main requirement of possessing a Y-R-N loop, the CDE-like stem-loop deviates from the consensus in one important criterion. The 3' part of the stem contains several pyrimidine residues instead of purine bases at apical positions, including the closing base pair, interfering with purine stacking. Since purine stacking was considered to be a central determinant of the loop conformation, the apical 3' pyrimidine bases could cause decreased Roquin-1 binding affinity to the CDE-like stem-loop, as compared to the CDE (Codutti et al., 2015).

Sequence inspection of the newly identified miR-101 TS stem-loop revealed that the potential stem-loop might actually be longer than predicted by the LocARNA software (Figure 47). Allowance of one bulge nucleotide added two more base pairs to the stem, thereby transforming it into a 7 nt-stem. Regarding the CDE consensus structure, the miR-101 TS stem-loop again meets the main requirement of possessing a Y-R-N loop, but violates the consensus CDE structure in two other points. The closing base pair consists of an A-U pairing instead of the more stable G-C base pair, and three nucleotides on the 3' side of the stem including the closing base pair are pyrimidine instead of purine residues. Importantly, when introducing compensatory mutations into the closing base pair and the upper stem of the miR101-TS stem-loop or the CDE-like stem-loop, we observed that regulation was fully restored (Figure 36). This again is in contrast to the *TNF* CDE, where reversion of the two stem-closing base pairs continued to strongly inhibit Roquin-1 binding and function (Codutti et al., 2015; Leppek et al., 2013). Therefore, the predicted purine stacking interactions do not seem to be functionally important for regulation by the miR-101 TS stem-loop and the CDE-like stem-loop.

I wondered how the discovery of the CDE-like and the stem-loop in the miR-101 target sequence as new potential Roquin-1-targeted *cis*-elements in the 3' UTR of human *ICOS* mRNA fit with the proposed selective Roquin-1 binding to tri-loop structures of a strict CDE consensus-type. Luckily, interesting hints were provided by recent publications. A detailed analysis of Roquin-1 *cis*-elements in the *Ox40* 3' UTR revealed that more violations to the consensus CDE are tolerated by Roquin-1 than previously anticipated (Janowski et al., 2016). Functional assays demonstrated that Roquin-1 was also able of binding a non-consensus CDE-like tri-loop (*Ox40* CDE-like) with lower affinity, and most surprisingly, also a hexa-loop structure (Figure 47) with high affinity. In the Roquin-1-bound hexa-loop the Tyr<sub>250</sub> of the ROQ domain emerged as a new loop-stabilizing element engaging in stacking interactions with two nucleotides of the loop and a purine base of the closing base pair. Purine stacking of the 3' apical part of the stem enforcing a specific conformation of hairpin may therefore not be required in general. The configuration of the alternative tri-loop structure of the miR-101 TS stem-loop and recognition by the ROQ domain are therefore open questions. Attempts of crystallization and/or NMR analysis of the ROQ domain in combination with the CDE-like stem-loop and the newly identified alternative tri-loop structure in the miR-101 target site will be informative. Identification of the determinants of loop conformation for these alternative tri-loops will help us to develop a new, more

relaxed consensus for Roquin-1 *cis*-elements, which will be useful for the prediction of different target mRNAs and alternative binding modes of Roquin-1.

### **5.3.1.2 Future aspects concerning the coregulation of Roquin-1 *cis*-elements by Nufip2**

Overall, we identified the CDE-like stem-loop and a mapped target region (nt 2211 – 2271) that includes the miR-101 TS stem-loop as a new potential Roquin-targeted *cis*-element on human *ICOS* mRNA using two different reporter systems with overexpressed and endogenous Roquin-1 levels (Figure 34). Our reporter cell system with endogenous Roquin-1 expression can only identify high-affinity binding sites due to its low dynamic range, however, the Roquin-1-overexpression cell system appears sufficiently sensitive to detect the whole range of low- and high-affinity *cis*-elements. For this reason we think the latter identified the CDE-like stem-loop as a low-affinity binding site for Roquin-1, which contributes to a repressive effect that requires the miR-101 TS stem-loop. However, impaired ICOS regulation of some deletion constructs cannot be explained by those two *cis*-elements, suggesting the presence of low-affinity Roquin-1 binding sites distributed over the whole length of *ICOS* 3' UTR. This might point towards the presence of several different high- and low affinity Roquin-1 binding sites in the 3' UTR of *ICOS*, as it has recently been suggested in the literature (Jeltsch & Heissmeyer, 2016).

After identifying the most important Roquin-1 target regions on *ICOS*, the question arises whether Nufip2, which has been demonstrated to interact with mRNA (Bardoni et al., 2003) regulates ICOS through the same or different *cis*-elements. This can be solved by testing all available ICOS deletion constructs in the CRISPR/Cas9 Nufip2 knockout- and reconstitution system that has been established in this study (Figure 26). Moreover, it would be highly interesting to evaluate whether *ICOS* is the only target that is coregulated by Nufip2 and Roquin-1. This can be evaluated on a small scale employing the CRISPR/Cas9 Nufip2 knockout- and reconstitution system with individual reporters where different Roquin-1-regulated 3' UTRs are fused to the ICOS CDS (Jeltsch et al., 2014). A complete picture on Nufip2-regulated mRNAs and binding sites would be obtained by applying high-throughput crosslinking- and immunoprecipitation (CLIP) techniques. These involve crosslinking of the protein of interest to its target mRNAs, followed by protein pulldown and target identification by deep sequencing and have successfully been employed to identify target mRNAs and binding sites for Roquin-1 and Regnase-1 (Mino et al., 2015; Murakawa et al., 2015).

### 5.3.2 Interactions between Roquin-1, Nufip2 and other potential cofactors

After validation of Nufip2 as a cofactor of Roquin-1 in post-transcriptional gene regulation of *ICOS*, we set out to further explore this largely uncharacterized protein and its role in Roquin-1-induced gene repression. NUFIP2 co-immunoprecipitated with Roquin-1 in an RNase-independent manner (Figure 28), suggesting the potential direct protein/protein interaction. In fact, a binary interaction of purified protein fragments in surface plasmon resonance experiments was determined (Figure 20). Interestingly, this direct interaction took place between the N-terminus of Roquin-1, containing RING finger, ROQ domain and Zinc finger, and the FMRP-interacting part of the NUFIP2 protein. The enrichment of almost equal parts of Nufip2 and Roquin-1 proteins after Roquin-1 immunoprecipitation from MEF cell extracts suggests that most of the endogenous Roquin-1 molecules are engaged in a complex with Nufip2 (Figure 29). This idea is further supported by the fact that both proteins interact with high affinity in *in vitro* experiments ( $K_d$  of < 200 nM) (Figure 20). Nufip2 was thus demonstrated as an important direct binding partner of Roquin-1.

The same fragment of Nufip2 that interacts with Roquin-1 has earlier been published to engage in a direct protein/protein interaction with FMRP (Bardoni et al., 2003; Ramos et al., 2006), which forms homo- and heterodimers with its family members FXR1 and FXR2 (Chapter 1.1.4.1) (Winograd & Ceman, 2011). Furthermore, Roquin-1 has been shown to colocalize with *Fmrp* in stress granules in response to arsenite-induced oxidative stress (Glasmacher, 2010). Additionally, FXR1 was found to be one of the few proteins that were highly enriched after immunoprecipitation of an aptamer-fusion of the CDE stem-loop, together with Roquin-1 and Roquin-2 (Leppek et al., 2013). These results suggest that FMRP/FXR family proteins are linked to Roquin-1-induced gene repression, and their newly discovered direct interaction partner Nufip2, if ternary complexes can form, might be the missing link in this connection.

A second link between the function of Roquin- and FMR family members may be provided by Ago2 and the miRNA pathway. Several groups have reported examples where *Fmrp* or its family members make essential contributions to miRNA-mediated gene repression (Caudy et al., 2002; Edbauer et al., 2010; Li et al., 2014b) and *Fmrp* was found to associate with Dicer and Ago2 in mammalian cells (Caudy et al., 2002). A contribution of the miRNA pathway to Roquin-1-dependent target regulation is,

however, still under debate. It has been shown earlier that miRNAs are dispensable for Roquin-1 function (Glasmacher et al., 2010). I could reconfirm this result by unveiling that the formerly proposed miR-101 target site gains importance only because it is part of a conserved stem-loop structure that serves as a new potential Roquin-1 *cis*-element in the *ICOS* mRNA (Chapter 4.1.11.2). Nonetheless, it was recently proposed that Roquin-1-induced post-transcriptional repression of mouse *Icos* may be conferred by miR-146a, with a direct interaction between the N-terminus of Roquin-1 and miR-146a forming a complex with Ago2 (Srivastava et al., 2015). However, sequence alignments revealed that *Icos* 3' UTR sequence is ~600 nts longer in the mouse than in 24 other species, including humans (Anne Hoffmann, personal communication). Since one of the two mapped miR-146a binding sites in the mouse *Icos* 3' UTR is consequently missing in most other species, while the second target site is poorly conserved, it is questionable that the published mechanism of *Icos* regulation is of general importance. Nonetheless, miR-146a does seem to play a role in *mouse Icos* regulation (Pratama et al., 2015; Srivastava et al., 2015), and similarly, miR-101 overexpression induced a weak downregulation of *human ICOS* (Yu et al., 2007). Thus, the full extent of Roquin-mediated regulation may involve collaboration with the miRNA pathway and/or miRNA pathway components in the regulation of certain target mRNAs.

Considering the protein interactions described above, it is a possible scenario that a translational silencing complex consisting of Nufip2, Fmrp/Fxr1/Fxr2 and the miRISC complex associates with Roquin-1 on the Roquin-1-bound target mRNA (Figure 48). But how does this complex induce post-transcriptional repression? Roquin-1 is thought to induce deadenylation-dependent mRNA decay by recruitment of the CCR4-CAF1-NOT complex with its C-terminal domain, while the N-terminal domain of Roquin-1 may be responsible for recruiting the mRNA decapping complex. Support for this model comes from the finding that the C-terminus of Roquin-1 co-immunoprecipitated with CNOT1 and CNOT7 of the deadenylase complex (Leppek et al., 2013), while the Roquin-1 N-terminus interacted with Rck and Ecd4, two cofactors of mRNA decapping (Glasmacher, 2010). However, it is unclear whether or not any of these interactions are direct. Interestingly, both NUFIP2 and FXR1/FXR2 were recently identified as interactors of RCK (Bish et al., 2015), suggesting that Nufip2 may support or even induce the recruitment of the mRNA decapping complex. As the miRISC complex is also known to induce deadenylation-dependent mRNA decay (Huntzinger & Izaurralde, 2011), it is tempting to speculate that all proteins surrounding

Roquin-1 in a complex may act in concert to initiate mRNA decay. Besides, RCK has been shown to induce translational inhibition (Coller & Parker, 2005), which is also possible for Roquin-1 based on my initial finding of Roquin-1-mediated repression being far more pronounced on the protein compared to the mRNA level (Figure 10).

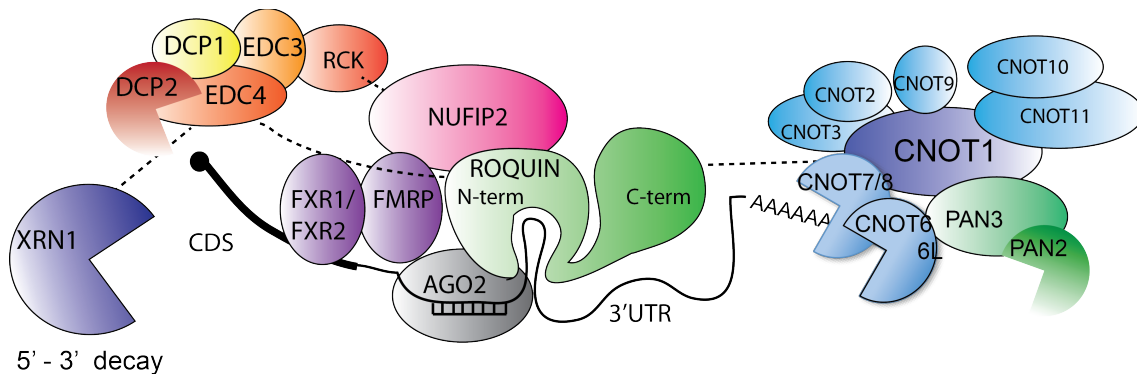


**Figure 48: Different cofactors are involved in Roquin-1-mediated post-transcriptional gene regulation.**

As demonstrated in this study, the N-terminus of ROQUIN-1 engages in a direct protein/protein interaction with NUFIP2, which itself has been shown to directly interact with FMRP (Bardoni et al., 2003; Ramos et al., 2006). FMRP and ROQUIN-1 were both shown to interact with AGO2 of the miRNA-induced silencing complex (miRISC) (Li et al., 2014b; Pratama et al., 2015; Srivastava et al., 2015). For inducing mRNA decay, the C-terminus of ROQUIN-1 is thought to recruit the CCR4-CAF1-NOT complex (Leppek et al., 2013), while the N-terminus can bind to the cofactors of decapping RCK and EDC4 (Glasmacher, 2010). Interaction with RCK can also be mediated by NUFIP2 (Bish et al., 2015). The exonuclease XRN1 is recruited via interaction with EDC4 (Braun et al., 2012; Chang et al., 2014), and initiates 5' – 3' mRNA decay.

The translational silencing complex assembling around Roquin-1 might thus induce target gene repression by a combination of mRNA decay and translational inhibition. Regnase-1 was left out in this model although deficiency of the Regnase-1 encoding gene leads to elevation of ICOS levels (Jeltsch et al., 2014). Although Regnase-1 was not essential for Roquin-1 dependent ICOS regulation and did therefore not emerge as a Roquin-1 cofactor in our screen, it turned out to be highly important for Roquin-1-dependent regulation of the *CDE260* reporter (Figure 18). Regnase-1 might thus be a selective cofactor for a subset of Roquin-1 targets. Different theories exist, however, on how Roquin-1 and Regnase-1 cooperate or antagonize in target regulation, making it difficult to include in the model (Jeltsch et al., 2014; Mino et al., 2015).

Although my model (Figure 48) provides a first draft of how Roquin-1 might collaborate with different cofactors to induce post-transcriptional gene regulation, it

still requires experimental validation, especially concerning the roles of Fmrp and Nufip2. The question arises how Roquin-1 and Fmrp can directly interact with the same domain of Nufip2. This paradox cannot be answered yet, but will be clarified in future experiments. In collaboration with Dr. Dirk Niessing's group, we will perform advanced surface plasmon resonance studies with all three interacting protein fragments in order to elucidate whether Roquin-1 and Fmrp indeed bind simultaneously to the same Nufip2 domain. An alternative, likewise possible scenario would be mutual exclusive binding of both proteins, which would require an adaptation of our model.

As a burning question it remains to be answered what exactly Nufip2 contributes to in Roquin-1-mediated *ICOS* repression. Future experiments discerning Nufip2 *cis*-elements in *ICOS* might reveal whether besides engaging in a protein/protein interaction with Roquin-1 and other post-transcriptional regulators, Nufip2 increases the affinity of Roquin-1 to certain target mRNAs by simultaneously binding to the same RNA (Chapter 5.3.1). By directly interacting with Roquin-1, Nufip2 might mediate Roquin-1's interaction with indirect binding partners, such as Rck or Fmrp. This can be evaluated in immunoprecipitations of Roquin-1 and systematic analysis of interacting cofactors in cells that are either deficient for EDC4, NUFIP2, RCK and FMRP compared to wildtype counterparts. With the advent of the CRISPR/Cas9 genome editing technology, this approach is feasible, and it will eventually provide insights into the order of events during the assembly of the mRNP that coordinates Roquin-1-mediated mRNA degradation.

Another possible scenario of how Nufip2 might support Roquin-1-dependent post-transcriptional regulation arises from its ability to accumulate together with Roquin-1 in stress granules upon arsenite-induced oxidative stress (Figure 31). The observation that Roquin-1, as well as its target mRNA *ICOS* (Yu et al., 2007), can localize to both P bodies and stress granules (Athanasopoulos et al., 2010; Glasmacher et al., 2010) favors the recently proposed theory of a dynamic relationship between actively transcribed mRNAs and their localization to stress granules or P bodies for temporal storage or mRNA degradation, respectively (Decker & Parker, 2012). Sorting of Roquin-1-containing mRNPs to one of the two respective sites may depend on binding partners. Recent literature suggests that P body formation is initiated by recruitment of P body factors to the messenger RNA, while aggregation of multiple mRNPs into cytoplasmic granules is the second step that is mediated by Q/N rich regions of the

aggregating proteins (Anderson & Kedersha, 2009). Since Nufip2 possesses such a Q/N rich protein aggregation domain, it was recently proposed to take part in the assembly of stress granules (Bish et al., 2015). Whether Nufip2 is responsible for aggregation of Roquin-1-mRNPs can be tested in a new experimental approach of selective precipitation (Kato et al., 2012). Incubation of cytoplasmic cell lysates with a biotinylated version of the chemical compound isoxazole (b-isox) leads to reversible aggregation of RNA granule-like structures, which can subsequently be pulled down with streptavidin beads. In this assay aggregation was found to be mediated by low complexity (LC) polypeptide sequences, which were found in most of the 106 precipitated proteins, including Nufip2 and all members of the FMR protein family. To address whether Nufip2 is essential for Roquin-1-mRNPs aggregation, we will perform b-isox treatment and streptavidin pulldown of RNA-granules in cell lysates from arsenite-treated Nufip2-wildtype and -knockout cells. Western blot detection of Roquin-1 will enable us to quantify the extent of Roquin-1-mRNP aggregation in the presence and absence of endogenous Nufip2 and after Nufip2 overexpression.

### **5.3.3 Roquin-1 cofactors regulate ICOS in different phases after T cell activation**

It is now clear that Nufip2 regulates Icos, however, it is still elusive whether this is a constitutive contribution to Roquin-1 function or a dynamic one. Nufip2 might have a general impact on Roquin-1's function and also influence the regulation of other Roquin-1 targets. This aspect of Nufip2 function was not part of this research work, which focused on the regulation of Icos as a critical costimulatory molecule of the antibody-dependent immune response. Considering a possible dynamic contribution to Roquin-1 function, we wondered whether the known *trans*-acting factors of post-transcriptional regulation of Icos were constantly expressed in T cells or whether their expression was dynamically regulated. The expression of these proteins was therefore analyzed over a 2-week Th1 culture. Interestingly, they showed very different expression maxima over the course of differential Icos expression (Figure 33). Roquin and Nufip2 were coexpressed with highest levels at day 1-4 after anti-CD3/CD28 stimulation so was Fxr1. Ago proteins had their expression maxima earlier, before and shortly after stimulation, while Fmrp and Regnase-1 appeared later, from day 3 till day 6 after activation. Since ICOS is very dynamically regulated and strongly induced by transcriptional upregulation (Tan et al., 2006), it is not clear when post-transcriptional regulation contributes the most. This will require further testing, which can be done

by using the 3' UTR of mouse *Icos* as a reporter system. Although it still needs to be clarified which of the changes in *Icos* expression are due to post-transcriptional regulation, the differential expression patterns of the *Icos* *trans*-acting factors allows the following interpretation: Ago proteins and thus the miRNA pathway can influence early Roquin regulation, while Nufip2 and Fxr1 can contribute later in the course of T cell activation and resting. The strongest coregulation of *Icos* by Roquin-1 and Nufip2 can thus be assumed between day 1-3, the time when ICOS levels change dramatically. Knowing the time point where the coregulatory effect on *Icos* can become maximal opens the way for testing Nufip2-dependency of *Icos* regulation in T cells. In a future experiment, we will introduce Nufip2-targeting shRNAs into CD4<sup>+</sup> T cells and analyze *Icos* expression between day 3 and day 5 after restimulation, since this is the time point where one would expect maximal contribution of Nufip2. This experiment will shed light on the role of Nufip2 in *Icos* repression following T cell activation.

## 5.4 Conclusion

Over their whole lifetime mRNAs remain associated with *trans*-acting factors such as RNA-binding proteins in the form of mRNA-protein complexes (mRNPs). Although the landscape of active RNA-binding proteins has recently been determined in human cells, the function of many RBPs is still elusive. In this research work, a new function was attributed to the previously uncharacterized RBP Nufip2 by unveiling its critical importance for Roquin-1-mediated post-transcriptional gene regulation of the inducible T cell costimulatory receptor *Icos* in a high-throughput screening approach. Functional validation demonstrated that Nufip2 engages in a direct interaction with the N-terminus of Roquin-1, and Nufip2 is herewith its first proven direct interactor. This new finding provides a starting point for further investigation of the mRNP composition that directs Roquin function. mRNPs are remodeled during different functional stages of mRNAs and their composition is believed to be a critical determinant of the mRNA fate. It was demonstrated in this research work that the known post-transcriptional regulators of *Icos* including Nufip2 display strikingly different expression kinetics following T cell activation suggesting a dynamic contribution to Roquin-1 function. Since composition and dynamics of mRNP formation that are involved in post-transcriptional gene regulation are still poorly investigated, this finding opens up a window of opportunity to understand the complex regulation of *Icos* by Roquin-1 and its cofactors.



---

## References

- Afkarian, M. et al., 2002. T-bet is a STAT1-induced regulator of IL-12R expression in naive CD4<sup>+</sup> T cells. *Nat Immunol*, 3(6), pp.549-557.
- Akiba, H. et al., 2005. The role of ICOS in the CXCR5<sup>+</sup> follicular B helper T cell maintenance in vivo. *J Immunol*, 175(4), pp.2340-2348.
- Alberts, B. et al. 2002. *Molecular Biology of the Cell* (Vol. 4). New York: Garland Science. ISBN 0-8153-3218-1.
- Allen, B. L. et al., 2015. The Mediator complex: a central integrator of transcription. *Nat Rev Mol Cell Biol*, 16(3), pp.155-166.
- Anderson, P. et al., 2009. RNA granules: post-transcriptional and epigenetic modulators of gene expression. *Nat Rev Mol Cell Biol*, 10(6), pp.430-436.
- Ascano, M., Jr. et al., 2012. FMRP targets distinct mRNA sequence elements to regulate protein expression. *Nature*, 492(7429), pp.382-386.
- Aslam, A. et al., 2009. The Ccr4-NOT deadenylase subunits CNOT7 and CNOT8 have overlapping roles and modulate cell proliferation. *Mol Biol Cell*, 20(17), pp.3840-3850.
- Athanasopoulos, V. et al., 2010. The ROQUIN family of proteins localizes to stress granules via the ROQ domain and binds target mRNAs. *Febs j*, 277(9), pp.2109-2127.
- Badertscher, L. et al., 2015. Genome-wide RNAi Screening Identifies Protein Modules Required for 40S Subunit Synthesis in Human Cells. *Cell Rep*, 13(12), pp.2879-2891.
- Baltz, A. G. et al., 2012. The mRNA-bound proteome and its global occupancy profile on protein-coding transcripts. *Mol Cell*, 46(5), pp.674-690.
- Bardoni, B. et al., 2003. 82-FIP, a novel FMRP (fragile X mental retardation protein) interacting protein, shows a cell cycle-dependent intracellular localization. *Hum Mol Genet*, 12(14), pp.1689-1698.
- Beier, K. C. et al., 2000. Induction, binding specificity and function of human ICOS. *Eur J Immunol*, 30(12), pp.3707-3717.
- Bernstein, E. et al., 2001. Role for a bidentate ribonuclease in the initiation step of RNA interference. *Nature*, 409(6818), pp.363-366.
- Birmingham, A. et al., 2006. 3' UTR seed matches, but not overall identity, are associated with RNAi off-targets. *Nat Methods*, 3(3), pp.199-204.

- Bish, R. et al., 2015. Comprehensive Protein Interactome Analysis of a Key RNA Helicase: Detection of Novel Stress Granule Proteins. *Biomolecules*, 5(3), pp.1441-1466.
- Bollig, N. et al., 2012. Transcription factor IRF4 determines germinal center formation through follicular T-helper cell differentiation. *Proc Natl Acad Sci U S A*, 109(22), pp.8664-8669.
- Booker, M. et al., 2011. False negative rates in Drosophila cell-based RNAi screens: a case study. *BMC Genomics*, 12, p.50.
- Braun, J. E. et al., 2012. A direct interaction between DCP1 and XRN1 couples mRNA decapping to 5' exonucleolytic degradation. *Nat Struct Mol Biol*, 19(12), pp.1324-1331.
- Breitfeld, D. et al., 2000. Follicular B helper T cells express CXC chemokine receptor 5, localize to B cell follicles, and support immunoglobulin production. *J Exp Med*, 192(11), pp.1545-1552.
- Brekke, O. H. et al., 2003. Therapeutic antibodies for human diseases at the dawn of the twenty-first century. *Nat Rev Drug Discov*, 2(1), pp.52-62.
- Bronevetsky, Y. et al., 2013. T cell activation induces proteasomal degradation of Argonaute and rapid remodeling of the microRNA repertoire. *J Exp Med*, 210(2), pp.417-432.
- Brustle, A. et al., 2007. The development of inflammatory T(H)-17 cells requires interferon-regulatory factor 4. *Nat Immunol*, 8(9), pp.958-966.
- Buehler, E. et al., 2012a. C911: A bench-level control for sequence specific siRNA off-target effects. *PLoS One*, 7(12), e51942.
- Buehler, E. et al., 2012b. siRNA off-target effects in genome-wide screens identify signaling pathway members. *Sci Rep*, 2, p.428.
- Burkhard, P. et al., 2001. Coiled coils: a highly versatile protein folding motif. *Trends Cell Biol*, 11(2), pp.82-88.
- Busse-Wicher, M. et al., 2014. The exostosin family: proteins with many functions. *Matrix Biol*, 35, pp.25-33.
- Calabretta, S. et al., 2015. Emerging Roles of Disordered Sequences in RNA-Binding Proteins. *Trends Biochem Sci*, 40(11), pp.662-672.
- Campeau, E. et al., 2009. A versatile viral system for expression and depletion of proteins in mammalian cells. *PLoS One*, 4(8), e6529.
- Caput, D. et al., 1986. Identification of a common nucleotide sequence in the 3'-untranslated region of mRNA molecules specifying inflammatory mediators. *Proc Natl Acad Sci U S A*, 83(6), pp.1670-1674.

- Carballo, E. et al., 1997. Bone marrow transplantation reproduces the tristetraprolin-deficiency syndrome in recombination activating gene-2 (-/-) mice. Evidence that monocyte/macrophage progenitors may be responsible for TNF $\alpha$  overproduction. *J Clin Invest*, 100(5), pp.986-995.
- Castello, A. et al., 2012. Insights into RNA biology from an atlas of mammalian mRNA-binding proteins. *Cell*, 149(6), pp.1393-1406.
- Caudy, A. A. et al., 2002. Fragile X-related protein and VIG associate with the RNA interference machinery. *Genes Dev*, 16(19), pp.2491-2496.
- Chang, C. T. et al., 2014. The activation of the decapping enzyme DCP2 by DCP1 occurs on the EDC4 scaffold and involves a conserved loop in DCP1. *Nucleic Acids Res*, 42(8), pp.5217-5233.
- Chen, C. Y. et al., 2011. Mechanisms of deadenylation-dependent decay. *Wiley Interdiscip Rev RNA*, 2(2), pp.167-183.
- Chen, G. et al., 2011. The NF-kappaB transcription factor c-Rel is required for Th17 effector cell development in experimental autoimmune encephalomyelitis. *J Immunol*, 187(9), pp.4483-4491.
- Chen, J., 2016. The Cell-Cycle Arrest and Apoptotic Functions of p53 in Tumor Initiation and Progression. *Cold Spring Harb Perspect Med*, 6(3).
- Codutti, L. et al., 2015. A Distinct, Sequence-Induced Conformation Is Required for Recognition of the Constitutive Decay Element RNA by Roquin. *Structure*, 23(8), pp.1437-1447.
- Coller, J. et al., 2005. General translational repression by activators of mRNA decapping. *Cell*, 122(6), pp.875-886.
- Cooke, A. et al., 2010. Translational repression by deadenylases. *J Biol Chem*, 285(37), pp.28506-28513.
- De Boulle, K. et al., 1993. A point mutation in the FMR-1 gene associated with fragile X mental retardation. *Nat Genet*, 3(1), pp.31-35.
- De Silva, N. S. et al., 2015. Dynamics of B cells in germinal centres. *Nat Rev Immunol*, 15(3), pp.137-148.
- Decker, C. J. et al., 2012. P-bodies and stress granules: possible roles in the control of translation and mRNA degradation. *Cold Spring Harb Perspect Biol*, 4(9), a012286.
- Dharmacon. What is siRNA and how do you use it? Retrieved from <http://dharmacon.gelifesciences.com/applications/rna-interference/sirna/>

- Didiot, M. C. et al., 2009. Cells lacking the fragile X mental retardation protein (FMRP) have normal RISC activity but exhibit altered stress granule assembly. *Mol Biol Cell*, *20*(1), pp.428-437.
- Dixon, S. J. et al., 2012. Ferroptosis: an iron-dependent form of nonapoptotic cell death. *Cell*, *149*(5), pp.1060-1072.
- Dolzhanskaya, N. et al., 2006. Methylation regulates the intracellular protein-protein and protein-RNA interactions of FMRP. *J Cell Sci*, *119*(Pt 9), pp.1933-1946.
- Duncan, G. et al., 2001. The link between heparan sulfate and hereditary bone disease: finding a function for the EXT family of putative tumor suppressor proteins. *J Clin Invest*, *108*(4), pp.511-516.
- Duprez, L. et al., 2009. Major cell death pathways at a glance. *Microbes Infect*, *11*(13), pp.1050-1062.
- Edbauer, D. et al., 2010. Regulation of synaptic structure and function by FMRP-associated microRNAs miR-125b and miR-132. *Neuron*, *65*(3), pp.373-384.
- Ellis, R. J., 1996. Discovery of molecular chaperones. *Cell Stress Chaperones*, *1*(3), pp.155-160.
- Eulalio, A. et al., 2007. P-body formation is a consequence, not the cause, of RNA-mediated gene silencing. *Mol Cell Biol*, *27*(11), pp.3970-3981.
- Fan, Y. H. et al., 2013. USP7 inhibitor P22077 inhibits neuroblastoma growth via inducing p53-mediated apoptosis. *Cell Death Dis*, *4*, e867.
- Ferguson, S. E. et al., 1996. CD28 is required for germinal center formation. *J Immunol*, *156*(12), pp.4576-4581.
- Fernandes-Alnemri, T. et al., 2007. The pyroptosome: a supramolecular assembly of ASC dimers mediating inflammatory cell death via caspase-1 activation. *Cell Death Differ*, *14*(9), pp.1590-1604.
- Fos, C. et al., 2008. ICOS ligation recruits the p50alpha PI3K regulatory subunit to the immunological synapse. *J Immunol*, *181*(3), pp.1969-1977.
- Fullgrabe, J. et al., 2014. The return of the nucleus: transcriptional and epigenetic control of autophagy. *Nat Rev Mol Cell Biol*, *15*(1), pp.65-74.
- Galluzzi, L. et al., 2009. Guidelines for the use and interpretation of assays for monitoring cell death in higher eukaryotes. *Cell Death Differ*, *16*(8), pp.1093-1107.
- Galluzzi, L. et al., 2012. Molecular definitions of cell death subroutines: recommendations of the Nomenclature Committee on Cell Death 2012. *Cell Death Differ*, *19*(1), pp.107-120.

- Gammoh, N. et al., 2012. Role of autophagy in histone deacetylase inhibitor-induced apoptotic and nonapoptotic cell death. *Proc Natl Acad Sci U S A*, 109(17), pp.6561-6565.
- Gerstberger, S. et al., 2014. A census of human RNA-binding proteins. *Nat Rev Genet*, 15(12), pp.829-845.
- Gilks, N. et al., 2004. Stress granule assembly is mediated by prion-like aggregation of TIA-1. *Mol Biol Cell*, 15(12), pp.5383-5398.
- Glasmacher, E., 2010. *Roquin binds to ICOS mRNA for P body-dependent and miRNA-independent posttranscriptional gene silencing*. (PhD thesis), Ludwig Maximilians Universitaet, Muenchen.
- Glasmacher, E. et al., 2010. Roquin binds inducible costimulator mRNA and effectors of mRNA decay to induce microRNA-independent post-transcriptional repression. *Nat Immunol*, 11(8), pp.725-733.
- Goronzy, J. J. et al., 2015. High-throughput sequencing insights into T-cell receptor repertoire diversity in aging. *Genome Med*, 7(1), p.117.
- Gossen, M. et al., 1995. Transcriptional activation by tetracyclines in mammalian cells. *Science*, 268(5218), pp.1766-1769.
- Gross, J. A. et al., 1992. Identification and distribution of the costimulatory receptor CD28 in the mouse. *J Immunol*, 149(2), pp.380-388.
- Hameyer, D. et al., 2007. Toxicity of ligand-dependent Cre recombinases and generation of a conditional Cre deleter mouse allowing mosaic recombination in peripheral tissues. *Physiol Genomics*, 31(1), pp.32-41.
- Han, J. et al., 2004. The Drosha-DGCR8 complex in primary microRNA processing. *Genes Dev*, 18(24), pp.3016-3027.
- Heckl, D. et al., 2014. Generation of mouse models of myeloid malignancy with combinatorial genetic lesions using CRISPR-Cas9 genome editing. *Nat Biotechnol*, 32(9), pp.941-946.
- Heissmeyer, V. et al., 2005. A plague of autoantibodies. *Nat Immunol*, 6(7), pp.642-644.
- Henderson, M. C. et al., 2013. High-throughput RNAi screening for the identification of novel targets. *Methods Mol Biol*, 986, pp.89-95.
- Hoefig, K. P. et al., 2008. MicroRNAs grow up in the immune system. *Curr Opin Immunol*, 20(3), pp.281-287.
- Hoffmann, A., 2015. *RNA secondary structure determinants of Roquin - RNA interactions*. (Master thesis), Martin-Luther-University Halle-Wittenberg, Halle (Saale).

- Huang, W. et al., 2015. The signaling symphony: T cell receptor tunes cytokine-mediated T cell differentiation. *J Leukoc Biol*, 97(3), pp.477-485.
- Huber, M. et al., 2008. IRF4 is essential for IL-21-mediated induction, amplification, and stabilization of the Th17 phenotype. *Proc Natl Acad Sci U S A*, 105(52), pp.20846-20851.
- Hug, N. et al., 2016. Mechanism and regulation of the nonsense-mediated decay pathway. *Nucleic Acids Res*, 44(4), pp.1483-1495.
- Huntzinger, E. et al., 2011. Gene silencing by microRNAs: contributions of translational repression and mRNA decay. *Nat Rev Genet*, 12(2), pp.99-110.
- Hutloff, A. et al., 1999. ICOS is an inducible T-cell co-stimulator structurally and functionally related to CD28. *Nature*, 397(6716), pp.263-266.
- Ivanov, P. et al., 2013. Post-transcriptional regulatory networks in immunity. *Immunol Rev*, 253(1), pp.253-272.
- Jacquemin, C. et al., 2015. OX40 Ligand Contributes to Human Lupus Pathogenesis by Promoting T Follicular Helper Response. *Immunity*, 42(6), pp.1159-1170.
- Janeway, C. A., Jr., 2001. How the immune system works to protect the host from infection: a personal view. *Proc Natl Acad Sci U S A*, 98(13), pp.7461-7468.
- Janeway, C. A. J. et al. 2005. *The immune system in health and disease* (6 ed.): Garland Science Publishing. ISBN 0-8153-4101-6.
- Janowski, R. et al., 2016. Roquin recognizes a non-canonical hexaloop structure in the 3'-UTR of Ox40. *Nat Commun*, 7, pp.11032.
- Jeltsch, K. M. et al., 2016. Regulation of T cell signaling and autoimmunity by RNA-binding proteins. *Curr Opin Immunol*, 39, pp.127-135.
- Jeltsch, K. M. et al., 2014. Cleavage of roquin and regnase-1 by the paracaspase MALT1 releases their cooperatively repressed targets to promote TH17 differentiation. *Nat Immunol*, 15(11), pp.1079-1089.
- Jennes, I. et al., 2009. Multiple osteochondromas: mutation update and description of the multiple osteochondromas mutation database (MObd). *Hum Mutat*, 30(12), pp.1620-1627.
- Jiang, H. et al., 2011. Human adenovirus type 5 induces cell lysis through autophagy and autophagy-triggered caspase activity. *J Virol*, 85(10), pp.4720-4729.
- Jin, P. et al., 2000. Understanding the molecular basis of fragile X syndrome. *Hum Mol Genet*, 9(6), pp.901-908.

- Jinek, M. et al., 2012. A programmable dual-RNA-guided DNA endonuclease in adaptive bacterial immunity. *Science*, 337(6096), pp.816-821.
- Jinek, M. et al., 2013. RNA-programmed genome editing in human cells. *Elife*, 2, e00471.
- Jonas, S. et al., 2015. Towards a molecular understanding of microRNA-mediated gene silencing. *Nat Rev Genet*, 16(7), pp.421-433.
- Jung, C. H. et al., 2009. ULK-Atg13-FIP200 complexes mediate mTOR signaling to the autophagy machinery. *Mol Biol Cell*, 20(7), pp.1992-2003.
- Kalebic, N. et al., 2016. CRISPR/Cas9-induced disruption of gene expression in mouse embryonic brain and single neural stem cells in vivo. *EMBO Rep*, 17(3), pp.338-348.
- Kato, M. et al., 2012. Cell-free formation of RNA granules: low complexity sequence domains form dynamic fibers within hydrogels. *Cell*, 149(4), pp.753-767.
- Kawai, T. et al., 2009. The roles of TLRs, RLRs and NLRs in pathogen recognition. *Int Immunol*, 21(4), pp.317-337.
- Kedersha, N. et al., 2005. Stress granules and processing bodies are dynamically linked sites of mRNP remodeling. *J Cell Biol*, 169(6), pp.871-884.
- Kim, C. H. et al., 2001. Subspecialization of CXCR5+ T cells: B helper activity is focused in a germinal center-localized subset of CXCR5+ T cells. *J Exp Med*, 193(12), pp.1373-1381.
- Kim, J. H. et al., 2011. High cleavage efficiency of a 2A peptide derived from porcine teschovirus-1 in human cell lines, zebrafish and mice. *PLoS One*, 6(4), e18556.
- Koike-Yusa, H. et al., 2013. Genome-wide recessive genetic screening in mammalian cells with a lentiviral CRISPR-guide RNA library. *Nat Biotechnol*.
- Komander, D. et al., 2009. Breaking the chains: structure and function of the deubiquitinases. *Nat Rev Mol Cell Biol*, 10(8), pp.550-563.
- Kon, N. et al., 2010. Inactivation of HAUSP in vivo modulates p53 function. *Oncogene*, 29(9), pp.1270-1279.
- Korn, T. et al., 2008. IL-6 controls Th17 immunity in vivo by inhibiting the conversion of conventional T cells into Foxp3+ regulatory T cells. *Proc Natl Acad Sci U S A*, 105(47), pp.18460-18465.
- Krutzik, P. O. et al., 2011. Fluorescent cell barcoding for multiplex flow cytometry. *Curr Protoc Cytom, Chapter 6, Unit 6.31*.
- Krutzik, P. O. et al., 2006. Fluorescent cell barcoding in flow cytometry allows high-throughput drug screening and signaling profiling. *Nat Methods*, 3(5), pp.361-368.

- Labbé, K. et al. 2011. *The inflammasomes*: Springer Basel. 978-3-0348-0147-8.
- Lazzaretti, D. et al., 2009. The C-terminal domains of human TNRC6A, TNRC6B, and TNRC6C silence bound transcripts independently of Argonaute proteins. *Rna*, 15(6), pp.1059-1066.
- Leavenworth, J. W. et al., 2015. A p85alpha-osteopontin axis couples the receptor ICOS to sustained Bcl-6 expression by follicular helper and regulatory T cells. *Nat Immunol*, 16(1), pp.96-106.
- Lee, S. K. et al., 2011. B cell priming for extrafollicular antibody responses requires Bcl-6 expression by T cells. *J Exp Med*, 208(7), pp.1377-1388.
- Lee, S. K. et al., 2012. Interferon-gamma excess leads to pathogenic accumulation of follicular helper T cells and germinal centers. *Immunity*, 37(5), pp.880-892.
- Lee, Y. et al., 2003. The nuclear RNase III Drosha initiates microRNA processing. *Nature*, 425(6956), pp.415-419.
- Leppek, K. et al., 2013. Roquin promotes constitutive mRNA decay via a conserved class of stem-loop recognition motifs. *Cell*, 153(4), pp.869-881.
- Li, B. et al., 2013. Sodium arsenite induced reactive oxygen species generation, nuclear factor (erythroid-2 related) factor 2 activation, heme oxygenase-1 expression, and glutathione elevation in Chang human hepatocytes. *Environ Toxicol*, 28(7), pp.401-410.
- Li, M. et al., 2004. A dynamic role of HAUSP in the p53-Mdm2 pathway. *Mol Cell*, 13(6), pp.879-886.
- Li, W. et al., 2014a. MAGeCK enables robust identification of essential genes from genome-scale CRISPR/Cas9 knockout screens. *Genome Biol*, 15(12), p.554.
- Li, Y. et al., 2014b. FMRP regulates miR196a-mediated repression of HOXB8 via interaction with the AGO2 MID domain. *Mol Biosyst*, 10(7), pp.1757-1764.
- Liang, J. et al., 2010. MCP-induced protein 1 deubiquitinates TRAF proteins and negatively regulates JNK and NF-kappaB signaling. *J Exp Med*, 207(13), pp.2959-2973.
- Lin, R. J. et al., 2013. MCPIP1 ribonuclease exhibits broad-spectrum antiviral effects through viral RNA binding and degradation. *Nucleic Acids Res*, 41(5), pp.3314-3326.
- Linterman, M. A. et al., 2009. Roquin differentiates the specialized functions of duplicated T cell costimulatory receptor genes CD28 and ICOS. *Immunity*, 30(2), pp.228-241.
- Liu, X. et al., 2014. Transcription factor achaete-scute homologue 2 initiates follicular T-helper-cell development. *Nature*, 507(7493), pp.513-518.

- Maggio, I. et al., 2014. Adenoviral vector delivery of RNA-guided CRISPR/Cas9 nuclease complexes induces targeted mutagenesis in a diverse array of human cells. *Sci Rep*, 4, p.5105.
- Maier, E. et al., 2012. STAT6-dependent and -independent mechanisms in Th2 polarization. *Eur J Immunol*, 42(11), pp.2827-2833.
- Mali, P. et al., 2013. Cas9 as a versatile tool for engineering biology. *Nat Methods*, 10(10), pp.957-963.
- Manjunath, N. et al., 2013. Newer gene editing technologies toward HIV gene therapy. *Viruses*, 5(11), pp.2748-2766.
- Marine, S. et al., 2012. Common seed analysis to identify off-target effects in siRNA screens. *J Biomol Screen*, 17(3), pp.370-378.
- Maruyama, T. et al., 2014. Roquin-2 Promotes Ubiquitin-Mediated Degradation of ASK1 to Regulate Stress Responses. *Sci Signal*, 7(309), ra8.
- McAdam, A. J. et al., 2001. ICOS is critical for CD40-mediated antibody class switching. *Nature*, 409(6816), pp.102-105.
- McHeyzer-Williams, L. J. et al., 2015. Class-switched memory B cells remodel BCRs within secondary germinal centers. *Nat Immunol*, 16(3), pp.296-305.
- McKee, A. E. et al., 2007. Systems perspectives on mRNA processing. *Cell Res*, 17(7), pp.581-590.
- Mino, T. et al., 2015. Regnase-1 and Roquin Regulate a Common Element in Inflammatory mRNAs by Spatiotemporally Distinct Mechanisms. *Cell*, 161(5), pp.1058-1073.
- Molle, C. et al., 2013. Tristetraprolin regulation of interleukin 23 mRNA stability prevents a spontaneous inflammatory disease. *J Exp Med*, 210(9), pp.1675-1684.
- Murakawa, Y. et al., 2015. RC3H1 post-transcriptionally regulates A20 mRNA and modulates the activity of the IKK/NF-kappaB pathway. *Nat Commun*, 6, p.7367.
- Nikoletopoulou, V. et al., 2013. Crosstalk between apoptosis, necrosis and autophagy. *Biochim Biophys Acta*, 1833(12), pp.3448-3459.
- Ohn, T. et al., 2008. A functional RNAi screen links O-GlcNAc modification of ribosomal proteins to stress granule and processing body assembly. *Nat Cell Biol*, 10(10), pp.1224-1231.
- Okamoto, K. et al., 2010. IkappaBzeta regulates T(H)17 development by cooperating with ROR nuclear receptors. *Nature*, 464(7293), pp.1381-1385.
- Onishi, R. M. et al., 2010. Interleukin-17 and its target genes: mechanisms of interleukin-17 function in disease. *Immunology*, 129(3), pp.311-321.

- Oropallo, M. A. et al., 2014. Germinal center reaction: antigen affinity and presentation explain it all. *Trends Immunol*, 35(7), pp.287-289.
- Park, W. R. et al., 2004. A mechanism underlying STAT4-mediated up-regulation of IFN-gamma induction in TCR-triggered T cells. *Int Immunol*, 16(2), pp.295-302.
- Phillips, T., 2008. Regulation of transcription and gene expression in eukaryotes. *Nature Education*, 1(1), pp.199.
- Pratama, A. et al., 2013. Roquin-2 shares functions with its paralog Roquin-1 in the repression of mRNAs controlling T follicular helper cells and systemic inflammation. *Immunity*, 38(4), pp.669-680.
- Pratama, A. et al., 2015. MicroRNA-146a regulates ICOS-ICOSL signalling to limit accumulation of T follicular helper cells and germinal centres. *Nat Commun*, 6, pp.6436.
- Rabani, M. et al., 2011. Metabolic labeling of RNA uncovers principles of RNA production and degradation dynamics in mammalian cells. *Nat Biotechnol*, 29(5), pp.436-442.
- Ramos, A. et al., 2006. The structure of the N-terminal domain of the fragile X mental retardation protein: a platform for protein-protein interaction. *Structure*, 14(1), pp.21-31.
- Reijns, M. A. et al., 2008. A role for Q/N-rich aggregation-prone regions in P-body localization. *J Cell Sci*, 121(Pt 15), pp.2463-2472.
- Reinhard, K. et al., 2011. c-Rel promotes type 1 and type 17 immune responses during Leishmania major infection. *Eur J Immunol*, 41(5), pp.1388-1398.
- Rolf, J. et al., 2010. Phosphoinositide 3-kinase activity in T cells regulates the magnitude of the germinal center reaction. *J Immunol*, 185(7), pp.4042-4052.
- Ruan, Q. et al., 2011. The Th17 immune response is controlled by the Rel-RORgamma-RORgamma T transcriptional axis. *J Exp Med*, 208(11), pp.2321-2333.
- Said, N. A. et al., 2014. Whole-genome multiparametric screening to identify modulators of epithelial-to-mesenchymal transition. *Assay Drug Dev Technol*, 12(7), pp.385-394.
- Salomon, B. et al., 2000. B7/CD28 costimulation is essential for the homeostasis of the CD4+CD25+ immunoregulatory T cells that control autoimmune diabetes. *Immunity*, 12(4), pp.431-440.
- Sanjana, N. E. et al., 2014. Improved vectors and genome-wide libraries for CRISPR screening. *Nat Methods*, 11(8), pp.783-784.
- Schlundt, A. et al., 2014. Structural basis for RNA recognition in roquin-mediated post-transcriptional gene regulation. *Nat Struct Mol Biol*, 21(8), pp.671-678.

- Schlundt, A. et al., 2016. RNA recognition by Roquin in posttranscriptional gene regulation. *Wiley Interdiscip Rev RNA*.
- Schmitt, N. et al., 2015. Regulation of human helper T cell subset differentiation by cytokines. *Curr Opin Immunol*, 34, pp.130-136.
- Schwarz, D. S. et al., 2003. Asymmetry in the assembly of the RNAi enzyme complex. *Cell*, 115(2), pp.199-208.
- Schwarzer, C. et al., 2014. Pseudomonas aeruginosa homoserine lactone triggers apoptosis and Bak/Bax-independent release of mitochondrial cytochrome C in fibroblasts. *Cell Microbiol*, 16(7), pp.1094-1104.
- Seglen, P. O. et al., 1982. 3-Methyladenine: specific inhibitor of autophagic/lysosomal protein degradation in isolated rat hepatocytes. *Proc Natl Acad Sci U S A*, 79(6), pp.1889-1892.
- Shahinian, A. et al., 1993. Differential T cell costimulatory requirements in CD28-deficient mice. *Science*, 261(5121), pp.609-612.
- Shalem, O. et al., 2014. Genome-scale CRISPR-Cas9 knockout screening in human cells. *Science*, 343(6166), pp.84-87.
- Shaner, N. C. et al., 2005. A guide to choosing fluorescent proteins. *Nat Methods*, 2(12), pp.905-909.
- Sharif, H. et al., 2013. Architecture of the Lsm1-7-Pat1 complex: a conserved assembly in eukaryotic mRNA turnover. *Cell Rep*, 5(2), pp.283-291.
- Sharma, S. et al., 2013. An siRNA screen for NFAT activation identifies septins as coordinators of store-operated Ca<sup>2+</sup> entry. *Nature*, 499(7457), pp.238-242.
- Sharma, S. et al., 2009. RNAi screening: tips and techniques. *Nat Immunol*, 10(8), pp.799-804.
- Shen, B. et al., 2014. Efficient genome modification by CRISPR-Cas9 nickase with minimal off-target effects. *Nat Methods*, 11(4), pp.399-402.
- Sheng, Y. et al., 2006. Molecular recognition of p53 and MDM2 by USP7/HAUSP. *Nat Struct Mol Biol*, 13(3), pp.285-291.
- Shirai, Y. T. et al., 2014. Multifunctional roles of the mammalian CCR4-NOT complex in physiological phenomena. *Front Genet*, 5, p.286.
- Siess, D. C. et al., 2000. A human gene coding for a membrane-associated nucleic acid-binding protein. *J Biol Chem*, 275(43), pp.33655-33662.
- Sigoillot, F. D. et al., 2012. A bioinformatics method identifies prominent off-targeted transcripts in RNAi screens. *Nat Methods*, 9(4), pp.363-366.

- Simon Davis, D. A. et al., 2013. Heparan sulfate: a ubiquitous glycosaminoglycan with multiple roles in immunity. *Front Immunol*, 4, p.470.
- Simpson, J. C. et al., 2012. Genome-wide RNAi screening identifies human proteins with a regulatory function in the early secretory pathway. *Nat Cell Biol*, 14(7), pp.764-774.
- Sims, D. et al., 2011. High-throughput RNA interference screening using pooled shRNA libraries and next generation sequencing. *Genome Biol*, 12(10), R104.
- Sojka, D. K. et al., 2008. Mechanisms of regulatory T-cell suppression - a diverse arsenal for a moving target. *Immunology*, 124(1), pp.13-22.
- Srivastava, M. et al., 2015. Roquin binds microRNA-146a and Argonaute2 to regulate microRNA homeostasis. *Nat Commun*, 6, p.6253.
- Stone, E. L. et al., 2015. ICOS coreceptor signaling inactivates the transcription factor FOXO1 to promote Tfh cell differentiation. *Immunity*, 42(2), pp.239-251.
- Sudbery, I. et al., 2010. Systematic analysis of off-target effects in an RNAi screen reveals microRNAs affecting sensitivity to TRAIL-induced apoptosis. *BMC Genomics*, 11, p.175.
- Suh, W. K. et al., 2004. The inducible costimulator plays the major costimulatory role in humoral immune responses in the absence of CD28. *J Immunol*, 172(10), pp.5917-5923.
- Tan, A. H. et al., 2006. Regulation of mouse inducible costimulator (ICOS) expression by Fyn-NFATc2 and ERK signaling in T cells. *J Biol Chem*, 281(39), pp.28666-28678.
- Tan, D. et al., 2014. The ROQ domain of Roquin recognizes mRNA constitutive-decay element and double-stranded RNA. *Nat Struct Mol Biol*, 21(8), pp.679-685.
- Taylor, G. A. et al., 1996. A pathogenetic role for TNF alpha in the syndrome of cachexia, arthritis, and autoimmunity resulting from tristetraprolin (TTP) deficiency. *Immunity*, 4(5), pp.445-454.
- Tharun, S., 2009. Lsm1-7-Pat1 complex: a link between 3' and 5'-ends in mRNA decay? *RNA Biol*, 6(3), pp.228-232.
- Tubo, N. J. et al., 2014. TCR signal quantity and quality in CD4 T cell differentiation. *Trends Immunol*, 35(12), pp.591-596.
- Uehata, T. et al., 2013. mRNA degradation by the endoribonuclease Regnase-1/ZC3H12a/MCPIP-1. *Biochim Biophys Acta*, 1829(6-7), pp.708-713.
- Uehata, T. et al., 2013. Malt1-induced cleavage of regnase-1 in CD4(+) helper T cells regulates immune activation. *Cell*, 153(5), pp.1036-1049.

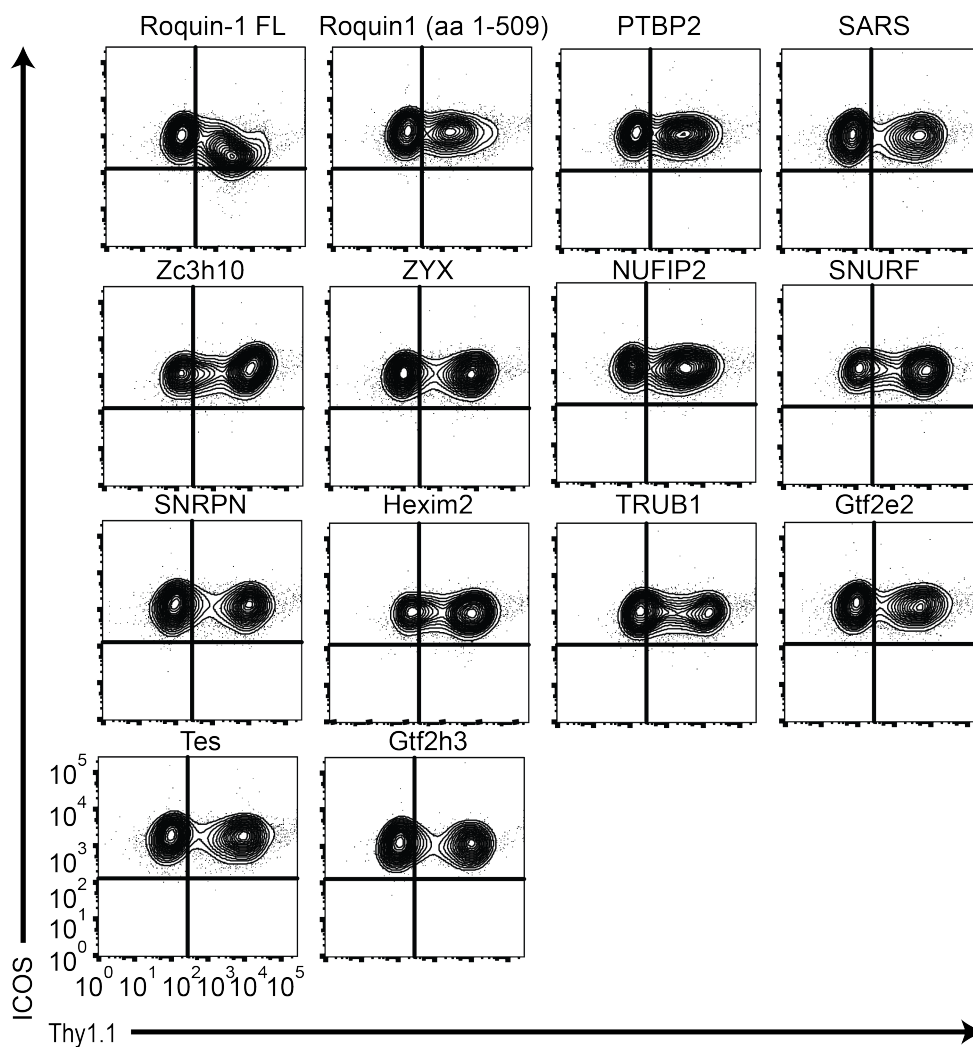
- Vaish, N. et al., 2011. Improved specificity of gene silencing by siRNAs containing unlocked nucleobase analogs. *Nucleic Acids Res*, 39(5), pp.1823-1832.
- van Loosdregt, J. et al., 2013. Stabilization of the transcription factor Foxp3 by the deubiquitinase USP7 increases Treg-cell-suppressive capacity. *Immunity*, 39(2), pp.259-271.
- Vasilyev, N. et al., 2015. Crystal structure reveals specific recognition of a G-quadruplex RNA by a beta-turn in the RGG motif of FMRP. *Proc Natl Acad Sci U S A*, 112(39), E5391-5400.
- Vinuesa, C. G. et al., 2005. A RING-type ubiquitin ligase family member required to repress follicular helper T cells and autoimmunity. *Nature*, 435(7041), pp.452-458.
- Vinuesa, C. G. et al., 2016. Follicular Helper T Cells. *Annu Rev Immunol*.
- Vogel, K., 2012. *Roquin family proteins control T cell co-stimulation and differentiation*. (PhD thesis), Ludwig-Maximilian-Universität München.
- Vogel, K. U. et al., 2013. Roquin paralogs 1 and 2 redundantly repress the Icos and Ox40 costimulator mRNAs and control follicular helper T cell differentiation. *Immunity*, 38(4), pp.655-668.
- Vucic, D. et al., 2011. Ubiquitylation in apoptosis: a post-translational modification at the edge of life and death. *Nat Rev Mol Cell Biol*, 12(7), pp.439-452.
- Walker, L. S. et al., 1999. Compromised OX40 function in CD28-deficient mice is linked with failure to develop CXC chemokine receptor 5-positive CD4 cells and germinal centers. *J Exp Med*, 190(8), pp.1115-1122.
- Wang, T. et al., 2015. Identification and characterization of essential genes in the human genome. *Science*, 350(6264), pp.1096-1101.
- Wang, T. et al., 2014. Genetic screens in human cells using the CRISPR-Cas9 system. *Science*, 343(6166), pp.80-84.
- Warnatz, K. et al., 2006. Human ICOS deficiency abrogates the germinal center reaction and provides a monogenic model for common variable immunodeficiency. *Blood*, 107(8), pp.3045-3052.
- Warner, J. R. et al., 1963. A multiple ribosomal structure in protein synthesis. *Proc Natl Acad Sci U S A*, 49, pp.122-129.
- Weber, J. P. et al., 2015. ICOS maintains the T follicular helper cell phenotype by down-regulating Kruppel-like factor 2. *J Exp Med*, 212(2), pp.217-233.
- Wells, S. E. et al., 1998. Circularization of mRNA by eukaryotic translation initiation factors. *Mol Cell*, 2(1), pp.135-140.

- Wiedenheft, B. et al., 2012. RNA-guided genetic silencing systems in bacteria and archaea. *Nature*, 482(7385), pp.331-338.
- Wilkinson, K. D., 2009. DUBs at a glance. *J Cell Sci*, 122(Pt 14), pp.2325-2329.
- Will, S. et al., 2012. LocARNA-P: accurate boundary prediction and improved detection of structural RNAs. *Rna*, 18(5), pp.900-914.
- Will, S. et al., 2007. Inferring noncoding RNA families and classes by means of genome-scale structure-based clustering. *PLoS Comput Biol*, 3(4), e65.
- Winograd, C. et al., 2011. Fragile X family members have important and non-overlapping functions. *Biomol Concepts*, 2(5), pp.343-352.
- Xie, Y. et al., 2016. Ferroptosis: process and function. *Cell Death Differ*, 23(3), pp.369-379.
- Yamane, H. et al., 2013. Early signaling events that underlie fate decisions of naive CD4(+) T cells toward distinct T-helper cell subsets. *Immunol Rev*, 252(1), pp.12-23.
- Yamashita, A. et al., 2005. Concerted action of poly(A) nucleases and decapping enzyme in mammalian mRNA turnover. *Nat Struct Mol Biol*, 12(12), pp.1054-1063.
- Yong, P. F. et al., 2009. The role of costimulation in antibody deficiencies: ICOS and common variable immunodeficiency. *Immunol Rev*, 229(1), pp.101-113.
- Yu, D. et al., 2007. Roquin represses autoimmunity by limiting inducible T-cell co-stimulator messenger RNA. *Nature*, 450(7167), pp.299-303.
- Zhang, J. H. et al., 1999. A Simple Statistical Parameter for Use in Evaluation and Validation of High Throughput Screening Assays. *J Biomol Screen*, 4(2), pp.67-73.
- Zhang, M. et al., 1997. Spermine inhibits proinflammatory cytokine synthesis in human mononuclear cells: a counterregulatory mechanism that restrains the immune response. *J Exp Med*, 185(10), pp.1759-1768.
- Zheng, D. et al., 2008. Deadenylation is prerequisite for P-body formation and mRNA decay in mammalian cells. *J Cell Biol*, 182(1), pp.89-101.
- Zheng, Q. et al., 2014. Precise gene deletion and replacement using the CRISPR/Cas9 system in human cells. *Biotechniques*, 57(3), pp.115-124.
- Zhou, Y. et al., 2014. High-throughput screening of a CRISPR/Cas9 library for functional genomics in human cells. *Nature*, 509(7501), pp.487-491.
- Zhu, J. et al., 2010. Peripheral CD4+ T-cell differentiation regulated by networks of cytokines and transcription factors. *Immunol Rev*, 238(1), pp.247-262.

## Appendices

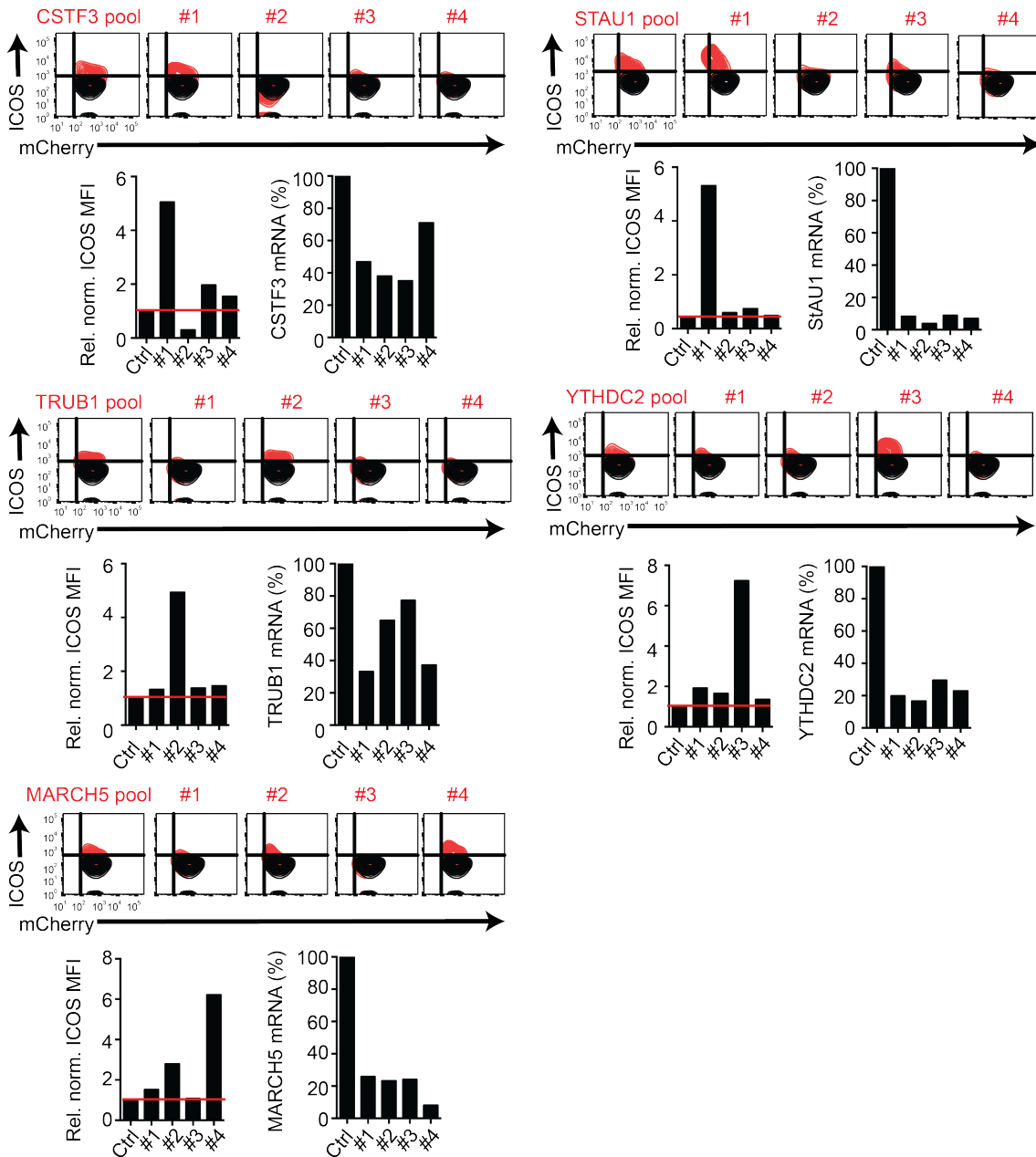
### *Appendix I: Validation of candidates from the RBP subset by overexpression.*

Flow cytometric analysis of ICOS and Thy1.1 expression in HeLa cells with constitutive ICOS expression upon overexpression of mouse or human cDNA encoding 12 RNA-binding candidates from the targeted Roquin-1 cofactor screen. Roquin-1 full-length (FL) was employed as a positive control, while Roquin-1 (1-509) served as a negative control. Thy1.1 was used as a marker for retroviral transduction with the overexpression constructs.



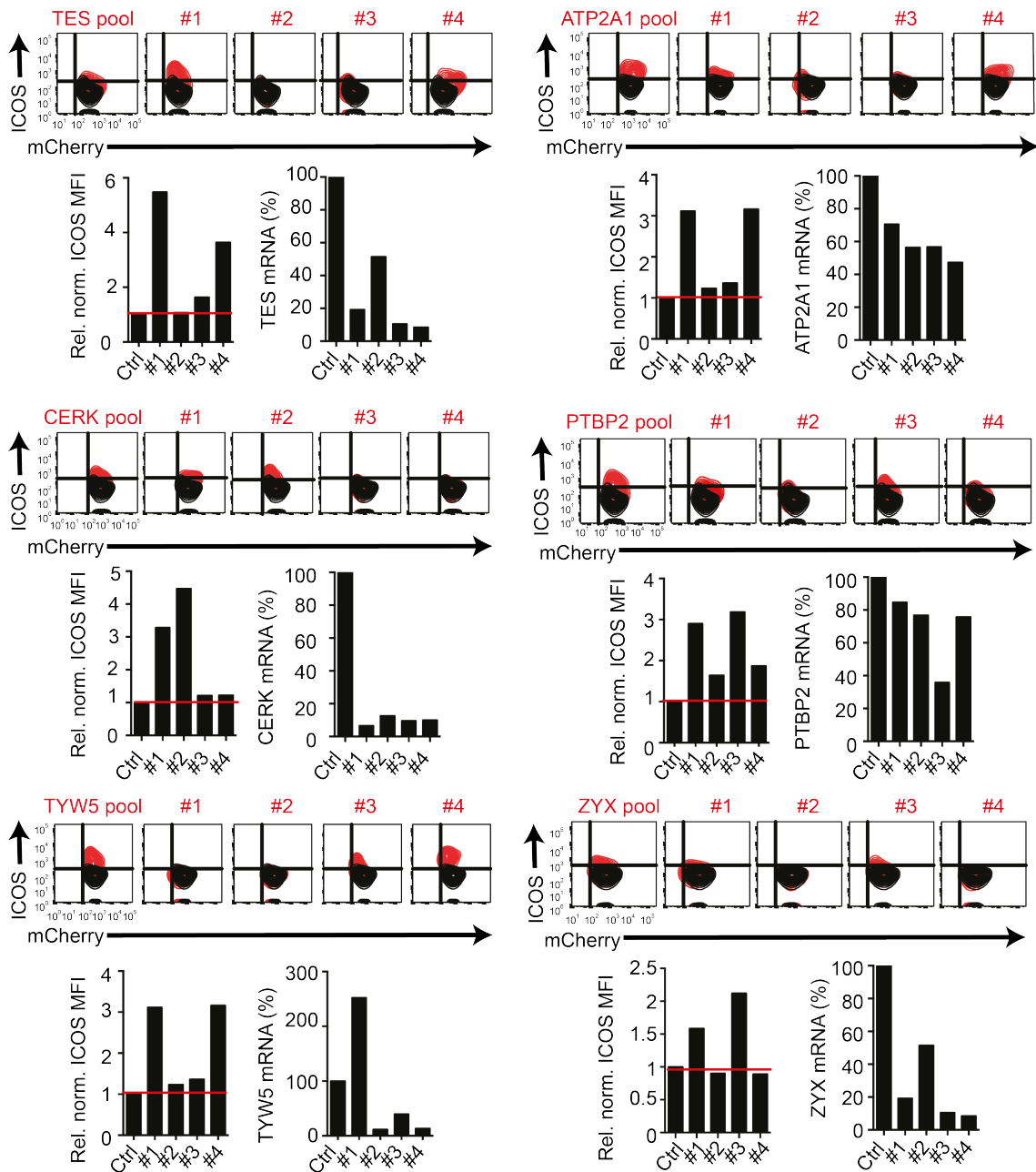
## Appendix II: Deconvolution of siRNA pools into individual siRNAs identifies five single hitters.

Flow cytometric analysis of ICOS and mCherry expression for deconvolution of siRNA pools into individual siRNAs is shown for 5 candidates, where only one siRNA in the pool was responsible for ICOS derepression.



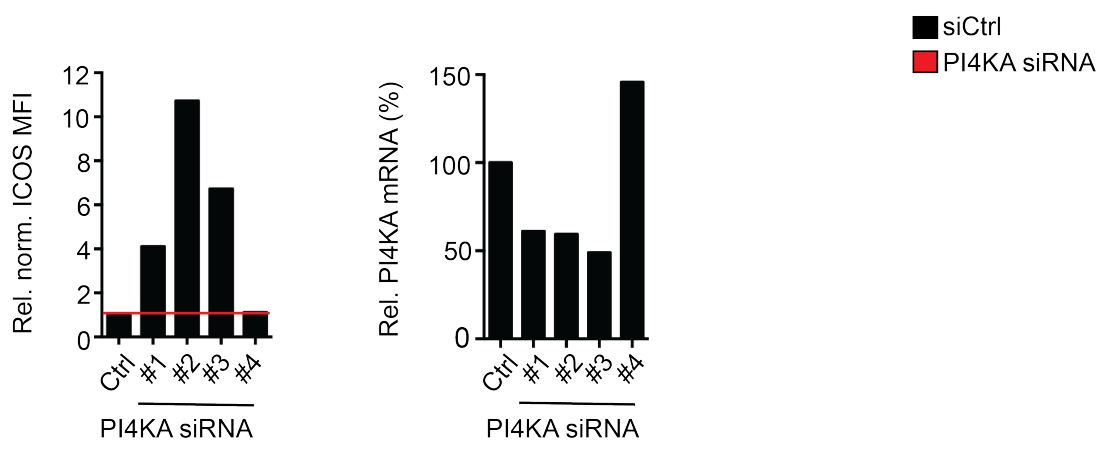
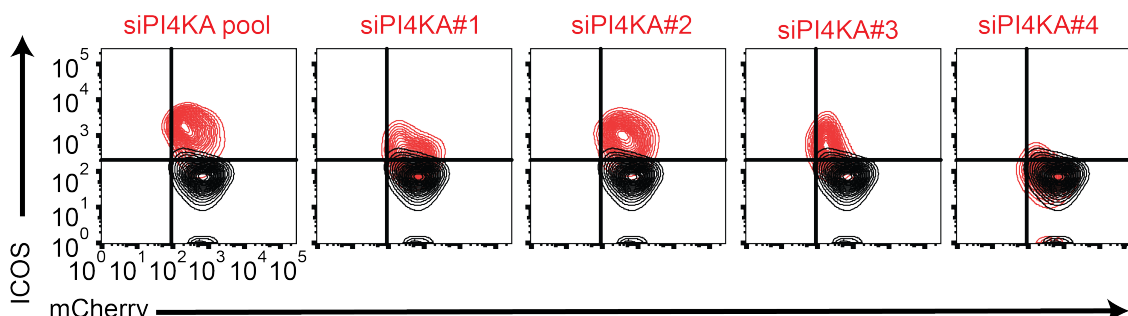
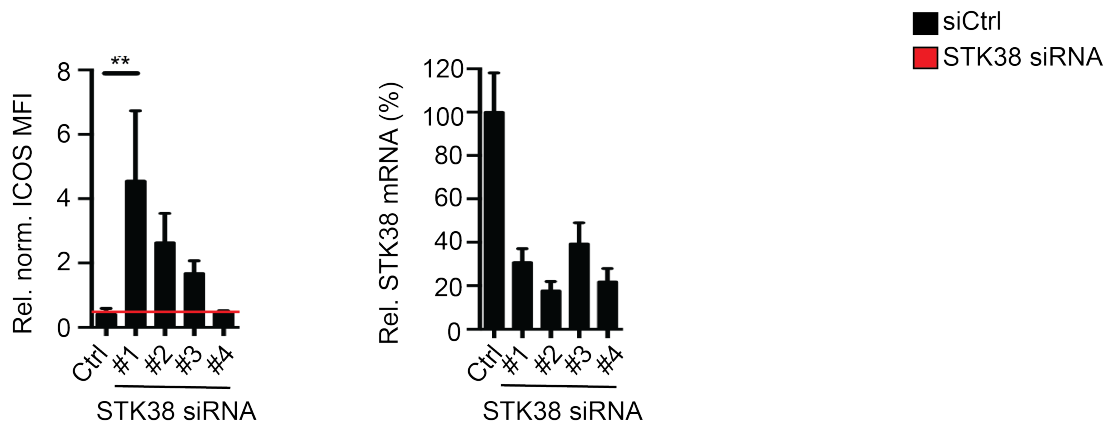
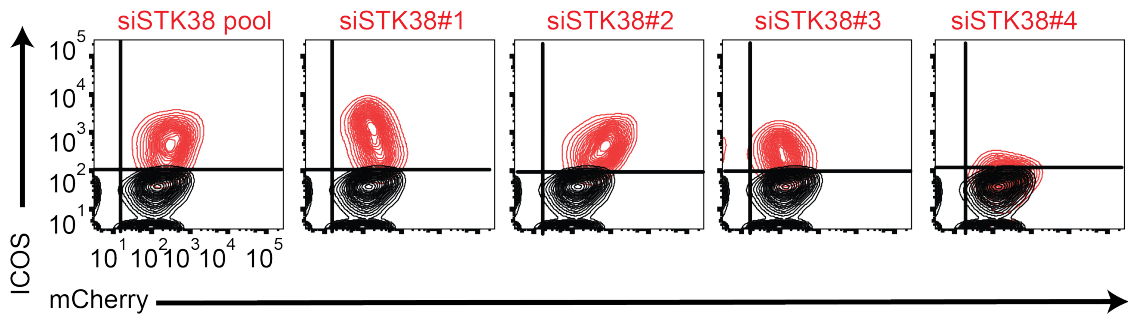
**Appendix III: Deconvolution of siRNA pools into individual siRNAs identifies six candidates with two scoring siRNA.**

Flow cytometric analysis of ICOS and mCherry expression for deconvolution of siRNA pools into individual siRNAs is shown for six candidates where two siRNA mediated the effect of the pool.



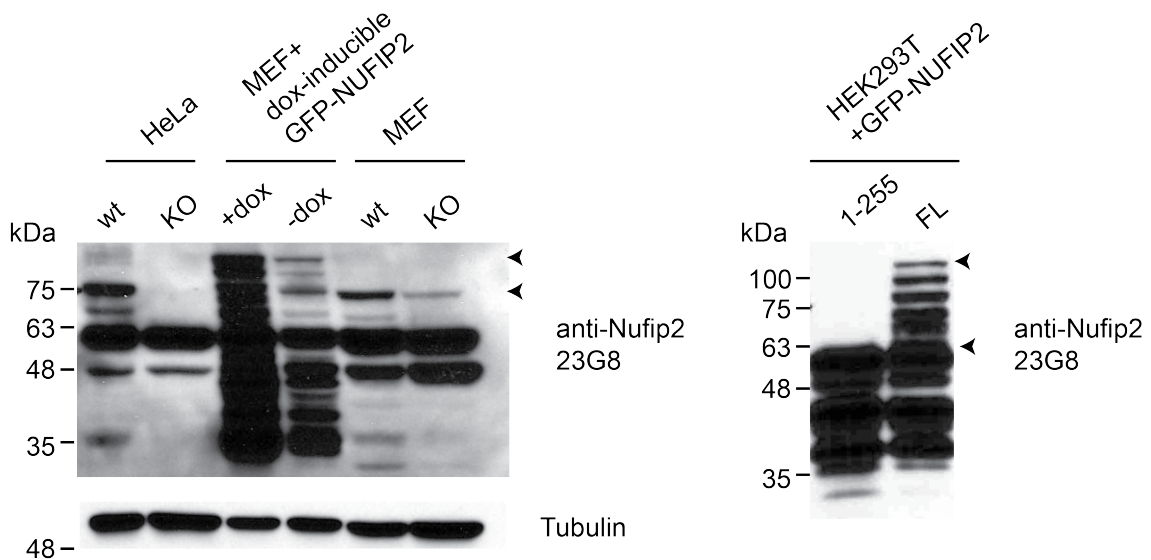
**Appendix IV Deconvolution of the PI4KA and STK38 siRNA pools shows a strong correlation between knockdown efficiency and ICOS derepression for multiple siRNAs.**

Flow cytometric analysis of ICOS and mCherry expression for deconvolution of siRNA pools into individual siRNAs is shown for the kinases STK38 and PI4KA.



**Appendix V: A new monoclonal Nufip2-antibody recognizes the N-terminus of Nufip2 with high affinity and specificity.**

Immunoblot analysis of whole cell lysates from different cell lines probed with the newly established monoclonal Nufip2 antibody (23G8). Nufip2 knockout (KO) HeLa and MEF cells were created by transduction with lentiCRISPR encoding a human or mouse Nufip2-targeting sgRNA, respectively. From HeLa cells, a stable clone was generated, showing no Nufip2 signal, while bulk cells with some residual Nufip2 expression are shown for MEF cells. In addition to the specific Nufip2 signals at 75 kDa for endogenous Nufip2 and 110 kDa for overexpressed GFP-NUFIP2 (black arrows), the antibody shows two unspecific bands at 63 and 48 kDa. Detection of the N-terminal part of NUFIP2 was shown by overexpression of GFP-NUFIP2 (aa 1-255) versus GFP-NUFIP2 full-length (FL).



## Publications

### Articles connected to this thesis

Jeltsch KM\*, Hu D\*, Brenner S\*, Zöller J, Heinz GA, Nagel D, Vogel KU, **Rehage N**, Warth SC, Edelmann SL, Gloury R, Martin N, Lohs C, Lech M, Stehklein JE, Geerlof A, Kremmer E, Weber A, Anders HJ, Schmitz I, Schmidt-Supprian M, Fu M, Holtmann H, Krappmann D, Ruland J, Kallies A, Heikenwalder M, Heissmeyer V. **Cleavage of roquin and regnase-1 by the paracaspase MALT1 releases their cooperatively repressed targets to promote T(H)17 differentiation.** *Nat Immunol.* 2014 Nov;15(11) pp. 1079-89 \*equal contribution

### Additional articles

Chauvistré H, Küstermann C, **Rehage N**, Klisch T, Mitzka S, Felker P, Rose-John S, Zenke M, Seré KM. **Dendritic cell development requires histone deacetylase activity.** *Eur J Immunol.* 2014 Aug;44(8) pp. 2478-88

Ma HC, Liu Y, Wang C, Strauss M, **Rehage N**, Chen YH, Altan-Bonnet N, Hogle J, Wimmer E, Mueller S, Paul AV, Jiang P. **An interaction between glutathione and the capsid is required for the morphogenesis of C-cluster enteroviruses.** *PLoS Pathog.* 2014 Apr 10;10(4)

Hosszu KK, Valentino A, Ji Y, Matkovic M, Pednekar L, **Rehage N**, Tumma N, Peerschke EI, Ghebrehiwet B. **Cell surface expression and function of the macromolecular c1 complex on the surface of human monocytes.** *Front Immunol.* 2012 Mar 5;3:38

Séré KM, Lin Q, Felker P, **Rehage N**, Klisch T, Ortseifer I, Hieronymus T, Rose-John S, Zenke M. **Dendritic cell lineage commitment is instructed by distinct cytokine signals.** *Eur J Cell Biol.* 2012 Jun-Jul;91(6-7) pp. 515-23

---

## Poster presentations connected to this thesis

Nina Rehage , Eunhae Lee , James Gray , Sonia Sharma and Vigo Heissmeyer. **A targeted siRNA screen for Roquin cofactors in posttranscriptional regulation of ICOS.** La Jolla Institute for Allergy and Immunology, Annual Retreat 2013

Nina Rehage, Eunhae Lee, James Gray, Sonia Sharma, Stephanie Edelmann, and Vigo Heissmeyer. **Screening for Roquin Cofactors in Posttranscriptional Gene Regulation.** 3rd European CRISPR meeting, Berlin, Germany from May 14 -16, 2014

Nina Rehage , Eunhae Lee , James Gray , Sonia Sharma and Vigo Heissmeyer. **Screening for Roquin Cofactors in Posttranscriptional Gene Regulation.** Midwinter Conference “Advances in Immunology”, Seefeld, Austria from January 17 – 21, 2015

Nina Rehage, Jenny Stehklein, Eunhae Lee, Sonia Sharma and Vigo Heissmeyer. **High-throughput RNAi screening for cofactors of post-transcriptional gene regulation.** 13<sup>th</sup> annual Discovery on Target conference, Boston, MA, USA, September 21 – 25, 2015

## Acknowledgements

I would like to thank all people who contributed to the development and accomplishment of this research project.

First of all, I would like to thank my supervisor Prof. Dr. Vigo Heissmeyer for providing me with this challenging and fascinating project and for guiding me through my thesis as a great mentor.

Furthermore I would like to express my gratitude to Dr. Anjana Rao and Dr. Sonia Sharma from *La Jolla Institute for Allergy and Immunology* for giving me the opportunity to perform the siRNA screen at the *Functional Genomics Center* under their committed supervision. I would also like to thank James Gray and Eunhae Lee from the *Functional Genomics Center* for excellent technical support and HELENA for funding this part of my project in the form of a lab exchange.

Special thanks to the members of my thesis advisory committee Prof. Dr. Daniel Krappmann, Prof. Dr. Ludger Klein and Dr. Kamyar Hadian for their valuable input.

I would like to thank Dr. Kai Höfig for the fruitful cooperation on the CRISPR/Cas9 screening project and for committed proofreading of my thesis.

Deep sequencing of the CRISPR/Cas9 knockout screen samples was kindly performed by Dr. Stefan Krebs in the lab of Dr. Helmut Blum at the *Gene Center Munich*, whom I would also like to thank. In addition, I cordially thank Dr. Dirk Repsilber and Dr. Brynjar Bjarnason from *Örebro Universitet Sweden* for bioinformatics analyses of the next generation sequencing data.

I deeply thank Jenny Stehklein for providing the Nufip2 project with outstanding technical support in the form of qPCR assays, co-immunoprecipitations and immunoblotting assays and especially for reliable testing of the 72 anti-Nufip2 hybridoma antibody supernatants.

I deeply thank our collaborators,

Prof. Dr. Dierk Niessing and Elena Davydova from the *Department for Cell Biology, LMU München*, for providing us with the Biacore experiment (Figure 30) that shows direct interaction between Nufip2 and Roquin-1 and for the valuable collaboration on the Nufip2 project.

Dr. Jörg Hackermüller, Dr. Kristin Reiche and Anne Hoffmann from *UFZ Leipzig* for modeling the secondary structure of human *ICOS* 3' UTR by multiple sequence and structure alignment (Figure 35).

Moreover, I am very grateful for the help of Christine Conrad, Aicha Jeridi, Dr. Sven Brenner, Dr. Desheng Hu and Christoph Mayr who contributed to individual experiments. Christine Conrad performed the T cell activation time course (Figure 33), Aicha Jeridi performed the immunoprecipitation of endogenous Roquin (Figure 29), Dr. Sven Brenner evaluated the cooperativity between Roquin-1 and Regnase-1 on the *TNF* CDE and *ICOS* 3' UTR (Figure 18), Dr. Desheng Hu sorted mcherry<sup>+</sup> cells and mcherry<sup>-</sup> cells of the CRISPR screen repeat and Christoph Mayr conducted the overexpression experiment of ubiquitin conjugation candidates (Figure 16) under my supervision. I would also like to thank Claudia Lohs for help and advice on all kinds of lab techniques, and for cloning the *ICOS* Δ700-800 construct. Moreover, I would like to thank all my colleagues and former lab members for the nice working atmosphere.

In addition, I would like to thank all staff of the animal facility, especially Michael Hagemann, for their outstanding cooperativeness.

I would like to thank Dr. Elisabeth Kremmer and Dr. Regina Feederle for the generation of monoclonal Nufip2 antibodies and Dr. Arie Geerlof for the purification of the Nufip2 protein.

Last, but not least, I would like to thank my family and my friends for their help and support throughout my PhD.